Lateral-Torsional-Roll Buckling of Uncracked and Cracked Long-Span Prestressed Concrete Girders

Henry Knight

A thesis

submitted in partial fulfillment of the

requirements for the degree of

Master of Science

University of Washington

2023

Committee:

Richard Wiebe

John Stanton

Paolo Calvi

Program Authorized to Offer Degree:

Civil and Environmental Engineering

University of Washington

Abstract

Lateral-Torsional-Roll Buckling of Uncracked and Cracked Long-Span Prestressed Concrete Girders

Henry Knight

Chair of the Supervisory Committee:

Richard Wiebe

Civil and Environmental Engineering

Lateral instability in long-span prestressed concrete girders during handling, transportation, and construction can result in disruptive, damaging, and even deadly failures. Historically, the predominant instability mechanism in these girders has been buckling in the form of a rigid-body roll combined with lateral bending. As increasingly longer bridge spans are designed, their girders become more susceptible to lateral stability issues and, notably, see increased twisting deformations—which have frequently been neglected in lateral stability analysis during transportation and handling. This work will include the effects of torsional deformations, strong-axis bending, prestressing deflections, overhangs, and imperfections in developing closed-form buckling loads and equilibrium paths for lateral instability. From these buckling loads, it will

develop and test closed-form models that can predict the lateral stability behavior and equilibrium angle of a long-span girder under different applied loads.

This work seeks to robustly characterize the instability mechanisms of girders during transportation and handling. It incorporates the effects of, and the interactions between, torsional deformations, strong-axis bending, prestressing deflections, overhangs, imperfections, and cracking to predict buckling loads and equilibrium paths that describe lateral instability. In the pre-cracking regime (which is often preferred by design) it develops and evaluates closed-form models that can predict the lateral stability behavior and equilibrium angle of a long-span girder under different applied loads. For post-cracking behavior, a computational model was developed and compared to previous results in the literature. This model was then used to conduct a parametric study to determine which prestressed concrete girder design parameters most impact the onset of cracking, post-cracking stiffness, and ultimate failure angle. This information about cracking was combined with the closed-form buckling equations to propose a new design procedure for prestressed concrete girder lateral stability that works for both uncracked and cracked girders. This procedure was used to explore trends in long-span girder design, and to identify potential limiting parameters that could control the maximum designable length of present-day girder cross sections.

Acknowledgements

I would like to thank Professor John Stanton and Professor Richard Wiebe for their mentorship throughout these last two years. Their advice, guidance, and wisdom made it possible, not just to complete this work, but to truly enjoy the difficult and rewarding process that research is. They taught me that “sometimes there is no answer in the back of the book,” to trust my education and instincts, and, most importantly, to approach challenges and problems with an open mind and a willingness to work hard. I am grateful for all that you have done.

I would also like to thank Professor Paolo Calvi for agreeing to be on my thesis defense committee. I have taken quite a few classes from Professor Calvi, and I have always appreciated his knowledge of structural engineering, excellent teaching, and mentorship.

This work was made possible by the support of the Washington State Department of Transportation (WSDOT), Precast/Prestressed Concrete Institute (PCI), and the Accelerated Bridge Construction-University Transportation Center (ABC-UTC.) Thank you.

Table of Contents

List of Figures

List of Tables

1. Introduction

1.1. **Motivation**

Long-span prestressed concrete bridge girders are susceptible to lateral instability failure, and when they do fail, the results are damaging, dangerous, expensive, and even life-threatening.

Longer girders are more desirable than shorter ones for their overall economy: less infrastructure, fewer lane closures in the middle of highways or waterways, and fewer girders required to be delivered to site all contribute to lower costs. For example, the Washington State Department of Transportation (WSDOT) recently constructed a 223-foot-long single-span bridge over train tracks and the Puyallup River in Washington State using prestressed lightweight concrete (West, 2019). Accelerated Bridge Construction (ABC) is improved by the use of long-span bridge girders.

The principal elements of lateral buckling are lateral deflection, twisting, and rigid body roll. Historically, a large portion of the lateral stability literature has been focused on Lateral-Torsional-Buckling (LTB) of steel girders, e.g., the work by Timoshenko and Gere (1961). In LTB, the supports of the girder are prevented from rotating, and when buckled, the midspan has twisted and deflected laterally relative to the supports. Rigid body roll is seldom an issue in steel lateral instability because, at the time when roll is possible during erection, the self-weight is typically too small to induce buckling. Larger loads occur during the service life of the structure but, by then, the ends of the girders are restrained against rotation and rigid body roll is impossible. The relatively slender nature of steel cross-sections contributes to their low torsional stiffness, hence why they have frequently been the focus of lateral stability work.

For prestressed concrete girders, the opposite is true. Compared to steel girders, they have stockier cross-sections and thus higher self-weights and torsional stiffnesses. The large

self-weight is in place during handling, transportation, and erection, when rigid body roll is not fully restrained. Due to their large self-weight, any eccentricity between center of gravity and support reaction will lead to a corresponding rotation to achieve moment equilibrium. That rotation leads to self-weight bending primarily in the weak-axis direction, which causes the girder to roll even further. This negative feedback cycle of rotations and deflections continues until the girder achieves an equilibrium configuration, or buckling occurs. This is Lateral-Roll-Buckling (LRB) and is contrasted with LTB in that the supports are free to roll, and no differential twisting occurs along the length of the girder. Once the girders ends are braced against rotation, the only possible form of lateral buckling is LTB, but, because of the girders' high torsional stiffness, the associated buckling load is very high.

Torsional deformations have frequently been neglected in LRB formulations for simplicity and because torsional deformations were small for historical girders (Mast, Lateral Stability of Long Prestressed Concrete Beams, Part 1, 1989) (Stratford & Burgoyne, The toppling of hanging beams, 1999); however, modern day girders continue to be designed for increasingly longer spans, which only increases the prevalence of torsional deformations, making the assumption that torsion is negligible questionable. When additional torsional deformations are added into the LRB phenomenon, it becomes Lateral-Torsional-Roll-Buckling (LTRB). An example of LTRB occurred in Washington State recently, when 223-foot-long WSDOT WF100G girders on the 70th Avenue bridge replacement project in Fife, WA suffered noticeable midspan twist compared to the support roll during lifting and handling. Further, to save costs on formwork, girders are typically made deeper to accommodate increased loading from longer span lengths, but the flanges are not made any wider. This makes the lateral stiffness relatively

lower compared to the increased vertical stiffness, which only exacerbates lateral bending, increasing the torsional moment on the girder.

It is important then to know how LTRB, rather than LRB, affects girder lateral stability. Additionally, how do factors like strong-axis bending deflections, prestressing deflections, and overhangs (which are all omnipresent during lifting and transportation but sometimes neglected in stability analyses) affect the LTRB behavior or a long-span girder? It is essential to know how these factors modify the buckling load so modern-day girders can continue to be safely designed.

Furthermore, prestressed concrete girders are designed for transportation and handling considering tolerances for imperfections like lateral sweep and lifting loop eccentricity. These imperfections cause pre-buckling deformations, and it is important to know how these imperfections affect the stability of long-span girders. Ultimately, a designer needs to be able to determine the final equilibrium angle of a girder quickly and easily to the most accurate degree possible. That procedure ideally includes all the complicating (but realistic) parameters, like imperfections and the aforementioned factors affecting the buckling load. Developing a procedure that accurately predicts the final equilibrium angle of a girder is one of the primary motivations of this work.

To predict LTRB behavior most accurately and ensure safety in design, it is also essential to know how prestressed concrete girders perform after cracking. Current Precast/Prestressed Concrete Institute (PCI) recommended practice is to ensure a factor of safety of at least 1.0 against cracking (Precast/Prestressed Concrete Institute, 2016). Can a girder in fact crack and still remain upright during transportation and handling? In 1993, Mast explored this question and proposed an equation for the effective moment of inertia of a girder that has cracked (Mast, 1993). Whether Mast's cracking proposals are still justified for today's girders, with torsion,

strong-axis bending, prestressing deflections, and overhangs incorporated in the behavior, is a primary motivation for this work. Further, if cracking does occur, it is of interest to see which shipping and handling design parameters most impact the post-cracking behavior of a prestressed concrete girder. This could include the overhang length, the concrete strength, or the span-to-depth ratio of the girder, to name a few.

Ultimately, ensuring safe but cost-effective designs is the final goal of any project on the lateral stability of long-span prestressed concrete girders. To that end, there needs to be a design methodology that accounts for all of the realistic and complicating factors in the LTRB behavior and has the capability to handle girder cracking, if need be. Further, is there an upper bound to girder length, beyond which either lateral stability, or some other factor, prevents that girder from being safely used? Answering that need and solving this question are the final motivations of the work presented herein.

1.2. **Literature Review**

An extensive literature exists on the LRB of hanging and supported from below girders, buckling, and the effects of cracking and torsion on lateral stability. This literature review will attempt to tell this story by dividing the relevant work into the following main sub-categories:

1. General LTB and Imperfection Amplification
2. LRB of Hanging Girders
3. Incorporation of Torsional Deformations
4. Effects of Cracking
5. Girders Supported from Below
6. Most Relevant Recent Work

The story of each sub-category will be told chronologically but will have the works of some authors linked together where necessary.

1.2.1. **General LTB and Imperfection Amplification**

A tremendous volume of work has been done on general LTB, most of it for steel structures, as noted in Section 1.1. There is not space here, nor is it entirely relevant to this work, to repeat those contributions here. As noted, Timoshenko and Gere (1961) made significant contributions, as did Bleich (1952) and Trahair (1993). Trahair (1993) also noted that strong-axis bending deflections had a stabilizing effect on the buckling load. More recently, Hurff and Kahn (2012) found that LTB occurs similarly in both reinforced concrete and prestressed concrete structures, and that their LTB behavior is sensitive to geometric imperfections.

On the subject of the pre-buckling amplification of imperfections, Southwell (1932) explored this topic for axially loaded columns with imperfections and found that initial imperfections were amplified by the inverse of $\left(1-\frac{P}{P_{cr}}\right)$, where P is an applied load and P_{cr} is the critical load. Later, Meck (1977) found that Southwell's framework was applicable not just to column buckling, but to LTB as well. Mandal and Calladine (2002) later concluded that Southwell's amplification form was adequate for LTB and did not need to be modified, as was suggested by Allen and Bulson (1980), and later by Stratford and Burgoyne (1999), who found that imperfection amplification for LTB was related to the inverse of $\left(1-\left(\frac{q}{q_{cr}}\right)^2\right)$, where q is an applied distributed load (typically the self-weight in this application) and q_{cr} is the critical load. Other authors have also explored the form of the expression for the amplification of imperfections, and their findings will be mentioned in the following sections where appropriate.

1.2.2. **LRB in Hanging Girders**

This section will focus on the literature concerning hanging girders undergoing LRB specifically. Muller (1962) was one of the first to explore this subject, exploring lateral buckling that occurs before material failure (cracking.) He calculated the vertical load necessary to induce buckling for slender rectangular beams and I-beams, and even suggested that an upwards point load be applied (such as a third crane support point) to promote stability (Muller, 1962).

Shortly thereafter, Anderson (1971), who was a business partner with Robert Mast, motivated by an example of lateral instability when lifting a girder from a casting bed, published a precursor to the work that Mast would expound upon 18 years later. Before Mast published the first part of his work, Imper and Laszlo (1989) noted that the increasing slenderness of prestressed girders was leading to lateral stability concerns, and potentially even cracking and collapse if overhangs weren't used during lifting. Most importantly, they noted that temporary top flange prestressing strands could be used as a method to arrest tensile stresses and cracking over the supports of girders with overhangs (Imper & Laszlo, 1987).

In 1989, Mast published the first of three papers on lateral stability that would prove to be instrumental to that field, and to this day form the basis for the PCI lateral stability design procedure (Precast/Prestressed Concrete Institute, 2016). Mast (1989) ignored torsional deformations and strong-axis bending and used equilibrium to determine the final roll angle of a girder lifted by cables. He developed an expression for the factor of safety against buckling for a girder with an initial imperfection that closely mirrors the form of Southwell's amplification equation (Mast, 1989). Additionally, Mast proposed several methods for improving lateral

stability, namely increasing the overhang lengths, even mentioning Imper and Laszlo's (1987) advocacy for temporary top strands (Mast, 1989). Mast's later work, which focused on supported from below girders and cracking, will be discussed in the following sections.

Stratford and Burgoyne published a series of papers on lateral stability in 1999. While they explored three support conditions (simply supported (essentially LTB), transport supported (one end rotationally flexible, the other end rotationally fixed), and hanging), the results of their hanging work is discussed here (Stratford & Burgoyne, 1999). They neglected torsion and warping, but their girders were relatively short. Using FEM as a computational vehicle, they found the hanging case to be the most critical for lateral stability of their three support conditions. It is important to note that they distinguish between LTB and LRB for the form the imperfection amplification equation takes. For LTB, they agree with the form proposed by Allen and Bulson (1980), but for LRB, they agreed with the work preceding them of Southwell (1932) and Meck (1977). Stratford, Burgoyne, and Taylor (1999) found a stabilizing factor for the effect of overhangs on the buckling load that explicitly accounts for girders lifted with vertical cables, and also produced design charts for girders lifted with inclined cables, which did not have a closed-form stabilizing factor. There they noted that cracking may even precede buckling (Stratford, Burgoyne, & Taylor, 1999). In a third article on "The toppling of hanging beams," Stratford and Burgoyne (1999) dove into the governing differential equations for girders subjected to wind loads, centripetal forces, and imperfections, but without strong-axis bending, prestressing deflections, or torsion. Here, they explicitly showed that torsional deformations were negligible at the time, but overall, their derivations were specific, complicated, and with applicability depending on conditions matching the exact assumptions they made (Stratford & Burgoyne, 1999).

Later on, Krahl, Lima, and El Debs (2015) found buckling loads in agreement with those predicted by Stratford and Burgoyne via an eigenvalue analysis of an FEM formulation. In 2019, Krahl, et al looked at lateral stability in long span Ultra-High-Performance-Fiber-Reinforced-Concrete (UHPFRC) beams lifted with overhangs and inclined cables. They used an analytical Rayleigh-Ritz and Potential Energy Model to show that lateral buckling occurred in the hanging case at a load approximately 3.7 times less than the service LTB failure load with rotationally fixed ends—indicating that stability considerations control the design over service loading. Their model assumed no prestressing, torsion, or strong-axis bending, but was closed-form and produced imperfection amplification results that agreed with Southwell (1932), Meck (1977) and Mandal and Calladine (2002) (Krahl, Martins, Carrazedo, Silva, & El Debs, 2019).

Also in 2019, de la Fuente, Bairan and Cavalaro performed an experimental case study and a parametric study on lifted girders to compare to Mast's (1989, 1993) results. Their work agreed with Mast's, but they found cracking and large deflections, despite code compliance (de la Fuente, Bairán, & Cavalaro, 2019).

1.2.3. **Incorporating Torsional Deformations**

The literature review of this section is not on LTB, but on LTRB—where torsional deformations are incorporated into LRB. Lebelle (1959) and Swann and Godden (1966) incorporated torsion via numerical methods; however, their works are complicated and would not translate well to a design equation. Tarnai (1978) included torsion and warping in his work, which used a Ritz-Galerkin method to examine a beam hung from different heights on each end with a varying applied load along the length; however, Tarnai admits that the methods proposed are very difficult to use. Dux and Kitpornchai (1990) looked at the flexural-torsional buckling of

beams lifted by inclined cables. Their governing differential equations included lateral bending and torsion but no strong-axis bending or imperfections. They found buckling loads and the theoretical optimum lifting points, but their work is for elastic buckling and is, as they note, not very applicable to real structures (Dux & Kitpornchai, 1990). Peart, Rhomberg, and James (1992) included twist and investigated the effects of camber. Referencing Lebelle (1959), they used differential equations to obtain infinite series solutions that are not very usable in practice but do show that camber lowers stability and the buckling load, albeit not significantly (Peart, Rhomberg, & James, 1992).

Plaut, Moen, and Cojocaru (2011) accounted for strong-axis bending and twist, but their analytically derived and numerically presented results are very specific to their exact conditions of horizontally curved, doubly symmetric, prismatic, linear elastic girders with equal overhangs. The horizontally curved assumption in their formulation causes a singularity when the beam is straight; further, as they note, their work is mainly for steel girders where self-weight buckling is unlikely (Plaut , Moen, & Cojocaru, 2011). In their Master's thesis, Cojocaru (2012) used previous equations from Plaut and Moen, but analyzed singly symmetric members instead with the shear center separated from the center of gravity. In addition to finding less than a 5% difference in behavior due to separating the shear center from the center of gravity, Cojocaru also performed a statistical analysis on the magnitude of imperfections typically seen in girders (Cojocaru, 2012). Plaut and Moen (2013) made the same assumptions as their 2011 work, but more explicitly showed their derivations and governing equations. The work was still complicated, specific, and not broadly applicable.

While including torsion has been attempted in the literature to date, there is a need for a separate attempt at the treatment of the behavior of torsion combined with LRB (LTRB) that can

result in an easily usable design equation. This was done by Galik, Stanton, and Wiebe (2022) and will be discussed at the end of this section.

1.2.4. **Effects of Cracking**

A handful of authors have attempted to solve the problem of the lateral stability of cracked concrete girders. Hansell and Winter (1959) proposed an equation for the cracked critical bending moment, but it was for a straight rectangular reinforced concrete beam undergoing LTB. Siev (1960) also looked at LTB in cracked reinforced concrete beams and used infinite polynomial series solutions to differential equations, modified by different stiffness factors to account for different cracking states.

Mast (1993) again published a very influential work, this time on including the effects of cracking in the lateral stability of prestressed girders. He wrote a computer program to solve the post-cracking lateral stability behavior—without torsion or strong-axis bending—but no details were given. Additionally, he described full-scale tests that validated his work and computer program. Most importantly, he provided an approximate, equation that related the effective lateral stiffness of a cracked girder to its roll angle. The equation represents a lower bound for the stiffness and was obtained by curve fitting. Noting that the girder does not fail immediately upon cracking, he published equations for factors of safety against cracking, and against failure—presumed to take place at 0.4 radians. This work was for both hanging and supported from below girders (Mast, 1993). The next year, Mast (1994) published a paper describing his physical tests in detail. Experimentally, he found good agreement with his analytical predictions and that the midspan twist angle of the girder was approximately proportional to the square of

the support roll angle—but he claimed the twist was still negligible for practical purposes (Mast, 1994).

Later, Lima and El Debs (2005) studied the influence of flexural cracking on torsional stiffness. They noted that the influence of torsion was small relative to flexure, but that flexural cracking resulted in an approximately 20% decrease in torsional stiffness; however, their work was for reinforced concrete girders with no prestressing and practically no strong-axis bending (Lima & El Debs, 2005). In 2012, de la Fuente, et al developed a numerical cracking model that accounted for material nonlinearities in the steel and concrete and loading from different construction stages, but their work did not examine lateral stability (de la Fuente, Aguado, Molins, & Armengou, 2012).

1.2.5. **Girders Supported from Below**

Quite an extensive literature exists for the lateral stability of girders supported from below by rotationally flexible supports. This is still LRB or LTRB—the supports provide some rotational restraint but do not completely fix the rotational degree of freedom. Work on the rotational stiffness of elastomeric bearing pads has been done by Yazdani, Eddy, and Cai (2000) and Stanton, et al (2008).

Instability in girders supported from below is most likely to occur in two circumstances: during transportation on a truck, and immediately after placement on a bearing but before end bracing restraining rotation has been installed. Once end bracing is in place, it is generally stiff enough to prevent rotation about the longitudinal axis, and the problem becomes one of LTB. As discussed previously, the torsional stiffness of prestressed concrete girders is high enough to preclude instability by LTB in practice. There have been some instances of girder collapse due to

insufficient bearing or bracing stiffness. For example, Tremblay and Mitchell (2006) identified a real-world instance of a bridge collapsing partially due to insufficient stiffness in the pot bearings it was resting upon. Oesterle et al (2007) also described an instance of bridge collapse. Bairán and Cladera (2014) described the collapse of a beam supported on bearing pads due to eccentric loading, noting torsional cracks approximately at the quarter-span points and that the bearings were not stiff enough.

During transportation, the rotational stiffness of the truck is one of the most critical parameters for determining stability, but requirements for truck stiffness vary widely among states. Hurff and Kahn (2012) found that the rotational support stiffness greatly influences the girder's behavior. For stability during erection, it is common practice in many states in the US to release the crane from the girder only after end bracing is in place; however, when this procedure is not adopted, girder stability depends on the rotational stiffness of the bearing support system alone, and it is on this case that much of the previous research has been focused.

A couple of years after their original lateral stability work, Burgoyne and Stratford (2001) published a work on the self-weight buckling of beams supported on bearing pads at its ends. They ignored twist (LRB) and found imperfection amplification that agreed with the form predicted by Southwell (1932) (Burgoyne & Stratford, 2001).

In his doctoral dissertation, Hurff (2010) looked at the LRB of imperfect girders on bearing pads. He found that rollover was the most critical case for stability, that lack of flatness of the girder soffit greatly decreased stability because it promoted rocking on the bearing, and that Mast's 1993 work predicted the behavior well (Hurff, 2010). Later, Hurff and Kahn (2012) (separate from their 2012 paper on LTB) found the same results, but they emphasized that the

stability behavior was very dependent on the width and stiffness of the bearing, also noting that increasing the size of the bottom flange could improve stability.

Lee (2012) looked at girders during construction stages with sweep, initially rotated bearings, and thermal imperfections using 3D-nonlinear-FEM. Lee did not find instability due to self-weight in perfect girders but noted that imperfections may cause instability (Lee, Behavior of precast prestressed concrete bridge girders involving thermal effects and initial imperfections during construction, 2012). Later, Lee (2017) looked at the critical load and imperfection amplification of bearing supported girders with zero net camber, but with torsional effects. Lee found very little difference between the imperfection amplifications proposed by Southwell (1932) and Allen and Bulson (1980) and proposed a compromise where imperfections were amplified by the inverse of $\left(1-\left(\frac{q}{q_{cr}}\right)^{3/2}\right)$ (Lee, 2017). In that same year, Lee, et al (2017) looked at the critical wind load to cause rollover in a girder with zero net camber and no torsion, finding that the critical wind load was very closely inversely related to the girder's length.

Consolazio, Hamilton, and Beery (2012) performed full scale tests and used FEM to analyze bearing supported girders, finding that initial bearing slope and skew were detrimental to stability, and that together they could reduce bearing stiffness to the point where self-weight buckling might occur. Plaut and Moen (2014) looked at girders with imperfections supported at their ends by bearing pads subjected to wind loads using a procedure similar to Mast (1993). They developed factors of safety against cracking and sliding and found that their work resulted in lower factors of safety than predicted by recommended practice at the time (Plaut & Moen, 2014). Chamorro-Varilla and Dario-Aristiazabal Ochoa (2016) developed an analytical model with support from the differential equations in Plaut and Moen (2013) to get closed-form equations for girders with overhangs, imperfections, and a crane support at midspan on nonlinear

elastic bearings on cross slopes. They assumed there was no torsion, warping, shear deformations, vertical imperfections, or prestressing deflections. While their results are closed-form, they depend upon 168 separate coefficients and many different equations, making it intractable for a simple design procedure (Chamorro-Varilla & Dario Aristiazabal-Ochoa, 2016).

Krahl has made quite a few contributions to this area of lateral stability alongside several others. Krahl, Carrazedo, and El Debs (2018) used a Rayleigh-Ritz and Minimum Potential Energy method to develop closed-form analytical solutions for the rollover load of girders on bearing pads. They neglected torsion, found that rollover occurred before cracking, and that their results matched those of Hurff and Kahn (2012) and Conzolazio, Hamilton and Beery (2012) best when using the Southwell (1932) amplification form (Krahl, Carrazedo, & El Debs, 2018). Krahl, et al (2020) used the same Rayleigh-Ritz and Minimum Potential Energy procedure to derive a series of critical loads of increasing complexity, including the effects of sweep, initial roll, and camber, but no torsion or strong-axis bending. They allowed for liftoff and found an unstable post-buckling equilibrium path. They agreed with Allen and Bulson (1980) and Stratford and Burgoyne (1999) (for LTB) that the inverse of $\left(1-\left(\frac{q}{q_{cr}}\right)^2\right)$ best predicted the peak rollover load, not including cracking (Krahl, Oliveira, Siqueira, & Lima, 2020). Oliveira, Krahl, and Lima (2020) used the same Rayleigh Ritz and Minimum Potential Energy procedure and performed a parametric study to determine what design parameters most impacted the design load. They found that the cross-section shape and the bearing rotational stiffness were most important, and that cracking occurs before rollover, so preventing cracking would likely guard against rollover (Oliveira, Krahl, & Lima, 2020).

Reis, Krahl, and Lima (2020) used an FEM model to analyze rollover instability and found that rotations decreased the bearing stiffness, and that the girder's lateral stiffness was

more important for stability than its depth. Recently, Costa, Krahl, and Lima (2023) analytically looked at the liftoff and rollover of UHPC girders supported by nonlinear rotationally stiff bearing pads. They did not consider cracking or torsion but did include lateral imperfections and camber and again found an unstable post-buckling equilibrium path. The UHPC girders they studied could only take 1.08 times more load than the self-weight load, showing that lateral stability is a concern for UHPC girders (Costa, Krahl, & Lima, 2023).

1.2.6. **Most Relevant Recent Work**

The report to PCI by Galik, Stanton, and Wiebe (2022) is the most similar and relevant work to that presented here. They established the critical LRB load similar to Mast (1989), but then modified it by closed-form factors to account for the effects of strong-axis bending, prestressing deflections, and torsion. Each factor has a simple form and depends on physical attributes of the girder. They also developed a factor accounting for the effects of overhangs that agreed with Stratford and Burgoyne (1999) for their specific case of a girder lifted by vertical cables. Further, they proposed a method to convert girders supported from below to equivalent hanging girders in order to use the same analysis approach for both support conditions. Finally, they developed a numerical tool, Rollbuck, that served as a way to validate their closed-form analytical expressions (Galik, Stanton, & Wiebe, 2022). This work will incorporate and expand upon some of their results. The scope of the material covered in this thesis is described in the following section.

1.3. **Scope**

This work will begin by deriving the critical load for baseline LRB, with no other complicating factors incorporated, in Chapter 2. From there it will explicitly account for strong-axis bending, prestressing deflections, overhangs, and torsion via factors that modify the baseline LRB load. Modifications to the work presented by Galik, Stanton, and Wiebe (2022) will primarily occur in the form of factors that modify the baseline LRB load to account for prestressing deflection, overhang, and torsional deformations. The conversion from a supported from below girder to an equivalent hanging girder will also be updated to account for roadway cross slope.

Chapter 3 will characterize different lateral imperfections by the initial pre-bending-deformation roll angle they cause and will establish the frameworks necessary for the imperfection amplification study conducted in Chapters 4 and 5. It will present different models for predicting the final equilibrium angle of a girder undergoing LRB or LTRB with imperfections, including two related analytical models and a description of Rollbuck 2021, originally developed by Galik, Stanton, and Wiebe (2022).

Chapters 4 and 5 will conduct an imperfection sensitivity study. They will explore the amplification of initial imperfections with increasing applied loads for girders governed by different buckling loads and assumptions. While they both follow the same format, Chapter 4 will explore LRB and Chapter 5 will explore LTRB. The analytical models presented in Chapter 3 will be evaluated to see how accurately they predict the imperfection amplification measured by the numerical tool, Rollbuck 2021.

Through Chapter 5, the girders had been assumed to be uncracked and linear elastic. In Chapter 6, the effects of cracking will be incorporated. Rollbuck 2022, a second version of

Rollbuck 2021, accounts for the effects of cracking and material nonlinearities and will be evaluated and validated in Chapter 6. One of the primary goals of this work is to determine whether or not Mast's (1993, 1994) work on cracking is still valid for modern-day girders. Chapter 6 will explore this question.

Chapter 7 will primarily conduct a parametric study on different design parameters to see which aspects of a girder's design have the greatest impact on its post-cracking lateral stability. To do this, a Standard Configuration for girder designs will be established, from which the parametric study can be centered around and vary design parameters from. Different girder series will be explored in the Standard Configuration before the actual parametric study is conducted to see how they perform relative to Mast's (1993, 1994) results.

Chapter 8 proposes a new lateral stability design procedure that simplifies the existing design procedure while still accounting for the increased layers of complexity considered here, namely strong-axis bending, prestressing deflections, overhangs, torsion, and cracking. Equations for the tilt angle where cracking begins and the angle at which allowable compressive stress limits are violated will be presented. Three case studies will be presented. The first will compare the proposed design procedure to the existing lateral stability design procedure (Precast/Prestressed Concrete Institute, 2016). The next two will explore separate examples using the proposed lateral stability design procedure.

The final chapter of this thesis, Chapter 9, explores a series of long-span girder designs using the proposed lateral stability design procedure and a particular girder cross-section. It illustrates, through a series of plots, trends in relevant design requirements as functions of girder length. Where design limits exist and are violated with increasing span-lengths, they are identified with the goal of establishing what the likely upper-bound length of modern-day girders

is. The efficacy of factors of safety against cracking and ultimate failure are discussed and new controlling design limits are proposed.

2. Buckling

This chapter provides a summary of prior work on the critical load of precast girders during transport and handling. Additionally, it updates some of the buckling loads presented by Galik, Stanton, & Wiebe (2022). It includes the LRB load, the effects of strong-axis bending and prestressing deflections, effects of overhangs, the additional deflections and reduced critical load due to torsion, and the effect of different support conditions (hanging vs. supported from below). Complete details of the formulation can be found in the report by Galik, Stanton, & Wiebe (2022) and differences will be noted where appropriate. These results are used to develop models for predicting imperfection amplifications in Chapter 3 and in the imperfection sensitivity study in Chapters 4 and 5.

2.1. **Lateral-Roll Buckling**

Buckling of a member, and calculation of the load at which it occurs, can be defined by several different criteria. This is true for most types of buckling, including buckling of columns under axial load, circular rings and arches under radial load, lateral buckling of beams under vertical load, etc. Four common criteria for buckling are:

The equilibrium criterion. The equations of equilibrium are written in the deformed configuration. The buckling load is then given by the load at which two separate equilibrium configurations first become possible: the pre-buckled shape and the post-buckled shape. This load appears as the solution of an eigenvalue problem of a homogeneous equation. In many practical problems, there is no pre-buckling deformation (in the instability direction) and hence this is often called the “trivial” solution. This scenario also allows for the use of small deformation theory.

The imperfection criterion. The equilibrium equations are again written in the deformed configuration but, in this case, an initial imperfection (e.g., lack of straightness) is assumed to exist. The equilibrium equation is no longer homogeneous, so it no longer represents an eigenvalue problem. Solving for the equilibrium shape reveals (again using small deflection assumptions) that the lateral deflection is a multiple of the magnitude of the assumed initial imperfection. The amplification factor is related to the load. The buckling criterion is that the amplification of the initial imperfection becomes infinite when the load reaches the buckling load.

The energy criterion. The total potential energy of the problem is determined. Minimizing the potential energy with respect to each of "*N*" degrees of freedom considered results in *N* equilibrium equations. Then, the gradient of each minimum potential energy equilibrium equation results in an *N x N* matrix. Buckling occurs when the determinant of this matrix is equal to zero, and the buckling loads and mode shapes are represented by the eigenvalues and eigenmodes respectively. This scenario occurs when a local minimum in the potential energy becomes either saddle-shaped or a local maximum, which are both indicative of an unstable configuration.

The dynamic criterion. The problem is set up as a vibration problem for small (i.e., linear) oscillations about an equilibrium configuration. The natural frequencies for the small oscillations completely characterize stability. For example, in the column problem, the vibrations are lateral, and the load is axial. The frequency is a function of the axial load, and the buckling criterion is that the vibration frequency drops to zero. The buckling load is defined as the load required to achieve that zero frequency.

In all cases the value of the buckling load is the same, even though the buckling loads were derived using different criteria.

As pre-buckling deformations are often small, or identically zero, the critical load is calculated with small-deformation theory. For the post-buckled response, on the other hand, the assumption of small deflections must be abandoned, which renders the equations more complicated but, generally, shows that the member can resist loads higher than the linearized buckling load, albeit at the cost of relatively large deflections.

Here, we use the imperfection criterion to find the lateral buckling load buckling load of a beam that is flexible in bending (about both axes) but is torsionally rigid (for now). It is supported from above (e.g., by lifting cables), and is free to rotate as a rigid body, or to roll, about the axis through the two supports. This behavior is LRB, defined initially in Chapter 1. The equilibrium equations are first written in the most general form, accounting for large deflections, which can thus be used to find the exact equilibrium path, even when the roll angle is large enough that small angle assumptions, e.g., $sin\phi \approx \phi$, are no longer valid. The equations are then simplified by imposing the assumption of small deflections/rotations, and the imperfection criterion is used to find the linearized buckling load.

The coordinate system used throughout this work is shown in Figure 2.1. The global coordinates, x_{glo}, y_{glo}, and z_{glo} correspond to lateral, vertical, and longitudinal directions, respectively. They are associated with corresponding displacement terms as well: u_{glo}, v_{glo}, and w_{glo} (the latter of which is not used in this work.) Positive directions/displacements are to the right, downwards, and longitudinally into the page, as defined by the right-hand rule between the x and y axes. Correspondingly, clockwise rotations are positive as well. Global coordinate axes and displacement directions remain in the same orientation no matter the girder's displacement.

The local coordinate axes displace and rotate with the girder and remain in the orthogonal directions for the displaced girder. They are labelled as x_{loc}, y_{loc}, and z_{loc} and u_{loc}, v_{loc}, and w_{loc} correspondingly. The roll angle, ϕ, is essentially the angle between the global and local co-ordinate systems. As will be seen later, the twist deformation will significantly complicate the picture, as ϕ then varies with the z-coordinate.

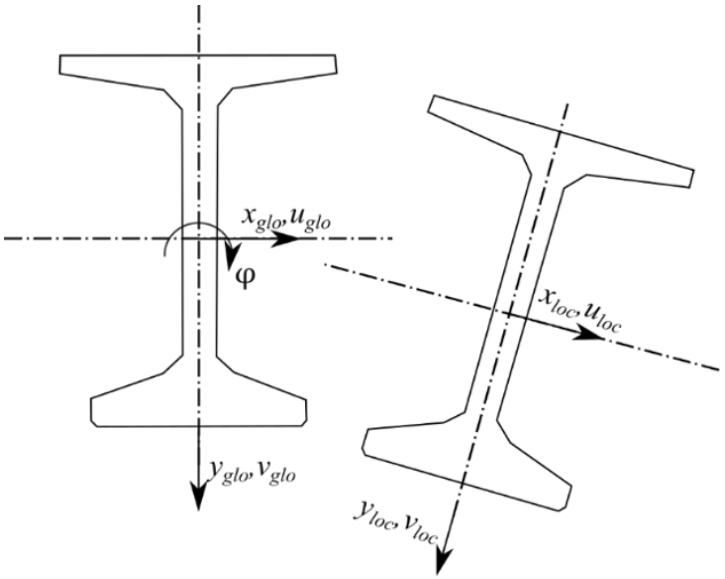

Figure 2.1 Co-Ordinate System and Associated Displacements

Consider the girder in Figure 2.2 lifted from loops placed at a lateral eccentricity to the average center of gravity of the girder. The eccentric lifting loops result in a lever arm between the reactions and the self-weight at the center of gravity. This causes the girder to roll to satisfy rotational equilibrium. However, a component of the self-weight then loads the weak axis of the rolled girder. This load causes an additional deflection of the center of gravity and additional roll. This results in a competition between the stabilizing lateral restoring force seeking to straighten the girder, and destabilizing torque cause by the self-weight. At loads beyond buckling, the destabilizing forces win the competition resulting in the girder equilibrating at a

non-zero roll angle. This phenomenon is Lateral Roll Buckling (LRB), and the load at which the non-trivial configuration appears is the LRB load.

The critical load for LRB is a function of the position of the rolled girder's center of gravity. The average lateral deflection of a simply supported beam under a uniform distributed load describes the position of the girder's center of gravity at midspan. The deflection of a simply supported and uniformly loaded beam is:

$$u(z) = \frac{q}{24EI_{yy}}(z^4 - 2Lz^3 + L^3z), \qquad (2 - 1)$$

where z defines the longitudinal position, q is an applied load per unit length, EI_{yy} is the girder's weak axis moment of inertia multiplied by the Modulus of Elasticity, and L is the overall length of the girder. The average of Equation (2 – 1) is

$$\overline{u} = q\overline{\Delta}_x, \qquad (2 - 2)$$

where

$$\overline{\Delta}_x = \frac{L^4}{120EI_{yy}}. \qquad (2 - 3)$$

Equation (2 – 3) describes $\overline{\Delta}_x$, the average deflection caused by a unit uniformly distributed load. It is essentially a flexibility coefficient and has units of length-squared/force.

The critical load for LRB can be derived by considering equilibrium of the girder, after rolling in the positive direction and deflecting laterally, as shown in Figure 2.2. The solid cross section represents the orientation at the supports while the dashed cross section represents the deflected position of the center of gravity at midspan.

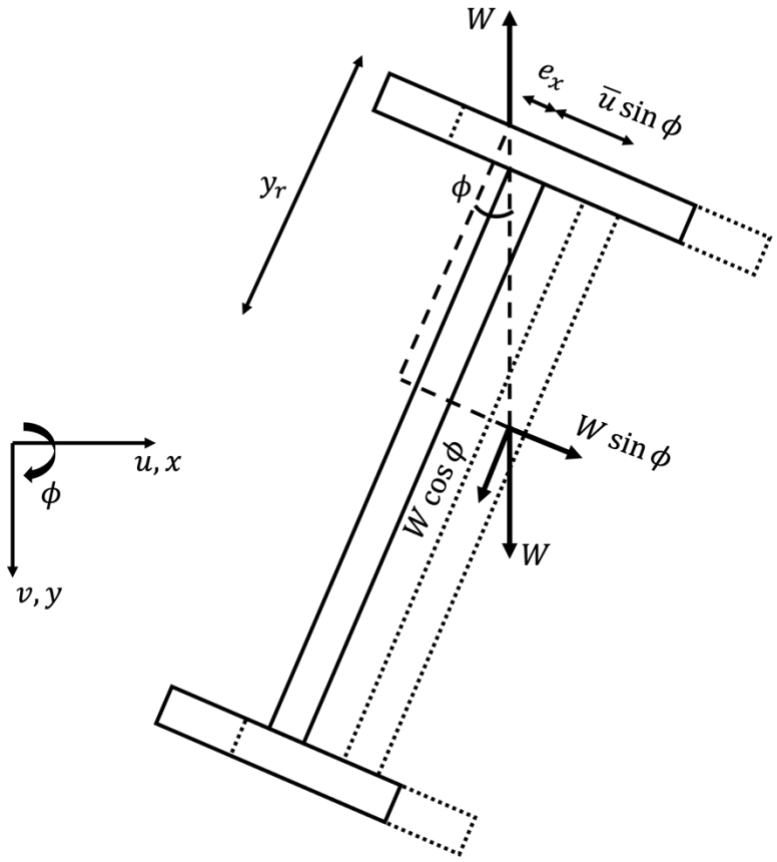

Figure 2.2 Rolled Girder with Symmetry Breaking Imperfection: Configuration and Free Body Diagram

Figure 2.2 shows W rather than q. W is the total weight of the girder, equal to:

$$W = qL. \qquad (2 - 4)$$

In this rolled configuration, only a component of the applied load, $W \sin\phi$, acts in the local lateral direction perpendicular to the girder web. Considering a distributed load instead of a concentrated load, similarly only $q \sin\phi$ would act in the local lateral direction.

Imperfections lead to initial deformations by moving the center of gravity away from the centerline, thus causing a moment imbalance. The imperfection in Figure 2.2 is a lifting loop eccentricity, e_x, which laterally shifts the reaction. In the adapted coordinate system, note that a negative lifting loop eccentricity leads to a positive roll angle (hence the negative e_x in Equation

(2 – 6)). Only the local component of the average deflection of the girder contributes to the lateral deflection of the center of gravity in the rolled configuration. If the roll angle is ϕ, the component of the load acting in the local x-direction is $q \sin\phi$. The deflection in the local x-direction is then

$$\overline{u}\sin\phi = q\overline{\Delta}_x \sin\phi = \frac{qL^4}{120EI_{yy}}\sin\phi. \qquad (2 - 5)$$

Moment equilibrium about the roll axis gives:

$$W \sin\phi\, y_r + W\cos\phi\,(\overline{u}\sin\phi - e_x) = 0, \qquad (2 - 6)$$

noting that in this coordinate system, the roll axis height, y_r, and the lifting loop eccentricity, e_x, are both negative. Substituting for $\overline{u}$ and re-arranging gives

$$y_r \tan\phi + \frac{qL^4 \sin\phi}{120EI_{yy}} - e_x = 0. \qquad (2 - 7)$$

The equilibrium path of applied load versus roll for LRB, $q(\phi)$, neglecting Strong-Axis Bending (SAB), prestressing deflections, torsional deformations, and overhangs, comes from rearranging Equation (2 – 7)

$$q(\phi) = \frac{120EI_{yy}}{L^4 \sin\phi}(e_x - y_r \tan\phi). \qquad (2 - 8)$$

The girder will be very close to straight initially with a roll angle near zero. Assuming small angles such that $\sin\phi \approx \tan\phi \approx \phi$, Equation (2 – 8) can be rearranged to give a closed-form expression for ϕ as a function of the applied load, q:

$$\phi = \frac{e_x}{\left(\frac{qL^4}{120EI_{yy}} + y_r\right)}. \qquad (2 - 9)$$

According to the Imperfection Criterion, buckling occurs when the equilibrium deflection (roll in this case) grows without bound for any small initial imperfection. This occurs when the

denominator of Equation (2 – 9) leads to a singularity. Solving for that load, the critical load for LRB is

$$q_{LRB,o} = -\frac{120EI_{yy}y_r}{L^4}, \qquad (2 - 10)$$

where $q_{LRB,o}$ is the baseline LRB load that neglects the effects of SAB, prestressing deflections, overhangs, and torsion, hence the "o" subscript in Equation (2 – 10). Additional subscripts will be added in later sections to indicate the inclusion of complicating effects on the critical load. Note that y_r is negative, so despite the negative sign, the critical load corresponds to a positive downwards applied load. Further, note that the buckling load is independent of the initial imperfection.

The foregoing derivation for the baseline LRB load assumed the imperfection was a lifting loop eccentricity. The same baseline LRB load can be derived using a lateral sweep as the imperfection. A positive x-direction lateral sweep causes a positive roll angle, as opposed to a negative x-direction lifting loop eccentricity causing a positive roll. Equation (2 – 6) thus becomes:

$$W \sin\phi \, y_r + W \cos\phi \left(\overline{u} \sin\phi + 0.64u_{sweep}\right) = 0, \qquad (2 - 11)$$

where u_{sweep} is the maximum lateral sweep imperfection, measured at mid-span relative to the chord between the girder ends. The lateral sweep is assumed to be of the shape of a simply supported beam subjected to uniform distributed load. If Equation (2 – 2) represents the average deflection of a simply supported beam subjected to a uniform distributed unit load, that average is 64 percent of the maximum deflection from a unit load, which is a function of $\frac{L^4}{384EI}$. Analogously, the average position of the center of gravity due to a sweep deflection is then

$0.64u_{sweep}$. Following the same steps as the derivation considering lifting loop eccentricity, one can arrive at the roll angle as a function of the sweep imperfection and the applied load:

$$\phi = \frac{-0.64u_{sweep}}{\left(\frac{qL^4}{120EI_{yy}} + y_r\right)}. \qquad (2 - 12)$$

The critical load will still take the same form as Equation (2 – 10). Thus, both lateral sweep and lifting loop eccentricity give imperfections give the same critical load. Therefore, the critical load of the girder does not depend upon either the magnitude of imperfection or the type of imperfection. Relationships between lifting loop eccentricity, lateral sweep, and other types of imperfections will be explored more in Chapter 3.

Figure 2.3 shows the equilibrium paths of several girders, both with and without imperfections, and with and without making small angle assumptions. If the buckling load of Equation (2 – 10) is substituted into Equation (2 – 9), the roll angle is indeterminate. That unbounded displacement at the linearized (small angle) buckling load shows up as the black-dashed horizontal line in Figure 2.3—the girder could theoretically be at equilibrium at any roll angle. The blue, orange, and gray curves shown in Figure 2.3 depict the nonlinear (large angle) equilibrium path for a girder undergoing LRB. The green curve depicts a girder with an imperfection, but with an equilibrium path that assumes small angles.

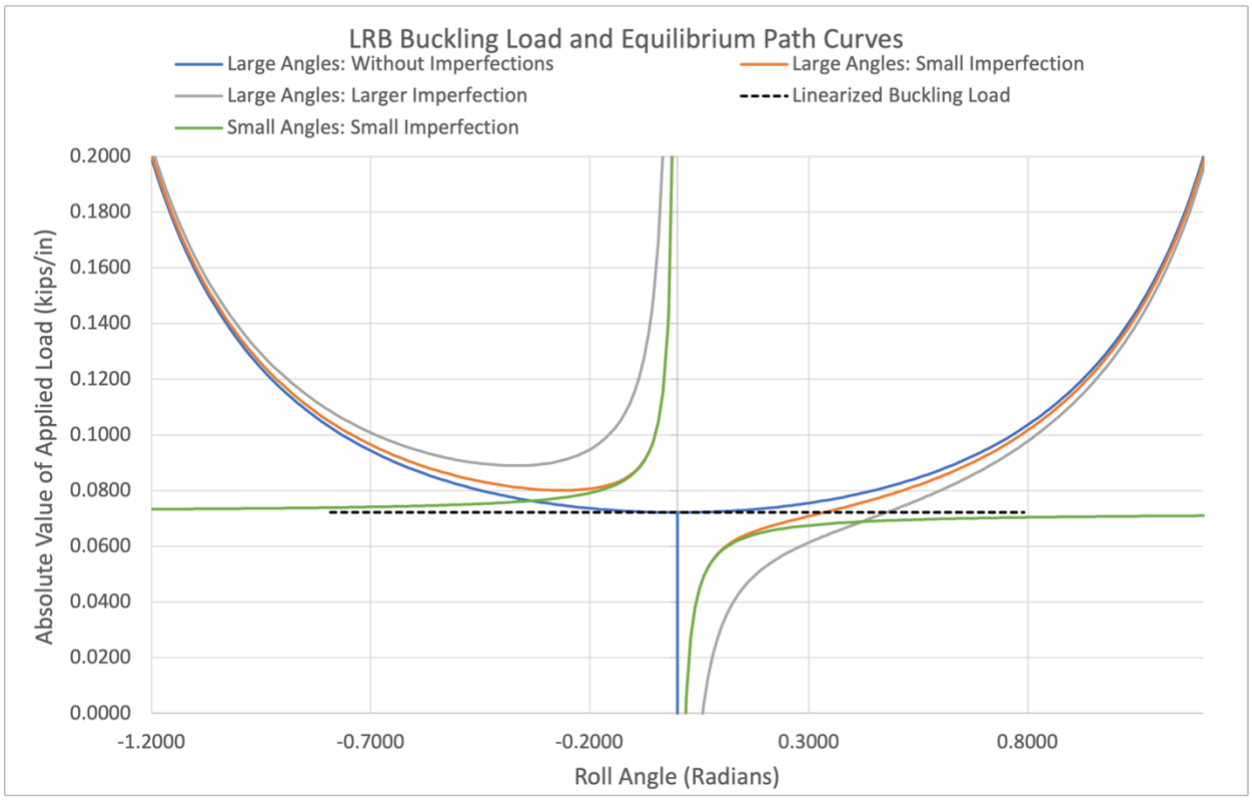

Figure 2.3 LRB Buckling Load and Equilibrium Paths for Girders with and without Imperfections

A girder without any imperfections (blue curve) buckles at the linearized buckling load, and the nonlinear equilibrium path predicts residual post-buckling strength. This indicates that designing to completely prevent buckling is not strictly required, as the girder should not immediately collapse at the onset of buckling.

The orange and gray curves in Figure 2.3 represent girders with relatively small and large imperfections, respectively. The rate of change of roll angle increases as the applied load approaches the buckling load and the girders with imperfections undergo pre-buckling deformations, while the otherwise perfect girder does not. This concept can be seen in Equation (2 – 9). For a girder without imperfections ($e_x = 0$), the roll angle will always be zero until the critical load is applied, at which point the singularity in the denominator occurs and theoretically any roll angle could occur. The green curve, representing a girder with an imperfection

undergoing a linearized equilibrium path, also has pre-buckling deformations, but does not exhibit post-buckling stiffness. It has the same imperfection magnitude as the orange curve. Their behaviors are identical until the applied load approaches the buckling load, at which point the small angle assumption and differences due to linearization occur. If there is an imperfection, there will be a non-zero roll angle before the critical load is applied, and if a small angle assumption is not made, there will be post-buckling stiffness.

The foregoing development assumes linear-elastic behavior. If the concrete were to crack, or the steel to yield, the results would no longer be valid at the onset of the material nonlinearity. The effects of cracking on lateral stability will be explored in detail from Chapter 6 onwards.

2.2. **Effects of Strong-Axis Bending and Prestressing Deflections**

Section 2.1 neglected SAB and prestressing deflections when deriving the baseline LRB load. The report by Galik, Stanton, & Wiebe (2022) runs through the implications of incorporating these effects into the buckling load in detail. The same approach as their work is taken here, but the results are modified.

With SAB deflections included the roll axis height in Figure 2.2 is changed. Moment equilibrium about the roll axis then becomes:

$$-W \sin\phi \, (\overline{v} \cos\phi - y_r) + W \cos\phi \, (\overline{u} \sin\phi - e_x) = 0, \qquad (2 - 13)$$

noting that $\overline{v}$ is the average vertical deflection, analogous to $\overline{u}$, the average lateral deflection, and is equal to

$$\overline{v} = \frac{qL^4}{120EI_{xx}}. \qquad (2 - 14)$$

Expanding $\overline{u}$ and $\overline{v}$ and rearranging Equation (2 – 13) gives

$$\tan\phi = \frac{e_x - \frac{qL^4 \sin\phi}{120EI_{yy}}}{y_r - \frac{qL^4 \cos\phi}{120EI_{xx}}}. \quad (2 - 15)$$

This intermediate form on the way to determining the equilibrium path and critical load will be helpful when prestressing deflections are accounted for shortly. Rearranging Equation (2 – 15) gives

$$e_x - y_r \tan\phi = \frac{qL^4 \sin\phi}{120}\left(1 - \frac{I_{yy}}{I_{xx}}\right). \quad (2 - 16)$$

Solving for q as a function of ϕ gives the equilibrium path for LRB with SAB incorporated:

$$q(\phi) = \frac{(e_x - y_r \tan\phi)}{\left(1 - \frac{I_{yy}}{I_{xx}}\right)} \frac{120EI_{yy}}{L^4 \sin\phi}. \quad (2 - 17)$$

By assuming small angles, Equation (2 – 17) can be solved for ϕ, as was done in Section 2.1:

$$\phi = \frac{e_x}{\left(\frac{qL^4\left(1 - \frac{I_{yy}}{I_{xx}}\right)}{120EI_{yy}} + y_r\right)}. \quad (2 - 18)$$

Again, the critical load occurs when the denominator equals zero and the roll angle is indeterminate:

$$q_{LRB,v} = -\frac{120EI_{yy}y_r}{L^4\left(1 - \frac{I_{yy}}{I_{xx}}\right)}, \quad (2 - 19)$$

where the subscript "v" indicates that SAB deflections are accounted for in the LRB load.

Since the weak axis moment of inertia is typically lower than the strong axis moment of inertia, incorporating strong axis bending is a stabilizing effect on the girder critical load. The smaller denominator raises the critical load for LRB. In cases where $EI_{yy} > EI_{xx}$ the buckling load is negative, implying that the member is unconditionally stable and could not buckle under

any uniform load, including its own self-weight. A double tee girder provides an example of this behavior.

Prestressing deflections may be similarly incorporated into the critical load formulation. Galik, Stanton, & Wiebe (2022) derived a critical load that accounts for the effects of prestressing deflections; however, that work there relied on a specific interpretation of the relationship between the girder self-weight, q_{sw}, and the equivalent upwards load due to prestressing, q_p. It considered the ratio of q_p to q_{sw} to be constant for a given girder configuration—the applied load on the girder was then limited to only the self-weight. The work here considers a constant q_p value and a varying applied load, q, not necessarily equal to the self-weight, when deriving the critical buckling load. The imperfection sensitivity study later evaluates girder stability over a range of applied loads, not just at a constant load (the self-weight.) Therefore, it is most appropriate to proceed forward in this instance with the buckling load derived for an arbitrary applied load, q, and a constant q_p value.

It is convenient to treat the tendon profile as if it were parabolic, thereby giving rise to a uniform equivalent upwards load due to the prestressing strand, q_p. Similar to the average deflections due to the self-weight loads, the average deflection caused by a uniformly distributed upwards prestressing force for a simply supported beam is then

$$\overline{v}_p = \frac{q_p L^4}{120 E I_{xx}}. \qquad \textit{(2 - 20)}$$

While a pretensioned girder with a combination of straight and harped strands would not identically have a uniform q_p, it is assumed here that the approximation is close enough for practical purposes. In a typical girder, about one third of the strands are harped at points at approximately 40 and 60 percent of the length. The upwards deflection at mid-span due to

prestressing is then 1.11 times greater than the upwards deflection in a beam with the same mid-span prestressing moment, but a truly parabolic tendon profile. As shown in Equation (2 – 13) the critical dimension for strong axis deflections is $(\overline{v}\cos\phi - y_r)$, and typically $|y_r| \gg \overline{v}$, so a small error in the net vertical deflection accounting for SAB and prestressing deflections will have a very small effect on the buckling load and the amplification of imperfections.

In the critical load derivation for a girder undergoing SAB only, the average vertical deflection was modified by the cosine of the roll angle to account for gravity always pointing globally downwards. The equivalent prestressing force is always directed locally vertically upwards, no matter the roll angle, so the cosine of the roll angle should not be applied to the average prestressing deflection when determining the girder's center of gravity position. Accounting for this, Equation (2 – 15) becomes:

$$\tan\phi = \frac{e_x - \frac{qL^4\sin\phi}{120EI_{yy}}}{y_r - \frac{L^4}{120EI_{xx}}(q\cos\phi + q_p)}. \qquad (2 - 21)$$

This can be re-organized into a form like Equation (2 – 16) for the SAB only case with an additional term due to prestressing deflections:

$$e_x - y_r\tan\phi = \frac{qL^4}{120EI_{yy}}\sin\phi\left(1 - \frac{I_{yy}}{I_{xx}}\right) - \frac{q_pL^4}{120EI_{xx}}\tan\phi \qquad (2 - 22)$$

From this equation, the prior work by Galik, Stanton, & Wiebe (2022) set the symmetry breaking imperfection to zero and assumed small angles. Additionally, the ratio $q_{sw}(\frac{q_p}{q_{sw}})$ was substituded for q_p. Then, the q and q_{sw} terms were grouped. That expression is fundamentally the same as Equation (2 – 22), but the ratio $(\frac{q_p}{q_{sw}})$ was assumed to be a constant. While this is a reasonable assumption for a specific scenario with a set applied load equal to the self-weight, it is less suitable in the presentation of equilibrium paths as a function of a varying applied load, q.

The constant ($\frac{q_p}{q_{sw}}$) assumption implies that the prestress force would be added at the same rate as the applied load, if the applied load varies, to maintain the same $\frac{q_p}{q_{sw}}$ ratio. The result reported there (but unused here) is

$$q_{cr} = -\frac{120EI_{yy}y_r}{L^4\left(1-\frac{I_{yy}}{I_{xx}}\left(1+\frac{q_p}{q_{sw}}\right)\right)} \qquad (2 - 23)$$

Herein, the q_p value is instead kept as an independent parameter that is not necessarily equal to the self-weight. This allows for the critical load formulation to account for any arbitrary applied load for a given prestressing amount. This is most appropriate for the imperfection study conducted in later sections, which evaluates a girder's stability at different applied loads.

Solving Equation (2 – 22) for q as a function of ϕ yields the equilibrium path for LRB accounting for both SAB and prestressing deflections:

$$q(\phi) = \frac{120EI_{yy}}{L^4\sin\phi\left(1-\frac{I_{yy}}{I_{xx}}\right)}\left(e_x + \tan\phi\left(\frac{q_pL^4}{120EI_{xx}} - y_r\right)\right). \qquad (2 - 24)$$

Assuming small angles and solving for ϕ:

$$\phi = \frac{e_x}{\frac{qL^4\left(1-\frac{I_{yy}}{I_{xx}}\right)}{120EI_{yy}} - \left(\frac{q_pL^4}{120EI_{xx}} - y_r\right)}. \qquad (2 - 25)$$

As before, the critical load occurs when the denominator of Equation (2 – 25) is equal to zero. Solving, and simplifying:

$$q_{LRB,vp} = -\frac{120EI_{yy}y_r}{L^4}\frac{\left(1-\frac{q_pL^4}{120EI_{xx}y_r}\right)}{\left(1-\frac{I_{yy}}{I_{xx}}\right)} = q_{LRB,o}\frac{\left(1-\frac{\overline{v}_p}{y_r}\right)}{\left(1-\frac{I_{yy}}{I_{xx}}\right)}, \qquad (2 - 26)$$

where $\bar{v}_p$ is defined above in Equation (2 – 20). Expressing Equation (2 – 26) in terms of $\bar{v}_p$ adds utility to the expression in that the critical load no longer relies upon the equivalent uniform upwards load due to a parabolic prestressing strand profile. Rather, it is simply a function of the average position of the prestressing deflections. If the maximum prestressing deflection is taken as $v_{p,max}$, and the prestressing deflection is assumed to take the shape of a simply supported beam subjected to a uniform load, the average prestressing deflection is then

$$\overline{v}_p = 0.64 v_{p,max}. \qquad (2 - 27)$$

This decouples the critical load from the equivalent q_p term. While using q_p is convenient for the Imperfection Sensitivity study conducted in Chapters 4 and 5, it is most applicable in practice to express prestressing effects in terms of their maximum deflection. The maximum deflection approach will be used in the design examples presented in Chapters 8 and 9.

If prestressing deflections are ignored or are equal to zero, this simplifies to the LRB load with SAB of Equation (2 – 19). The uniform prestressing load, q_p, is directed upwards, is therefore negative, and reduces the magnitude of the positive LRB load. Prestressing deflections are destabilizing. Effectively, prestressing deflections decrease the magnitude of the roll axis height, which in turn would lower the buckling load.

Since SAB is stabilizing, there should be a prestressing level where SAB and prestressing cancel out, and the resulting critical load is the baseline LRB load, $q_{LRB,o}$. Prestressing deflection and SAB effects cancel each other out when $\frac{\overline{v}_p}{y_r}$ is equal to $\frac{I_{yy}}{I_{xx}}$. Solving for the q_p that satisfies this condition:

$$q_{p,bal} = \frac{120 E I_{yy} y_r}{L^4}, \qquad (2 - 28)$$

or, in terms of the average prestressing deflection

$$\overline{v}_p = y_r \frac{I_{yy}}{I_{xx}}. \qquad (2 - 29)$$

Equation (2 – 28) is the negative of the baseline LRB critical buckling load, and $q_{p,bal}$ is the equivalent upwards prestressing load that balances the effects of strong axis bending and camber. This can be seen in Figure 2.4 which compares the critical load accounting for SAB and camber, normalized by the baseline LRB load, versus the equivalent uniform prestressing load, normalized by the baseline LRB load as well, for different WSDOT WF Series girders.

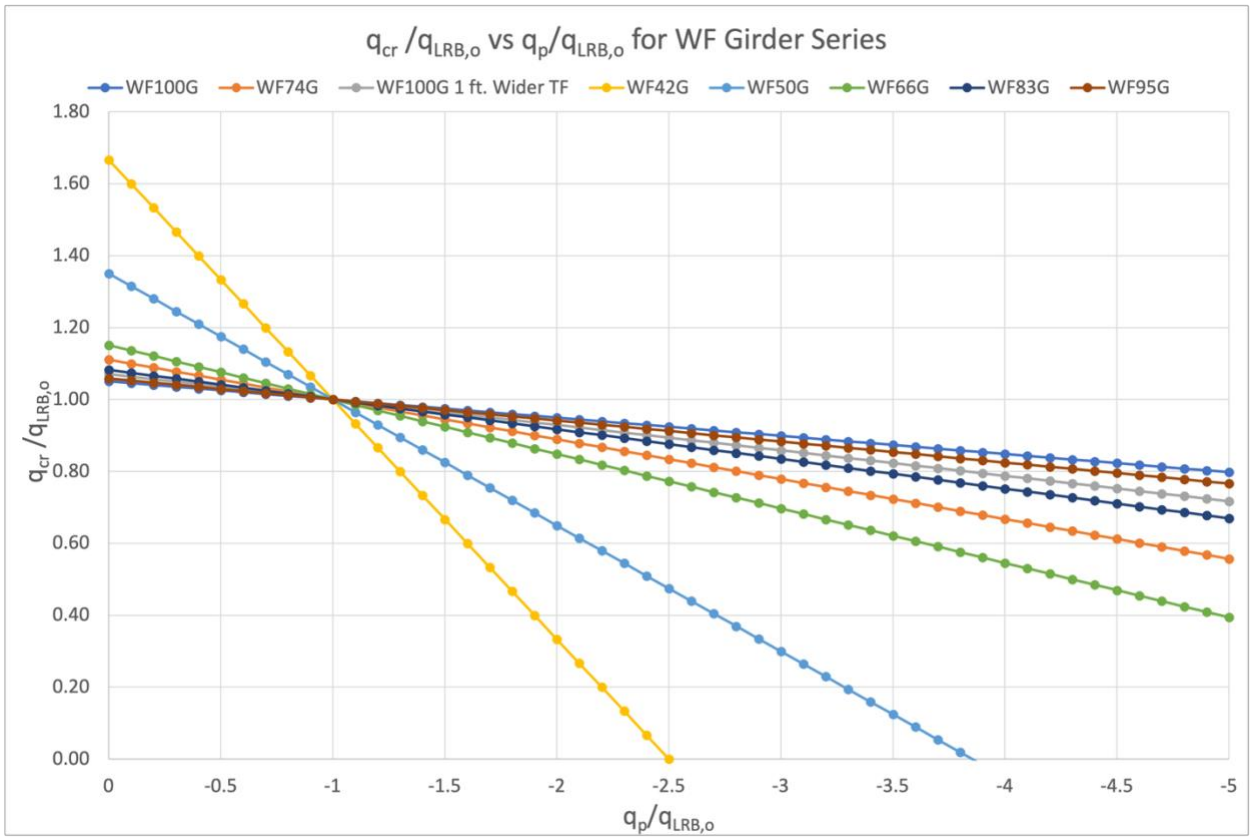

Figure 2.4 Critical Load Normalized by the Baseline LRB Load versus Applied Prestressing Load Normalized by the Baseline LRB load.

Note that Figure 2.4 is valid only strictly for end supported girders. If torsion or overhangs were incorporated, a similar expression to Equation (2 – 28) could be determined, but it would take on a separate form. For all the girders evaluated, when the prestressing load is equal to the baseline

LRB load, the critical load is equal to the baseline LRB load. For ratios where $\frac{q_p}{q_{LRB,o}} < 1.0$, the girder is relatively stabilized by SAB. For ratios greater than 1.0, the girder is increasingly destabilized by the prestressing deflections.

Per Equation (2 – 26), there is theoretically a prestressing deflection that would cause the buckling load to be zero, no matter the SAB deflections, if there were no overhangs. To do this, $\overline{v}_p$, the average prestressing deflection, would need to be equal to y_r, the roll axis height. Physically, this implies that the center of mass of the girder would be at the level of the roll axis, so the system has a zero "pendulum stiffness" and so is unconditionally unstable. For a WSDOT WF100G girder that is hanging from lifting loops at its ends, this would be an *average* prestressing deflection of upwards of 50 inches. This is physically unrealistic and would almost certainly not occur in practice. If the equivalent q_p load were used to measure this condition instead, the resulting unconditionally unstable load would be

$$q_{p,unstable} = \frac{120EI_{xx}y_r}{L^4}. \qquad (2 - 30)$$

Interestingly, it is of the exact same form as the baseline LRB load, but with the strong axis moment of inertia instead of the weak axis moment of inertia. This level of prestressing would almost certainly not exist in practice.

2.3. **Effect of Overhangs**

Almost universally, bridge girders are lifted by loops or supported on trucks by rotationally flexible supports that are offset inwards from the girder's ends. Just as a cantilevered overhang on a gravity loaded beam reduces maximum moment and deflection at midspan, the balancing effect of overhangs reduces the maximum rotation at midspan, thereby increasing lateral stability.

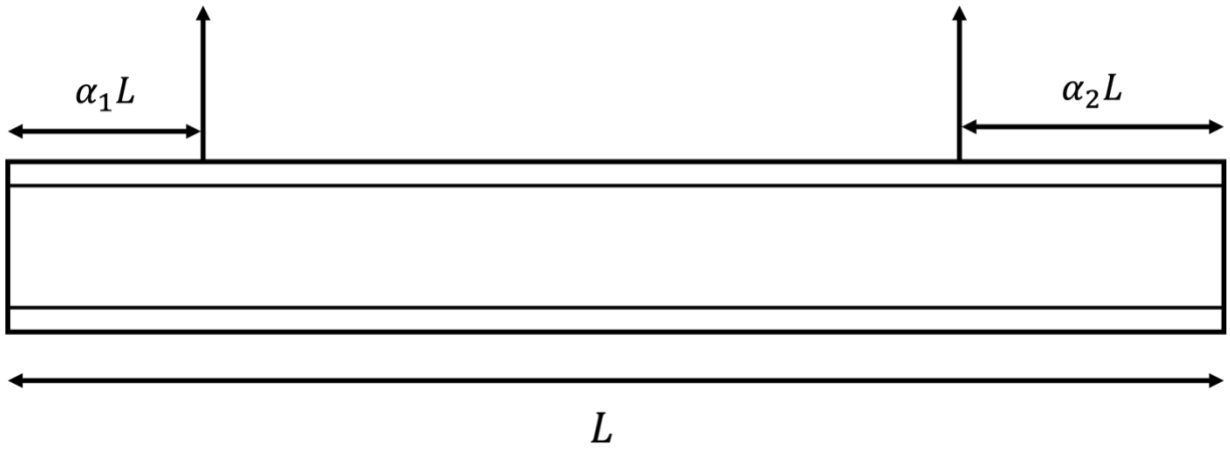

Figure 2.5 Layout of Girder with Overhangs

Overhangs affect the LRB load. The details and implications of overhangs on the buckling load are described by Galik, Stanton, & Wiebe (2022). This section summarizes the results described there.

The layout of a girder with overhangs is shown above in Figure 2.5. The ratio of the overhang length to the overall length of the girder is labelled α. Mast (1989) and Stratford and Burgoyne (1999) showed that overhangs greatly improve lateral stability during transportation and handling. For symmetrically placed vertical lifting loops with equal overhang lengths, the average deflection of the center of gravity of the girder was reduced by a factor, $f_{LRB}(\alpha)$ and the buckling load was increased by $\frac{1}{f_{LRB}(\alpha)}$, where that factor is

$$f_{LRB}(\alpha) = 1 - 10\alpha + 30\alpha^2 - 20\alpha^3 - 10\alpha^4. \qquad (2 - 31)$$

Galik, Stanton, & Wiebe (2022) extended this result to capture the effects of overhangs on girders with asymmetrically placed lifting loops. This modified the $f_{LRB}(\alpha)$ factor to

$$f_{LRB}(\alpha, t) = \sum_{j=0}^{4} c_j s_j(t) \alpha_m^j, \qquad (2 - 32)$$

where

$$\alpha_1, \alpha_2 \quad Overhang\ ratio\ at\ each\ end, \tag{2 – 33a}$$

$$a_m = 0.5(\alpha_1 + \alpha_2) \quad The\ mean\ overhang\ ratio, \tag{2 – 33b}$$

$$t = \frac{\alpha_1 - \alpha_2}{\alpha_1 + \alpha_2} \quad The\ asymmetry\ parameter, \tag{2 – 33c}$$

$$c_j = [1, -10, 30, -20, -10], \tag{2 – 33d}$$

$$s_j(t) = \left[1,1,\left(1 - \frac{t^2}{3}\right), (1 - 3t^2), (1 - t^2) * (1 + 3t^2)\right]. \tag{2 – 33e}$$

If the overhangs are equal, Equation (2 – 32) simplifies to Equation (2 – 31). The critical LRB load accounting for overhangs (asymmetric or not) is

$$q_{LRB,\alpha} = \frac{q_{LRB,o}}{f_{LRB}(\alpha, t)}. \tag{2 – 34}$$

Galik, Stanton, & Wiebe (2022) showed that the optimum α value for stability is approximately 23 percent. However, overhangs at the end of the girder cause increased tension in the top-flange near the pick-point. Combined with the top flange tension induced by prestressing before service loading, large overhangs could lead to excessive tension in the girder top-flange, which could cause the girder to crack. For this reason, overhang ratios would not typically be increased to 23 percent. To mitigate this problem, girders are frequently transported and erected with temporary prestressing strands in the top flange to prevent excessive tensile stresses from developing.

For a girder with both asymmetric overhangs and different roll-axis heights at each end, the torque resisting the overturning moment at each end will be different. This will affect the buckling load. It can be shown that the effective roll axis height for a prismatic girder undergoing LRB with asymmetric overhangs and unequal roll axis heights is

$$y_{r,eff} = \frac{y_{r1}(0.5 - \alpha_2) + y_{r2}(0.5 - \alpha_1)}{1 - \alpha_1 - \alpha_2}. \tag{2 – 35}$$

2.3.1. **Modified Effect of Prestressing Deflections with Overhangs**

The derivation of the critical load accounting for prestressing deflections assumed that the girder was supported from its ends. If the girder has overhangs, the prestressing strands still deflect the beam roughly in the shape of simply supported beam with a uniform upwards load applied; however, the self-weight deflections due to the gravity loads are now modified because of the overhangs. A modification must be made to the critical load to account for this effect.

To this point, deflections relative to the ends of the girder have been equal to deflections relative to the supports of the girder. Now, the maximum prestressing deflection is still relative to the ends of the beam, but the average position of the self-weight deflections is relative to the supports. The shifted position of the center of gravity due to prestressing deflections must be accounted for relative to the supports. Figure 2.6 presents a schematic of the various measurements made for calculation of the center of gravity position of the girder (relative to the supports) due to prestressing deflections.

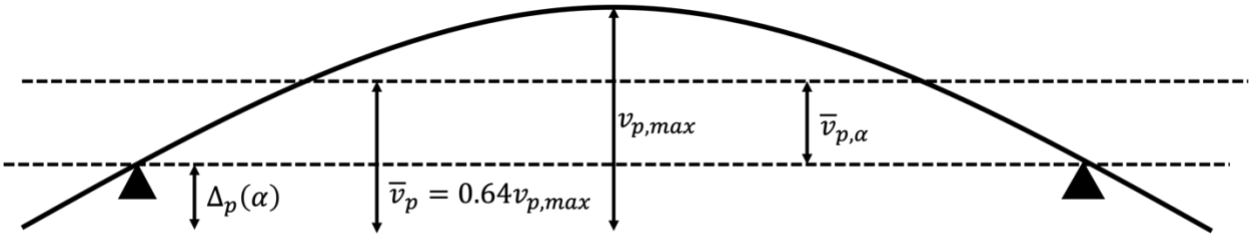

$$\overline{v}_{p,\alpha} = \overline{v}_p - \Delta_p(\alpha)$$

Figure 2.6 Schematic of Prestressing Deflection Measurements

The shape of the prestressing deflections is assumed to still be that of a simply supported beam with a uniform distributed load applied. The prestressing deflections at the supports, relative to the ends, for a given (symmetric) overhang ratio, are then

$$\Delta_p(\alpha) = v_{p,max}\left(3.2\alpha(1 - 2\alpha^2 + \alpha^3)\right) \qquad (2-36)$$

where $v_{p,max}$ is the maximum prestressing deflection relative to the ends of the girder. The average shifted center of gravity position due to the prestressing deflections, relative to the ends is still $\overline{v}_p$ and is 64 percent of the maximum prestressing deflection. The shifted center of gravity position due to prestressing deflections, relative to the girder supports, is then

$$\overline{v}_{p,\alpha} = \overline{v}_p - \Delta_p(\alpha). \qquad (2-37)$$

Accounting for this effect, Equation (2 – 21) becomes

$$\tan\phi = \frac{e_x - \dfrac{qL^4 \sin\phi}{120EI_{yy}}}{y_r - \dfrac{qL^4\cos\phi}{120EI_{xx}} - \overline{v}_{p,\alpha}} \qquad (2-38)$$

Expanding $\overline{v}_{p,\alpha}$ and solving for the equilibrium path gives

$$q(\phi) = \tan\phi\left(\frac{q_p L^4}{120EI_{xx}} - \Delta_p(\alpha) - y_r\right)\left(\frac{120EI_{yy}}{L^4\left(1 - \dfrac{I_{yy}}{I_{xx}}\right)\sin\phi}\right). \qquad (2-39)$$

Making a small angle assumption and solving for the roll angle gives the critical load. This derivation is for a girder with symmetric overhangs. The $f_{LRB}(\alpha)$ factor must be factored in as well.

$$q_{LRB,vp\alpha} = \frac{q_{LRB,o}}{f_{LRB}(\alpha)}\frac{\left(1 + \dfrac{1}{y_r}\left(\Delta_p(\alpha) - \overline{v}_p\right)\right)}{\left(1 - \dfrac{I_{yy}}{I_{xx}}\right)} \qquad (2-40)$$

2.4. **Effect of Torsional Flexibility**

The buckling loads developed in the previous sections assumed torsional rigidity. This reflects the assumption in Mast's (1989) work, as well as in the papers by Stratford and Burgoyne (1999), which was made because ignoring torsional deformations greatly simplified the analysis and was found to have minimal impact on their results. Mast (1989), as well as Stratford and Burgoyne (1999) performed a simple check that showed that, for the girder sections and spans typical of the day, torsional deformations were indeed small enough to justify ignoring them. This was further validated by a full-scale test to destruction of a prestressed concrete girder, published by Mast (1993, 1994). There, it was observed that the twist angle was only 2-4 percent of the total roll angle, even past the point of cracking and near collapse. However, as bridge girder spans have increased, it has become apparent that torsion no longer plays a negligible role in lateral stability. Longer girder spans have required deeper cross sections. While these sections have gotten deeper, they have not been made wider, in order to save on costs by using the same flange formwork. This has resulted in lower torsional and weak-axis stiffnesses relative to the strong-axis stiffness, which has caused twist to become more apparent during transportation and handling.

Incorporating torsional flexibility greatly increases the complexity of the problem. Properly and exactly modelling torsional effects in girder lateral stability requires extensive model changes. No closed-form solution exits for the buckling load when both torsional and flexural deformations are included. Galik, Stanton, & Wiebe (2022) reported the governing differential equation for twist angle along a girder supported at its ends, with a uniformly distributed load (self-weight), no SAB or prestressing deflections, and no warping end-restraint as

$$\frac{d^2\phi(\zeta)}{d\zeta^2} + \frac{\kappa^2 L^6}{4}\zeta^2(1-\zeta)^2\,\phi(\zeta) = 0, \qquad (2-41)$$

Where z is the coordinate measured longitudinally along the length of the girder, ζ is the dimensionless ratio of $\frac{z}{L}$, and κ is a load parameter, equal to $q/\sqrt{GJEI_{yy}}$. Galik, Stanton, & Wiebe (2022) developed a factor that modifies the previously developed LRB load to account for the reduction in overall stiffness, and hence lateral buckling load, associated with torsional effects. They approximated the solution to the governing differential equation using a Ritz-Galerkin representation of the solution of Equation (2 – 41). For a girder supported at its ends, they chose shape functions for $\phi(\zeta)$ as odd sine functions and then used the first mode alone (to develop closed-form design expressions) to approximate the solution to the differential equation.

Lateral-Torsional-Roll-Buckling (LTRB) is an interaction between Lateral Torsional Buckling (LTB)—rotation restrained at the supports, but a torsionally flexible girder body—and Lateral Roll Buckling (LRB)—rotational flexibility at the supports but a torsionally rigid girder body. Galik, Stanton, & Wiebe (2022) used their approximate solution to the governing differential equation and an interaction equation between the LTB and LRB critical loads to develop a knockdown factor, $g(\eta_o)$ that modifies the baseline LRB load, $q_{LRB,o}$ to account for torsional deformations in the buckling load formulation. That interaction equation is

$$\left(\frac{q_{LTRB}}{q_{LTB}}\right)^2 + \frac{q_{LTRB}}{q_{LRB}} = 1.0 \qquad (2-42)$$

By isolating torsional effects into a knockdown factor, the same LRB loads developed in the preceding sections may still be used, with the option of including torsional effects. The knockdown factor, $g(\eta_o)$, is found from a series of unitless expressions:

$$\beta = \sqrt{\left(\frac{y_r}{L}\right)^2 \frac{EI_{yy}}{GJ}}, \quad (2 - 43)$$

the β factor is then plugged into η_o:

$$\eta_o = 71.9\beta^2. \quad (2 - 44)$$

The "o" subscript on η_o indicates that this value is valid for the baseline LTRB case: no SAB, prestressing deflections, or overhangs. The value of β, which is a property of the cross-section alone, remains the same for more complicated LTRB cases, such as when overhangs are included, for which the η is slightly modified. Those modifications will be presented in Sections 2.4.1 and 2.4.2. The final knockdown expression for the baseline LTRB case is:

$$g(\eta_o) = \frac{2}{\eta_o}\left(\sqrt{1 + \eta_o} - 1\right). \quad (2 - 45)$$

The baseline LTRB load is then:

$$q_{LTRB,o} = g(\eta_o) q_{LRB,o} \quad (2 - 46)$$

As the torsional stiffness increases, β tends towards 0.0 and $g(\eta_o)$ approaches 1.0. The interaction between LTB and LRB then trends towards LRB. As β increases (particularly beyond 2.0), the interaction between LTB and LRB trends towards approximating LTB (Galik, Stanton, & Wiebe, 2022).

While the $g(\eta_o)$ factor was derived using only the first mode response in the torsional calculations, it was shown, by separate numerical calculations in the Appendix of the work by Galik, Stanton, & Wiebe (2022) to approximate very closely the true, multi-mode, response. It was therefore proposed for universal use.

2.4.1. **Accounting for Strong-Axis Bending and Prestressing Deflections in LTRB**

To account for SAB and prestressing deflections in the torsional knockdown factor, the Equation (2 – 42) for the interaction between LTB and LRB can be modified to include the effects of SAB and prestressing deflections in both the LTB and LRB critical loads. The LTB load accounting for SAB and prestressing deflections then becomes

$$q_{LTB,vp} \cong q_{LTB,v} = q_{LTB,o}\sqrt{\frac{1}{1-\frac{I_{yy}}{I_{xx}}}} \qquad (2 - 47)$$

where $q_{LTB,o}$ is the LTB solution, in this instance, from Vacharajittiphan, et al (1974) with the assumption that $GJ/EI_{xx} \approx 0$ and that there is no warping restraint. The assumption that $q_{LTB,vp} \cong q_{LTB,v}$ arises from Peart, et al (1992) who found that prestressing deflections had a small effect on the buckling load. The LRB load accounting for SAB and prestressing deflections is Equation (2 – 26). Different results could be determined if separate LTB or LRB solutions were used with different assumptions.

Following the same procedure as Galik, Stanton, & Wiebe (2022) using their interaction equation, the modified η factor accounting for SAB and prestressing deflections becomes

$$\eta_{vp} = \eta_o \frac{\left(1-\frac{\overline{v}_p}{y_r}\right)^2}{\left(1-\frac{I_{yy}}{Ixx}\right)}. \qquad (2 - 48)$$

The β factor remains the same. The η factor is modified in the same was $q_{LRB,o}$ was when SAB and prestressing deflections are accounted for, except that the numerator is squared. The η_{vp} is then substituted for η_o in Equation (2 – 45) to calculate $g(\eta_{vp})$. The LTRB load accounting for SAB and prestressing (without overhangs) is then

$$q_{LTRB,vp} = g(\eta_{vp}) q_{LRB,vp}. \quad (2 - 49)$$

This result would hold even if prestressing deflections or SAB were neglected. If either effect were excluded, then the LRB load would also need to be correspondingly modified.

2.4.2. **Accounting for Overhangs in LTRB**

Overhangs modify the interaction equation between LRB and LTB. Galik, Stanton, & Wiebe (2022) in their report to PCI assumed that overhangs affected LTB and LRB equally in their interaction. It is assumed here, however, that overhangs effect LTB and LRB differently in their interaction. Section 2.3 showed the overhang factor for LRB, namely $f_{LRB}(\alpha)$. If it is assumed that the overhangs provide no twisting/warping restraint for the LTB case, then the LTB case with (equal) overhangs is essentially a simply supported span of length $(L - 2\alpha L)$. The LTB critical load is proportional to the third power of length, so it is proposed that the overhang factor for LTB is then

$$f_{LTB}(\alpha) = (1 - 2\alpha)^3. \quad (2 - 50)$$

If the LTB and LRB loads accounting for SAB and prestressing deflections (Equations (2 – 47) and (2 – 26)) are modified by their respective overhang factors and plugged into the interaction equation, it can be shown, after significant algebra, that the η factor becomes

$$\eta_{vp\alpha} = \eta_{vp} \left(\frac{f_{LTB}(\alpha)}{f_{LRB}(\alpha)} \right)^2. \quad (2 - 51)$$

Once again, the β factor remains the same. In addition, the η_{vp} factor must be modified to account for overhangs and the position of the center of gravity relative to the supports versus relative to the ends, just as the LRB load with SAB, prestressing deflections, and overhangs was. The η_{vp} for use in Equation (2 – 51) then becomes:

$$\eta_{vp} = \eta_o \frac{\left(1 + \frac{1}{y_r}\left(\Delta_p(\alpha) - \overline{v}_p\right)\right)^2}{\left(1 - \frac{I_{yy}}{Ixx}\right)}. \quad (2-52)$$

It is proposed that Equation (2 – 52) be used universally in the place of Equation (2 – 48) because Equation (2 – 52) is valid when overhangs are included but collapses to Equation (2 – 48) when there are no overhangs. Equation (2 – 48) is only valid when there are no overhangs. The $\eta_{vp\alpha}$ factor of Equation (2 – 51), which properly accounts for overhangs with the use of Equation (2 – 52) is then substituted into Equation (2 – 45) to calculate $g(\eta_{vp\alpha})$. The final torsional knockdown on the LRB load accounting for SAB, prestressing deflections, and overhangs is

$$q_{LTRB,vp\alpha} = g(\eta_{vp\alpha}) q_{LRB,vp\alpha}. \quad (2-53)$$

In an expanded form, $q_{LTRB,vp\alpha}$ is

$$q_{LTRB,vp\alpha} = \frac{q_{LRB,o}}{f_{LRB}(\alpha)} \frac{\left(1 + \frac{1}{y_r}\left(\Delta_p(\alpha) - \overline{v}_p\right)\right)}{\left(1 - \frac{I_{yy}}{I_{xx}}\right)} g(\eta_{vp\alpha}). \quad (2-54)$$

Each of the modifying factors in Equation (2 – 54) reduces to 1.0 when the associated effect is absent, so $q_{LTRB,vp\alpha}$ then reduces to $q_{LRB,o}$, as it should if only the baseline LRB load assumptions are made.

2.5. **Conversion from Supported from Below to Equivalent Hanging Girder**

Shipping a girder on a truck from the fabrication yard to a job site is a significant step in the early life and lateral stability design of a girder. During this time, the girder is supported from below by the truck which is rotationally flexible (because of the suspension), instead of from above by lifting loops suspended from a crane. These two cases seem quite different, and the literature has generally treated them as separate analyses; however, it is possible to convert the supported from below case to an equivalent hanging case because both represent supports with torsional stiffness.

Galik, Stanton, & Wiebe (2022) showed a similar derivation in their report. While these derivations share similar premises, there are two key differences between their work and the result reported here. First, their derivation assumed that the torsional spring support was located directly at the bottom of the girder. Second, their derivation implicitly assumed the roadway on which the truck was resting was not on a cross slope. Incorporating these changes does not change the procedure of the derivation, but it does change the details, variables, and the ability to linearize the final equation.

Figure 2.7 shows the problem set up for the derivation of the conversion from a supported below girder to an equivalent hanging girder. Here, ϕ is the total angle between the local y-axis and the vertical and α is the roadway cross slope.

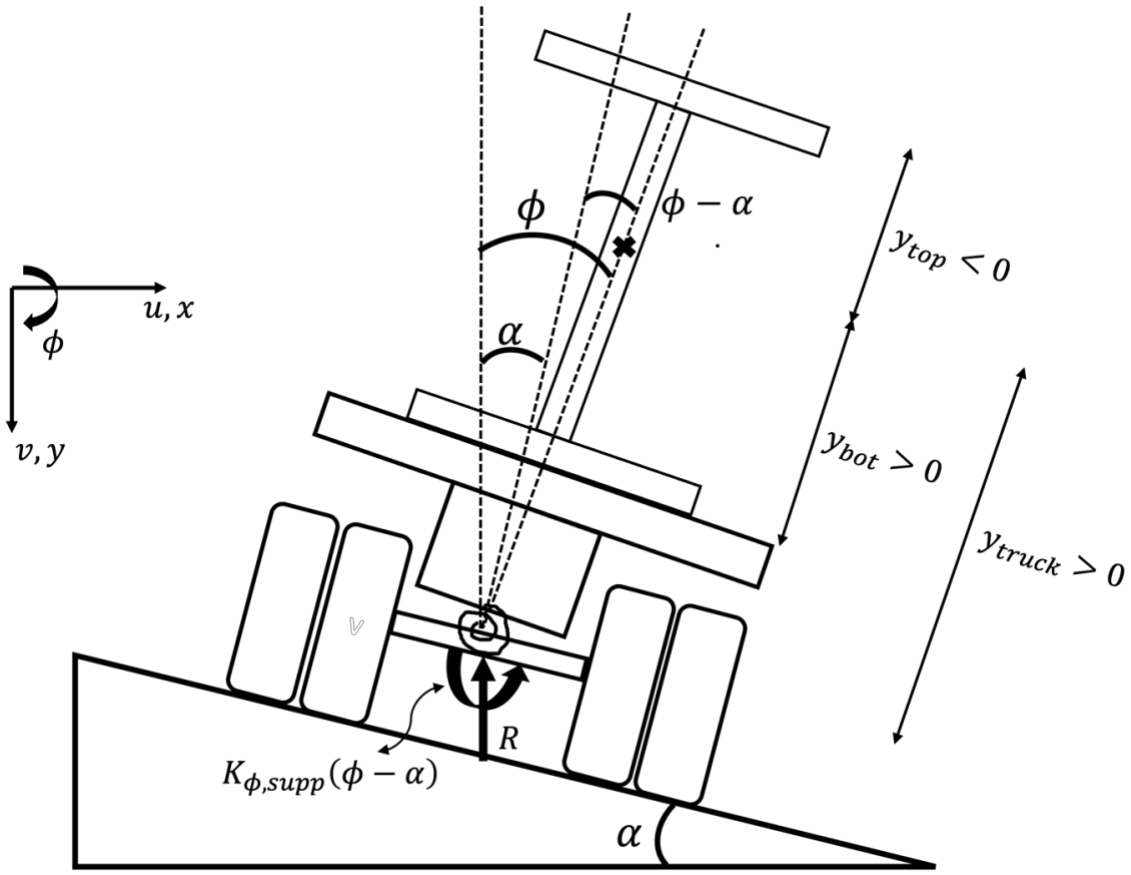

Figure 2.7 Free Body Diagram of Supported from Below Girder; Cross-Section at Support

Moment equilibrium about the centroid (represented by the "x" on the girder), noting that R is negative, gives

$$-\left(Ry_{truck}\sin\phi + K_{\phi,supp}(\phi - \alpha)\right) = 0. \qquad (2 - 55)$$

Extracting a sine from the parentheses, the total torsional stiffness can be expressed as

$$-\left(Ry_{truck} + \frac{K_{\phi,supp}(\phi - \alpha)}{\sin\phi}\right)\sin\phi = -K_{\phi}\sin\phi. \qquad (2 - 56)$$

Note the distinction between $K_{\phi,supp}$ (the torsional stiffness of the spring support) and K_{ϕ} the total rotational stiffness of the system, which is equal to the expression in the parentheses on the lefthand side of Equation (2 – 56). At this step in the derivation shown by Galik, Stanton, & Wiebe (2022) a small angle assumption was made, and since α, the roadway cross slope, was

assumed to be zero, the expression could be linearized and all dependence on ϕ removed. Including roadway cross slope precludes eliminating ϕ entirely from the expression. Therefore, the methods for solving for the equilibrium angle of the girder, which will be introduced in Chapter 3, will have to be at least slightly iterative for a supported from below girder on a cross slope, for the torsional stiffness of the system depends on the final angle, which is unknown at the start of the problem. While the method shown in Chapter 3 is closed-form and algebraic, it likely requires some iteration, easily programmed into a spreadsheet or similar. Therefore, requiring some iteration to solve for the total rotational stiffness of the system adds minimal complexity to the solution methods, which will be introduced shortly in Chapter 3.

Figure 2.8 shows the free body diagram at a cross section at the support for a hanging girder.

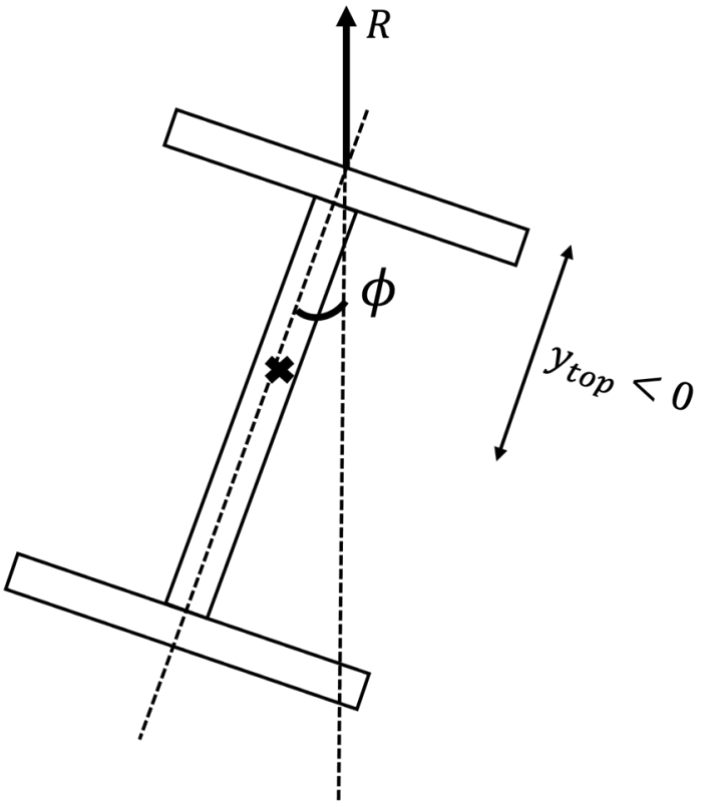

Figure 2.8 Free Body Diagram of Hanging Girder; Cross-Section at Support

Equating the total rotational stiffness of the supported from below girder (Equation (2 – 56)) to the rotational stiffness of the hanging girder (about the centroid), noting that here both *R* and y_{top} are negative, gives:

$$-K_{\phi} \sin\phi = -Ry_{top} \sin\phi. \qquad (2 - 57)$$

The sines and the negative signs cancel out. Expanding K_{ϕ}, the total rotational stiffness of a supported from below girder that gives an equivalent y_{top}, or equivalent roll axis height for a hanging girder, can be solved for:

$$y_{r,eq} = y_{top,eq} = y_{truck} + \frac{K_{\phi,supp}(\phi - \alpha)}{R \sin\phi} \qquad (2 - 58)$$

If, for example, y_{truck} is 85 inches, $K_{\phi,supp}$ is 20000 in-kip/radian, the final equilibrium angle, ϕ, is 0.085 Radians, the roadway cross slope is 0.02 Radians, and R is -100 kips, the equivalent roll axis height is -68.125 inches. The negative sign on the equivalent roll axis height matches with what the sign of the roll axis would be for an actual hanging girder.

Converting from a supported from below girder to an equivalent hanging girder allows both hanging and truck-supported girders to be treated in the same way—a second set of critical loads for supported from below girders does not need to be derived. All the equations previously presented in Chapter 2 still apply for supported from below girders, the equivalent roll axis height simply needs to be used instead of the distance from the centroid to the top flange. That will allow the imperfection study in this work to focus on the hanging case and eliminate the need to repeat the imperfection study for a second subset of girders that are supported from below. Ultimately, it will also allow hanging girders and hauled girders to be designed using the same procedure, just with different roll axis heights.

The above derivation assumes that the rotational stiffness of the truck's suspension is linearly proportional to the roll angle. The stiffness of the support is almost certainly nonlinear, however, and such a complication would have to be considered at large roll angles. This, however, would add complication to the equivalent roll axis height, and would add another layer of iteration to the solution. The imperfection study described below, and the design procedure proposed in Chapter 8, assume that the rotational support stiffness remains linear. Further, the assumption of linear rotational stiffness is most valid at small equilibrium angles. A typically designed girder would likely achieve equilibrium at an angle small enough that cracking would ideally not occur. For these smaller equilibrium angles, the linear rotational stiffness assumption is likely still reasonably valid. Incorporating cracking into girder LTRB stability will be explored beginning in Chapter 6.

3. Initial Roll Angle and Model Development for Uncracked Sections

3.1. **Study Framework and Initial Roll Angle**

In Chapter 2, critical loads were developed, both for the baseline case of a girder supported from above by lifting loops at the ends, and for more complex conditions which accounted for overhangs, SAB deflections, prestressing deflections, and torsion. A method for converting from a girder supported from below by rotationally flexible supports to an equivalent hanging girder was presented. The critical load derivations included the effects of imperfections, but the linearized (small angle) critical load ultimately did not depend on the magnitude, or type, of imperfection present. In this chapter, the effects of geometric imperfections, i.e., lateral symmetry-breaking imperfections, on the initial roll of the girder are explored.

The structural and load parameters that dictate the lateral stability behavior of girders can be broken up into two categories: those that shift the center of gravity of the girder laterally, causing an initial roll angle and pre-buckling deformations—herein called symmetry-breaking parameters—and those that change the critical load but do not shift the center of gravity laterally. The symmetry-breaking parameters are often called imperfections.

Figure 2.3 depicts both the linearized (small angles) and nonlinearized (large angles) equilibrium paths of girders with different magnitudes of symmetry-breaking imperfections. The horizontal black dashed line of Figure 2.3 shows the linearized buckling load of a perfect girder—herein termed as the bifurcation load. In the linearized case, as the load increases from zero, no roll occurs until the bifurcation load is reached, at which point the roll becomes indeterminate and no greater load is possible. The blue curve of Figure 2.3 shows the same girder but includes large angle deformations in the equilibrium path. The bifurcation point is the same, but the girder can withstand higher loads and has residual post-buckling stiffness. The orange

and gray curves likewise show the large angle equilibrium path of a girder, but they each have lateral imperfections, and as such undergo pre-buckling deformations and lack a hard bifurcation point. The pre-buckling deformations for those girders occur most rapidly as the applied load approaches the actual buckling load. The green curve depicts a girder with the same lateral imperfection as the orange curve but the small angle equilibrium path.

The imperfection study will be conducted in three phases:

- In the first, the relationship between initial and final roll angles of a girder is developed for baseline LRB (i.e., ignoring torsional deformations, prestressing and SAB deflections, and overhangs). It will explore the hypothesis that girders with different imperfection mechanisms (i.e., sweep versus eccentric lifting loops), but equal initial roll angles, result in identical pre- and post-buckling deformations.
- The second phase explores the effects that prestressing, SAB deflections, and overhangs have on the critical load, and how those modifications change the pre- and post-buckling deformations.
- The third phase repeats the first two phases, except the girder is no longer considered to be rigid in torsion, i.e., the girder undergoes LTRB.

The initial roll angle, ϕ_o, is defined as the roll angle that the girder would assume if its shape was frozen after the initial imperfection (sweep, eccentric lifting loop, etc.) was introduced, and it was allowed to roll freely. In other words, it is the rigid-body roll angle the girder would assume to achieve moment equilibrium, due to the imperfections, before deformations due to load took place. Freezing the shape would prevent any stress-based deformations due to applied loads that would, in fact, increase the eccentricity of the load and

hence, the roll angle. The initial roll will never occur in practice as the actual gravity loads will instantaneously magnify the imperfections, leading to more roll and ultimately the final equilibrium configuration, but it is a useful construct for calculations.

As an example, the initial roll angle for a girder with eccentric lifting loops may be calculated geometrically using the position of the center of gravity by examining Figure 2.2. If the stress-based lateral deflections of the center of gravity, $\overline{u}$, are zero (since the girder is "frozen" after its initial roll,) then the initial roll angle is

$$\tan \phi_o = \frac{e_x}{y_r}. \qquad (3 - 1)$$

Note that for the hanging girder of Figure 2.2, e_x is to the left and is therefore negative. That negative combines with the negative value of y_r for the hanging case to result in a positive initial roll angle.

3.2. **Relationship Between Initial and Final Roll Angles**

The relationship between the initial and final roll angle is developed here for the case of a girder with a lifting loop eccentricity as a symmetry breaking imperfection. The equilibrium path for baseline LRB, as shown by Equation (2 – 8) is

$$q(\phi) = \frac{120EI_{yy}}{L^4 \sin \phi}(e_x - y_r \tan \phi), \qquad (2 - 8)$$

and the corresponding critical load is

$$q_{LRB,o} = -\frac{120EI_{yy}y_r}{L^4}. \qquad (2 - 10)$$

Substituting Equation (2 – 10) into Equation (2 – 8) gives

$$q = -\frac{q_{LRB,o}}{\sin \phi}\left(\frac{e_x}{y_r} - \tan \phi\right). \qquad (3 – 2)$$

Recalling Equation (3 – 1), the definition of the initial roll angle, and simplifying leads to

$$\frac{q}{q_{LRB,o}}\sin\phi = \tan\phi - \tan\phi_o, \tag{3 – 3}$$

which can in turn be re-hashed into a form very similar to that seen in column buckling, where the baseline LRB load is replaced by q_{cr}, an arbitrary critical load:

$$\frac{\tan\phi}{\tan\phi_o} = \frac{1}{1-\frac{q}{q_{cr}}\cos\phi}. \tag{3 – 4}$$

If one makes a small angle assumption such that $\tan\phi \approx \phi$, $\tan\phi_o \approx \phi_o$, and $\cos\phi \approx 1$,

$$\frac{\phi}{\phi_o} = \frac{1}{1-\frac{q}{q_{cr}}}, \tag{3 – 5}$$

the result is what is herein termed the Simple Amplification Model (SAM). This result will be explored in Chapters 4 and 5 and can be used to predict the final roll angle of a girder with a known initial roll angle, critical load, and applied load. Note that the SAM agrees with Southwell (1932), Meck (1977), Mandal & Calladine (2002), and others (see the Literature Review in Chapter 1) for the form of the amplification of initial imperfections.

3.3. **Initial Roll Angles Caused by Different Imperfection Types**

The initial roll angle may alternatively be thought of as the total initial applied torsional moment divided by the torsional stiffness at the girder's supports,

$$\phi_o = \frac{M_{z,o}}{K_\phi}. \tag{3 - 6}$$

For small initial roll angles such that $\sin\phi \approx \phi$, the total torsional stiffness is approximately

$$K_\phi = \sum_{j=1}^{2} R_j y_{rj}, \tag{3 - 7}$$

where $R_j y_{rj}$ is the product of the reaction and roll axis height at each support. Note that, for the hanging girder, both R_j and y_{rj} are negative, so the stiffness is positive. The total initial applied torsional moment is given by Equation (3 – 8).

$$M_{z,o} = \int_0^L q_y u_o(z)\, dz + \int_0^L q_x v_o(z)\, dz + \int_0^L m_z(z)\, dz + \sum_{j=1}^{2} R_{y,o} e_x + \sum_{j=1}^{2} R_{x,o} e_y. \qquad (3 - 8)$$

The q terms are applied distributed loads in their respective directions, given by the "x" or "y" subscripts, at eccentricities along the length of the girder given by $u_o(z)$ and $v_o(z)$. The "o" subscripts indicate an initial starting value. Distributed torque along the length of the girder is given by $m_z(z)$ and the $R * e$ terms are eccentric support reactions in the directions shown.

For a girder with only lateral lifting loop eccentricities, the initial roll angle would then be

$$\phi_o \approx \frac{\sum_{j=1}^{2} R_{y,o} e_x}{\sum_{j=1}^{2} R_j y_{rj}\,,} = \frac{e_x}{y_r}, \qquad (3 - 9)$$

which is the same roll angle as calculated using geometry and the position of the center of gravity.

The imperfection study in Chapters 4 and 5 is conducted primarily considering lateral sweep as the symmetry breaking imperfection. Equations (3 – 6) through (3 – 8) may be used to determine the initial roll angle for a girder with an initial lateral sweep. Assuming the lateral sweep is in the profile of a simply supported beam under uniform load, with a maximum initial magnitude at mid-span of u_{sweep}, the average sweep deflection, $\bar{u}_{sweep}$, is 0.64 times the maximum. Then the applied torsional moment is just the first term of Equation (3 – 8)

$$M_{z,o} = \bar{u}_{sweep} qL, \qquad (3 - 10)$$

and the linearized rotational stiffness, summed for both supports assuming that y_r is equal at both supports, noting that the reaction against the self-weight load are negative, is

$$K_\phi = -qLy_r. \qquad (3 - 11)$$

Equation (3 – 9) contained two reactions, *R,* both negative. The applied load causing the torsional moment in Equation (3 – 10) is positive, while the reaction against that self-weight would be negative. Substituting into Equation (3 – 6) the initial roll angle for a girder with lateral sweep is

$$\phi_o = \frac{M_{z,o}}{K_\phi} = \frac{\bar{u}_{sweep} qL}{-qLy_r} = \frac{-\bar{u}_{sweep}}{y_r}. \qquad (3 - 12)$$

The negative preceding $\bar{u}_{sweep}$ is consistent with the overall sign convention used. It should be noted that positive sweeps and negative lifting loop eccentricities cause positive initial rolls. Equating the two initial roll angle expressions gives

$$e_x = -\bar{u}_{sweep} = -0.64u_{sweep}. \qquad (3 - 13)$$

The center of gravity of a girder with a lateral sweep is shifted in the direction of the sweep a distance equal to the average of the sweep deflection. Revisiting Figure 2.2, one can see that the center of gravity of a girder with a lifting loop eccentricity is shifted laterally by a magnitude equal to the lifting loop eccentricity. Examining Equations (3 – 12) and (3 – 13) one can see that the initial roll angles for the two different imperfection types are equal when their center of gravity shifts are identical, but opposite in sign. From this, it can be concluded that girders with identical center of gravity shifts will have equal initial roll angles. Since Equation (3 – 5) predicts the final roll angle based off a known initial roll angle, applied load, critical load, and no other parameters, it can be hypothesized that, all else being equal, imperfections with identical initial roll angles will lead to an identical final roll angle.

Reducing all symmetry breaking imperfections to an initial roll angle eliminates the need for multiple plots depicting the behavior of each imperfection. Instead, a single plot can be produced using initial roll angles alone. Further, in a design context, a designer may convert an imperfection of interest to an equivalent initial roll angle and determine the corresponding girder response.

3.4. **Modified Initial Roll Angle Calculation Accounting for Prestressing Deflections and Overhangs**

Equation (3 – 1) and Figure 2.2 are only identically correct for a simply supported girder without prestressing deflections or overhangs, which a prestressed concrete girder will almost certainly have in practice. Fortunately, incorporating these effects requires minimal modifications to the above procedure for calculating the initial roll angle.

As discussed in Section 2.2, to derive the critical load accounting for prestressing deflections, one must reduce y_r, the roll axis height, by the average prestressing deflection. This results in a simple modification to the initial roll angle for a girder with prestressing deflections and no overhangs:

$$\tan \phi_o = \frac{e_x}{y_r - \overline{v}_p}, \tag{3 - 14}$$

or if the imperfection is instead lateral sweep:

$$\tan \phi_o = \frac{-0.64 u_{sweep}}{y_r - \overline{v}_p}. \tag{3 - 15}$$

Recall that $\overline{v}_p$ was defined in Section 2.2 as the average vertical deflection of the girder due to prestressing deflections. SAB deflections do not modify the initial roll angle because it is calculated assuming that the girder is frozen in place after rolling due to its imperfections before gravity loads are applied.

Overhangs have a stabilizing effect on girder deflections, and the center of gravity position relative to the pick-points is changed when there are overhangs, both for lateral sweeps and for prestressing deflections. For a girder with lateral sweep that is lifted with overhangs, the overhangs do not change the profile of the lateral sweep, but instead the lifting points are brought in from the ends. The center of gravity of the girder relative to the ends is still 0.64 times the sweep magnitude, but the center of gravity position relative to the lifting points, in terms of an equivalent lifting loop eccentricity, becomes

$$e_x = -\left(0.64u_{sweep} - \Delta_{\mathrm{u}}(\alpha)\right) = -\overline{u}_{sweep,\alpha} \qquad (3 - 16)$$

where $\Delta_{\mathrm{u}}(\alpha)$ is the lateral displacement, relative to the ends, at the lifting point, and $\overline{u}_{sweep,\alpha}$ is the shifted center of gravity position due to sweep, analogous to $\overline{v}_{p,\alpha}$ of Equation (2 – 37). Figure 2.6 shows a schematic for various prestressing deflection values with overhangs included, but the figure also applies to lateral sweep deflections in the presence of overhangs. Assuming the sweep is in the shape of a simply supported girder with uniform load applied, $\Delta_{\mathrm{u}}(\alpha)$ is then

$$\Delta_u(\alpha) = u_{sweep}\left(3.2\alpha(1 - 2\alpha^2 + \alpha^3)\right), \qquad (3 - 17)$$

which is identical to Equation (2 – 36) for $\Delta_p(\alpha)$, but Equation (3 – 17) uses u_{sweep}, the maximum sweep imperfection, instead.

Thus, the initial roll angle for a girder with lateral sweep, overhangs, and no prestressing deflections is

$$\phi_o = \arctan\left(\frac{-\overline{u}_{sweep,\alpha}}{y_r}\right). \qquad (3 - 18)$$

For a girder with lifting loop eccentricity instead of lateral sweep, Equation (3 – 16) gives the lifting loop eccentricity that will give the same initial roll angle as a corresponding lateral sweep. The numerator of (3 – 18) is then just replaced by that value given by Equation (3 – 16).

The same concept also applies to a girder with prestressing deflections. The center of gravity will shift laterally, due to sweep, and now also vertically, which simply changes the roll axis height, y_r. Therefore, the initial roll angle is then

$$\phi_o = \arctan\left(\frac{-\overline{u}_{sweep,\alpha}}{y_r - \overline{v}_{p,\alpha}}\right), \qquad (3 - 19)$$

where $\overline{v}_{p,\alpha}$ is given in Chapter 2 by Equation (2 – 37). For a girder with lifting loop eccentricities, the numerator of Equation (3 – 19) is replaced by the equivalent eccentricity. The denominator of Equation (3 – 19) would remain unchanged since the same prestressing deflection profile would be the same in girders with both lateral sweep and lifting loop eccentricities.

If there was both a lifting loop eccentricity and a lateral sweep, the initial roll angles would combine. Then, the initial roll angle would be

$$\phi_o = \arctan\left(\frac{-\overline{u}_{sweep,\alpha}}{y_r - \overline{v}_{p,\alpha}}\right) + \arctan\left(\frac{e_x}{y_r - \overline{v}_{p,\alpha}}\right) = \arctan\left(\frac{-\left(\overline{u}_{sweep,\alpha} - e_x\right)}{y_r - \overline{v}_{p,\alpha}}\right). \qquad (3\text{-}20)$$

This condition will occur most often in practice and will be used in the proposed design procedure presented in Chapter 8.

The simple amplification shown in Section 3.2 was derived for the baseline LRB case. For a girder with SAB and prestressing deflections, the equilibrium path and critical load, respectively, are

$$q(\phi) = \frac{120EI_{yy}}{L^4 \sin\phi\left(1 - \frac{I_{yy}}{I_{xx}}\right)}\left(e_x + \tan\phi\left(\frac{q_p L^4}{120EI_{xx}} - y_r\right)\right), \qquad (2 - 24)$$

and

$$q_{LRB,vp} = -\frac{120EI_{yy}y_r}{L^4}\frac{\left(1-\frac{q_pL^4}{120EI_{xx}y_r}\right)}{\left(1-\frac{I_{yy}}{I_{xx}}\right)} = q_{LRB}\frac{\left(1-\frac{\overline{v}_p}{y_r}\right)}{\left(1-\frac{I_{yy}}{I_{xx}}\right)}, \qquad (2 - 26)$$

Dividing Equation (2 – 24) by Equation (2 – 26), and replacing $q_{LRB,vp}$ with q_{cr}, representing a generic critical load:

$$\frac{q}{q_{cr}}\sin\phi = \frac{e_x}{\frac{q_pL^4}{120EI_{xx}} - y_r} + \tan\phi. \qquad (3 - 21)$$

Recall from Section 2.2 that $\overline{v}_p = \frac{q_pL^4}{120EI_{xx}}$. Then, the first term of Equation (3 – 20) is the negative of Equation (3 – 14), and Equation (3 – 21) becomes Equation (3 – 3), repeated here,

$$\frac{q}{q_{cr}}\sin\phi = \tan\phi - \tan\phi_o, \qquad (3 – 3)$$

and the SAM results, as before in Section 3.2, if small angles are assumed. It is therefore hypothesized that the simple amplification will hold true, not just for the above derived cases, but also for girders with overhangs and with torsional flexibility. It can then be used to predict the final equilibrium angle for real girders with all the different imperfections and critical loads considered in the previous sections.

3.5. **Rollbuck 2021**

As part of the work presented by Galik, Stanton, & Wiebe, Rollbuck 2021, a computer program for determining the final equilibrium angle of a given girder layout, was produced. Rollbuck 2021 is described in detail in their work and in Appendix A of this document. A summary of Rollbuck 2021, including its general methods and capabilities, will be described here. It applies to uncracked girders. An updated version (Rollbuck 2022), which applies to both uncracked and cracked girders, is described in Chapter 6.

Rollbuck 2021 can determine the final equilibrium angle of a prestressed concrete girder that is either hanging from lifting loops or supported from below by rotationally flexible supports. It accounts for all the features described in Chapter 2, including SAB, prestressing deflections, overhangs, imperfections, and torsion. A girder cross section is inputted into the program. Its length, overhang length, prestressing amount, and the magnitudes of any imperfections are inputted as well. Using the algorithm briefly described below, the final equilibrium angles at nodes along the length of the girder are determined.

Figure 3.1 below shows a flowchart generally describing the Rollbuck 2021 algorithm.

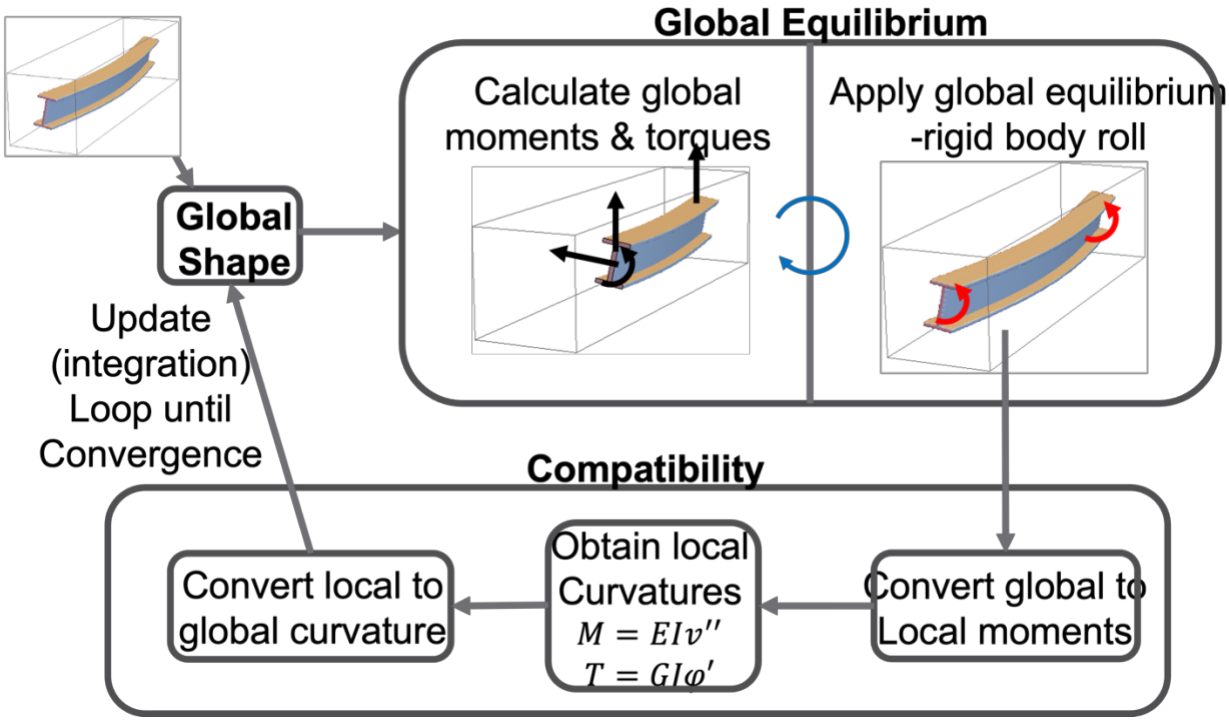

Figure 3.1 General Algorithm Flowchart for Rollbuck 2021

The program begins in the top left corner of Figure 3.1. An initial shape/layout of the girder is inputted into the program. This is where imperfections like lateral sweep or lifting loop eccentricity, overhang lengths, support stiffnesses, prestressing amount, etc., as well as applied loads, are inputted into the program. These inputs determine the “global shape” of the girder. The

girder is discretized into a set of nodes at which moments, curvatures, displacements, and rotations, etc., are calculated.

Rollbuck 2021 then enters the global equilibrium loop. From the global shape inputted into the program, the global moments, torques, and other forces are determined. Rollbuck 2021 then has the girder undergo a rigid body roll until the girder is in equilibrium. From there, the girder, in its rolled configuration, enters the compatibility loop. The global moments calculated in the equilibrium loop are converted to local moments using coordinate transformation matrices (described by Galik, Stanton, & Wiebe (2022)).

Rollbuck 2021 assumes that the girder is linear elastic. Once the local moments are known, the local curvatures at the various nodes of the girder are determined using linear elastic relationships. Using the coordinate transformation matrix used to convert from global to local moments in the opposite direction, the local curvatures at each node are transformed back into global curvatures. The curvature is then integrated (twice for deflections, once for rotations) to determine an updated global shape.

This new global shape then enters the equilibrium loop again. If it is not in equilibrium, the process described in the previous paragraphs is repeated until it is in equilibrium. Once all the loops are satisfied and the girder has converged upon its final solution (calculated deflections, rotations, moments, curvatures, etc., at each node) the program is finished, and post-processing of the results can be done. Galik, Stanton, and Wiebe (2022) describe the validation of Rollbuck 2021 in their report.

Rollbuck 2021 does the above-described process for one applied load (or girder layout) at a time. The equilibrium paths (applied load versus equilibrium angle) of a given girder can be determined by applying one load at a time and repeating the algorithm of Rollbuck 2021 in a

loop in a computer program. This will be done in Chapters 4 and 5 in the imperfection study and will allow for the comparison of equilibrium angles and applied loads, pre- and post-buckling, with different imperfections and parameters that affect the critical load considered.

3.6. **Rigid Link Model**

While the equilibrium angle of a girder during transportation and handling can be quickly and easily determined using Rollbuck 2021, it is desirable to have a closed-form equation that matches the numerical results very closely, or exactly, and does not rely on a computer program. One way to approximate the numerical results is via the simple amplification equation, initially derived in Section 3.2.

A second model for approximating the numerical results is proposed here. It is derived from an analogy of the girder as a rigid body, where the lateral bending, vertical bending, and rotational stiffnesses are represented by linear springs in each of those respective degrees of freedom. Figure 3.2 shows a schematic of the set-up of this Rigid Link Model (RLM). The node where the weight W is concentrated represents the center of gravity of the entire girder, at approximately mid-span, and the torsional spring with stiffness k_ϕ represents the supports and the torsional stiffness of the girder.

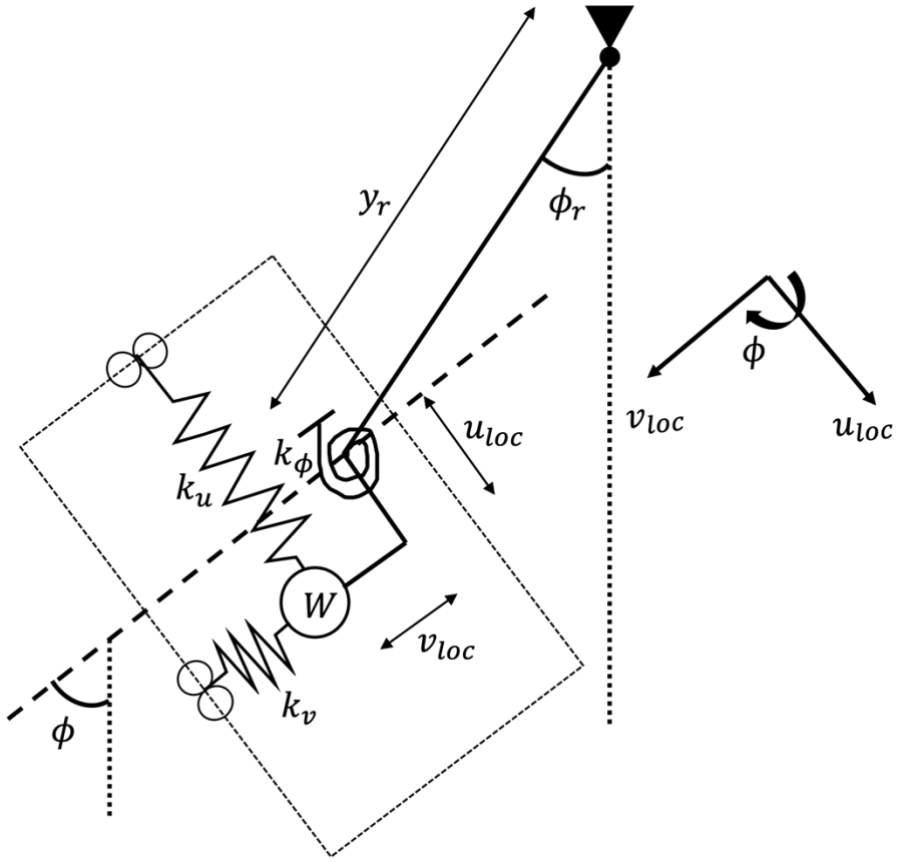

Figure 3.2 Set-Up for Derivation of the Rigid Link Model (RLM) Equation

In this diagram ϕ_r is the roll component only, ϕ is the total roll plus an additional twist component, W is the total weight of the girder, and u_{loc} and v_{loc} are the local lateral and vertical deflections, respectively. Assuming springs of representative stiffness in each of the degrees of freedom (lateral and vertical deflection, and twist) as shown in Figure 3.2, the total Potential Energy can be written as

$$\Pi = \frac{1}{2}k_u\left(u_{loc} - u_{loc,i}\right)^2 + \frac{1}{2}k_v\left(v_{loc} - v_{loc,i}\right)^2 + \frac{1}{2}k_\phi(\phi - \phi_r - \phi_i)^2 \qquad (3 - 22)$$

$$+ W\left(-y_r + (y_r\cos\phi_r - u_{loc}\sin\phi - v_{loc}\cos\phi)\right).$$

where k_u is the lateral stiffness, k_v is the vertical stiffness, k_ϕ is the rotational stiffness, and each of the terms with *"i"* subscripts are the initial imperfections in their respective degrees of freedoms, not shown in Figure 3.2 for clarity. The initial imperfections represent shifts in the

center of gravity due to those imperfections, not the maximum magnitude of the imperfections themselves. For example, for an end supported girder with lateral sweep, $u_{loc,i}$ would be $0.64u_{sweep}$.

Setting the gradient of the potential energy to zero presents this formulation in terms of minimum potential energy and results in:

$$\frac{\partial \Pi}{\partial u_{loc}} = k_u\left(u_{loc} - u_{loc,i}\right) - W\sin\phi = 0, \qquad \textit{(3 - 23a)}$$

$$\frac{\partial \Pi}{\partial v_{loc}} = k_v\left(v_{loc} - v_{loc,i}\right) - W\cos\phi = 0, \qquad \textit{(3 - 23b)}$$

$$\frac{\partial \Pi}{\partial \phi_r} = -k_\phi(\phi - \phi_r - \phi_i) - Wy_r\sin\phi_r = 0, \qquad \textit{(3 - 23c)}$$

$$\frac{\partial \Pi}{\partial \phi} = k_\phi(\phi - \phi_r - \phi_i) - Wu_{loc}\cos\phi + Wv_{loc}\sin\phi = 0. \qquad \textit{(3 - 23d)}$$

Solving Equations *(3 – 23a)*, *(3 – 23b)*, and *(3 – 23c)* for u_{loc}, v_{loc}, and $k_\phi(\phi - \phi_r - \phi_i)$, respectively, and then substituting into Equation *(3 – 23d)* and eliminating the W common to all terms yields:

$$-y_r\sin\phi_r - \cos\phi\left(\frac{W}{k_u}\sin\phi + u_{loc,i}\right) + \sin\phi\left(\frac{W}{k_v}\cos\phi + v_{loc,i}\right) = 0. \qquad \textit{(3 - 24)}$$

Equations (3 – 23) and (3 – 24) could also be derived using equilibrium. Solving for W results in

$$W = qL = \frac{y_r\sin\phi_r + u_{loc,i}\cos\phi - v_{loc,i}\sin\phi}{\sin\phi\cos\phi\,(\frac{1}{k_v} - \frac{1}{k_u})}. \qquad \textit{(3 – 25)}$$

Rearranging the stiffness terms gives

$$qL = \frac{k_u}{1 - \frac{k_u}{k_v}}\frac{y_r\sin\phi_r + u_{loc,i}\cos\phi - v_{loc,i}\sin\phi}{\sin\phi\cos\phi}. \qquad \textit{(3 – 26)}$$

For LRB, there is no distinction between ϕ_r and ϕ. Rearranging Equation (3 – 26),

$$qL = -\frac{k_u}{1-\frac{k_u}{k_v}}\frac{\left(y_r - v_{loc,i}\right)\sin\phi + u_{loc,i}\cos\phi}{\sin\phi\cos\phi}. \quad (3-27)$$

In the derivations of the buckling loads in Chapter 2, it was not necessary, but the initial lateral imperfection could be set to zero, as was done in the work by Galik, Stanton, and Wiebe (2022). Assuming small rotation angles and no initial lateral imperfections gives

$$q_{cr} = \frac{k_e(y_r - v_{loc,i})}{L}, \quad (3-28)$$

where

$$k_e = -\frac{k_u}{1-\frac{k_u}{k_v}}. \quad (3-29)$$

Substituting into Equation (3 – 27):

$$q = q_{cr}\frac{\sin\phi + \frac{u_{loc,i}}{y_r - v_{loc,i}}\cos\phi}{\sin\phi\cos\phi}. \quad (3-30)$$

Dividing by q_{cr} gives the result for the RLM that is hypothesized to predict the amplification of the initial imperfections due to a given applied load:

$$\frac{q}{q_{cr}} = \frac{\sin\phi + \frac{u_{loc,i}}{y_r - v_{loc,i}}\cos\phi}{\sin\phi\cos\phi}. \quad (3-31)$$

Equation (3 – 31) can be simplified further. The ratio of imperfections in the numerator is the negative of the tangent of the initial roll angle, analogous to Equation (3 – 19). To cause a positive initial roll angle, the sign of the lateral imperfection needs to be negative. Substituting the negative tangent of the initial roll angle, and then simplifying gives

$$\frac{q}{q_{cr}} = \sec\phi - \tan\phi_o\csc\phi, \quad (3-32a)$$

or alternatively,

$$\tan\phi = \frac{\tan\phi_o}{1 - \frac{q}{q_{cr}}\cos\phi}. \qquad (3-32b)$$

Equation (3 – 32b) is identical to Equation (3 – 4). For small roll angles, Equation (3 – 32b) will reduce to the SAM. The concept for the RLM was derived from a simple physical model that represents the real girder as closely as possible. The fact that it also gives the large-deflection amplification factor as does the differential equation for the girder suggests strongly that it can be used to predict the girder response. Its simple form, and its resemblance to the traditional column amplification factor, makes it attractive for use in practice (Southwell, 1932). For known q, q_{cr}, and ϕ_o, Equation (3 – 32b) can be solved iteratively for the final roll angle, ϕ. It could also be reduced to an explicit algebraic equation in $\tan\phi$ by making the substitution

$$\cos\phi = \frac{1}{\sqrt{1 + tan^2\phi}} \qquad (3-33)$$

However, that results in a 4th order polynomial in $\tan\phi$, for which there is no closed-form solution, so it is not useful in practice.

Chapters 4 and 5 will explore the application of the models developed in this chapter. There are three models which can be used to predict the final roll angle of a girder. The SAM, the RLM (equivalent to the SAM without a small angle assumption), and Rollbuck 2021, the numerical model developed by Galik, Stanton, & Wiebe (2022). If all the models agree, then the SAM or the RLM could be used in design to predict the equilibrium angle of a girder, with imperfections, SAB, prestressing deflections, overhangs, and torsion quickly and easily.

4. Imperfection Study Results: LRB

Chapter 4 describes the results of the imperfection sensitivity study for the LRB case. This study investigates lateral sweep and lifting loop eccentricity as symmetry breaking imperfections. The imperfection study begins with the baseline LRB case, and then is extended to include other factors affecting the critical load, namely, the combined effects of SAB and prestressing deflections as well as the stabilizing effect of overhangs due to lifting loop placement. The goals of this section are to

1. Using Rollbuck, explore whether girders with different symmetry breaking imperfections but equal initial roll angles do indeed have identical lateral stability behavior.
2. Explore the changes in imperfection amplification due to SAB, prestressing deflections, and overhangs as a result of their effect on the critical load.
3. Explore whether the SAM and RLM may be used to predict the final roll angle for a girder with lateral imperfections.

4.1. **Baseline LRB and Symmetry Breaking Imperfections**

4.1.1. **Baseline LRB with Lateral Sweep**

The study will first examine lateral sweep as the symmetry breaking imperfection. Section 3.3 predicts that imperfections that produce equivalent initial roll angles will result in the same load-deflection behavior and final roll angle. The results for lateral sweep will be shown first and then will be compared to lifting loop eccentricity imperfections that produce the same initial roll angle.

The industry tolerance for sweep is $1/8^{th}$ inches of sweep per 10 feet of girder length. For a 200-foot-long girder, this corresponds to a maximum sweep of 2.5 inches. Sweeps ranging from one inch to five inches were considered to evaluate the response for girders within and

outside of standard tolerances. This study was conducted on a 200-foot long WSDOT WF100G girder. While girders spanning longer than 200 feet have been constructed in Washington State, 200 feet was used to see the torsional deformations that occur in long spans without choosing a longer configuration that could result in very large roll angles and critical loads significantly lower than the self-weight. WF100G girders could realistically be used for a 200-foot-long span, as opposed to shorter and less vertically stiff girders.

Figure 4.1 shows the vertical load plotted against mid-span rotation as calculated by Rollbuck 2021 for a WF100G girder undergoing baseline LRB with no overhangs, no SAB, no prestressing deflections, initial lateral sweeps ranging from 0.1 to five inches, and a concrete density of 125 $\frac{lb}{ft^3}$. The figures in this section neglect SAB by artificially increasing the strong-axis stiffness of the WF100G to best reflect the baseline LRB case derived in Section 2.1. The dashed line represents the self-weight of a WF100G, and the dashed-dotted line represents the critical load. Under self-weight alone without overhangs, a 200 ft. long WF100G would buckle and theoretically experience roll angles around 0.7 radians, with some variation depending on the imperfection magnitude—if it did not crack. In practice, a girder that long would be lifted with overhangs to improve the lateral stability and prevent cracking. The positive concavity of the load-roll angle curve in the post-buckled regime indicates that the girder has residual strength and stiffness after buckling and can continue to carry additional load, if cracking does not occur, albeit at the expense of increased roll angles. However, cracking will almost certainly occur, approximately at an angle of 10 degrees (0.174 radians), so the finding is of limited use in practice, although it serves to show that Rollbuck 2021 is capable of predicting response out to these relatively large roll angles.

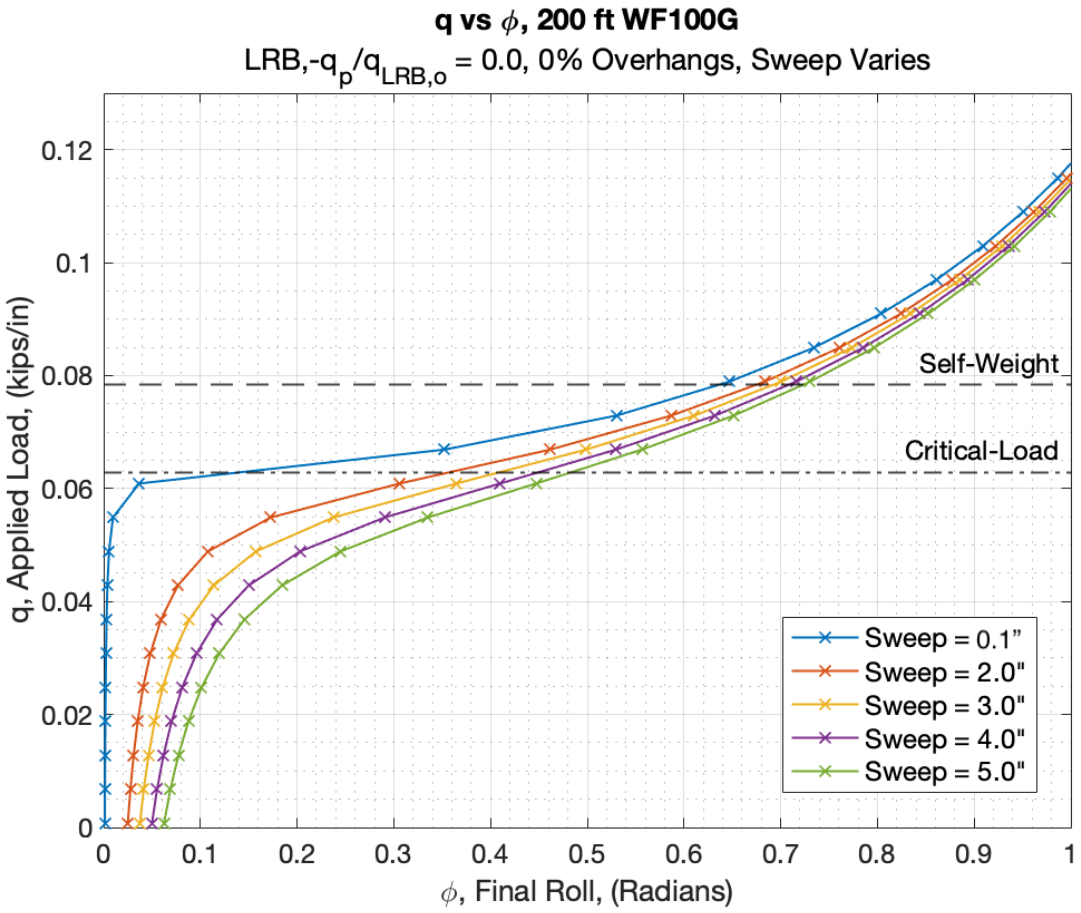

Figure 4.1 Final Roll Angle (Radians) vs. Applied Load (kips/in). LRB, Varying Sweep, No Overhangs, No SAB/Prestressing Deflections, 200 ft. WF100G Girder

As would be expected, the girder with the smallest imperfection has the lowest final roll angle at any given load. A nearly perfect girder with a very small sweep of 0.1 inches is shown in blue. It undergoes near-zero rotation until the applied load reaches the critical load. The lateral sweep imperfections cause pre-buckling deformations and prevent a hard bifurcation point from occurring, as can be seen from the curves representing larger initial sweeps. The roll angles slowly increase as the load approaches the critical level, the rate of change gradually increasing as the load approaches the buckling load.

Figure 4.1 presents unnormalized data of the applied load versus the final roll angle. Figure 4.2 presents the same data, but instead normalizes the applied load by the critical load,

and the final roll angle by the initial roll angle. The lateral sweep of 0.1 inches case is replaced by a girder with lateral sweep of 1.0 inches. As a result of the normalization, the horizontal axis becomes a measure of the amplification of the initial roll angle and the vertical axis a measure of the applied loads' value relative to buckling. All plots from this point onwards in the imperfection sensitivity study will be normalized unless otherwise noted.

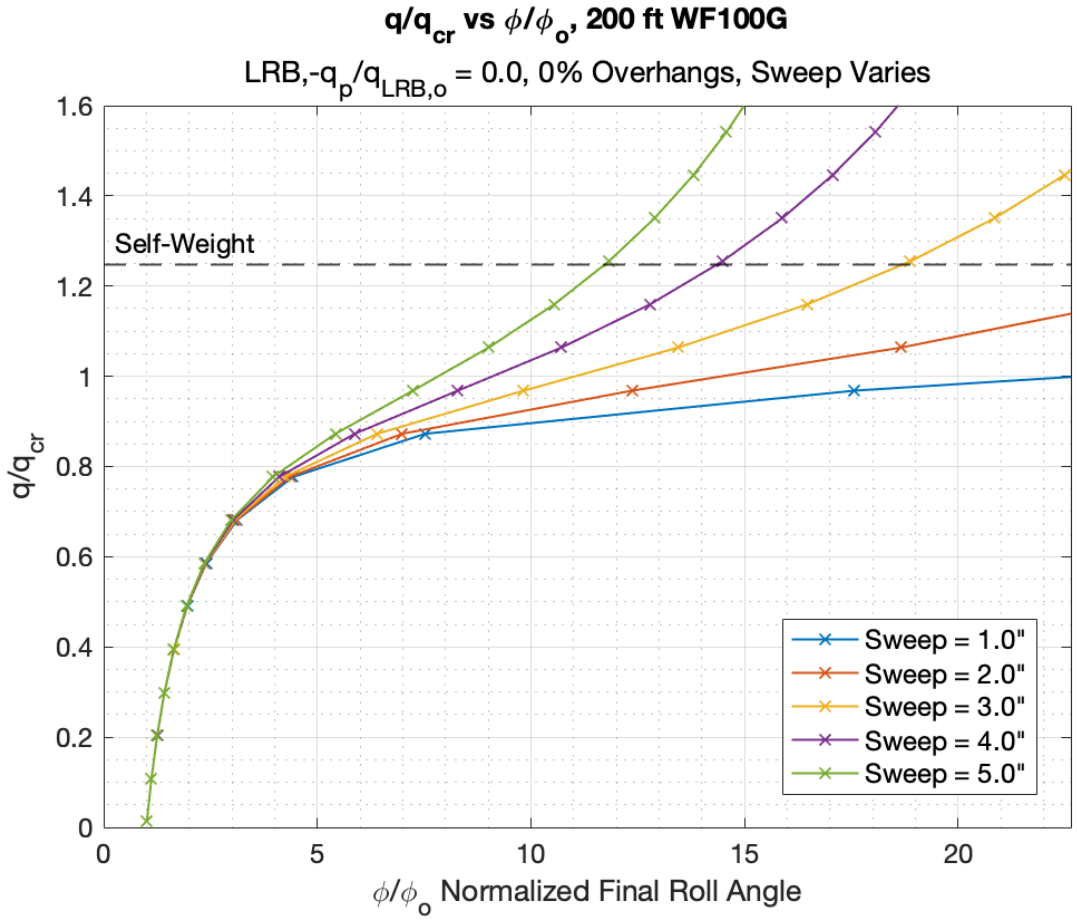

Figure 4.2 Final Roll Angle Normalized by Initial Roll Angle vs Applied Load Normalized by Critical Load. LRB, Varying Sweep, No Overhangs, No SAB/Camber, 200 ft. WF100G Girder

For low initial roll angle amplification (i.e., low final roll angles) it is notable that the normalized curves converge to the same line, despite different initial imperfections. This suggests that a single amplification equation could be used in design to easily predict the final

roll angle of a girder. A similar outcome occurs with column buckling. There, the final deflection of the buckled column can be predicted by

$$\delta = \frac{\delta_o}{1 - \frac{P}{P_{cr}}}, \qquad (4 - 1)$$

regardless of the size of the initial imperfection, δ_o. As suggested by Equation (3 – 5) in Section 3.2, an analogous simple amplification equation exists that predicts the final roll angle of a girder undergoing LRB at low roll angles. The SAM and the RLM will be explored in detail in section 4.3.

All the curves lie essentially on top of one another up to a $\frac{q}{q_{cr}}$ of about 2/3. Present practice is to require $q_{cr} > 1.5q$ (Precast/Prestressed Concrete Institute, 2020). This finding implies that a single amplification equation might be adequate for the range of practical cases, with very little error.

At higher $\frac{q}{q_{cr}}$ ratios, the amplification of the initial roll angle appears to be larger when the initial roll angle is small. While the amplification is indeed larger, the final roll angle is still smaller for small initial roll angles. Figure 4.1 most clearly shows this.

4.1.2. **Baseline LRB with Lifting Loop Eccentricity**

It was shown algebraically in Chapter 3 that imperfections that result in the same initial roll angle lead to the same imperfection amplification, if both cases have equal critical loads. Recall from Section 3.3 and Equation (3 – 13) that lifting loop eccentricities and lateral sweeps produce the same initial roll angle when

$$e_x = -\bar{u}_{sweep} = -0.64u_{sweep}. \qquad (3 - 13)$$

Therefore, lifting loop eccentricities that correspond to Equation (3 – 13) and the lateral sweep values used in Section 4.1.1 will be used to determine whether equal initial roll angles do in fact lead to identical pre- and post-buckling behavior. Lifting loops eccentricities of this magnitude may not actually be allowed per fabrication tolerances, or may even be physically impossible, given the narrow girder web in which the loops must be placed. WF series girders have a standard and constant web width, so lifting loop eccentricity imperfections likely have an upper bound magnitude. These potentially unrealistic lifting loop eccentricities are included to determine if the same initial roll angles as the lateral sweep case will result in the same final roll angle. If these lifting loop eccentricities are indeed unrealistic, then this provides a conservative upper bound on the final roll behavior expected due to this imperfection. Furthermore, that would then indicate that lateral sweeps are likely the controlling imperfection, at least for long girders, for prestressed concrete girders during transportation and handling. For short girders with lower sweep magnitudes, lifting loop eccentricity could potentially be more controlling than lateral sweep. However, they are less likely to experience stability problems.

Figure 4.3 shows the normalized results for girders with lifting loop eccentricities that produce the same initial roll angle as the lateral sweeps considered above.

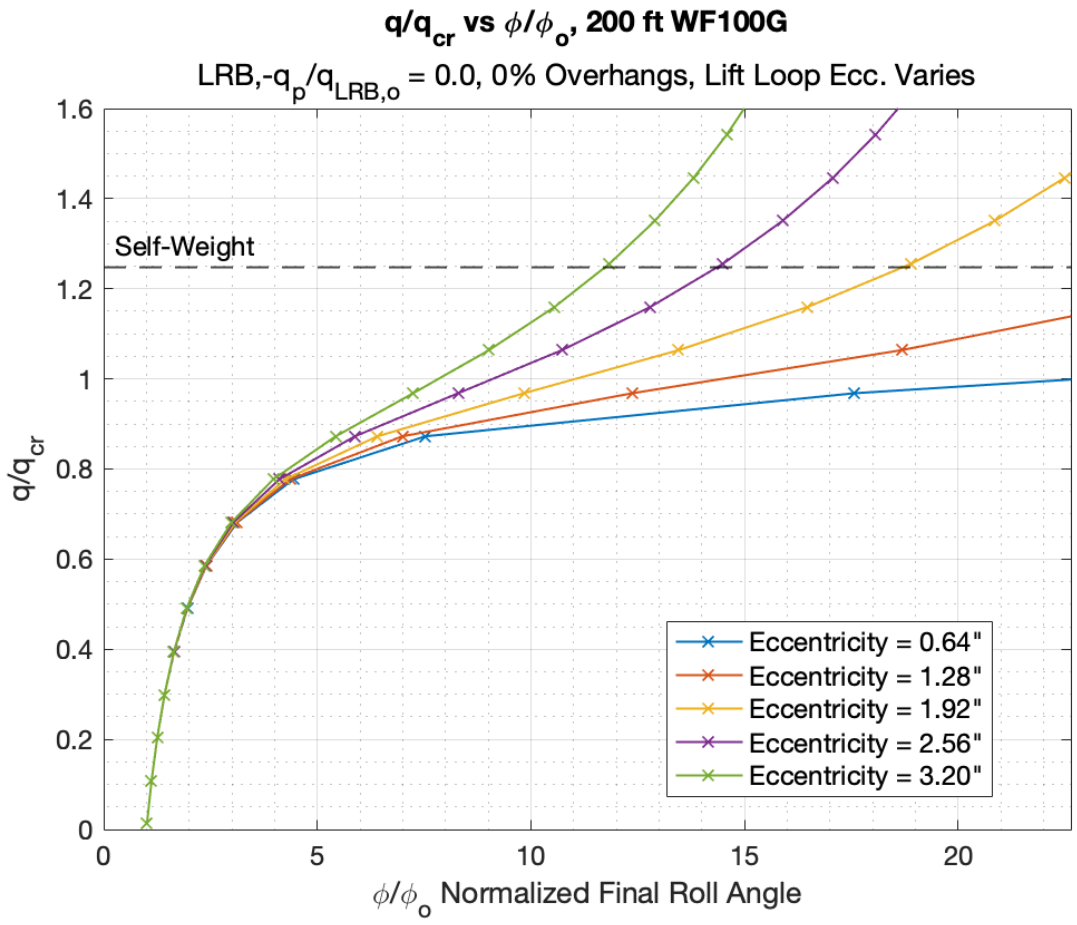

Figure 4.3 Final Roll Angle Normalized by Initial Roll Angle vs Applied Load Normalized by Critical Load. LRB, Lifting Loop Eccentricity Varies, No Overhangs, No SAB/Camber, 200 ft. WF100G Girder

Comparison of Figures 4.2 and 4.3 shows that the two different versions of the analysis produce identical results. This indicates that the hypothesis of this section was indeed correct: symmetry breaking imperfections that produce the same initial roll angle have identical imperfection amplifications for a given critical load. This simplifies studying parameters affecting the critical load and their effect on buckling loads and imperfection amplification in that only one imperfection type needs to be considered. In a design context, this could allow designers to reduce different imperfections to a combined initial roll angle and then determine the response from there.

4.2. **Modified LRB Load with Symmetry Breaking Imperfections**

Section 4.1 showed that different symmetry breaking imperfections that produce the same initial roll angle also result in the same imperfection amplification for a given critical load. The analyses were conducted within the framework of the baseline LRB load established in Section 2.1. This section will explore how modifications to the girder's critical load due to inclusion of SAB, prestressing deflections, and overhangs will stabilize or destabilize the girder with the same initial roll angles considered in Section 4.1. For the remainder of this chapter, the symmetry breaking imperfection will be represented by sweep alone.

4.2.1. **LRB with Strong-Axis Bending, Prestressing Deflections, and Sweep Imperfections**

Section 2.2 derived the critical LRB load accounting for strong axis bending and camber, repeated here:

$$q_{LRB,vp} = -\frac{120EI_{yy}y_r}{L^4}\frac{\left(1-\frac{q_pL^4}{120EI_{xx}y_r}\right)}{\left(1-\frac{I_{yy}}{I_{xx}}\right)} = q_{LRB,o}\frac{\left(1-\frac{\overline{v}_p}{y_r}\right)}{\left(1-\frac{I_{yy}}{I_{xx}}\right)}, \qquad (2\text{ - }26)$$

If there is no equivalent upwards load due to prestressing, q_p, then the critical load equation collapses back to the baseline LRB critical load, with the stabilizing effect of SAB now accounted for. If $I_{xx} \gg I_{yy}$ there is practically no SAB and the critical load reduces to the baseline LRB value.

SAB and prestressing deflection effects are treated here as independent modifications to the critical load and were not incorporated into the previous examination of symmetry breaking imperfections. While different prestressing deflections could be thought of as a type of

imperfection, prestressing deflections are not symmetry breaking imperfections; however, as Equation (3 – 19) shows, they do influence the calculation of initial roll angle due to the lifting loop eccentricity or lateral sweep.

While the effects of prestressing deflections and SAB on the critical load can be derived independently, they will never occur independently of one another. As such, they will not be separated in this study. For a given girder cross-section, the SAB will always modify the critical load in the same way, as it is simply a function of the girder's moments of inertia. Therefore, this section will present results for girders with different prestressing q_p values to explore the interaction between the stabilizing effect of SAB and the destabilizing effect of various q_p levels. Section 2.2 showed that when the equivalent upwards prestressing load was equal to the magnitude of the baseline LRB buckling load, $q_p = -q_{LRB,o}$, the critical load, even with the corresponding modifications from strong axis bending and prestressing deflection, was equal to the baseline LRB load. Therefore, this section will present different prestressing levels in terms of the ratio *"N"*:

$$N = -\frac{q_p}{q_{LRB,o}}. \qquad (4 - 2)$$

Figure 4.4 presents the first level of prestressing considered where $N = 0$. Recall that, until this point, strong axis bending effects have been neglected by artificially increasing EI_{xx}. To incorporate strong axis bending into Rollbuck 2021, EI_{xx} was returned to its normal value. Therefore, Figure 4.4 shows the same girders considered in Section 4.1.1 since the same initial imperfections are used, but q_{cr} will be stabilized (increased in magnitude) by the strong axis bending factor. Since there is no prestressing in this iteration, there is no destabilizing effect due to q_p.

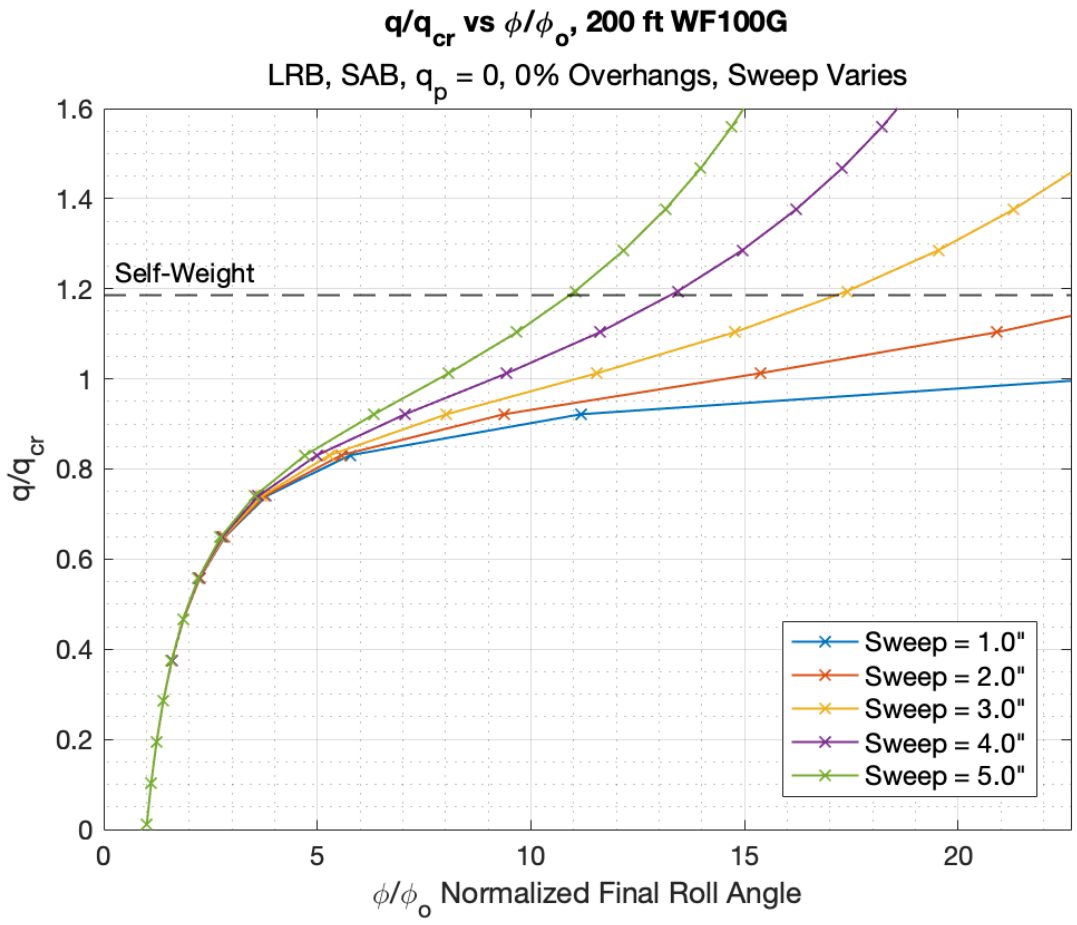

Figure 4.4 Final Roll Angle Normalized by Initial Roll Angle vs Applied Load Normalized by Critical Load. LRB, Varying Sweep, SAB with $N = 0$, No Overhangs, 200 ft. WF100G Girder

The self-weight in Figure 4.4 is just below $1.20q_{cr}$, while in Figure 4.2 it is just below $1.25q_{cr}$. This means that the critical load has indeed increased when SAB is included. Note that this stabilizing effect is quite small—the girder has still buckled at the self-weight load. At self-weight, assuming cracking does not occur, a sweep of 5.0-inches results in a final roll of approximately 39 degrees with SAB, versus approximately 41.85 degrees without. While this case is more realistic than the baseline LRB case, it still does not include prestressing deflections and overhangs, both of which would almost certainly be present in a real girder.

Figure 4.5 shows multiple $N = -\frac{q_p}{q_{LRB,o}}$ prestressing values ranging from $N = 0.0$ to $N = 3.0$, for girders with lateral sweeps of 3.0 inches (slightly larger than the sweep tolerance). This allows for a quick evaluation of the destabilizing effect increased prestressing deflections have on a girder's LRB behavior. The self-weight line for each N ratio considered is different. This is not due to a changing self-weight, but to the critical load dropping in magnitude as the prestressing level increases. The roll angle amplification at the self-weight line correspondingly increases as the prestressing level increases.

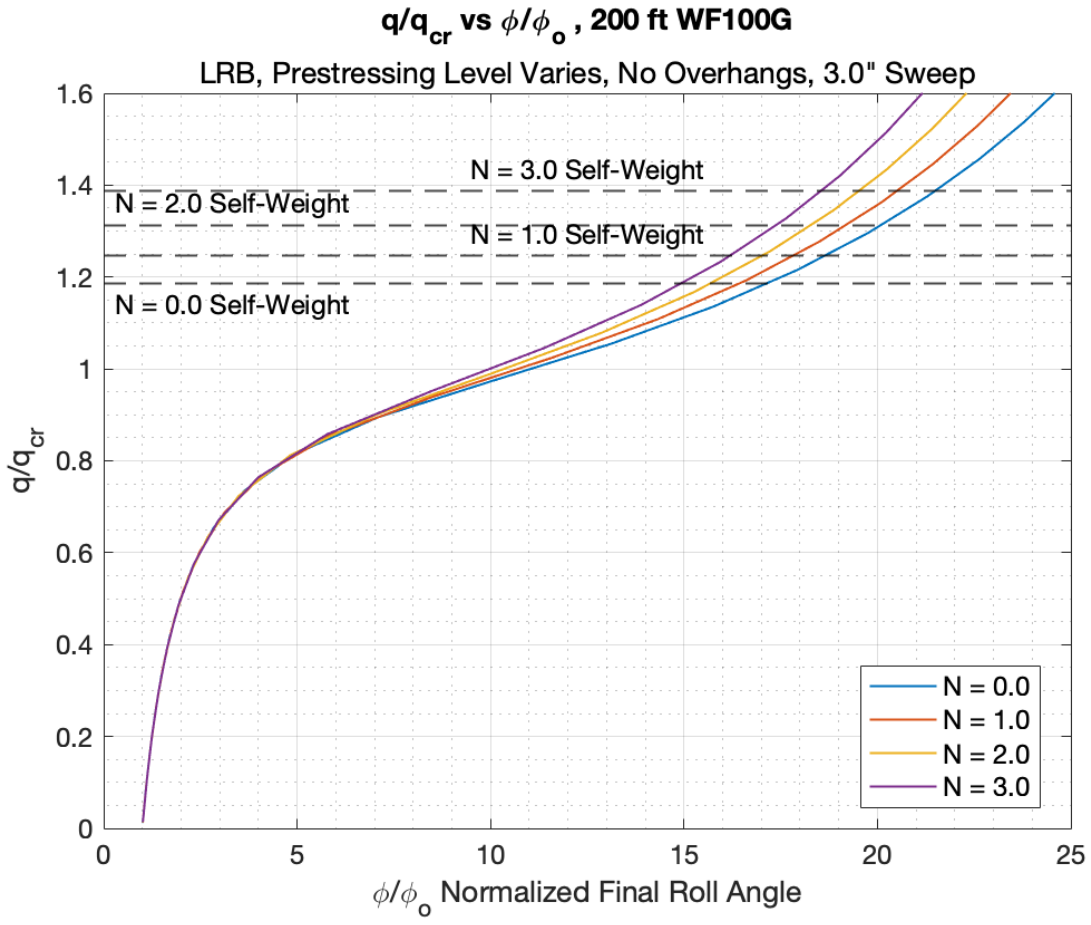

Figure 4.5 Final Roll Angle Normalized by Initial Roll Angle vs Applied Load Normalized by Critical Load. LRB, Sweep = 3.0", Prestressing Level $N = -\frac{q_p}{q_{LRB,o}}$ Varies, No Overhangs, 200 ft. WF100G Girder

When $N = -\frac{q_p}{q_{LRB,o}} = 1$, the stabilizing effect of SAB deflections exactly balances out with the destabilizing effect of the upwards deflection caused by prestressing, resulting in a critical load equal to the baseline LRB load. The self-weight line in Figure 4.2 and the *N = 1.0* self-weight line here in Figure 4.5 are both at 1.25—indicating that the critical load is indeed the same for both cases. Interestingly, while the critical loads are the same for the *N=1.0* case in Figure 4.5 and the girders evaluated in Figure 4.2, the final roll angles are different. This can be seen by evaluating the points that intersect the self-weight line, which will be at the same location vertically because of the equal critical loads. In Figure 4.2, the roll angle amplifications corresponding to a sweep 3.0 inches is just under 19. In Figure 4.5 the same roll angle amplification is approximately 18—clearly less. So, even though the critical loads are equal, the girder that has realistic major axis stiffness and an equivalent upwards prestressing load equal to the baseline LRB load has lower final roll angle amplification. A more physically familiar expression of the prestressing level, $\frac{q_p}{q_{sw}}$, perhaps sheds more light onto this relative stabilization. While the critical load for $N = -\frac{q_p}{q_{LRB}} = 1$ in this case is equal to the baseline LRB load, the ratio of the equivalent upwards prestressing load to self-weight is $\frac{q_p}{q_{sw}} = 0.8021$. Therefore, despite the critical loads being equal, the center of gravity of the girder will still have a net deflection downwards when evaluated at an applied load equal to the self-weight. As a result, the SAB effects outweigh the prestressing effects when $N = -\frac{q_p}{q_{LRB}} = 1$ and the final roll angles are less than the case shown in Figure 4.2 without strong axis bending or prestressing.

Both $N = -\frac{q_p}{q_{LRB}} = 2.0$ and $N = -\frac{q_p}{q_{LRB}} = 3.0$ are perhaps more realistic equivalent upwards loads due to prestressing, corresponding to $-\frac{q_p}{q_{sw}} = 1.6$ and $-\frac{q_p}{q_{sw}} = 2.4$, respectively.

These cases are shown in Figure 4.5 as the yellow and purple curves, respectively. Increasing the prestressing level effectively lowers the magnitude of the roll axis height, and in turn the critical load—shown by the self-weight line moving upwards for increasing camber. There is an increase in roll angle amplification for increasing prestressing levels in Figure 4.5, but the change is quite small, especially as the prestressing level gets larger. Prestressing deflections combined with SAB generally do not result in large changes to the roll angle amplification.

4.2.2. **LRB with Overhangs and Sweep Imperfections**

The previous section explored how incorporating the effects of SAB and prestressing deflections affected the amplification of imperfections. This section will turn SAB and prestressing deflections off again and will instead focus on the stabilizing effect of overhangs on a girder's LRB behavior. The equations to calculate $f_{LRB}(\alpha)$, the factor necessary to convert the critical load from baseline LRB to that for a girder with overhangs, are shown in Section 2.3.

While the optimum α value for stability is 23.86%, that would likely result in an unreasonably large overhang, causing excessive tension in the girder's top flange during transportation and handling (Galik, Stanton, & Wiebe, 2022). For this study, more realistic overhang ratios of 5%, 10%, and 12.5% are considered.

Figure 4.6 shows the normalized roll-angle vs load curves for multiple 200-foot long WF100G girders with lateral sweeps of 3.0 inches but varying overhang ratios. As the overhang ratio increases, the buckling load increases but the self-weight remains the same. It therefore becomes a smaller proportion of the buckling load.

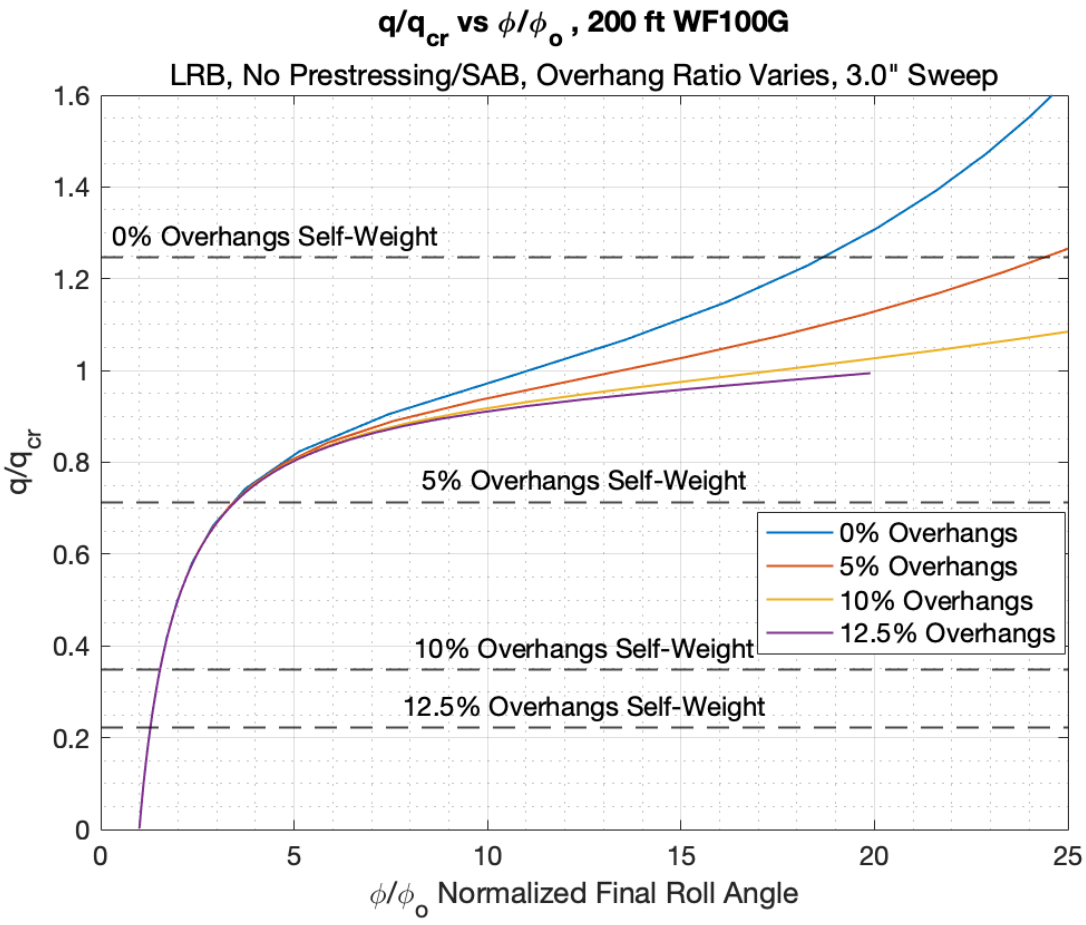

Figure 4.6 Final Roll Angle Normalized by Initial Roll Angle vs Applied Load Normalized by Critical Load. LRB, Sweep = 3.0", Overhang Ratios Vary, No Prestressing/SAB, 200 ft. WF100G Girder

Examining the self-weight lines for each of the four cases presented offers the best comparison of the relative stability of each girder configuration. For constant self-weight, the critical load becomes higher in magnitude (more stable) for increasing overhang ratios. A girder without overhangs has a self-weight approximately 1.25 times the critical load while a girder with 12.5% overhangs has a self-weight approximately 0.225 times the critical load. The final roll angle amplifications are correspondingly lower for each of the more stable girders with larger overhang ratios. The stabilizing effect of overhangs cannot be overstated. Without overhangs, a 200-foot long WF100G girder will buckle and roll significantly, likely cracking,

possibly resulting in failure during transportation or handling. With just five percent overhang ratios on each end, the girder will not buckle, and it will have a lower roll angle amplification. This stabilizing effect only becomes more pronounced as the overhang ratio increases. This finding has been recognized by Mast (1989), Stratford and Burgoyne (1999), and others.

4.3. **LRB Approximations with the Rigid Link Model and the Simple Amplification Model**

4.3.1. **RLM and SAM with Baseline LRB Behavior**

The work done thus far has assumed that the girders remain linear and elastic and are uncracked. This is a realistic assumption until a roll angle of approximately 10 degrees, at which point the girder will likely crack (Mast, 1993, 1994). After the girder has rolled approximately 10 degrees, the equations have less physical meaning and are likely not valid.

Figure 4.7 shows the comparison between the Rollbuck predicted results, the RLM, and the SAM for baseline LRB. Only three of the previous five girders with imperfections are included in Figure 4.7 to reduce the busyness of the plot. The curves from the RLM and the Rollbuck 2021 results are essentially identical, over the full range of roll angles shown. They both match the SAM well at loads below about $\frac{2}{3}q_{cr}$, after which the simple amplification overpredicts the roll angle for any given load, and so may be considered conservative. However, these analyses ignore cracking, which Mast found would have occurred at a roll angle of at least 10-degrees (Mast, 1993, 1994). Consequently, lines that show where each girder reaches a roll of 10-degrees, which represents approximately the limit of validity of the equations, are shown here. For roll angles of less than 10 degrees, even the fit with the simple amplification is very close. At higher roll angles, the results are not strictly valid but the good fit between the numerical and RLM results still provides confidence in both approaches.

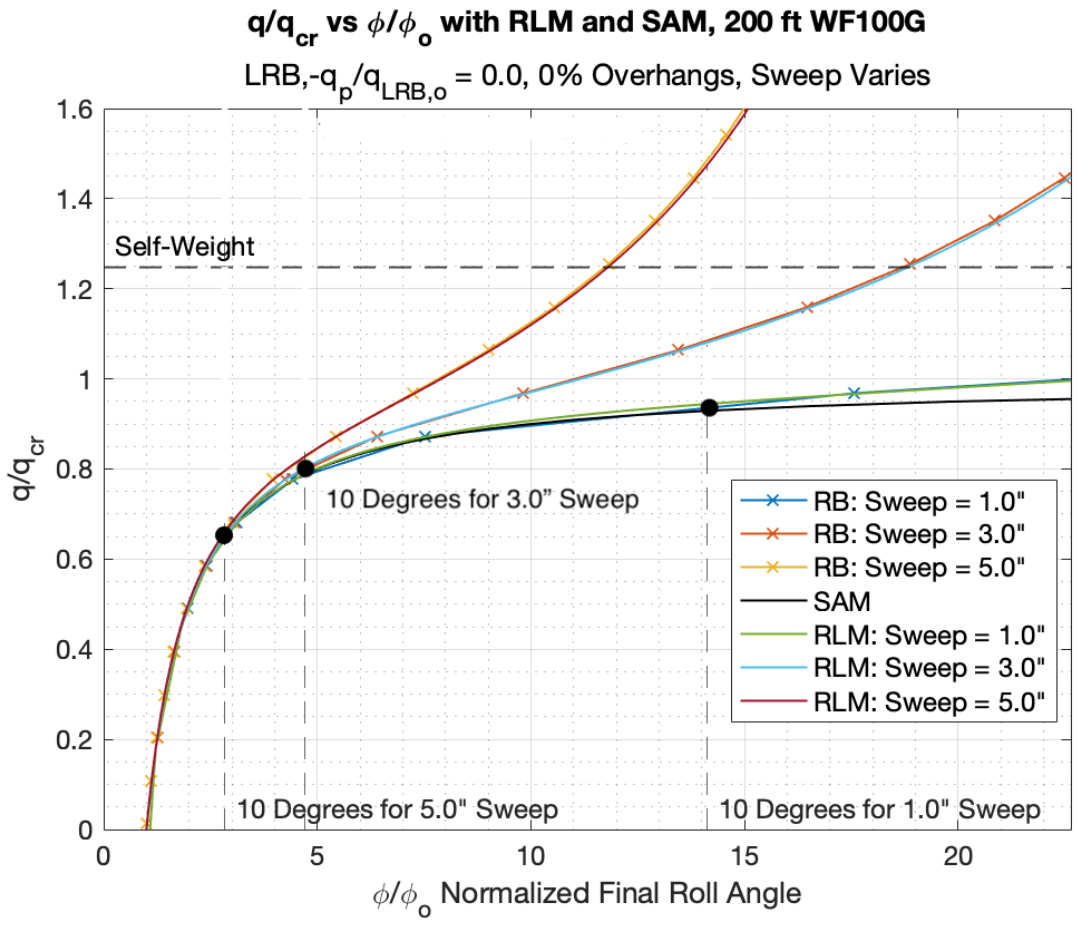

Figure 4.7 Comparison of Rollbuck Results with RLM and SAM. LRB, Varying Sweep, No Overhangs, No SAB/Prestressing Deflections, 200 ft. WF100G

Note that the actual self-weights of the girders shown here would result in buckling and rolls exceeding 10-degrees. Overhangs would need to be included to ensure the girder does not crack. Predicting the Rollbuck results for girders with overhangs and/or prestressing deflections and SAB will be explored in the next section.

Recall Equation (3 – 32b) from Chapter 3 for the RLM, shown below:

$$\tan\phi = \frac{\tan\phi_o}{1 - \frac{q}{q_{cr}}\cos\phi} \qquad (3-32b)$$

If small angles are assumed such that $\tan\phi \approx \phi$ and $\cos\phi \approx 1$, Equation (3 – 32b) reduces to the SAM. Figure 4.8 shows Equation (3 – 32b) plotted alongside the simple amplification

Equation (3 – 4), which is equivalent to Equation (3 – 32b) with $\cos\phi = 1.0$. The horizontal axis is in terms of the tangent of the roll angle to be consistent with Equation (3 – 32b).

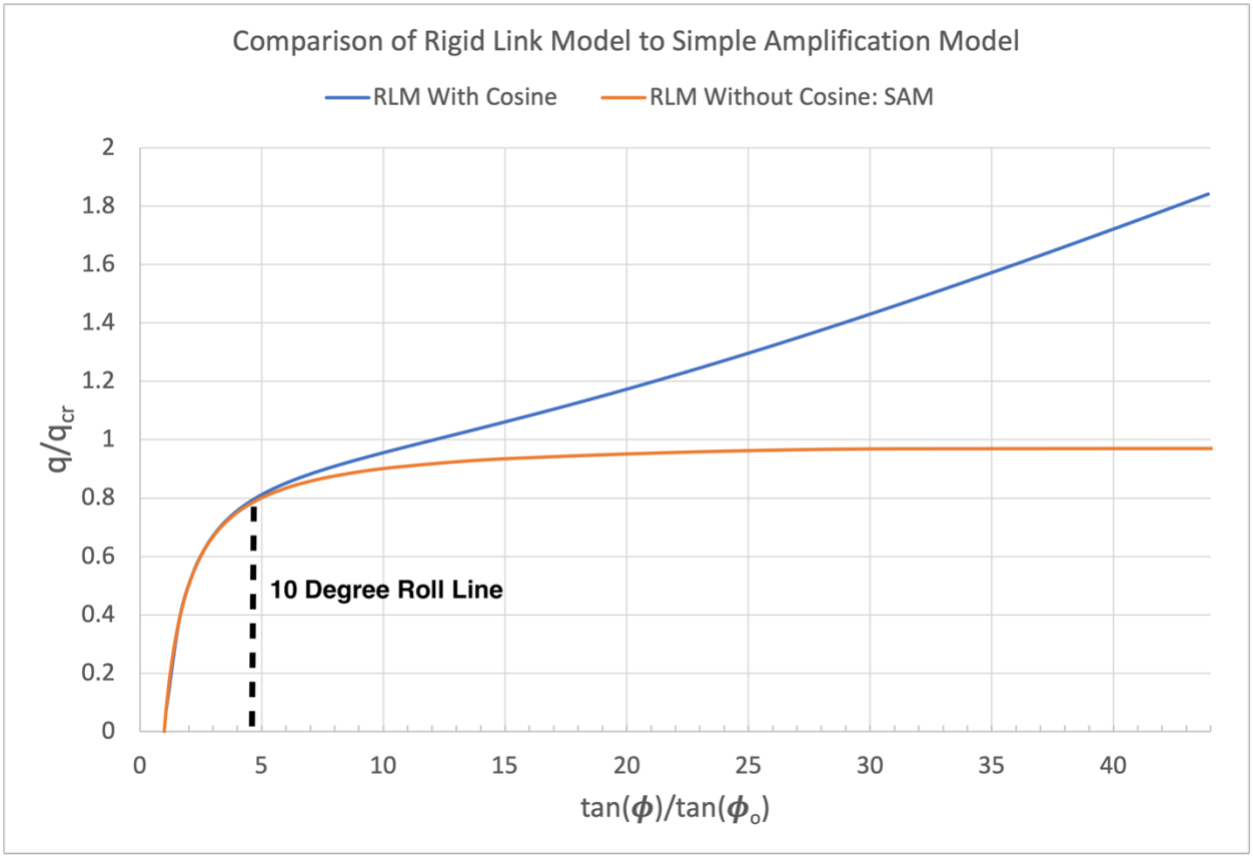

Figure 4.8 Comparison of Rigid Link Model and Simple Amplification Model

Figure 4.8 shows that the cosine term in Equation (3 – 32b) does not significantly deviate the RLM from the SAM until the girder exceeds about 10-degrees of roll and has likely cracked. Note that the "10 Degree Roll Line" in Figure 4.8 depends on the initial roll angle, and in this case corresponds to a girder with 3-inches of lateral sweep. This helps to explain why the SAM and the RLM are such excellent matches in the low roll angle regime but diverge as the roll angle increases. Both models validate one another, and additionally both match with the Rollbuck results. Either the SAM or the RLM can be used to quickly and accurately predict the final roll angle of a girder that remains uncracked during transportation and handling. Both give very good results for roll angles less than about 10 degrees. For higher roll angles, the RLM is more

accurate, but slightly more complicated. However, in that range, cracking is likely to render both models invalid.

4.3.2. RLM and SAM for LRB with Overhangs and/or SAB/Prestressing Deflections

Since the applied load in the RLM equation is normalized by the critical load, it is hypothesized that the RLM will still match the Rollbuck results for girders with modified critical loads due to overhangs and/or SAB/prestressing deflections. No actual changes are required to the RLM equation to incorporate more complicated effects than baseline LRB—those changes are handled entirely by normalizing by the critical load. Figure 4.9 compares the RLM results with the SAM and the Rollbuck results for girders with 10% overhangs, but no SAB or prestressing deflections.

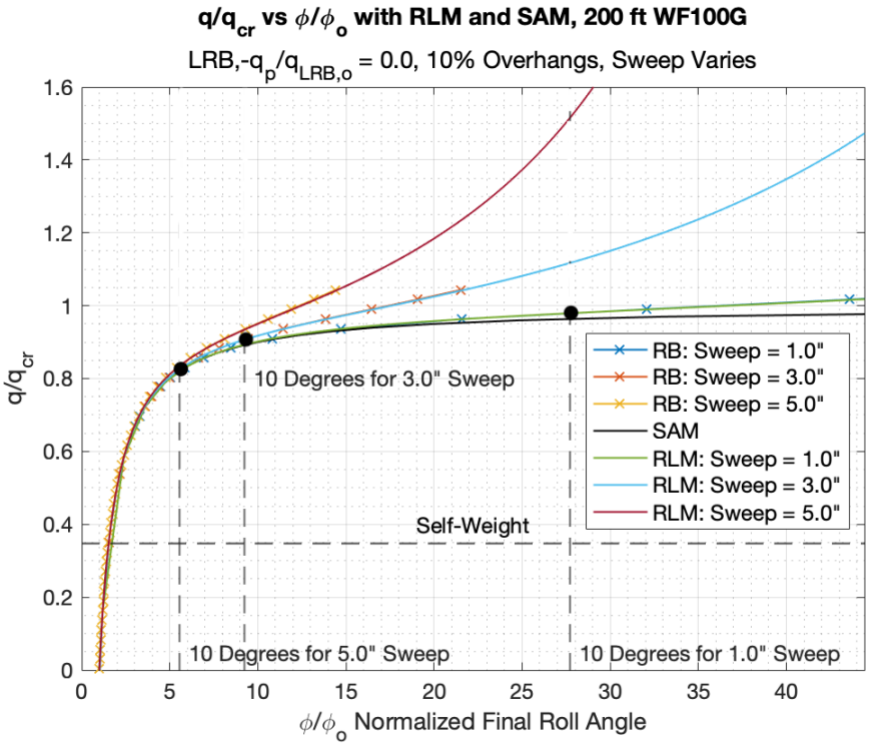

Figure 4.9 Comparison of Rollbuck Results with RLM and SAM. LRB, Varying Sweep, 10% Overhangs, No SAB/Prestressing Deflections, 200 ft. WF100G

The RLM is a perfect match with the Rollbuck results over the entire range of applied loads and roll angles considered. This finding verifies that the result of Equation (3 – 32b)—the RLM—which was developed in the absence of overhangs, also holds true with overhangs considered. The stabilizing effect of overhangs is evident, in that the self-weight line occurs at approximately 35% of the critical load. A real girder's final roll angle in this configuration could reasonably be predicted by any of the methods as the self-weight line occurs before the 10-degree roll point for all three girders. Thus, the linear elastic and uncracked assumption is still valid. For this reason, the SAM is an excellent predictor of the Rollbuck results. The SAM only deviates from the Rollbuck and RLM curves after each girder's 10-degree roll line has been crossed. Therefore, the RLM appears to sufficiently predict the final roll angle and LRB behavior of girders with overhangs. The SAM does as well, provided the roll angle does not exceed approximately 10 degrees.

The RLM was a perfect match to the Rollbuck results for girders with overhangs. It is hypothesized that the same will hold true for girders with camber and strong axis bending, but no overhangs. Figure 4.10 shows the comparison between the Rollbuck results, the RLM, and the SAM for a girder with a prestressing level of $N = -\frac{q_p}{q_{LRB,o}} = 3.0$.

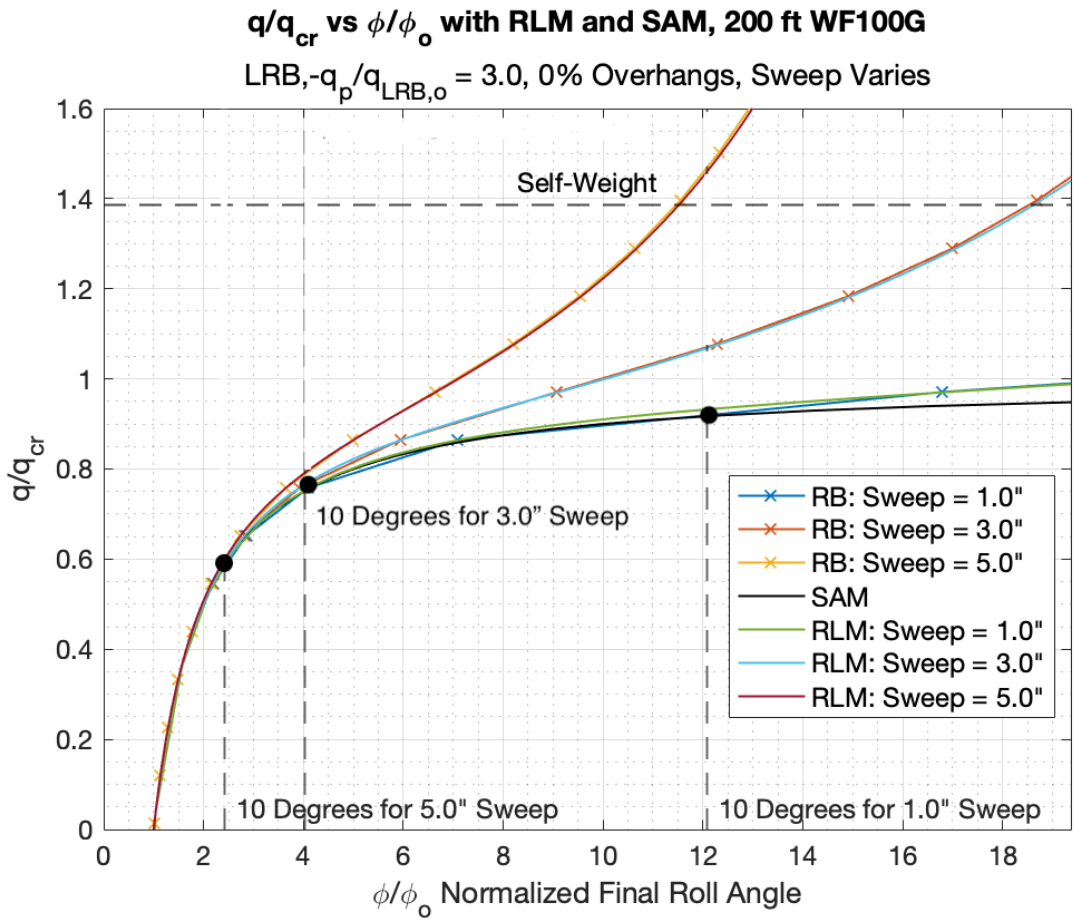

Figure 4.10 Comparison of Rollbuck Results with RLM and SAM. LRB, Varying Sweep, No Overhangs, $\frac{-q_p}{q_{LRB,o}} = 3.0$, 200 ft. WF100G

Once again, the RLM is a perfect match with the Rollbuck results. The SAM is as well, but only up until approximately each girder's 10-degree roll line. Due to the destabilizing effect of prestressing deflections, the girders hit 10-degrees relatively quickly compared to Figures 4.7 and (especially) Figure 4.9. In addition, the self-weight is approximately 1.4 times the critical load and occurs beyond the 10-degree roll line for each girder. So, while the RLM is an excellent predictor of the Rollbuck results, the prediction is not valid at an applied load equal to self-weight if the girder has no overhangs, for the girder would have likely cracked.

Figure 4.11 explores the match between the RLM and Rollbuck for girders with overhangs, prestressing deflections, and SAB. This is the most realistic case considered thus far, as a girder in practice would have all of these effects.

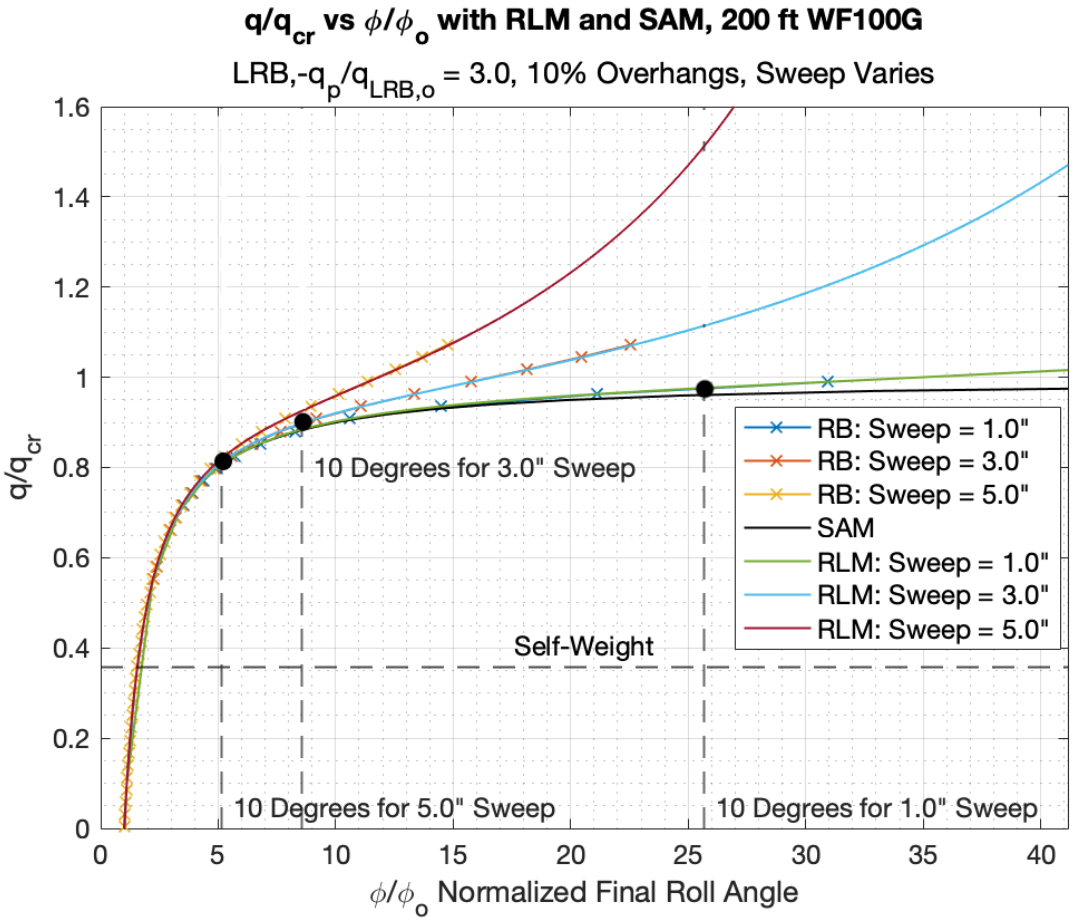

Figure 4.11 Comparison of Rollbuck Results with RLM and SAM. LRB, Varying Sweep, 10% Overhangs, $\frac{-q_p}{q_{LRB,o}} = 3.0$, 200 ft. WF100G

When all factors are considered simultaneously, the RLM still matches perfectly with the Rollbuck 2021 results. The SAM is a good match as well, with its usual divergence from the RLM Rollbuck results at around the 10-degree roll line for each girder. The match here between the RLM, SAM, and Rollbuck is good in a design context, since this is the most realistic case. Matches between models not including overhangs or SAB/prestressing deflections are helpful for validating those models, but those cases do not contribute in a helpful way to design. While the

match is excellent throughout the range of loads/rolls explored, the match in the approximately uncracked region of rolls less than 10-degrees is most helpful for design. A designer could quickly and easily use the RLM or the SAM to predict the final angle of an uncracked girder, considering all the complicating critical load factors and imperfections, without having to use a numerical program.

5. Imperfection Study Results: LTRB

Chapter 4 of the imperfection study considered LRB. It is necessary to extend the imperfection study work to include the effects of torsion in the load-displacement behavior of the girder, i.e., LTRB. The solution to the governing differential equation describing the twist angle of a girder along its length does not have a closed-form solution, so it is necessary to rely on results predicted by the numerical tool, Rollbuck 2021. This chapter will seek to determine whether the hypotheses developed for LRB also apply for the LTRB case. Namely:

1. Do different imperfections that result in equal initial roll angles still produce the same pre- and post-buckling behavior for LTRB, just as they did for LRB?
2. Do SAB, prestressing deflections, and overhangs modify the girder responses similarly to LRB?
3. Finally, do the SAM and the RLM, which was derived considering LRB only, still accurately predict the results from Rollbuck? Does the shape of the amplification of the initial roll angle change significantly for LTRB, and if not, does the modification to the critical load accounting for torsion adequately account for torsion's effects in the RLM?

These questions are based on the hypothesis that the $g(\eta_o)$ factor (and the subsequent modifications to η_o) developed in Section 2.4 accurately capture the softening effect of torsion in the load-deformation behavior of a precast prestressed girder.

5.1. **Baseline LTRB and Symmetry Breaking Imperfections**

5.1.1. **Baseline LTRB with Lateral Sweep**

The overarching goal of analyzing the different symmetry breaking imperfections is to show that the amplification of the corresponding initial roll angle is the same, both pre- and post-buckling, given equal initial roll angles and critical load. This proved to be true for LRB, and Section 5.1 will seek to prove that that result also holds true for LTRB. If that is the case, the different symmetry breaking imperfections can be reduced to an initial roll angle as a common metric, eliminating the need for a different methodology for each imperfection type. The initial roll angle calculation is shown in Chapter 3 and is unchanged for LTRB.

Figure 5.1 shows the initial roll angle amplification curves for lateral sweep imperfections. The curves with data points represented as an "x" depict the final equilibrium angle, consisting of roll and twist, while those represented by an "o" depict only the roll component of the final equilibrium. Only lateral sweeps of 1.0, 3.0, and 5.0 inches are included to improve plot clarity. Qualitatively, the plot appears to be very similar to the baseline LRB case, indicating that the general shape of the initial roll angle amplification is similar for both LRB and LTRB. Even for a 200 ft. long WF100G such as this, torsion does not lower the critical load significantly. In this case, $g(\eta_o) = 0.93$, corresponding to a 6.7% reduction in the critical load. This slight reduction can best be seen in Figure 5.1 by examining the self-weight line. For the LRB case, self-weight is approximately 1.25 times the critical load. For the LTRB case, it is just under 1.35 times the critical load. This roughly corresponds to the change predicted from $g(\eta_o)$.

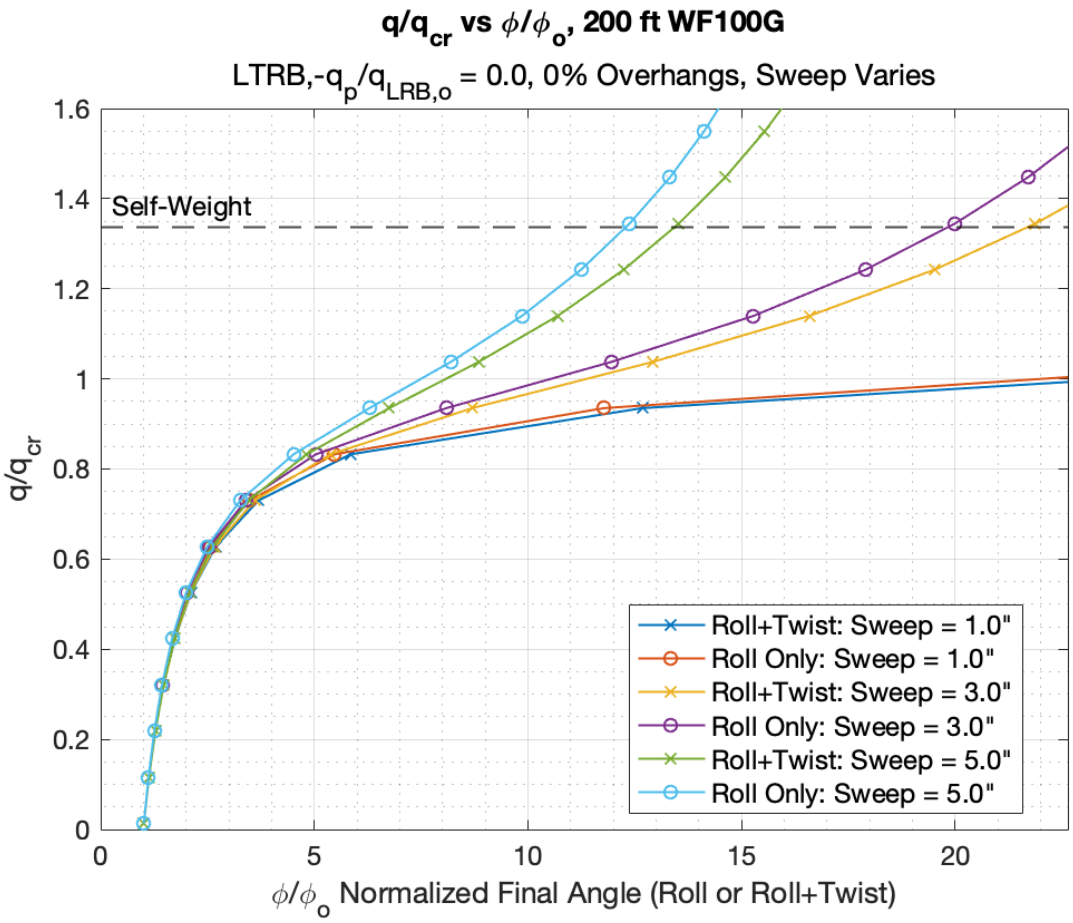

Figure 5.1 Final Roll and Roll+Twist Angle Normalized by Initial Roll Angle vs Applied Load Normalized by Critical Load. LTRB, Varying Sweep, No Overhangs, No SAB/Prestressing Deflections, 200 ft. WF100G Girder

As the applied load increases, the twist component of deflection—the gap between the roll and roll plus twist curves—correspondingly increases. This suggests that torsion plays a larger role in the deflection behavior at higher applied loads. At the self-weight line, a girder with a sweep of 5.0 inches now has an initial roll angle amplification of approximately 13.5. In the LRB case that amplification was approximately 11.75. Additionally, the incorporation of torsion slightly increases even the roll only component of the deflection. This occurs because the addition of twist causes the center of mass to be more eccentric and thus to increase the torque causing roll. In the LTRB case, the 5.0-inch sweep girder has a final roll-only angle just under 12.5 times the initial roll angle —greater than the approximately 11.75 in the corresponding LRB

case. While including torsional deformations does not significantly alter the results, the increase in initial roll angle amplification is not negligible.

Figure 5.2 shows a plot of the twist only component of the final tilt versus the roll only component for the three of the girders considered above.

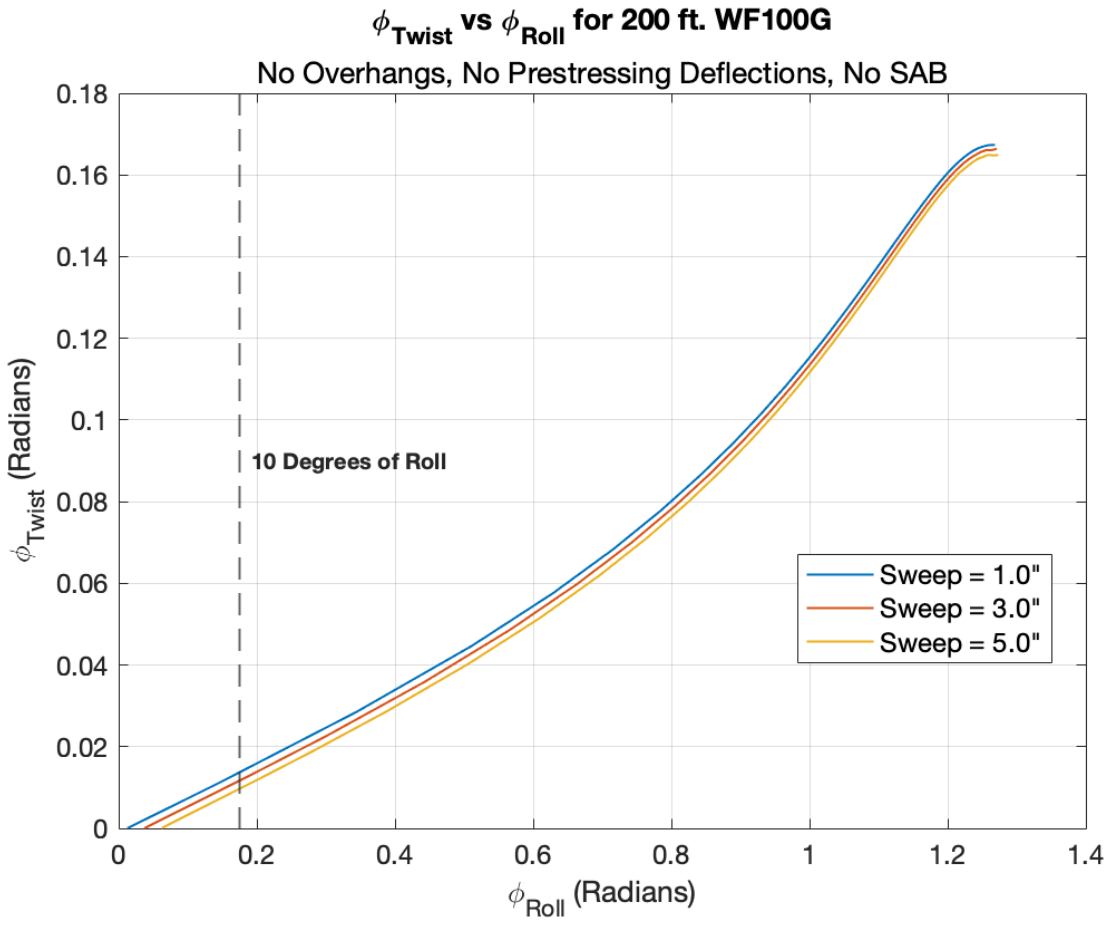

Figure 5.2 Twist Angle versus Roll Angle. 200 ft. WF100G without Overhangs or Prestressing Deflections/SAB

As the roll angle increases, the twist angle correspondingly increases. This reflects the results seen in Figure 5.1. This trend appears to be approximately linear until a roll angle of roughly 0.5 radians, at which point the rate of change in twist relative to roll increases. That rate appears to level out near the end of the curve—perhaps due to the total roll plus twist approaching 90 degrees, at which point the girder would stop rolling/twisting and only bend in

the weak-axis direction. A line depicting the approximate cracking point at 10 degrees of roll is shown. This linear elastic uncracked model is only strictly valid up to approximately this point, and the twist increases linearly relative to the roll. After 10 degrees of roll, the girder is likely cracked, and this linear elastic uncracked model loses its applicability. Furthermore, the girder could crack in bending, torsion, or both, and the different forms of cracking could initiate at different roll or twist angles. The reduction in stiffness in each mode would determine the subsequent response. Flexural cracking is addressed in Chapter 6. Torsional cracking lay beyond the scope of the project because no test data was available on which to build a computational model.

5.1.2. **Baseline LTRB with Lifting Loop Eccentricity**

Figure 5.3 shows five girders with lifting loop eccentricities that produce initial roll angles equal to those produced by the lateral sweeps considered above. For LRB behavior, different imperfections that produced equal initial roll angles resulted in identical imperfection amplification for a given critical load. It is hypothesized that the same will hold true for LTRB.

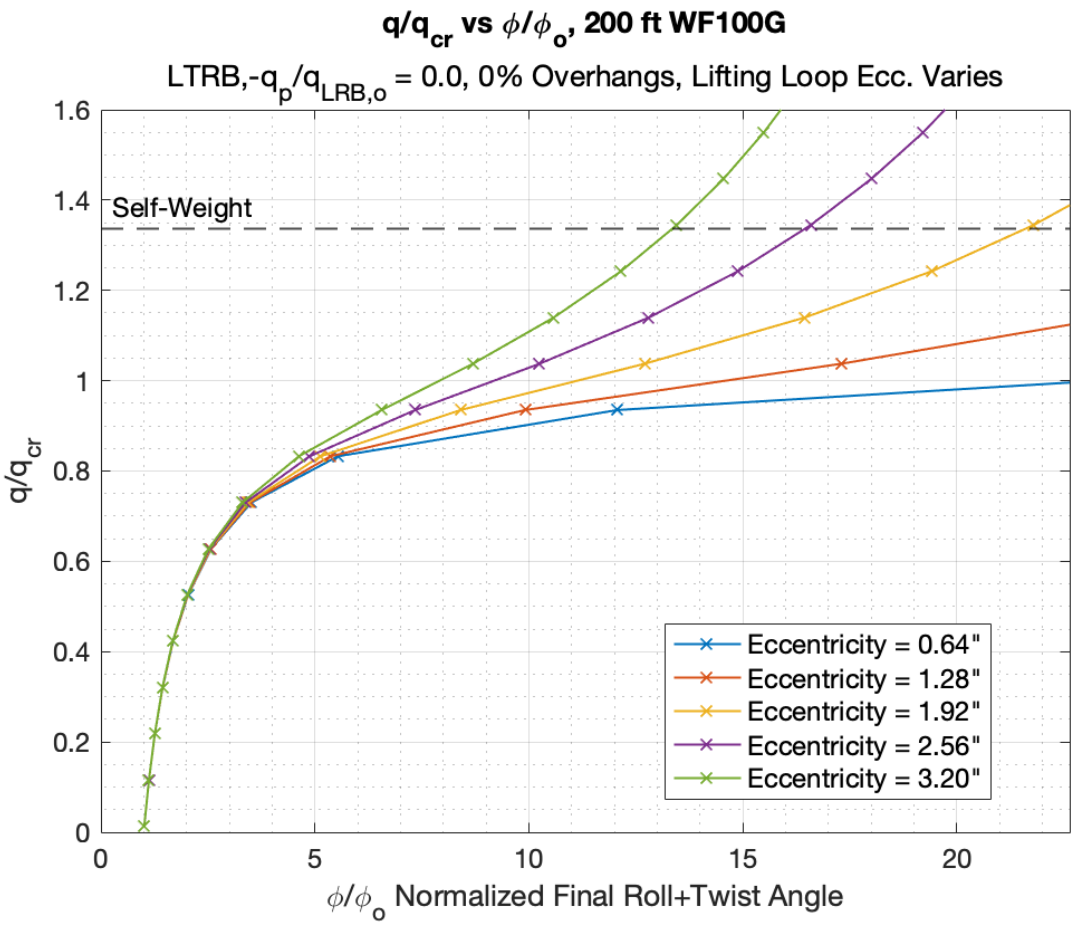

Figure 5.3 Final Roll+Twist Angle Normalized by Initial Roll Angle vs Applied Load Normalized by Critical Load. LTRB, Varying Lifting Loop Eccentricities, No Overhangs, No SAB/Prestressing Deflections, 200 ft. WF100G Girder

Again, the two different symmetry breaking imperfections produce the same initial roll angle amplification for equal initial roll angles and critical loads. This further confirms the possibility of converting different imperfections to a single measurement—the initial roll angle—to reduce the number of plots and types of analyses required for sufficient analysis and design. Additionally, the identical imperfection amplification behavior allows a designer to combine the different initial roll angles into one total initial roll angle that will be amplified, for a given applied and critical load, to determine the final equilibrium angle.

5.2. **Modified LTRB Load with Symmetry Breaking Imperfections**

Section 5.1 showed that different symmetry breaking imperfections that result in the same initial roll angle have identical amplifications of those imperfections for a given critical LTRB load. This section will expand upon the baseline LTRB critical load to include the effects of SAB and prestressing deflections or overhangs, and it will examine how those different parameters relatively stabilize or destabilize the imperfection amplification compared to the baseline LTRB case. In addition, it will compare the results to the analogous LRB results to show the destabilizing effect of torsion.

5.2.1. **LTRB with Strong-Axis Bending, Prestressing Deflections, and Sweep Imperfections**

The critical LTRB load accounting for prestressing deflections and SAB can be determined by multiplying the corresponding LRB load, $q_{LRB,vp}$, by the $g(\eta_{vp})$ factor. Figure 5.4 shows the initial roll angle amplification curves for girders with different prestressing levels but constant lateral sweep imperfections. The strong-axis moment of inertia is not inflated in order to include the stabilizing effect of SAB in addition to the destabilizing effect of prestressing deflections.

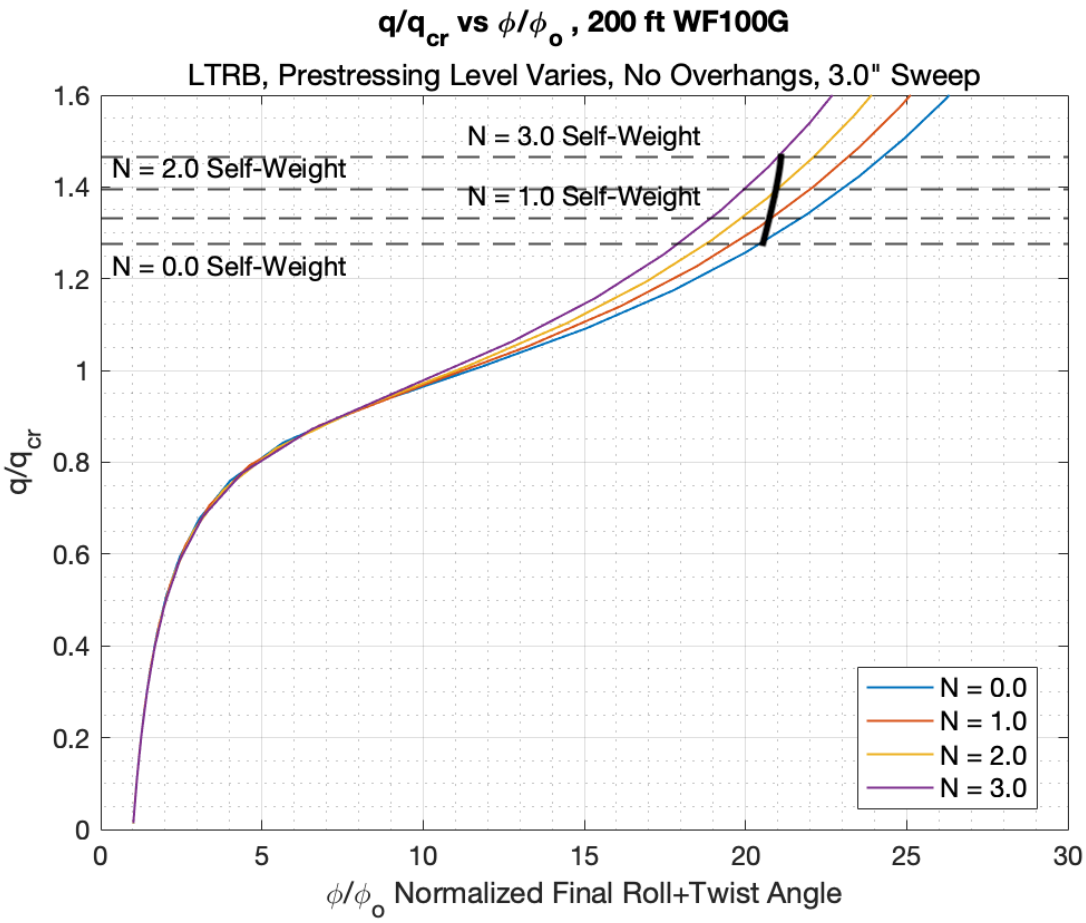

Figure 5.4 Final Roll+Twist Angle Normalized by Initial Roll Angle vs Applied Load Normalized by Critical Load. LTRB, Sweep = 3.0", Prestressing Level $N = -\frac{q_p}{q_{LRB}}$ Varies, No Overhangs, 200 ft. WF100G Girder

For girders with larger prestressing levels, the normalized self-weight line is located increasingly higher on the plot. This occurs because the critical load drops, relative to the self-weight, when upwards deflections due to prestressing are considered. Correspondingly, the initial roll angle amplification at a given load increases with increasing prestressing level. Comparisons between the cases are best made at the self-weight lines. The black curve connects the intersections between the self-weight lines and their corresponding amplification curves. A girder with no prestressing (and thus only strong axis bending stabilization) has an initial roll angle amplification of approximately 20.5 at self-weight load while the *N=3.0* case has an

amplification of approximately 21. The increase in amplification is very small. So, while increasing prestressing does reduce the critical load, it does not appear to have a significant impact on initial roll angle amplification. The same trend held true for girders undergoing LRB, although the increased amplification due to prestressing was slightly more pronounced.

The girders in Figure 5.1 did not have any prestressing and had a normalized self-weight load line at just under 1.35. In Figure 5.4, the self-weight load line for the girder without prestressing is at approximately 1.275. This shows the stabilizing effect SAB has on imperfection amplification.

In Figure 5.4, the self-weight load lines ranged anywhere from approximately 1.275 to 1.45 times the critical LTRB load. In Figure 4.5, the corresponding plot for LRB, the self-weight load lines ranged from just under 1.20 to just under 1.40. The self-weight is the same for all the girders considered, so this reflects the destabilizing effect torsional deformations have on the critical load. Thus, including torsional deformations results in earlier buckling and increased amplification of the initial roll angle.

5.2.2. **LTRB with Overhangs and Sweep Imperfections**

The critical load for LTRB for a girder with overhangs can be determined from Equation (5 – 1), which is just a modified form of Equation (2 – 54) with the SAB and prestressing deflection factors removed:

$$q_{LTRB,\alpha} = g(\eta_\alpha) q_{LRB,\alpha.} = g\left(\eta_o \left(\frac{f_{LTB}(\alpha)}{f_{LRB}(\alpha)}\right)^2\right) \frac{q_{LRB,o}}{f_{LRB}(\alpha)}. \qquad (5-1)$$

Note that Equation (2 – 54) could be substituted for Equation (5 – 1); if SAB and prestressing deflections are neglected or are non-existent, then Equation (2 – 54) would equal Equation (5 – 1).

Figure 5.5 shows the initial roll angle amplification curves for a series of 200-foot long WF100G girders with constant sweeps of 3.0 inches, but varying overhang lengths.

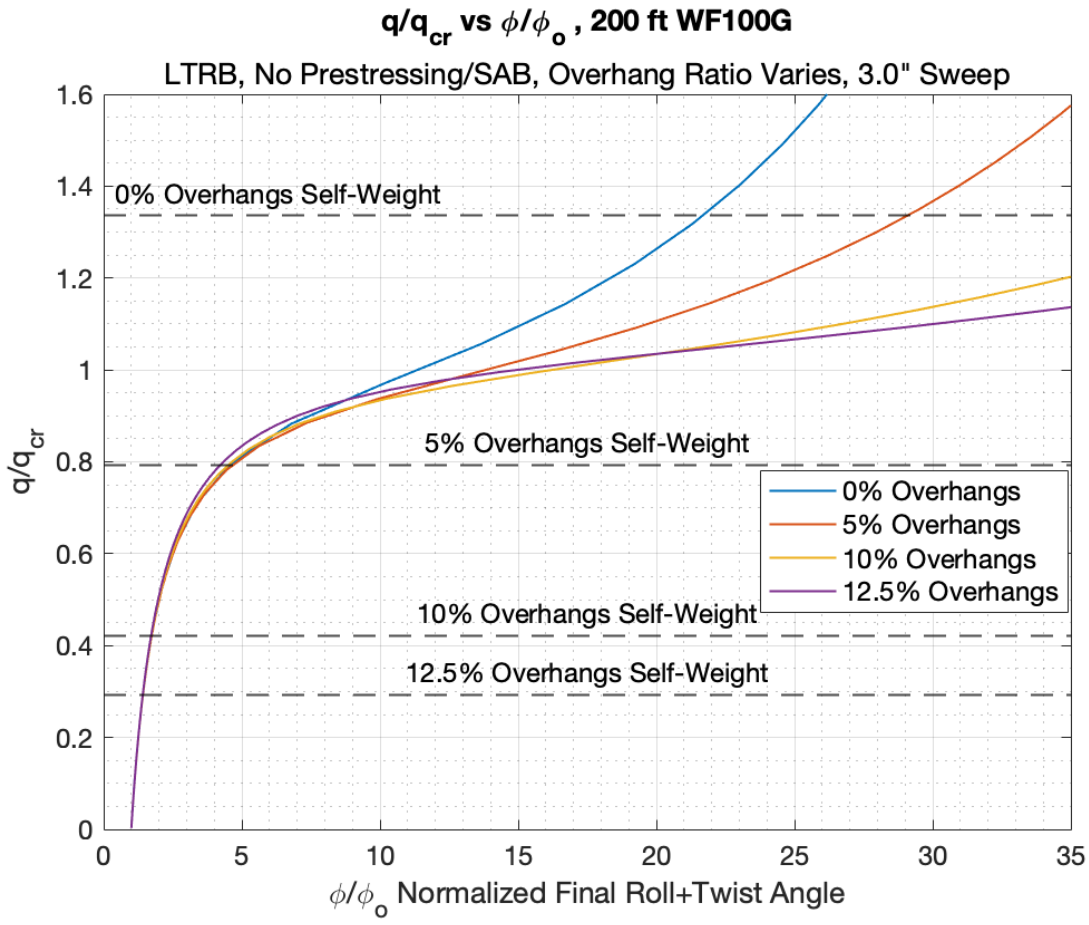

Figure 5.5 Final Roll+Twist Angle Normalized by Initial Roll Angle vs Applied Load Normalized by Critical Load. LTRB, Sweep = 3.0", Overhangs Vary, No Prestressing/SAB, 200 ft. WF100G Girder

Figure 5.5 shows that overhangs have a very large stabilizing effect on the critical load for girders undergoing LTRB, as was the case for LRB. This can be seen because the applied load (e.g., at the respective self-weight lines) was the same in all cases, but the ratio q/q_{cr} drops as the overhang ratio increases. Overhangs also provide benefits for the amplification of imperfections. At applied load equal to the self-weight, the normalized roll plus twist angle is

lower in the presence of large overhangs because the dashed horizontal self-weight line intersects the equilibrium path curve at lower values of both q/q_{cr} and ϕ/ϕ_o.

Compared to LRB, all the self-weight load lines have increased in magnitude on the vertical axis. This reflects the lower critical loads for LTRB compared to LRB. The two girders with 10 and 12.5 percent overhangs interestingly saw only slightly greater initial roll angle amplification at the self-weight line for LTRB compared to LRB; however, the girders with 5 percent and no overhangs at all had larger amplifications for LTRB than for LRB. This would indicate that LTRB does indeed have a destabilizing effect, but that large overhang ratios stabilize the girders to such a large degree that torsion does not have as large of an impact at the self-weight load for this case. The proportionally greater initial roll angle amplifications for girders with smaller overhangs seems to support this hypothesis.

To further emphasize that large overhangs lead to lower deflections at a given applied load, an unnormalized plot of the same girders in Figure 5.5 is shown in Figure 5.6. It shows that, when the overhang ratio is increased, not only is the amplification at any given load smaller, but also that the initial roll angle for a given sweep is also smaller. This represents a double benefit of using overhangs.

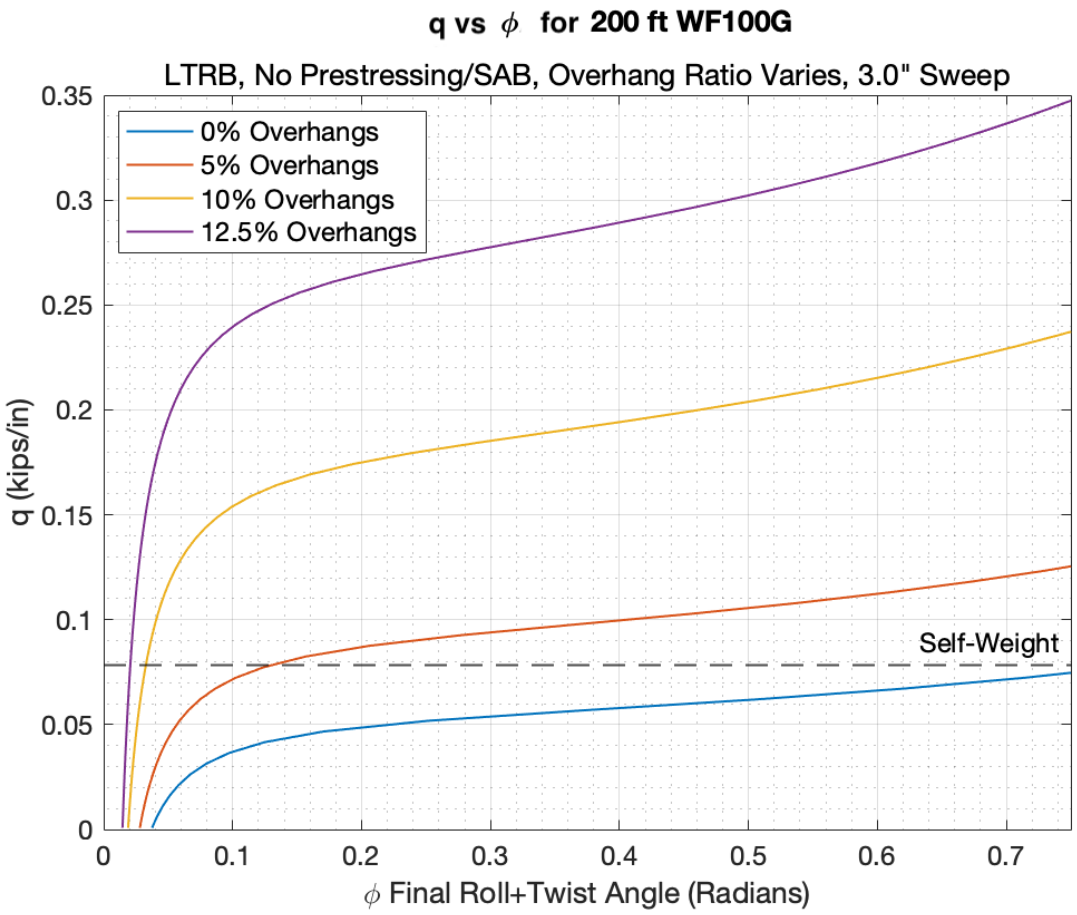

Figure 5.6 Final Roll plus Twist Angle vs Applied Load; Un-normalized. LTRB, Sweep = 3.0", Overhangs Vary, No Prestressing/SAB, 200 ft. WF100G Girder

Girders with larger overhangs require larger applied loads to reach a given final equilibrium angle. Alternatively, a given applied load causes a much higher final equilibrium angle (and initial roll angle amplification) for a girder with a small overhang than it does for a girder with a large overhang. Figure 5.6 also shows the approximate locations of the buckling loads for each overhang case plotted; as the load-deflection curve approaches horizontal, the girder has likely buckled. The relation of the approximate buckling loads relative to the self-weight line can also be seen. For the 200 ft. WF100G girders examined without SAB or prestressing deflections, an overhang ratio less than approximately five percent would lead to buckling at loads lower than the self-weight. The 10 and 12.5 percent overhang cases buckled at

loads much larger than the self-weight. The differences between the initial roll angles can also be seen by each curve's unique intersection with the horizontal axis.

5.3. LTRB Approximations with the Rigid Link Model and the Simple Amplification Model

5.3.1. RLM and SAM with Baseline LRB Behavior

The RLM derived in Section 3.6 was shown to approximate the LRB pre- and post-buckling results from Rollbuck to an exceptionally accurate degree. The SAM also was an excellent predictor of the Rollbuck results until the approximate point of cracking, roughly 10 degrees (Mast, 1993, 1994). This section will explore whether the RLM, as derived in Section 3.6, can also be used to predict the results from Rollbuck for a girder undergoing LTRB. As mentioned in Section 5.1.1, incorporating the effects of torsion on a 200-foot long WF100G girder without overhangs has only just under a seven percent reduction in the girder's critical load. It is hypothesized that since torsion does not significantly reduce the critical load, it therefore does not account for an outsized proportion of the final roll plus twist angle of the girder. Then, the shape of the imperfection amplification curve for a girder undergoing LTRB is not that different from a girder undergoing LRB, and the RLM can still predict the final equilibrium angle well. This is especially true if, as shown in Section 5.2, torsion does not play a large part in the final equilibrium angle until large loads are applied. As a result, this section will determine whether the RLM can accurately predict the load vs deflection behavior, especially at low applied load levels when the twist component of the final equilibrium angle is smaller.

Figure 5.7 compares the results from Rollbuck for girders with different lateral sweep imperfections undergoing LTRB to the results predicted by the RLM and the simple

amplification equation. The critical load used here to normalize the Rollbuck results is the one defined in Equation (2 – 46) that accounts for torsional deformations.

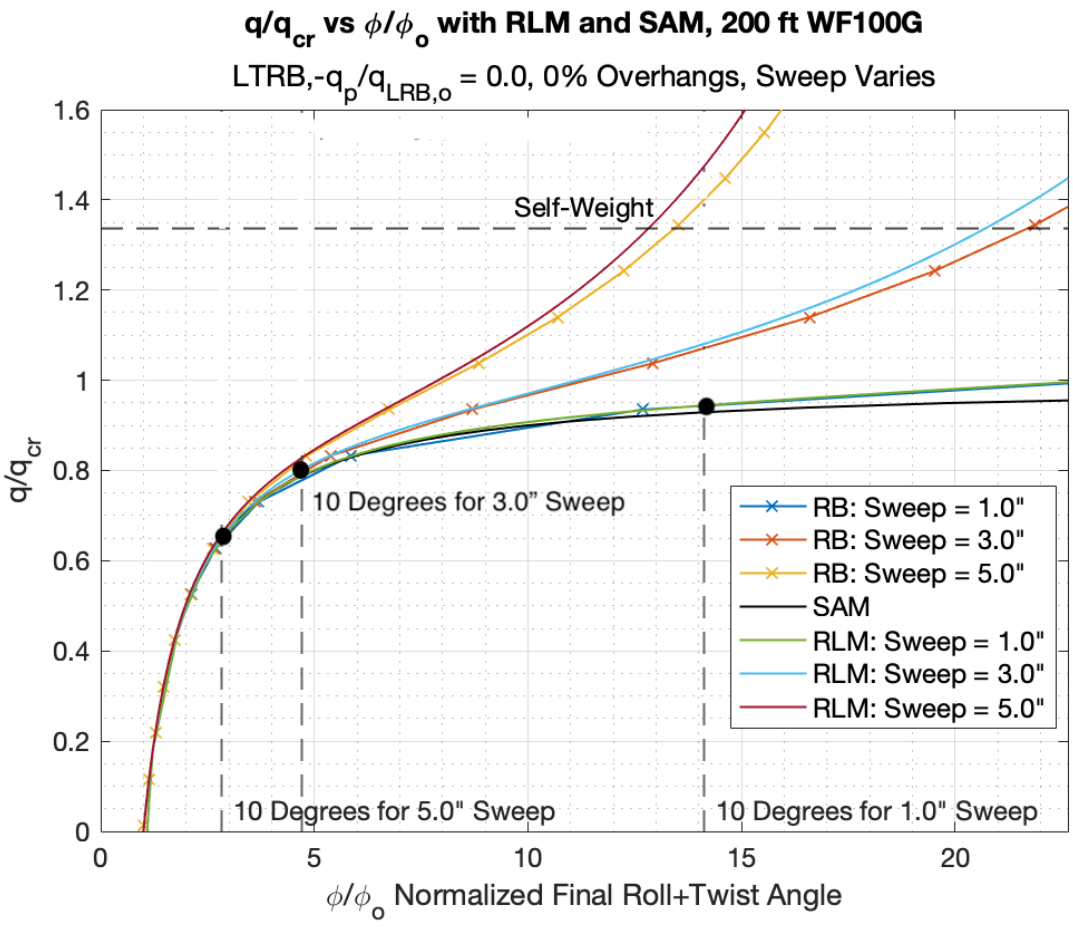

Figure 5.7 Comparison of Rollbuck Results with RLM and SAM. LTRB, Varying Sweep, No Overhangs, No SAB/Camber, 200 ft. WF100G

Once again, the RLM is largely an excellent match with the Rollbuck results throughout the range of applied loads explored. Unlike for LRB, the RLM and the Rollbuck results diverge at larger applied loads when the final roll plus twist angle is larger, approximately after the buckling load. This is likely due to the incorporation of torsion. The RLM was derived assuming a girder undergoing LRB, so it makes sense that Rollbuck and the RLM would not be in perfect agreement at large applied loads when torsion and twist are more prevalent. For small final roll plus twist angles, Rollbuck, the RLM, and the SAM are excellent matches. This indicates that, at

least for these girders, torsion does not play a large role in the total deformation for low applied loads or low total roll plus twist angles. Examining the 10-degree roll lines, one can see that the SAM quite accurately predicts the Rollbuck results up to this point. Afterwards, the girder is likely cracked, and the linear elastic model is no longer valid. This makes the growing discrepancy at larger applied loads between the RLM and Rollbuck results less relevant, as the model cannot accurately predict what would happen in the real world at those applied loads.

To best show the growing influence of torsion on the imperfection amplification as the applied load increases, Figure 5.8 shows the same results as Figure 5.7, but it also includes the "roll only" component of the girders' deflection without the twist. The RLM, derived for the LRB case, should theoretically follow the roll only component of deflection and diverge from the total roll plus twist as the applied load increases.

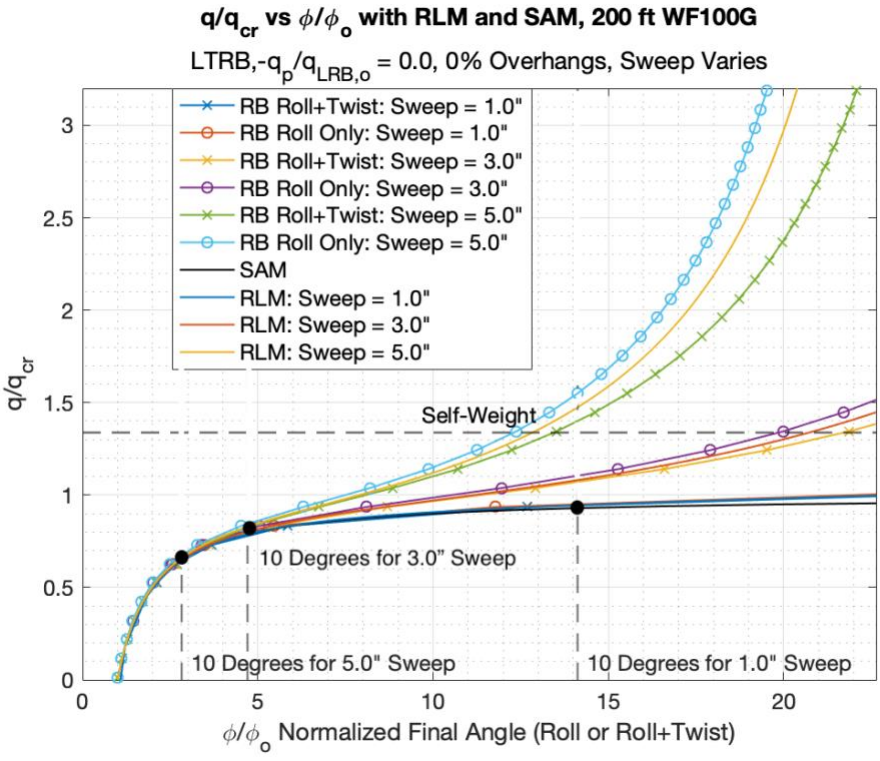

Figure 5.8 Normalized Rollbuck Results Broken into Roll and Roll+Twist Components with RLM and SAM. LTRB, Varying Sweep, No Overhangs, No SAB/Prestressing Deflections, 200 ft. WF100G

Figure 5.8 is zoomed out relative to the previous figures to better capture the RLM trending towards the roll angle component of the deflection as the applied load increases. This trend is most evident for the girder with 5.0-inches of lateral sweep. The RLM starts off following the total roll plus twist line, and as the load increases it trends towards only the roll component. Overall, the amount of twist relative to the roll increases as the applied load increases. While the RLM does not exactly match the roll-only component of a girder undergoing LTRB, it does follow the same *shape* as the roll-only component. At low loads, the *shape* of the imperfection amplification curve is the same for the roll-plus-twist curve as well as the roll-only curve. At higher loads, the roll-plus-twist shape, i.e., LTRB, begins to diverge from the roll-only shape, i.e., LRB. At low roll angles before the 10-degree roll line, all the girders examined show practically perfect matches between the roll component only, the total roll plus twist line, the RLM, and the SAM. This indicates that torsion does not play a huge role in the deflection at low applied loads/roll angles and that the RLM, derived assuming LRB, can be used to approximate LTRB behavior.

The shape of the RLM curve does not change from LRB to LTRB. This can be seen from Equation (3 – 32a). The ratio of the applied load to the critical load is a function only of the equilibrium angle and the initial roll angle. To minimize the numerical effort when plotting the RLM, different equilibrium angles are inputted, and the corresponding load ratio is outputted. The initial roll angles could be different from case-to-case, but if they are equal, the RLM will be the same shape for any case for both LRB and LTRB. The RLM, which was derived assuming LRB behavior, matches LRB perfectly, but it still works very well for LTRB. This is because the shape of the imperfection amplification curve does not change dramatically in the LTRB case until there are large equilibrium angles/applied loads. In other words, both LRB and LTRB

amplify imperfections in practically the same way at smaller loads and equilibrium angles. Differences between the LRB amplification shape (and by extension the RLM amplification shape) only appear *after* the 10-degree roll lines, at which point the girder has likely cracked and the Rollbuck results used to compare to the RLM are no longer valid.

5.3.2. RLM and SAM for LTRB with Overhangs and/or SAB/Prestressing Deflections

Section 5.3.1 explored matching the RLM and the SAM to the Rollbuck results for the baseline LTRB case. This section will explore matching the RLM and SAM to the Rollbuck results for more complicated LTRB cases that include overhangs, prestressing deflections and SAB, and a combination of the two. Figure 5.9 shows the results for three girders with different lateral sweeps and 10% overhangs.

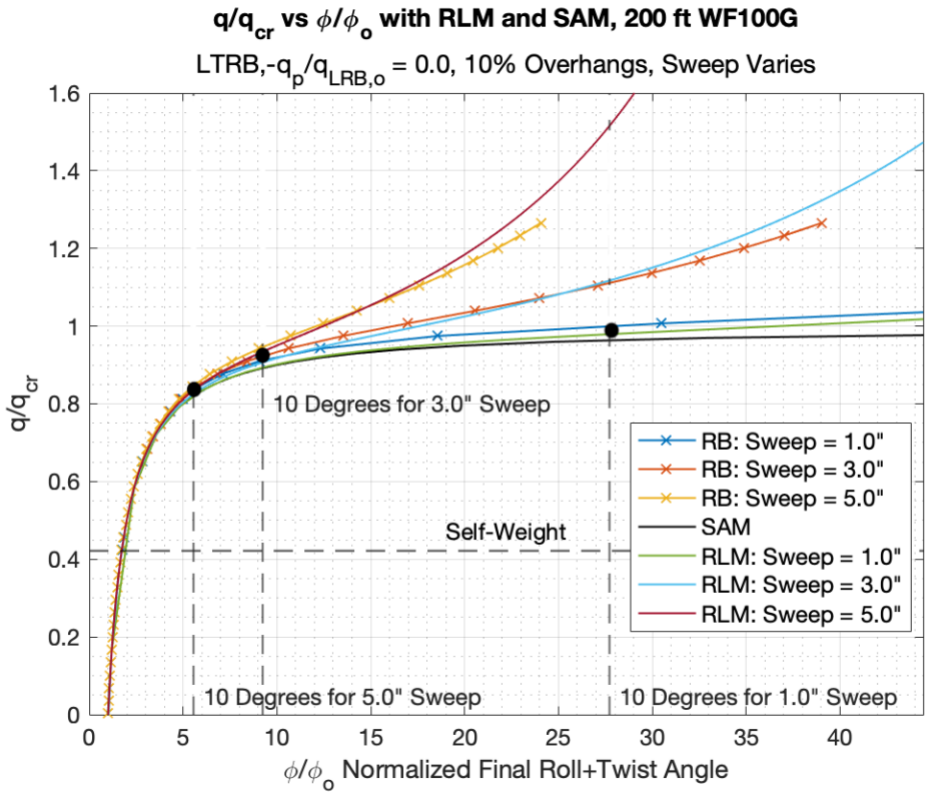

Figure 5.9 Comparison of Rollbuck Results with RLM and SAM. LTRB, Varying Sweep, 10% Overhangs, No SAB/Prestressing Deflections, 200 ft. WF100G

There is once again an excellent match between the Rollbuck predicted results, the RLM, and the SAM for roll angles less than 10 degrees. Girders with overhangs undergoing LTRB have an imperfection amplification very similar to the shape of the RLM, at least until torsional deformations become larger at higher applied loads, approximately greater than the buckling load. A real girder during transportation/handling would only have an applied load equal to the self-weight. At that load, all the models agree. Additionally, in this configuration the self-weight line occurs before all the 10-degree roll lines, indicating that the linear elastic and uncracked model is still valid at the self-weight load.

While the 3.0- and 5.0-inch sweep cases have good matches between the Rollbuck results and the RLM, there is a small gap between the Rollbuck and RLM results for the 1.0-inch sweep case. While the vertical gap between normalized applied loads at a given initial roll angle amplification is small, the horizontal gap between initial roll angle amplifications at a given normalized applied load appears to be larger. However, for a WF100G girder with one inch of sweep and 10% overhangs, the initial roll angle is approximately 0.0063 radians. At an applied load equal to the buckling load, Rollbuck predicts an amplification of approximately 28, while the RLM predicts approximately 36. This translates into a difference of approximately 2.9 degrees—the RLM predicts an equilibrium angle of roughly 13 degrees while Rollbuck predicts 10.1 degrees. Fortunately, this difference occurs at an applied load approximately twice the self-weight—it would not occur in practice during lifting and handling. This issue with a horizontal gap between the RLM and Rollbuck curves does not appear in any of the other curves. Further, at this point the girder would likely have cracked, and the linear elastic results would not be valid anymore.

The RLM and SAM can also be used to predict the LTRB behavior of a girder with prestressing deflections and SAB but no overhangs. Figure 5.10 shows three girders with varying initial lateral sweeps and constant prestressing levels where $-\frac{q_p}{q_{LRB}} = 3.0$.

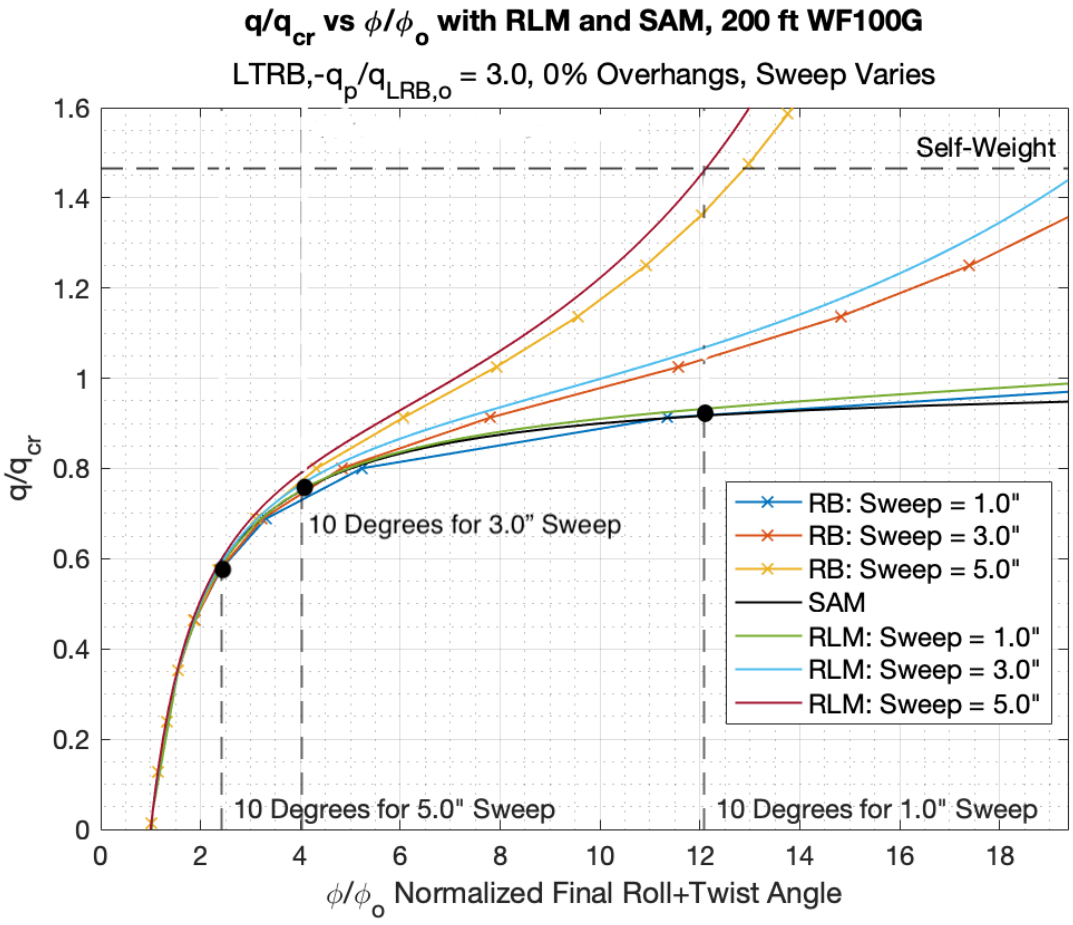

Figure 5.10 Comparison of Rollbuck Results with RLM and SAM. LTRB, Varying Sweep, No Overhangs, $q_p = -3.0q_{LRB}$, 200 ft. WF100G

For a girder undergoing LTRB with prestressing deflections and SAB included, the RLM is once again quite a good match with the amplification shape predicted by the Rollbuck results. The SAM continues to perform in the same way as before, predicting amplifications at equilibrium angles less than 10-degrees quite well. Without overhangs and with the destabilizing effects of prestressing deflections included, the girder buckles well before the self-weight load is fully applied. As such, the loads at which torsional deformations become more significant occurs

sooner than the case with overhangs but no prestressing deflections. The match in shape between the amplification curves is still good, but it is less perfect than before, and is certainly not as exact as the LRB cases. Fortunately, a girder is unlikely to ever be lifted or transported without overhangs, and so this scenario is unlikely to ever occur. Further, each girders intersection with the self-weight line occurs after cracking would have likely occurred, making the linear elastic results not valid in that region of equilibrium angles.

The most realistic real-world case including all the factors considered thus far is for a girder with overhangs, prestressing deflections, SAB, and torsional effects included. From a design context, a match between the RLM amplification shape and the Rollbuck amplifications results is most critical for this case. If the two results do match well, the RLM could in practice be used in a design procedure to predict the final equilibrium angle of a girder, considering all the realistic effects included above. The RLM curves and Rollbuck curves are shown in Figure 5.11 for girders with varying lateral sweeps, 10% overhangs, and $-\frac{q_p}{q_{LRB}} = 3.0$.

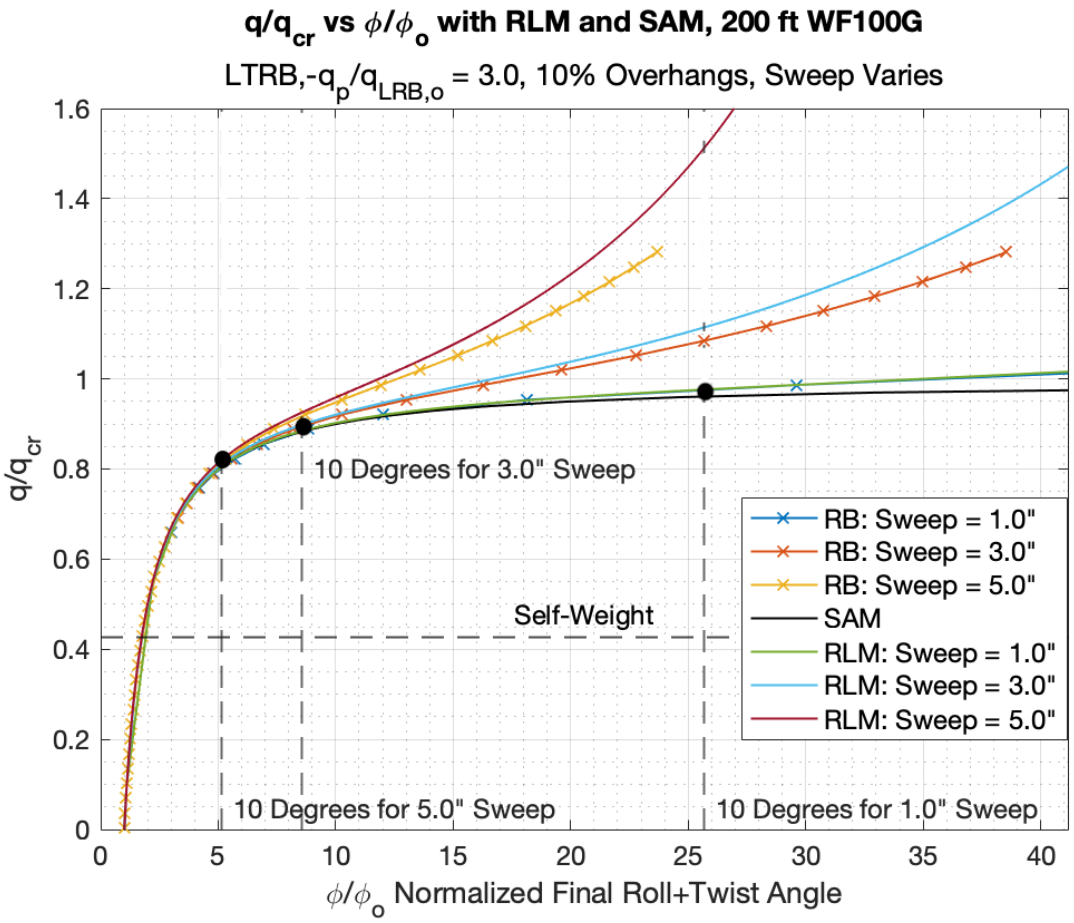

Figure 5.11 Comparison of Rollbuck Results with RLM and SAM. LTRB, Varying Sweep, 10% Overhangs, $q_p = -3.0q_{LRB}$, 200 ft. WF100G

There is a very good match between the Rollbuck initial roll angle amplification results and the amplifications predicted by the RLM. Torsional deformations only begin to cause a deviation between the two curves at loads much higher than the self-weight, the only practical weight that would be applied during transportation and handling. The SAM also performs well for equilibrium angles less than approximately 10-degrees. In the most realistic case possible, the methods for predicting initial roll angle amplification agree well. This suggests that the RLM could be used in a design context to predict final equilibrium angles.

5.4. **Takeaways from the Imperfection Studies**

The main takeaways from the LRB and LTRB imperfection study are as follows:

- For both LRB and LTRB, equal initial roll angles lead to equal imperfection amplification, no matter the source of the imperfection (e.g., lateral sweep vs lifting loop eccentricity.)
- Without overhangs, long-span girders like the 200 ft. WF100G girder explored here are susceptible to buckling and large imperfection amplifications.
- For girders undergoing LRB, the RLM predicted imperfection matched practically perfectly with Rollbuck throughout the range of applied loads explored. The SAM was valid through approximately 10 degrees of roll.
- For girders undergoing LTRB, the shape of the RLM imperfection amplification curve matches the Rollbuck predicted results until approximately the buckling load. Beyond this point, torsional deformations modify the amplification shape such that Rollbuck and the RLM begin to diverge in their predictions for LTRB. The SAM was valid through equilibrium angles of approximately 10 degrees.
- In the most realistic and design-applicable case—a girder undergoing LTRB with SAB, prestressing deflections, and overhangs—the RLM accurately predicts the imperfection amplification at the self-weight load.

6. Development and Validation of the Cracking Model (Rollbuck 2022)

6.1. **Modifications to Rollbuck 2021**

Rollbuck 2021 is described in Section 3.5, with a more detailed description of the Rollbuck program included in Appendix A. Rollbuck 2022 is more of an evolution than a revolution of the procedure of Rollbuck 2021. An update to the concept map shown in Section 3.5 is shown in Figure 6.1. It shows where the main conceptual change was made from Rollbuck 2021 to Rollbuck 2022 to account for the effects of cracking.

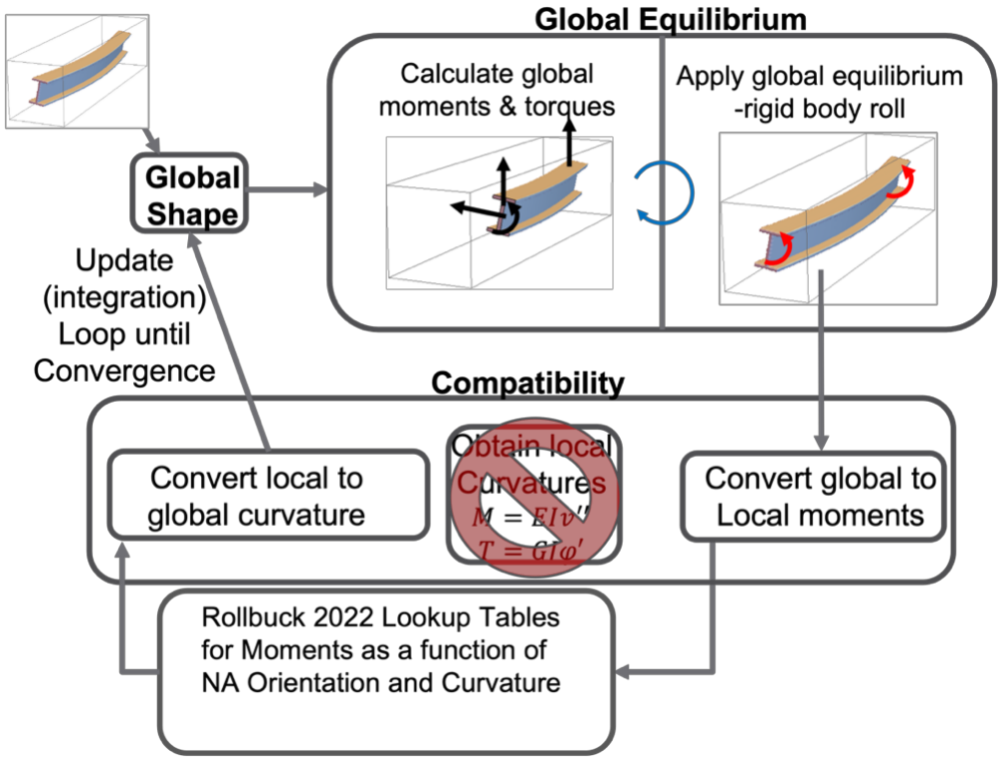

Figure 6.1 Rollbuck 2022 Concept Map

At the start of an analysis case, Rollbuck 2022 proceeds much the same as Rollbuck 2021. A nonlinear concrete model, like the Popovics model, is used instead of a linear concrete model, but for small strains they are quite similar (Popovics, 1970). Once the girder cracks, however, the largest change between Rollbuck 2021 and Rollbuck 2022 takes place. At this

point, Rollbuck 2022 no longer assumes that the moments are linearly related to the curvatures by the product of the moment of inertia and the modulus of elasticity (torques are still linearly related to the derivative of the tilt angle by the product *GJ.)* Instead, Rollbuck 2022 generates "lookup tables" for the moment in the local "x" and "y" directions that are functions of curvature and neutral axis orientation. The program essentially generates contour lines for constant "x" or "y" direction local moments as functions of neutral axis orientations and curvatures. With these two contour lines for each local moment direction, interpolation between the "lookup table" data points is used to find the point of intersection between the two contours. The intersection represents a single point of neutral axis orientation and curvature that satisfies both known local moment values. If there is no intersection, either the girder has failed—there is no neutral axis orientation and curvature combination that satisfies both local moments—or the user has simply not inputted a wide or dense enough range of curvatures or neutral axis orientations to find an intersecting value.

The neutral axis orientation angle is not necessarily the same as the rolled (or roll plus twist) angle of the girder. The curvature values found by the intersection of the two contours are converted back to the local "x" and "y" axes (from the coordinate space of the neutral axis orientation). At that point, Rollbuck 2022 can resume its normal path, converting from local to global curvatures, and determining whether the overall global shape of the girder has converged or not.

Rollbuck 2022 can be made to function like Rollbuck 2021. A linear elastic concrete model can be selected instead of a nonlinear model. Additionally, an artificially high tensile rupture stress can be inputted at the program setup. This way, the tensile stresses are never high

enough that the program will think the girder has cracked and it will never use the lookup tables to find the local curvatures.

A more detailed description of both Rollbuck 2021 and Rollbuck 2022 is included in Appendix A.

6.2. **Evaluation and Validation of Rollbuck 2022**

Before using the newly updated Rollbuck 2022 program to explore the effects of cracking, it was necessary to evaluate and validate Rollbuck 2022 against existing results. The first question to be checked was whether Rollbuck 2021 and Rollbuck 2022 produced the same results for uncracked girders. The second question was whether Rollbuck 2022 gave results that matched existing physical test results for cracked girders. No numerical results accounting for cracking in the lateral-torsional response of long-span prestressed concrete girders were known of, and thus Rollbuck 2022 could not be checked against them. This second validation attempt was conducted by inputting the same beam used in Mast's 1994 paper in his full-scale girder test into Rollbuck 2022 and comparing the results.

To compare Rollbuck 2022 to Rollbuck 2021 with a linear, elastic, and uncracked girder, a 200-foot long WSDOT WF100G girder with 7.5 percent overhangs and an equivalent upwards load due to prestressing of 0.169 kips per inch was inputted into each program. Figure 6.2 shows one demonstration of the match between the two programs.

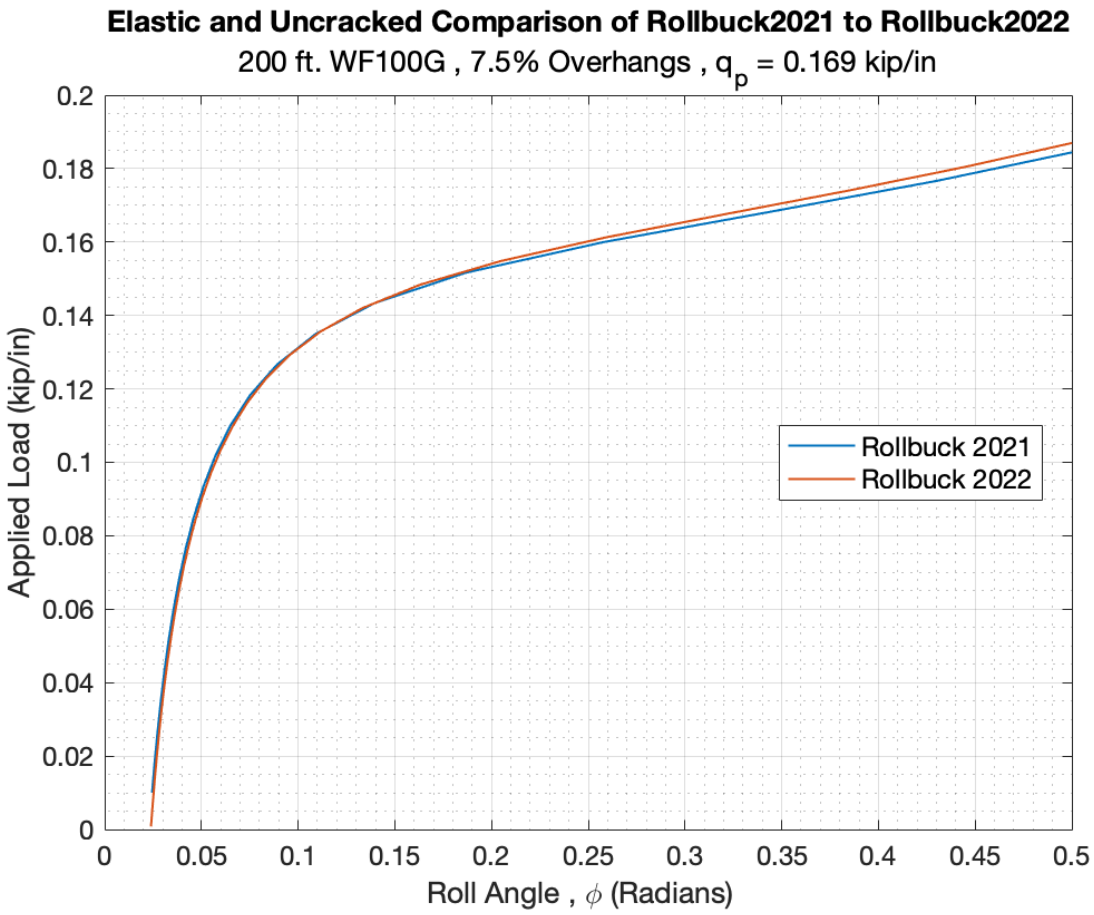

Figure 6.2: Comparison of Rollbuck 2021 to Rollbuck 2022

The match between the Rollbuck 2021 and Rollbuck 2022 results was nearly perfect, especially at the lowest roll angles. The slight deviation between the two curves in Figure 6.2 at large roll angles would only occur once the girder had almost certainly cracked and would no longer be linear elastic. The (small) discrepancies between the results can likely be explained by slight programming assumption differences between the two programs. For example, Rollbuck 2022 requires explicit definitions of the location, material type, and prestressing force for each bit of steel used in the girder. This more accurately describes the stresses due to prestressing within the girder—which is very necessary for implementing the cracking response into Rollbuck 2022. Rollbuck 2021 describes prestressing force as the equivalent upwards distributed load (q_p) coming from a theoretical parabolic strand profile passing through the center of gravity

at each end of the girder. As a second example of the differences in assumptions between the two programs, Rollbuck 2021 assumes that lateral sweep is in the profile of the deflected shape of a simply supported beam subjected to a uniformly distributed load. Due to the definition of prestressing in Rollbuck 2021, the max prestressing deflection is in this shape as well. Rollbuck 2022 assumes that the lateral sweep is in a parabolic profile. The prestressing deflection is calculated directly from the specific locations and prestressing forces of the strands. Figure 6.2 shows that these programming differences and assumptions do not lead to any serious discrepancies between the two programs. Because of the match in results, despite the differences in the underlying structures of the programs, Rollbuck 2022 could confidently be used to predict the behavior of linear elastic girders. From there, incorporating the effects of cracking on LTRB could begin to be explored.

A very limited amount of physical test data exists on cracking due to rollover during lifting and transportation of long span prestressed concrete girders. Fortunately, Mast's 1994 paper on his rollover test of a 149 ft. long prestressed concrete beam contains information about the configuration of the beam physically tested, as well as various results from that test that were used here (Mast, 1994).

Mast's beam was an older WSDOT section, now superseded by newer designs. It was 73.5 inches deep, approximately similar to the WSDOT WF74G in cross-section, 149 ft long, with 10.8 feet of overhangs (7.25% overhangs), and one inch of lateral sweep. At the time of the test, the concrete had a strength of approximately 10.35 ksi, density of 160 pounds per cubic foot, and the modulus of elasticity was reported by Mast as 6679 ksi. The prestressing strand configuration, as described by Mast, led to a jacking stress of 1111.1 kips (Mast, 1994). The beam also had end-blocks; however, their dimensions were not described. Fortunately,

consultation with Concrete Tech Corporation of Tacoma, WA and WSDOT revealed that they had on file plans for girders similar to Mast's beam, with end block dimensions detailed. They were adopted for use here, for want of a better alternative.

This configuration was inputted and ran through Rollbuck 2022 and a plot of twist at midspan versus support role was produced, similar to Figure 17 in Mast's 1994 paper. Initially, the end blocks were not included in the Rollbuck input as the program cannot handle non-prismatic cross sections at this time. This led to the Rollbuck 2022 results predicting higher twists than Mast's actual test results at a given support roll angle. This makes physical sense because the end blocks, which occur in the overhangs, balance out the moments at midspan more than an overhang of the regular cross-section would, resulting in less overall deformation. The end blocks, which essentially are the same cross section as in the main span but with a 17-inch-wide web, begin with their full increased area at the ends for 2'-10.5", and then taper towards the regular cross section over 7'-6", becoming the actual cross section 5.1" from the support. To account for the end blocks, the bending moment due to the overhang at the support was calculated for the regular cross section. Then, the bending moment was calculated due to the overhang at the support for the tapered end block cross section. The moments at the supports were matched by increasing the length of the overhang of the regular cross section. This led to a 25% increase in the overhang length. Upon making this adjustment in Rollbuck 2022, the Rollbuck 2022 results matched Mast's Figure 17 remarkably well. The midspan twist versus support roll plot for Mast's beam, as produced by Rollbuck 2022, is shown in Figure 6.3.

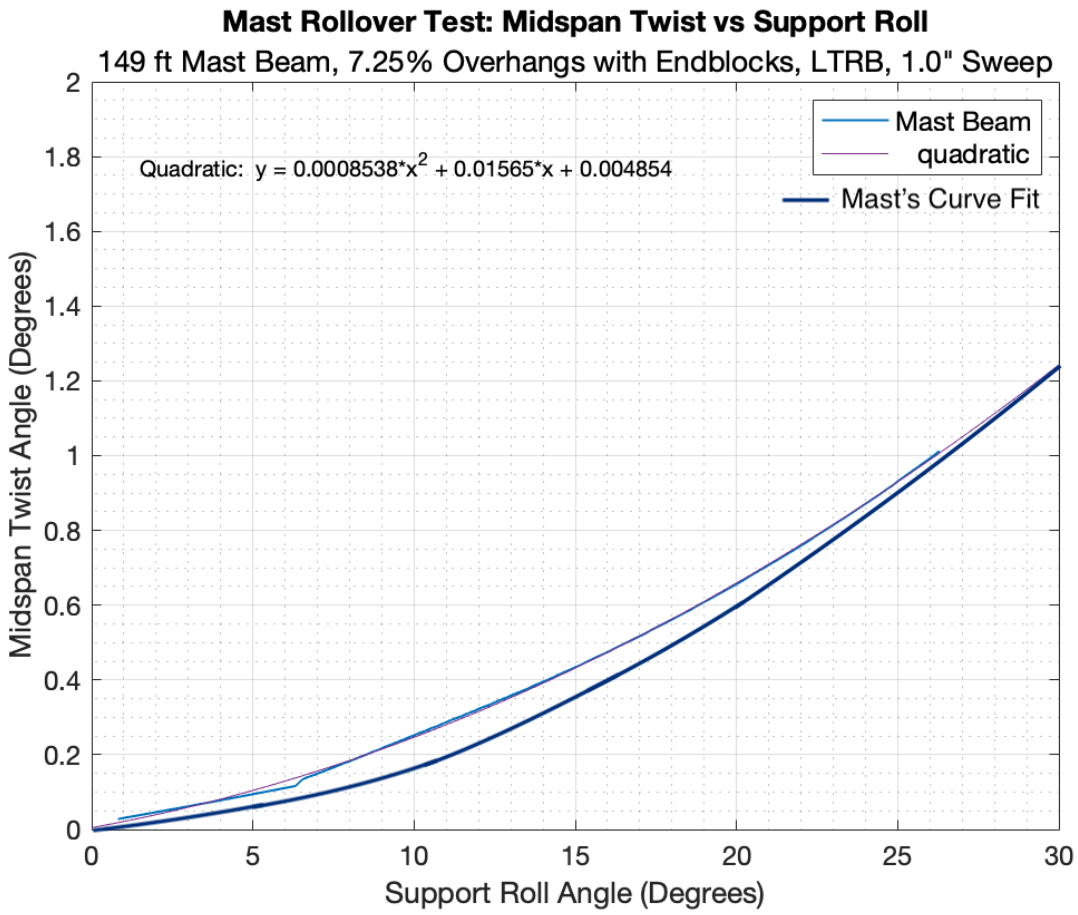

Figure 6.3: Rollbuck 2022 Midspan Twist versus Support Roll Results of Mast's Rollover Test Beam

The actual data from Rollbuck 2022, in blue, as well as a quadratic curve fit, in purple, (fitted to the Rollbuck 2022 data points) are shown in Figure 6.3. The curve-fit for Mast's results from Figure 17 of his 1994 paper is shown approximately in Figure 6.3 as the black curve. The two sets of results match quite well, with the maximum difference being approximately 0.1 degrees of twist at a given roll. Mast stated that the twist was approximately proportional to the square of the tilt angle. That trend holds up here. Considering the level of precision available with field measurement tools at the time, and the fact that measured field data is being compared to numerical results that rely on the accuracy of the measured field data and structural properties, the match is quite good.

The Rollbuck 2022 of Mast's beam in Figure 6.3 cracks at approximately 6.5 degrees of support roll, shown by the jump in the blue curve at that point. This location of the "kink" in the curve approximately matches the cracking point for the test results depicted in Figure 8 of Mast's 1993 paper (roughly 5 degrees) and serves to validate Rollbuck 2022 in that it predicts cracking at nearly the same point as when it occurred in a physical test (Mast, 1993).

Any differences between Rollbuck 2022 and Mast's test results can very likely be attributed to imprecision in testing data collection, curve fit error, assumed versus actual material behavior, and the fact that Rollbuck 2022 is a numerical program while Mast was fitting a curve to relatively scant collected data points. Additionally, the exact results from Rollbuck 2022 can vary slightly depending on the shear modulus, G, that is inputted into the program. While ACI 318-19 section R6.6.3.1 says that 40% of the modulus of elasticity may be used for G, Mast's paper does not specify what value, if any, —Mast assumed torsional rigidity—was used in his calculations (ACI Committee 318, 2019). Figure 6.3 was produced using a shear modulus that was 36% of the modulus of elasticity. This ratio makes quite a small difference in the overall results but can change the exact details of the twist at a given roll. Using a slightly stiffer G could perhaps result in an even closer match of the two curve-fits. Additionally, the effects of cracking on the torsional stiffness are unknown. The flexural cracking may lower the torsional stiffness, or torsional shear cracks could possibly form, which could reduce torsional stiffness as well. The fact that the two curves match as closely as they do, given all the above uncertainty, is good validation in that Rollbuck 2022's numerical methods reasonably predict results that were measured in the field, even with the effects of cracking and torsion included.

The preceding comparison provides confirmation at the "macro" level that the program can provide displacement results that match physical tests. However, displacements are easier to

match than “micro” quantities, especially those, such as strains, that depend on differentials of the displacements. The following checks provide information at the “micro” level and add confidence that the program is working as intended.

- *Approximate simulation of end blocks*. Incorporating the effects of end blocks in the Rollbuck 2022 evaluation of Mast’s beam led to a much better match with Mast’s results. Principles of mechanics were used to find an extended overhang value, and use of it greatly improved the match with Mast’s test results. This suggests that at least the overhang features were working correctly.
- *Cracking and failure.* The author was attempting to produce an applied load versus roll angle curve using Rollbuck 2022. The starting applied load was to be 0.01 kips per inch; however, when the program was run, Rollbuck 2022 predicted immediate failure of the girder. Due to just the loads from the prestressing in this girder, the stress in the top flange was 0.619 ksi and since the girder was presumed to be cracked already (and thus have zero tensile strength), the 0.01 kips per inch external load did very little to induce top flange compression. The author calculated that an applied load of 0.0516 kips per inch would put the top flange into compression, thus allowing the girder to not immediately fail and Rollbuck to run the applied load versus roll study. Inputting a starting load slightly higher than that allowed the program to run successfully. This suggests that the evaluation of cracking, which depends on the differential of displacements, was working as intended. Furthermore, the correct prediction of flexural cracking depends on many other features of the program functioning correctly. While it is possible that counteracting errors exist in the program that allowed it to predict the cracking within a relatively fine tolerance, it is improbable.

6.3. **Cracking Analysis on Girders with Plans**

6.3.1. **Procedure**

One of the main goals of this work was to determine whether existing design equations and frameworks are capable of reliably treating the much longer and heavier girders of today. Of primary interest in that regard was whether Mast's equation for the effective cracked lateral stiffness of a girder as a function of its roll angle was still applicable to modern girders. Mast's Equation 20 from his 1993 paper is repeated here as Equation (6 – 1)

$$\frac{I_{eff}}{I_{gr}} = \frac{1}{1 + 2.5\theta}, \qquad (6-1)$$

where I_{eff} is the effective moment of inertia for a cracked section, I_{gr} is the gross, uncracked, moment of inertia of the cross section, and θ is the equilibrium roll angle, more commonly notated with a ϕ in this work (Mast, 1993). Note that Rollbuck 2022 requires input of jacking stresses and then uses the transformed section properties accounting for the rebar and prestressing strands in its calculations. Properly, I_{gr} here would be I_{tr}, the transformed moment of inertia of an uncracked section. The important thing to note from Equation (6 – 1) is that the righthand-side relationship predicts the ratio of the cracked to uncracked moments of inertia—regardless of whether the gross or transformed section properties are used. The effective moment of inertia is the one that, when applied using the uncracked, closed-form equations, leads to the same lateral displacement as is found from using an analysis that explicitly includes cracking.

Rollbuck 2022 was used to perform controlled roll test simulations on girders, replicating the physical test conducted by Mast (1994). These analyses were performed on three different girders for which the researchers had structural plans: the actual 73.5-inch-deep beam Mast tested, a 150-foot long WSDOT WF100G girder designed for use on a Sound Transit (ST)

Project in the Seattle, WA area, and a 223-foot long WSDOT WF100G girder made of lightweight concrete (LWC) used on the 70th Ave Bridge Replacement project in Fife, WA. Hereafter, these beams will be referred to as the Mast beam, the ST girder, and the 70th Avenue girder.

To perform the virtual rollovers, the three different girders were inputted into Rollbuck as beams supported from below by torsional springs of stiffness much greater than that necessary to not be unconditionally unstable (see Section 2.5). Any concentrated torque applied to the girder support then caused a roll angle approximately equal to the torque divided by the rotational stiffness. This was adopted as a simple way of achieving a series of applied roll rotations. Torques of gradually increasing magnitude were applied to the girders at their supports, thus rolling the girders over. The girders' self-weight was constantly applied vertically downwards, and no other loads acted upon them. As the girders progressed through their roll rotation, data was collected from Rollbuck at each step in the loading. These data included the average support rotation, the total midspan rotation (roll plus twist angle), and the maximum and average deflections in the global lateral and vertical directions. Using the sign convention shown in Figure 2.1, the global deflections were transformed into local deflections using the coordinate transformation matrix shown below in Equation (6 – 2),

$$\begin{Bmatrix} u_{loc} \\ v_{loc} \end{Bmatrix} = \begin{bmatrix} \cos\phi & \sin\phi \\ -\sin\phi & \cos\phi \end{bmatrix} \begin{Bmatrix} u_{glo} \\ v_{glo} \end{Bmatrix}. \qquad (6-2)$$

To obtain the $\frac{I_{eff}}{I_{gr}}$ plots like those shown in Mast's paper, two cases had to be run through Rollbuck (Mast 1993). In the first case, the girder had its actual rupture stress inputted and was allowed to crack. In the second case, the girder was not allowed to crack and thus maintained its uncracked section properties. Once both cases had been run, to get the lateral $\frac{I_{eff}}{I_{gr}}$ ratio, the local

lateral deflection of the cracking allowed case was divided by the local lateral deflection of the cracking prevented case. If both girders hypothetically were controlled by the same deflection equation, all relevant properties such as applied load, modulus of elasticity, and length would all be equal at a given roll angle, but the moments of inertia would be different depending on if the girder was cracked or not. By dividing the cracking allowed deflection by the cracking not allowed deflection, this is effectively like taking the $\frac{I_{eff}}{I_{gr}}$ ratio. The deflection ratio had to be inverted to properly get $\frac{I_{eff}}{I_{gr}}$ as the moment of inertia is typically in the denominator of any elastic deflection equation.

To accurately plot the $\frac{I_{eff}}{I_{gr}}$ ratio versus the support roll angle as Mast had done, the cracking allowed and prevented cases had to be evaluated at the same tilt angle. However, once the girder had cracked, the same applied torque did not result in identical support roll angles for both the cracked and uncracked cases. To solve this problem linear interpolation between the data points was used to ensure that each support roll angle in one case was compared to an identical support roll angle in the other case. The steps in applied torque were sufficiently small that linear interpolation did not make a change in the qualitative results, but instead increased the number of data points included on the plots.

6.3.2. **Results**

Following this procedure, the Mast beam, ST girder, and 70th Avenue girder were inputted and run through Rollbuck 2022. The ST girder had temporary top flange prestressing strands in its original design. Two cases with and without temporary top strands were run on the ST girder. Mast's original curve (the above Equation (6 – 1)) is included as well. The results are shown in Figure 6.4.

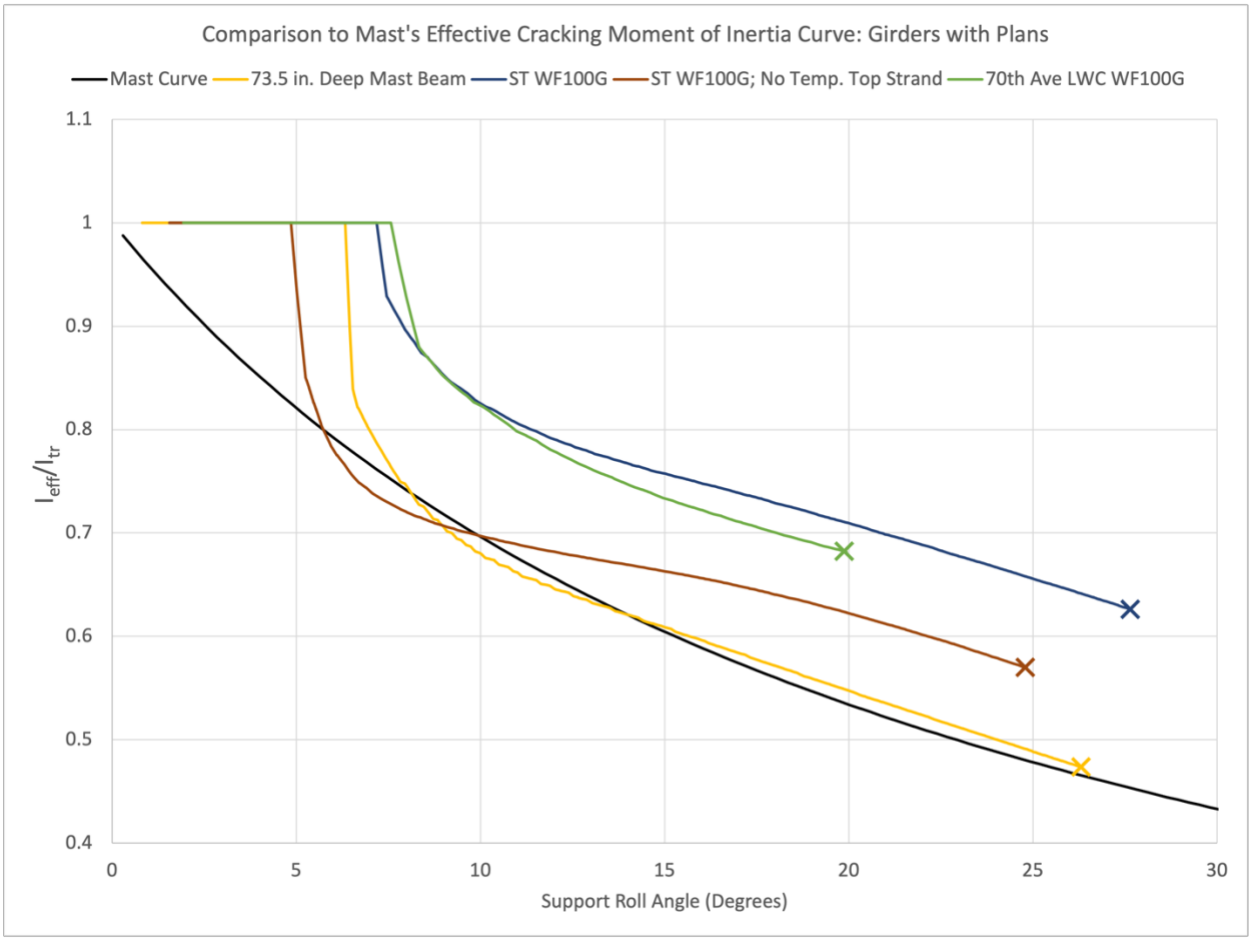

Figure 6.4: Comparison to Mast's Effective Cracking Moment of Inertia Equation for Girders with Structural Plans

Before cracking, each of the four girders has an effective moment of inertia equal to the transformed moment of inertia—represented as the plateau at 1.0 in the first part of the curves. Upon cracking, there is a rapid drop in stiffness that then gradually levels out until the final failure point, represented by the "X" at the end of each curve. Mast's curve is shown in black. Here the exact form of Equation (6 – 1) is depicted, whereas Mast began his depiction of that curve as a plateau at 1.0 that dropped down to the Equation (6 – 1) curve at the point of predicted cracking for a specific girder. Since multiple girders are presented on one plot and the exact cracking point of each girder was different, the exact equation form of Equation (6 – 1) is shown without the drop-off point.

The Mast beam is shown as the yellow curve. It closely follows Mast's lower bound curve. Mast (1993) showed a plot like Figure 6.4, with the results for several different girders. However, he did not label the girders, so it is not possible to compare the present results on a girder-for-girder basis The Mast beam curve calculated by Rollbuck 2022 closely follows one of the curves depicted there; it may or may not be his test girder. If indeed it is his girder, it serves to act as a further point of validation for Rollbuck 2022 in that it closely aligns with one of Mast's (albeit unlabeled) results.

The ST girder is a WF100G spanning 150 feet. It was designed to have three feet of overhangs during transportation and handling. Standard sweep tolerances of 1/8 of an inch per 10 feet of longitudinal length give a sweep of 1.875 inches (actual imperfection data was unknown.) The ST girder was analyzed using its 28-day strength properties of $f'c = 9\ ksi$ and a modulus of rupture of $f_r = 720\ psi$, determined from the AASHTO LRFD 2017 Sections 5.4.2.6 and 5.4.2.8

$$f_r = 0.24\lambda\sqrt{f'c}, \qquad (6-3)$$

where

$$0.75 \leq \lambda = 7.5\gamma_c \leq 1.0, \qquad (6-4)$$

and γ_c is the concrete density in kips per cubic foot and $f'c$ is the concrete strength in ksi (AASHTO, 2017). The ST girder was of normal-weight concrete with a density of 150 pounds per cubic foot. All prestressing strands were 0.6" diameter, 7-wire, 270 ksi, uncoated, low relaxation strands, that were initially jacked to 202.5 ksi. Rollbuck 2022 requires the jacking stress to be inputted and then it accounts for elastic shortening losses, but not the long-term losses due to creep and shrinkage. A lowered jacking stress must be inputted to account for those losses. That effective jacking stress accounting for long term losses was equal to approximately 179 ksi. There were 6 temporary top flange strands, 44 straight strands in the bottom flange, and

10 strands harped at 0.4L and 0.6L. The general strand layout for the WSDOT WF series is shown in Section 7.2.1. The bottommost rows of permissible straight strand locations were filled up first. The harped strand bundles were four inches from the bottom face of the girder between 0.4L and 0.6L.

This configuration is shown in Figure 6.4 as the dark blue curve. It cracks at approximately 7.5 degrees and then gradually drops off in stiffness until its approximate final failure point at roughly 27.5 degrees of support roll. Throughout its entire rollover, the Mast curve is a conservative lower bound on the effective stiffness of the ST girder at a given support roll angle.

While the Mast curve is conservative for the ST girder with temporary top strands, when temporary top strands are removed, the girder performs "worse" than the Mast curve for part of its rollover. Furthermore, when there are no temporary top strands present, the girder cracks much sooner at just under 5 degrees of support roll. The implications are twofold. The first is regarding validation of Rollbuck 2022. The girder is expected to crack in top flange tension on the "low" side of the girder as it rolls over. Removing the temporary top strands should exacerbate this issue—which it does. The cracks should then propagate more rapidly due to the relatively higher tensile stress in the top flange. This is reflected by the ST girder with no temporary top strands having a lower relative stiffness at a given roll angle than the ST girder with temporary top strands (indicating it has cracked more), and by the fact that it fails at a lower roll angle. The fact that Rollbuck 2022 predicts what would be expected from engineering principles provides further verification of the program. The second implication is that the industry practice of including temporary top strands is beneficial, effective, and makes the Mast curve conservative for at least this example of a modern-day girder. For all the girders shown in

Figure 6.4, cracking occurs in the midspan and not over the supports. Therefore, the temporary top strands achieve one of their design goals in that they prevent cracking from occurring in the top flange over the supports during lifting and handling due to the moment from the cantilevered overhangs.

The 70th Ave LWC bridge girder is shown in green in Figure 6.4. It spans 223 feet and was designed to have 27.5-foot-long overhangs during lifting. There were 10 such girders used in the 70th Ave bridge replacement project. The lateral sweep was typically about 2.85 inches in these girders. The LWC had density of 125 pounds per cubic foot. The girder was evaluated in Rollbuck in its state nearly immediately after the transfer of prestressing, when it would have been lifted out of the casting bed. Per its structural plans, it had at the time a concrete strength of approximately 8 ksi, $\lambda = 0.9375$, and $f_r = 636\,psi$. Each prestressing strand was inputted into Rollbuck as a jacking stress of 200 ksi, slightly reduced from 202.5 ksi to account for any long-term losses due to creep and/or shrinkage that may have occurred in the short term. There were 10 temporary top flange strands, 46 straight strands in the bottom flange, and 32 strands harped at 0.4L and 0.6L, all 0.6-inch diameter.

The long 70th Avenue girder performs quite similarly to the ST WF100G with temporary top strands and is conservatively lower bounded by Mast's equation. An insight that can be gleaned from these results is that there is "life after cracking." An industry concern ahead of this project was that modern-day long span girders susceptible to torsional deformations would have rapid deteriorations in stiffness and performance upon cracking and would pose safety risks. At least for the girders evaluated in Figure 6.4, this does not appear to be the case. While there is a drop off in stiffness upon cracking, it is neither precipitous nor debilitating—the girder continues to roll and have stiffness for quite some time before failure.

The comparisons between, and analyses of, these curves highlight the need for a systematic parametric study on the parameters affecting girder stability and cracking. While both the ST girder and the 70th Avenue girder appear qualitatively quite similar in Figure 6.4, they have drastically different designs, despite both being WF100G cross sections: the 70th Avenue girder is made of LWC, is nearly 75 feet longer than the ST girder, and has more temporary top strands, lower concrete strength, and bigger overhangs than the ST girder. Clearly, each of these parameters has unique effects on girder stability and performance upon cracking. Further, while one can draw the conclusion that there is "life after cracking" with the girders shown in Figure 6.4, it is not sound to reach that conclusion for all girders without exploring a wide range of design parameters, cross sections, and girder configurations.

7. Girder Cracking Parametric Study

The focus of this chapter is a parametric study which provides insights about the parameters that most affect girder cracking and lateral stability. It is difficult to know what exact parameter, or combination therein, makes each girder behave in its own unique way. To gain insights into the effects each specific design parameter has on the lateral stability behavior of cracked girders, the individual parameters must be methodically varied and the changes in performance tracked. To ensure the results are relevant to real-world scenarios, the parameters studied (i.e., the inputs such as span, girder depth, concrete type, etc.) are centered about a "Standard Configuration" which is representative of typical precast girders used in modern bridge construction. The results (i.e., the outputs) are thereafter presented using plots of the ratio of the cracked to uncracked moments of inertia (e.g., Figure 6.4).

The best way to glean insights into combinations of parameters that would most affect the design of a very long-span girder is to actually design and check the lateral stability and cracking behavior of a series of girders. This does not lend itself to a methodical parametric study approach, however, as it is difficult to predict how different design parameters will interact and which design cases will control the behavior. This chapter will focus on modifying individual parameters about basis of the Standard Configuration to see how they affect post-cracking behavior. Chapter 9 will examine trends and limitations in the designs of a series of long-span WF100G girders.

7.1. **The Standard Configuration**

The Standard Configuration introduced herein is not one specific girder, but rather, a set of parameter ratios consistent with industry standards across a range of spans. One of the advantages of using a standard configuration is that a unique girder does not need to be designed for every case that is studied. The Standard Configuration used here was developed by referencing the ST WF100G and 70th Avenue WF100G girders with plans described above in Section 6.3, and by studying typical layouts and design parameters for girders from industry design charts (Concrete Technology Corporation, 2009). The Standard Configuration links certain design parameters together in logical ways; modifying one characteristic—such as length—in turn changes another parameter—such as overhang length. Within the parametric study that follows, the parameters are varied about the standard configuration individually (i.e., partial derivatives) so that the importance of individual parameters and efficacy of certain design decisions may be evaluated. The parametric study was conducted on girders assumed to be in their lifting condition. The relationships and values used in the Standard Configuration will reflect this. To the extent possible, the parameters chosen for use are dimensionless ratios, such as span-to-depth or overhang ratio, etc. That choice allows generally applicable trends to be investigated without the need to investigate many different detailed designs.

The parameters considered in this work, their Standard Configuration value, and their ranges studied in the parametric study, are summarized in Table 7.1. The process for determining the Standard Configuration value is described below, while the ranges explored in the parametric study are discussed later.

Table 7.1 Design Parameters Considered in the Standard Configuration, Their Typical Value, and Range Explored in Parametric Study

Design Parameter	Standard Configuration Value	Range in Parametric Study
Concrete Modulus of Elasticity	$E_c = 120{,}000K_1 w_c^{2.0} {f_c'}^{0.33}$	$0.7E_c \; to \; 1.3E_c$
Concrete Shear Modulus	$G = 0.4E_c$	$G = 0.125E_c \; to \; LRB$
Concrete Density	$\gamma_c = 150 \; pcf$	$100 \; pcf \; to \; 160 \; pcf$
Prestressing Strand	$f_u = 270 \; ksi; E = 28500 \; ksi$	*Not Varied*
Reinforcing Steel[1]	$f_y = 65 \; ksi$, $f_u = 96 \; ksi$, *and* $E = 30000 \; ksi$	*Not Varied*
Span-to-Depth Ratio	*25*	*17.5 to 27.5*
Lateral Sweep	*1/8" per 10 ft. of Length*	*Not Varied*
Overhang Percentage[2]	$\alpha(\%) = 0.1415L - 19.22$	*7.5% to 17.5%*
Jacking Force-to-Gross Area Ratio[3]	*2.5 ksi*	*1.75 ksi to 3.25 ksi*
Initial Concrete Strength	$f_{ci}' = 8 \; ksi$	$0.7f_{ci}' \; to \; 1.3f_{ci}'$
Number of Straight vs. Harped Strands[4]	*2/3 Straight and 1/3 Harped*	*Ratio does not Change*
Number of Temporary Top Strands[5]	$N = 10 - \frac{12.33 - \alpha(\%)}{2.5825}$	$0.7N \; to \; 1.3N$

Notes: 1. *Six number five bars always uniformly distributed through top flange, two inches from top face.*

2. *Equation only applies for girders with length greater than 150 ft.*

3. *Number of Strands = Jacking Force-to-Gross Area ratio divided by prestressing force in one strand. Varied in the Linked Parameter Study Only.*

4*.Ratio does not change unless there are no more straight strand locations available. Then the remainder of strands are harped. Harped at 0.4L and 0.6L. Harped Strands are 6.625 inches from the bottom face.*

5. *Equation only applies for girders longer than 150 ft. Linear Interpolation between 4 and 6, 2 and 4, and 0 and 2 strands for girders 120 to 150, 90 to 120, and 60 to 90 feet long, respectively.*

The first set of parameters in the Standard Configuration are the assumed material properties and code equations used to calculate them. For the concrete modulus of elasticity, AASHTO LRFD-2017 Equation 5.4.2.4-1 was used:

$$E_c = 120{,}000 K_1 w_c^{2.0} {f_c'}^{0.33}, \qquad (7-1)$$

where w_c is the concrete density in kips per cubic foot, f_c' is the concrete strength in ksi, and K_1 is a correction factor related to aggregate properties (AASHTO, 2017). Consultation with Concrete Technology Corporation of Tacoma, WA revealed that K_1 is typically taken as 0.9 for concretes manufactured in the Pacific Northwest. The concrete tensile rupture strength used and the associated modification for LWC are described in Equations (6 – 3) and (6 – 4). In the Standard Configuration, concrete was assumed to be "normal weight," with a standard density of 150 pounds per cubic foot. The behavior of girders made of LWC were explored in the parametric study, shown in Section 7.4. To account for torsional deformations, the shear modulus was required. Per ACI 318-19 section R6.6.3.1, the shear modulus, *G,* was assumed to be forty percent of the modulus of elasticity of the concrete (ACI Committee 318, 2019).

The Popovics model was used to describe the stress-strain curve for the concrete (Popovics, 1970). The Menegotto-Pinto model was used to describe the stress-strain curve for the prestressing strands while the Raynor model was used for any reinforcing steel (Menegotto & Pinto, 1973) (Raynor, Lehman, & Stanton, 2002). The relevant properties of the prestressing strands and reinforcing steel are described above in Table 7.1.

A second set of parameters defined the geometry of the girder. For the Standard Configuration, the span-to-depth ratio was 25. This choice was based on the ratio commonly used by WSDOT for initial design of girders and implied in the span capability tables published by Concrete Technology Corporation (2009). That ratio also lies in the range of two girders for

which plans were available: the ST WF100G was 150 ft long—a span-to-depth ratio of 18—while the 70th Avenue WF100G was 223 ft long—a ratio of 26.76. Lateral sweeps were determined per PCI's tolerance of 1/8" per 10 feet of length.

Longer girders typically require longer overhangs to avoid instability problems during shipping and handling. As such, the overhang length was directly linked to the girder length in the Standard Configuration. This linkage was done via linear interpolation between the 3-foot-long overhangs of the ST WF100G and the 27.5-foot-long overhangs of the 70th Avenue WF100G. Equation (7 – 2) gives the overhang ratio of a girder (as a percentage) in the Standard Configuration as a function of its length:

$$\alpha(\%) = 0.1415L - 19.22, \qquad (7-2)$$

where L is in feet. Note that the ratio, and not just the overhang length itself, increases with girder length, reflecting the major role played by overhangs in improving stability. For all the girders in the WSDOT WF series between the WF42G and the WF100G, with length determined per the Standard Configuration, Equation (7 – 2) approximated the overhang lengths given by the CTC WSDOT WF Series girder span capability design chart (Concrete Technology Corporation, 2009). A lower bound overhang length of 3 ft was used, to reflect the practical difficulties of placing the lifting loops closer to the girder end. Thus, Equation (7 – 2) controls the overhang length only for girders over 150 feet long. For a theoretical girder that is approximately 312 feet long, the overhang would be nearly 25 percent of the total length. That extreme of an overhang length would be damaging to stability (Galik, Stanton, & Wiebe, 2022). Equation (7 – 2) is most applicable for girders of a reasonable span length that could be feasibly designed using current practices. For both the shortest and longest girders, strict adherence to Equation (7 – 2) would likely give impractical results.

The amount of prestressing in the Standard Configuration was chosen so that the ratio of jacking force to gross concrete area, $\frac{F_{pj}}{A_{gr}}$, was constant, at 2.5 ksi. This choice was made after reviewing the CTC WSDOT span capability design charts (Concrete Technology Corporation, 2009). The underlying logic is that, for highway bridges, the shallowest girder possible is usually chosen, because it leads to overall economy. Maximizing the span-to-depth ratio implies using the highest possible level of prestress, but that is limited by the initial concrete strength, f'_{ci}, economically available in the 12 – 16 hours usually available for curing, typically in the range of 7 – 8.5 ksi per the span capability design charts (Concrete Technology Corporation, 2009). Since the bottom concrete stress at release is slightly less than double the average stress, and is limited to $0.6f'_{ci}$, and the strand stress at release is 90% to 95% of the jacking stress, these conditions lead approximately to the concrete stress of $\frac{F_{pj}}{A_{gr}} \approx 2.5\ ksi$. For Standard Configuration designed girders, this ratio approximately matched the information available in the CTC WSDOT span capability design charts (Concrete Technology Corporation, 2009). The jacking force was selected, rather than the initial release force, both because it avoids the need to compute the elastic shortening loss for each individual case, and because the jacking stress is needed for input to Rollbuck 2022.

Each girder in the Standard Configuration was assumed to be reinforced with 0.6-inch diameter, 270 ksi, 7-wire strands. They would be jacked to $0.75f_{pu}$, or 202.5 ksi. Rollbuck 2022 requires the jacking stresses to be inputted, as it calculates elastic shortening losses internally, but it does not account for long-term losses. To account for any long-term losses due to creep, shrinkage, or some other loss, that may have occurred in the hours or days after the release of prestressing when initial lifting would occur, a jacking stress of 200 ksi was used in the Standard Configuration. This led to 43.4 kips per strand of prestressing force.

The number of strands was determined by dividing the F_{pj} required to reach the 2.5 ksi ratio by 43.4 kips per strand. This number of strands only includes the straight and harped strands in the bottom at midspan, because they are determined by the service conditions. The number of temporary top strands, which is controlled by the handling and transportation conditions, and particularly the overhang length, was determined by a separate calculation. Of the strands required to reach 2.5 ksi average prestressing, 2/3 of them were straight strands and 1/3 of them were harped strands. If the bottom flange ran out of space for the straight strands (the maximum is 46 in the WSDOT girder series), the remainder were included in harped strand bundles instead. This ratio was strictly maintained, even if it resulted in non-integer numbers of strands. While a realistic girder design would only have integer numbers of strands, the use of a consistent ratio in the parametric study was deemed more important than a slightly unrealistic number of prestressing strands. Non-integer strand amounts were used for both the bottom strands and the temporary top strands. The typical strand arrangement for different girder series will be shown in the proceeding sections when each considered girder series is introduced. At the ends of the girders, the center of gravity of the harped strands varied based on the number of strands, but, at midspan, all harped strands were assumed to be bundled 6.625 inches from the bottom face and harped at 0.4L and 0.6L.

The number of temporary top strands was directly linked to the length of the overhangs (and thus to the length of the girder and the depth of the cross section.) Longer overhangs require more temporary top strand to resist the cantilever gravity moments. The equation for the number of top strands, *N*, is given by Equation (7 – 3):

$$N = 10 - \frac{12.33 - \alpha(\%)}{2.5825}. \qquad (7-3)$$

This equation was determined by linear interpolation between the ST WF100G with two percent overhangs and six temporary top strands and the 70th Avenue WF100G with 12.33% overhangs and 10 temporary top strands. This rule generally matched the number of temporary top strands for a given girder in the Standard Configuration with the number of strands matching those of a girder indicated by CTC's span capability design chart for the WSDOT WF series (Concrete Technology Corporation, 2009). Equation (7 – 3) only applies for girders 150 ft. or longer. Because girders less than 150 ft. long consistently have three-foot-long overhangs in the Standard Configuration, their overhang percentage increases as the girders get shorter. If Equation (7 – 3) were used, these short girders would have more than six temporary top strands, which is not consistent with design practices. Therefore, to better match CTC's span capability design chart girders between 120 and 150 ft. long, 90 and 120 ft. long, and 60 and 90 ft. long had their number of temporary top strands determined by linear interpolation between six, four, and two strands, respectively (Concrete Technology Corporation, 2009). In this way, the shortest girders would have the fewest temporary top strands. Further, since the harped strands are harped at 0.4L and 0.6L, for girders with shorter overhangs, the harped strands are near the top of the cross section at the support points. In this way, the harped strands effectively act as temporary top strands, making the need for specifically designed temporary top strands less urgent. For girders with very long overhangs, the harped strands would contribute very little, if at all, to introducing compression in the top flange at the supports and counteracting the gravity moments from the cantilevered overhangs.

The temporary top strands were spaced consistently across the top flange of the girder throughout the parametric study. The arrangement pattern matched that of the 70th Avenue WF100G girder. The row closest to the top flange had strands beginning on either side 6.5 inches

from the centerline of the cross section, then placed every four inches, space allowing. If a second row of strands was required, it was placed two inches below the first (which itself was two inches from the top face), but the strands were laterally offset 1.5 inches inwards. They were then placed every four inches, if required, space allowing.

For each girder designed using the Standard Configuration, six number five reinforcing bars were uniformly spaced in the top flange. While allowable stresses were checked for Standard Configuration girders, ultimate strength was assumed to be adequate and not checked. Lifting and transportation occur before service loads are applied to the girder.

7.2. **The Standard Configuration Applied to Different Girder Series**

7.2.1. **WSDOT WF Girder Series**

The first girder series investigated under the Standard Configuration was the WSDOT WF girder series. This includes eight girders ranging between the shortest, the WF42G and the longest, the WF100G. The typical permissible location of strands for the WSDOT WF series is shown in Figure 7.1

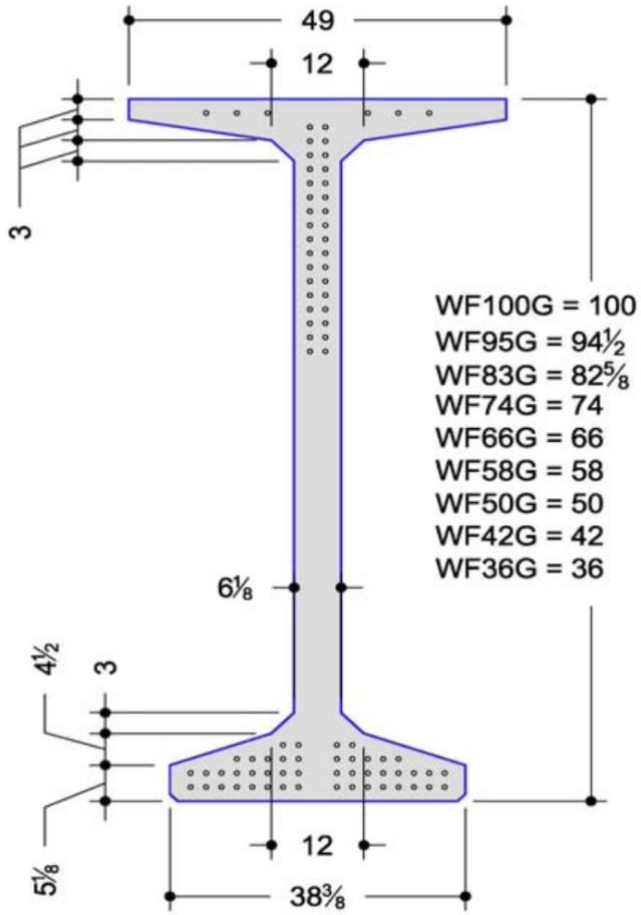

Figure 7.1 Typical Strand Locations and Dimensions of WSDOT WF Girder Series. Accessed from CTC Girder Span Capability Design Chart (Concrete Technology Corporation, 2009).

Straight strands were assumed to always fill the bottommost rows first. The harped strands were uniformly spaced beginning four inches from the top at the ends of the girder. If more than eight temporary top strands were required, a second row of temporary top prestressing strands would be started, in the pattern described at the end of Section 7.1. Using the allowable stress limits established by AASHTO for after the transfer of prestressing, all girders in the WSDOT WF series comfortably passed the stress checks (AASHTO, 2017). The Standard Configuration was initially checked against the compressive stress limit of $0.6f'_{ci}$ given by AASHTO (2017); however, the girder design example presented by WSDOT, described in Chapter 8, revealed that

WSDOT uses an allowable stress limit of $0.65f'_{ci}$ in the upright configuration, and $0.7f'_{ci}$ when tilted (Brice, 2023). So, while the Standard Configuration did pass stress checks using $0.6f'_{ci}$ as a limit, in practice there would have been even more of a margin. As a result, a greater amount of prestress could likely have been used, or a lower concrete strength. The most critical stress location was the initial compressive stress at the bottom of the girder at the harping point. The rest of the girder was always in compression before any rolling began. Stress checks in a girder's final equilibrium configuration will be explored more in the design examples of Chapter 8. The results for the WSDOT WF Series, in the format allowing for comparison to Equation (6 – 1), are shown in Figure 7.2.

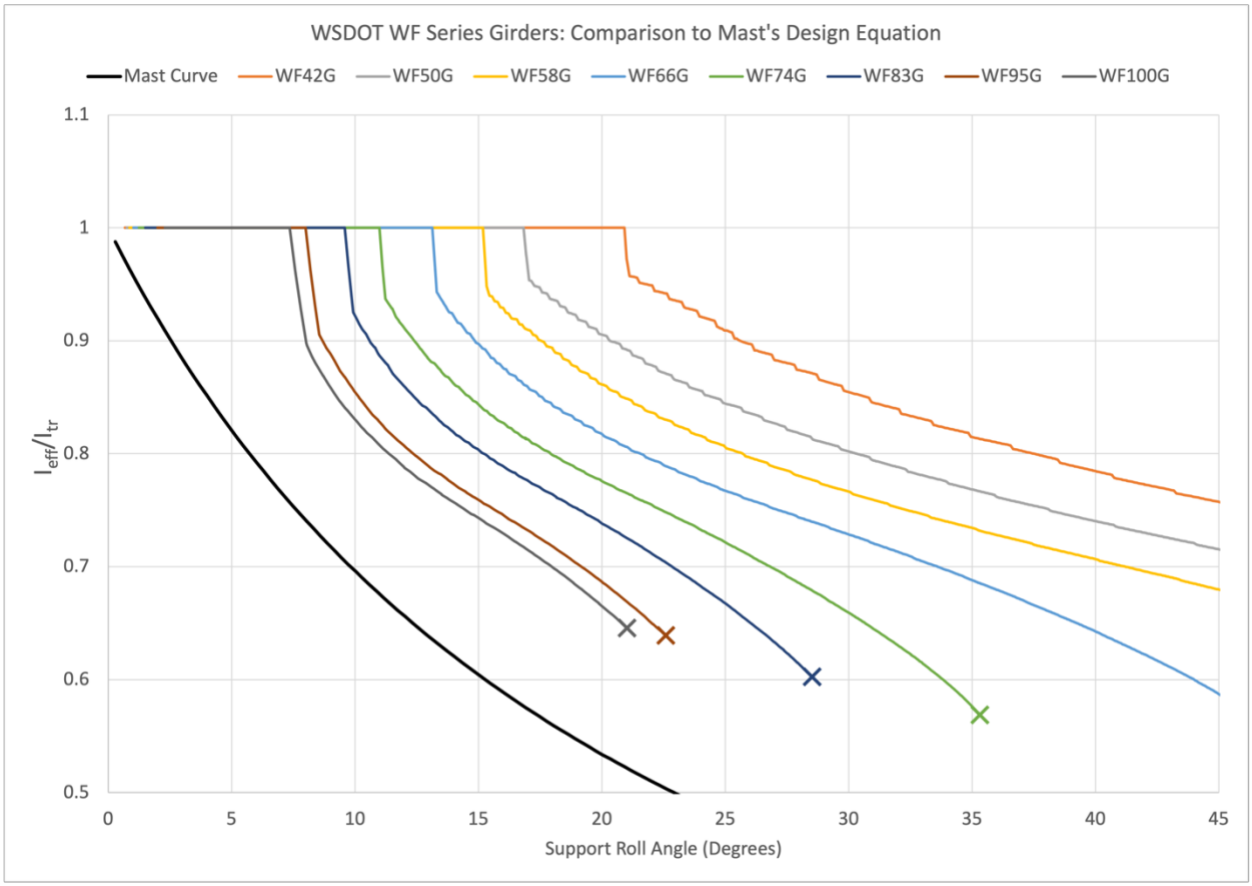

Figure 7.2 WSDOT WF Series Girders in the Standard Configuration Compared to Mast's Design Equation for the Effective Cracked Moment of Inertia

All the WSDOT girders run in the Standard Configuration are conservatively lower bounded by Mast's equation for I_{eff}. This indicates that Mast's equation could safely be used for evaluating the lateral stability of the WSDOT WF Series girders, though there may be some opportunity to update the equation to avoid an overly conservative result, especially with the smaller girders. The failure point, shown by an "X" at the end of each curve, denotes the point where Rollbuck 2022 failed to find an equilibrium configuration, which is likely indicative of collapse, or at the very least, a configuration where small roll angle changes lead to large changes in stability (undesirable both computationally and in practice). The WF74G, WF83G, WF95G, and WF100G all fail within the plot limits of 45 degrees or less. All the shorter girders did not fail until beyond 45 degrees—a regime of roll angles that would not realistically be allowed in design.

The trends in Figure 7.2 are clear: the shorter the girder (in depth and hence length) the better it performs in terms of cracking onset and ultimate failure point. The rate of decay of stiffness as the girder cracks and rolls is relatively consistent throughout the series. Additionally, each of the girders evaluated has a cracking mechanism controlled by top tension cracking at the midspan. In the WF100G, cracking occurs at a relatively smooth and constant rate as the girder rolls over. In the WF42G and WF50G, part of the girder will crack and then it will roll over more before cracking again—leading to the step-like appearance of the curve as the girders gradually roll over.

7.2.2. **AASHTO I-Beam Series**

The second girder series analyzed was the AASHTO I-Beam Series, accessed from the referenced PCI webpage of beam sections and properties (Precast/Prestressed Concrete Institute, 2023). Only the Type 3 through Type 6 girders were examined, as the 28- and 36-inch-deep Type 1 and 2 girders, respectively, were deemed too short to have significant lateral stability issues. The cross sections analyzed, and permissible strand locations are shown in Figure 7.3.

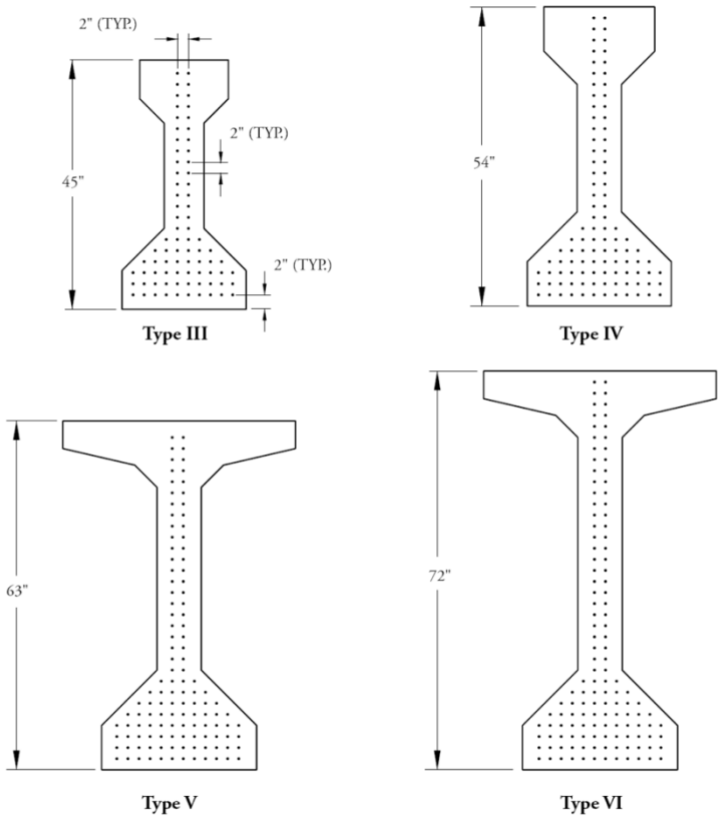

Figure 7.3 AASHTO I-Beam Cross Sections and Permissible Strand Locations. Accessed from Precast/Prestressed Concrete Institute (2023)

Prestressing strand locations were determined in the same manner as for the WSDOT WF Series—the only difference being that for the AASHTO I-Beams, the harped strands begin two inches from the top face instead of four inches for the WSDOT WF girders. When designed using the Standard Configuration, all the examined AASHTO I-Beams passed the AASHTO

allowable stress limits with the most critical location again being bottom compression at the harping point (AASHTO, 2017). The Standard Configuration results for the AASHTO I-Beams are shown in Figure 7.4.

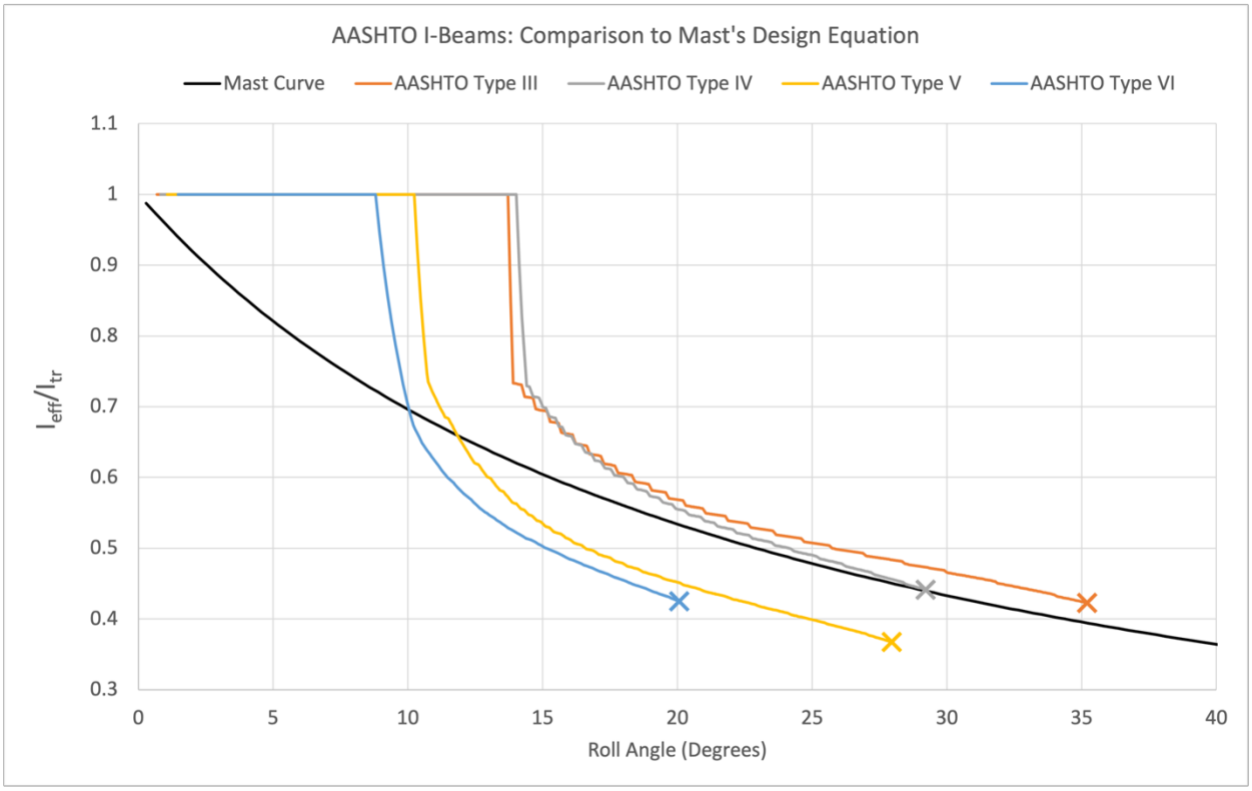

Figure 7.4 AASHTO I-Beams in the Standard Configuration Compared to Mast's Design Equation for the Effective Cracked Moment of Inertia

Interestingly, only the Type 3 and Type 4 girders are conservatively lower bounded by Mast's curve, and only barely, while the deeper Type 5 and Type 6 girders nearly immediately drop below Mast's curve at the onset of cracking. Therefore, AASHTO I-Beams exhibit a more brittle behavior with regards to cracking and lateral stability than the WSDOT WF Series girders do when both are designed according to the Standard Configuration. The curves appear to be broken up into two separate groups. This is because the Type 3 and Type 4 girders are of similar cross section while the Type 5 and Type 6 girders are less stocky. Just as with the WSDOT WF girders, the shorter girders perform better than the deeper and longer girders in terms of cracking

and ultimate failure point. All four of the AASHTO I-Beams plotted above appear to have similar slopes to the Mast design equation curve. This suggests that the Mast equation could perhaps be empirically adjusted to lower bound the AASHTO I-Beam girders.

The AASHTO I-Beam girder series was developed to provide a national design standard from which producers could easily manufacture girders using a standard set of forms. Spans were typically shorter in this era, and thus long-span lateral stability issues were not considered as much. As a result, the narrow but thick top flange was not a concern. However, in long-span applications, the girder cracks in the top flange at midspan largely due to weak-axis bending. The smaller top flange leads to a lower cracking moment/angle, and then an ultimately weaker section as the cracks propagate, both through the depth of the section and along the length of the girder. The Type 5 and Type 6 girders have wider top flanges. While they still exhibit brittle behavior and drop below Mast's curve, the drop is less abrupt and slightly more gradual than that of the Type 3 and Type 4 girders. Further, the webs and bottom flanges are quite thick in all the AASHTO I-Beams—the web thickness partially to facilitate concrete placement due to a lack of superplasticizers. In the context of top flange cracking in a lateral instability scenario, this extra thickness does little for the strength of the section, but does contribute to the self-weight bending, leading to more rapid cracking. All these factors may possibly contribute to the more brittle behavior seen here with the AASHTO I-Beams than in the relatively ductile WSDOT WF girder series.

7.2.3. **AASHTO-PCI Bulb Tee Beam Series**

The third girder series evaluated was the AASHTO-PCI Bulb Tee Beam Series, accessed from the PCI webpage on beam sections and properties (Precast/Prestressed Concrete Institute, 2023). All three of the listed Bulb Tees were analyzed: the BT-54, BT-63, and BT-72. Like the WSDOT WF Series, the top and bottom flange of the AASHTO-PCI Beams are the same size for each girder in the series with only the depth of the web changing. This is contrasted with the AASHTO beams which all had unique cross sections. The AASHTO-PCI Beams are quite similar in cross section to the AASHTO Type 5 and Type 6 girders, but they have less deep top and bottom flanges that more rapidly transition to the web thickness. The cross sections analyzed, and permissible strand locations (excluding temporary top strands,) are shown in Figure 7.5

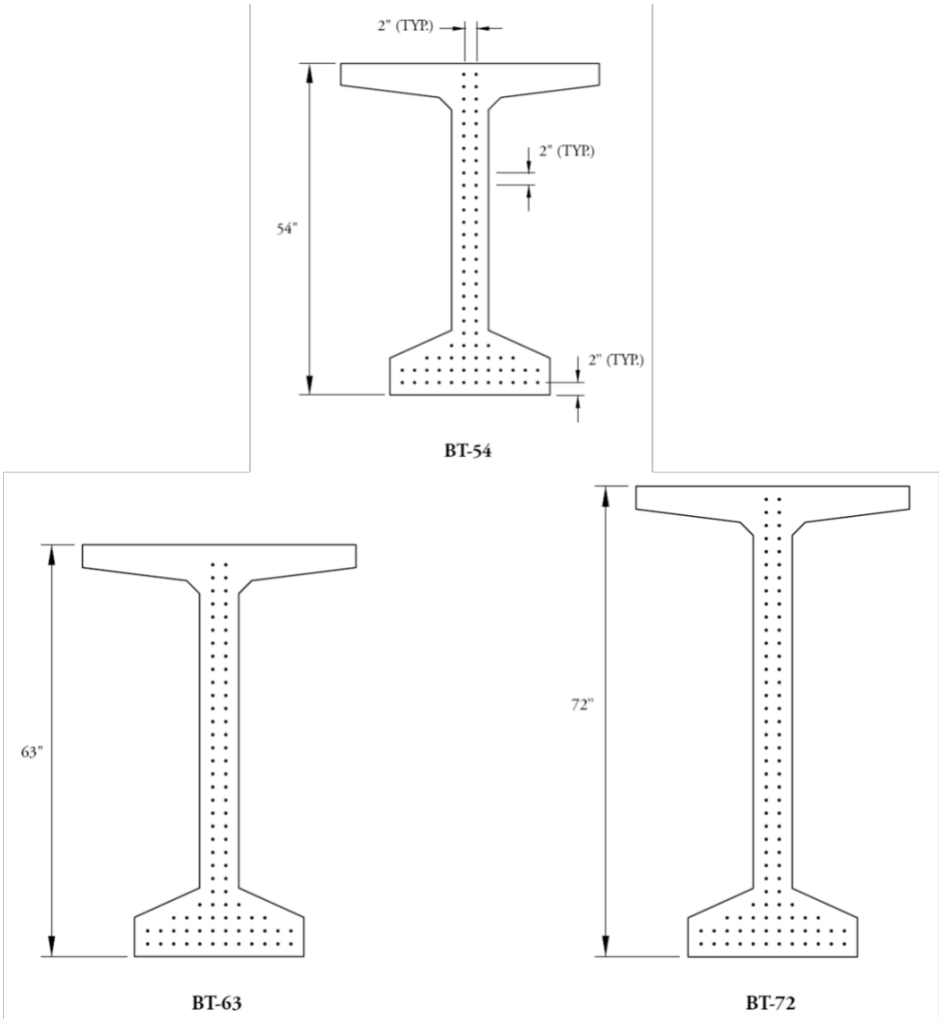

Figure 7.5 AASHTO-PCI Bulb Tee Beam Cross Sections and Permissible Strand Locations. Accessed from Prestressed/Precast Concrete Institute (2023)

All the AASHTO-PCI Bulb Tee Beams that were investigated passed the allowable stress limits. The most critical region was once again bottom compression at the harping point. The results from the AASHTO-PCI Beams are shown in Figure 7.6.

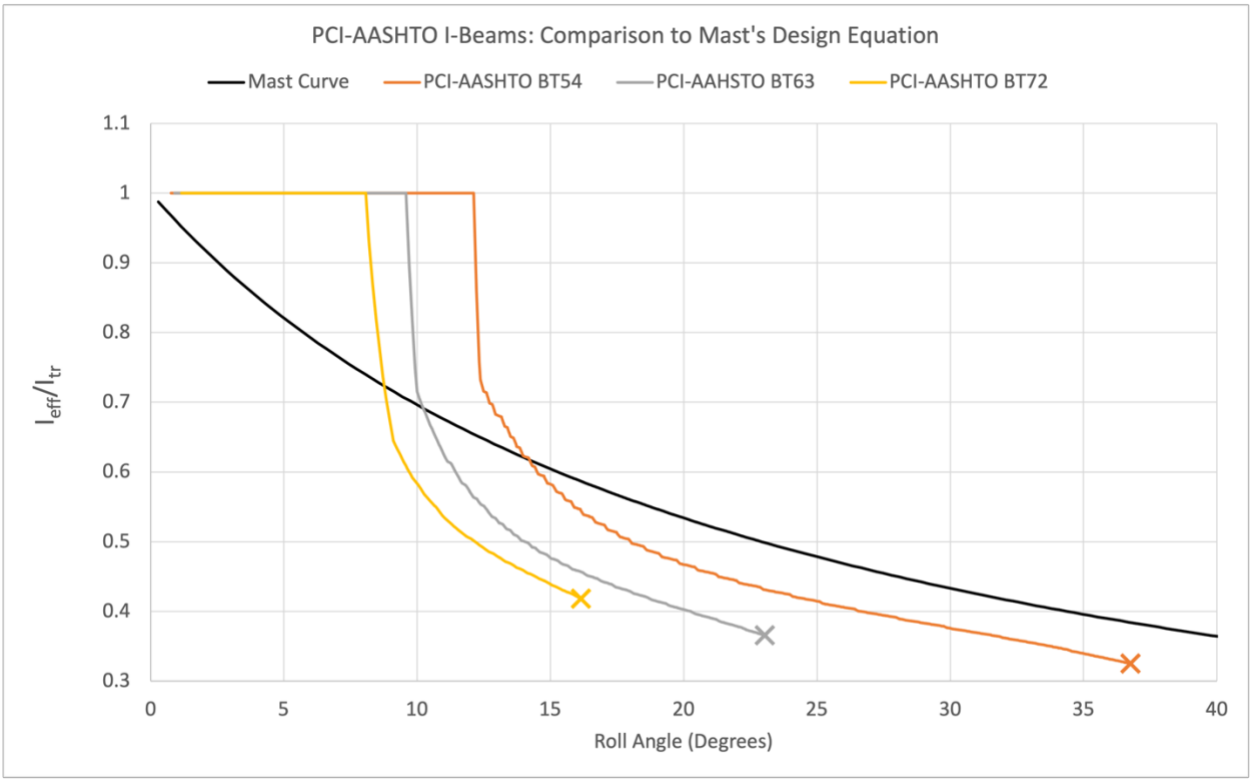

Figure 7.6 AASHTO-PCI Bulb Tee Beams in the Standard Configuration Compared to Mast's Design Equation for the Effective Cracked Moment of Inertia

Interestingly, none of the AASHTO-PCI Bulb Tee Beams are conservatively lower bounded by Mast's design equation for the effective cracked moment of inertia. All three of the girders appear to have similar slope to Mast's curve once they have cracked, but the initial drop in stiffness upon cracking immediately drops the results below Mast's curve. This would suggest that cracking should be prevented for these girders as Mast's curve is not conservative for any of them. Mast's curve could perhaps be empirically modified to act as a lower bound for the results plotted here if it was desired to still be used.

7.2.4. **PCI Deck Bulb Tees**

The final girders analyzed were the PCI Deck Bulb Tees, listed on the PCI webpage of beam sections and properties (Precast/Prestressed Concrete Institute, 2023). There were three

depths of Deck Bulb Tee listed there: 35-, 53-, and 65-inch-deep cross sections. Additionally, there were three top flange widths listed on the web page. The middle value of a 72-inch-wide top flange was selected. The 48-inch-wide option would lead to a top flange less wide than that of the WSDOT WF Series girders. Only the 53- and 65-inch-deep cross sections were analyzed. The only change between those two cross sections was the depth of the web. The cross section and permissible strand locations of the 53-inch-deep Deck Bulb Tee is shown in Figure 7.7.

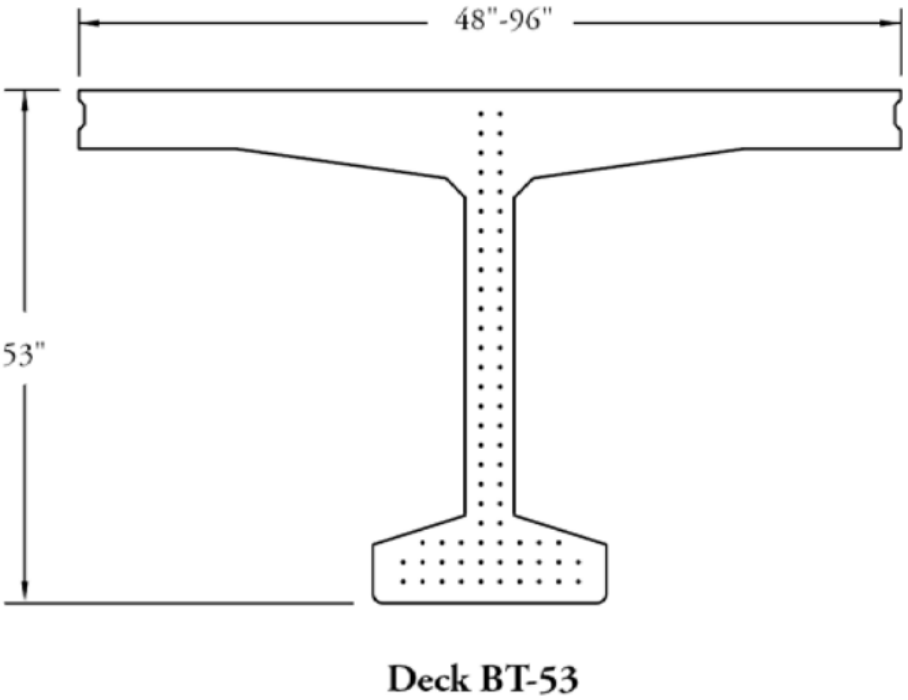

Figure 7.7 PCI Deck Bulb Tee Cross Section and Permissible Strand Locations. Accessed from (Precast/Prestressed Concrete Institute, 2023).

There was not enough space in the bottom flange for all the straight strands required per the Standard Configuration. It was assumed that the bottom flange could hold 24 straight strands: all the strand locations outside of the web (if the "web" extended down through the bottom flange), except for in the bottom row which used all 10 strand locations for straight strands. The other strand locations in the "web" of the bottom flange were not used to leave room for the

harped strands. Once all 24 straight strand locations were used, the remaining bottom strands were assigned as harped strands.

The cross section of the Deck Bulb Tees is unlike that of the other girders explored in the Standard Configuration. Because of the very wide top flange, they have large cross-sectional areas. As a result, they had many bottom strands assigned per the Standard Configuration; however, the bottom flange is relatively small compared to many of the other girder series. As such, both Deck Bulb Tees failed the initial compressive stress limit at the bottom of the girder at the harping point and midspan. This is not necessarily a failing of the Standard Configuration, which worked well for all the other girder series, but is indicative of the unique nature of Deck Bulb Tee girders. Therefore, two curves for each Deck Bulb Tee girder are shown in Figure 7.8. One explicitly uses the Standard Configuration while the other reduces the number of harped strands until the girder passes the initial compressive stress check ($0.6f'_{ci}$).

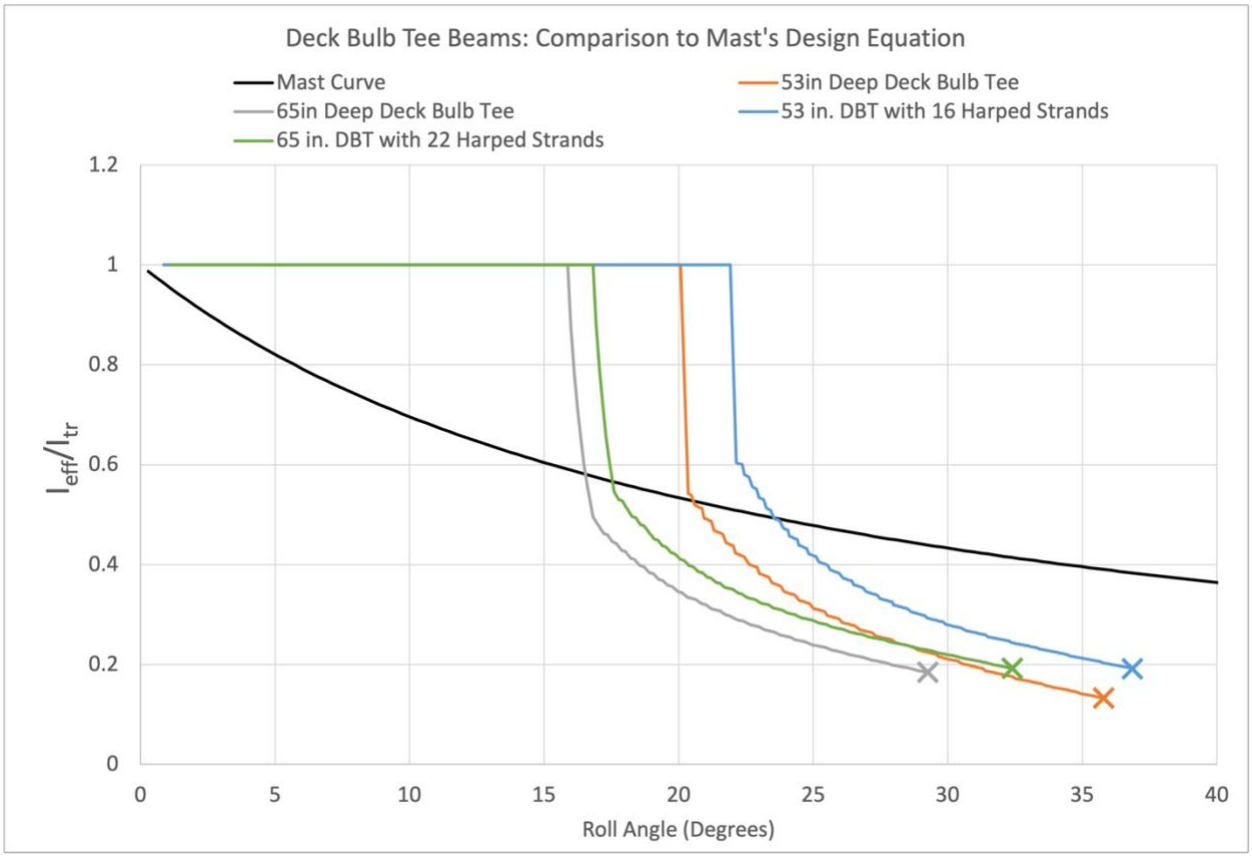

Figure 7.8 PCI Deck Bulb Tee Beams in the Standard Configuration Compared to Mast's Design Equation for the Effective Cracked Moment of Inertia

None of the Deck Bulb Tees studied, even those with reduced harped strand amounts, are conservatively lower bounded by Mast's design equation curve. They do not crack until subjected to large roll angles, presumably a function of the very wide top flange, but upon cracking, their effective stiffness immediately drops below Mast's curve. The stiffness degradation after cracking also appears to be more severe than that suggested by Mast's curve. It would seem that care should be taken to avoid cracking in the Deck Bulb Tee girders.

Reducing the number of harped strands improves the performance of both the 53- and 65-inch-deep Deck Bulb Tees. This makes sense as the controlling cracking mechanism is tension in the "low-side" corner of the top flange as the girder rolls over and bends in the weak-axis direction. Reducing the amount of prestressing increases the compressive stress in the top flange

in the upright configuration. However, even lowering the number of harped strands does not make the girders conservatively lower bounded by Mast's equation, nor does it make a large difference in post-cracking performance. There are clearly other features of the Deck Bulb Tee cross section that make it have a more brittle behavior compared to, for example, the WSDOT WF girder series.

7.3. **Takeaways from the Standard Configuration Evaluations**

Only the complete WSDOT WF Girder Series and some of the AASHTO I-Beams were conservatively lower bounded by Mast's design curve on the effective cracked moment of inertia. Even the AASHTO I-Beams that stayed "above" Mast's curve only just did. The WSDOT girders could continue to use Mast's equation in design, but the other girder series would either need to have cracking prevented or use a modified Mast equation.

While it is interesting to see the results for each girder series that was analyzed, and the results are more generalized than the girders with plans that were evaluated in Chapter 6, the analysis of the different girder series in the Standard Configuration only reveals so much about the parameters that most influence lateral stability and cracking. For example, the Deck Bulb Tee girders perform better with less prestressing, but it is unclear what aspect of that cross section causes their relatively brittle behavior. A parametric study that varies individual design parameters is necessary to best understand which choices in design will most impact the lateral stability and cracking behavior of long span prestressed concrete girders.

The parametric study is described in the following sections. The ultimate purpose of establishing the Standard Configuration was to have a reference design around which the parametric study could be centered. Now that it is known that the Standard Configuration passes all stress checks (except for in the unique case of the PCI Deck Bulb Tees,) and it is known how

each girder performs relative to Mast's curve, it can be used in the parametric study. Varying all the design parameters for each girder explored would create an intractable amount of information. Lateral stability is mostly a concern for long and deep girders that are most susceptible to torsional deformations. Therefore, the WSDOT WF100G will be evaluated in the parametric study as it is the deepest, and thus longest, girder available. The trends in the response will show how each parameter affects the performance of the WF100G. Then, a designer could take those trends into account to best optimize the parameters of their design in terms of lateral stability in the event of cracking.

7.4. **Parametric Study Results**

The parametric study seeks to understand trends in how modifying individual design parameter affects the response of a girder in terms of cracking, effective stiffness as it cracks, and final failure point. Only one parameter will be changed at a time, with the only linkages between parameters being changes in associated material properties because of code equations. For example, if one parameter increases or decreases the concrete strength, the tensile rupture strength, modulus of elasticity, and thus shear modulus will all change correspondingly. This best encapsulates the actual effect of varying that specific material property parameter.

7.4.1. **Modifying Shear Modulus, *G***

The first parameter examined was a variation in the shear modulus, *G*. One of the primary goals of this work is to investigate the way in which torsional flexibility affects the Lateral Roll Buckling mechanism in long span prestressed concrete girders. By varying the shear modulus, one sees how a less torsionally stiff girder would perform relative to a very torsionally stiff girder, especially once flexural cracking occurs. Furthermore, the torsional stiffness and

variation in *G* is of interest because the behavior of prestressed concrete under torsional shear cracking is relatively unknown. Lima and El Debs (2005) suggested that flexural cracking reduced the torsional stiffness by approximately 20%, but there work was for reinforced concrete. Rollbuck 2022 captures the effects of flexural cracking, but it does not reduce *G* or the polar moment of inertia, *J*, because of shear/torsional cracking, which it does not track. To simulate this theoretical degradation in torsional stiffness, *G* is decreased as a parameter. The results for the first parameter, *G,* are shown in Figure 7.9.

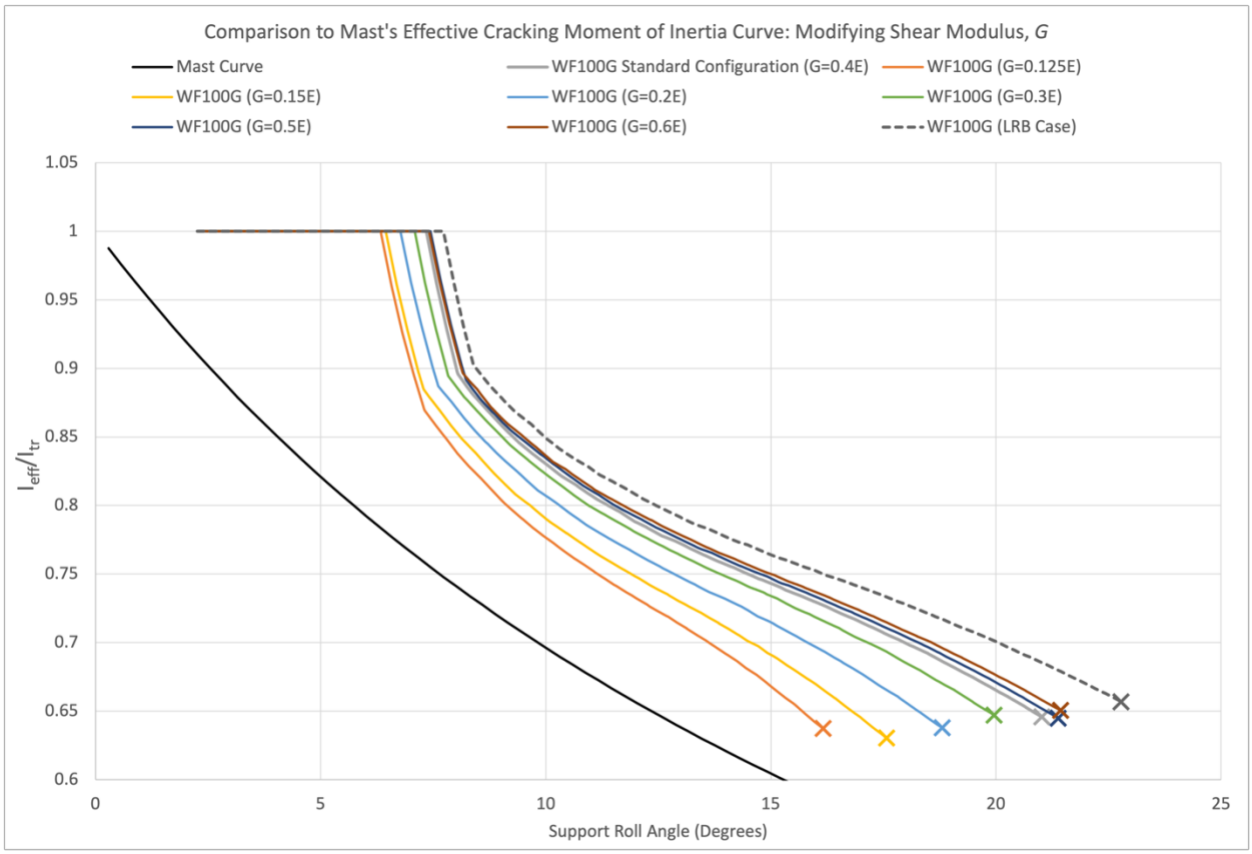

Figure 7.9 Independently Modifying the Shear Modulus, G

The Standard Configuration WF100G is shown in grey (and always will be in grey throughout the parametric study.) The LRB case (dashed curve) corresponds to $G = \infty$, and therefore provides an upper bound to the other curves. There is a clear degradation in performance as *G* is decreased, as both the cracking onset angle and the roll angle at final failure

correspondingly drop. Individually, however, these curves likely do not represent a realistic scenario. Rather, one should imagine "travelling" initially along the original grey Standard Configuration curve. As torsional cracking occurs one would "jump" down the curves in the direction of decreasing *G*, thus simulating what the effective lateral stiffness would be at a certain roll angle with both flexural and torsional cracks accounted for. The exact location/roll angle at which torsional cracking would occur is uncertain. While the magnitude of roll angle at the final failure point (very roughly) surrounds 20 degrees, the twist angle (difference between midspan and support roll) is only on the magnitude of a couple of degrees. Thus, the "jumps" between curves as torsional cracking occurs may not take place at the onset of flexural cracking, but rather somewhere else along the descending part of the curve.

The shear modulus, *G*, was also increased to capture the effects of a girder that is torsionally stiffer than expected. The positive effects of increasing *G* are relatively slight compared to the negative effects of decreasing *G*. This highlights the detrimental effect that including torsional flexibility has on girder stability. Furthermore, the true "curve-hopping" behavior noted above may result in a steeper effective stiffness degradation than what appears in Figure 7.9.

Some of the questions surrounding the behavior of prestressed concrete girders under torsion and torsional shear cracking may have the opportunity to be answered in the next year. The researchers have the opportunity to test the ST WF100G girders described above in Chapter 6. One of the tests will involve twisting one of the girders in pure torsion. From those tests, it is hoped to determine the twist angle at which torsional cracking initiates, and then to study how torsional stiffness drops as applied torque and twist angle increase.

7.4.2. **Modifying Concrete Modulus of Elasticity**

The next individual parameter explored in the parametric study was the concrete modulus of elasticity, E_c. One potential interest is how LWC lowers E_c , which in turn increases the lateral deflections, and then how that change in turn affects the lateral stability and performance of the girder upon cracking. By varying E_c individually here, the parametric study will offer insights into how, if at all, changing E_c affects performance and whether E_c is responsible for changes in performance due to using LWC. Note that the use of LWC provides an advantage due to the lower load, but a drawback because of the lower stiffness. It is not immediately clear which effect will dominate, although Galik, et al (2022) found that the overall effect was slightly beneficial. This will be explored in Section 7.4.4 which varies the concrete density as a design parameter. The E_c value determined by AASHTO (2017) Equation 5.4.2.4-1 will be empirically scaled up and down. Directly changing E_c also changes the shear modulus, *G*. No other material property parameters are directly affected by changing E_c. The results are shown in Figure 7.10.

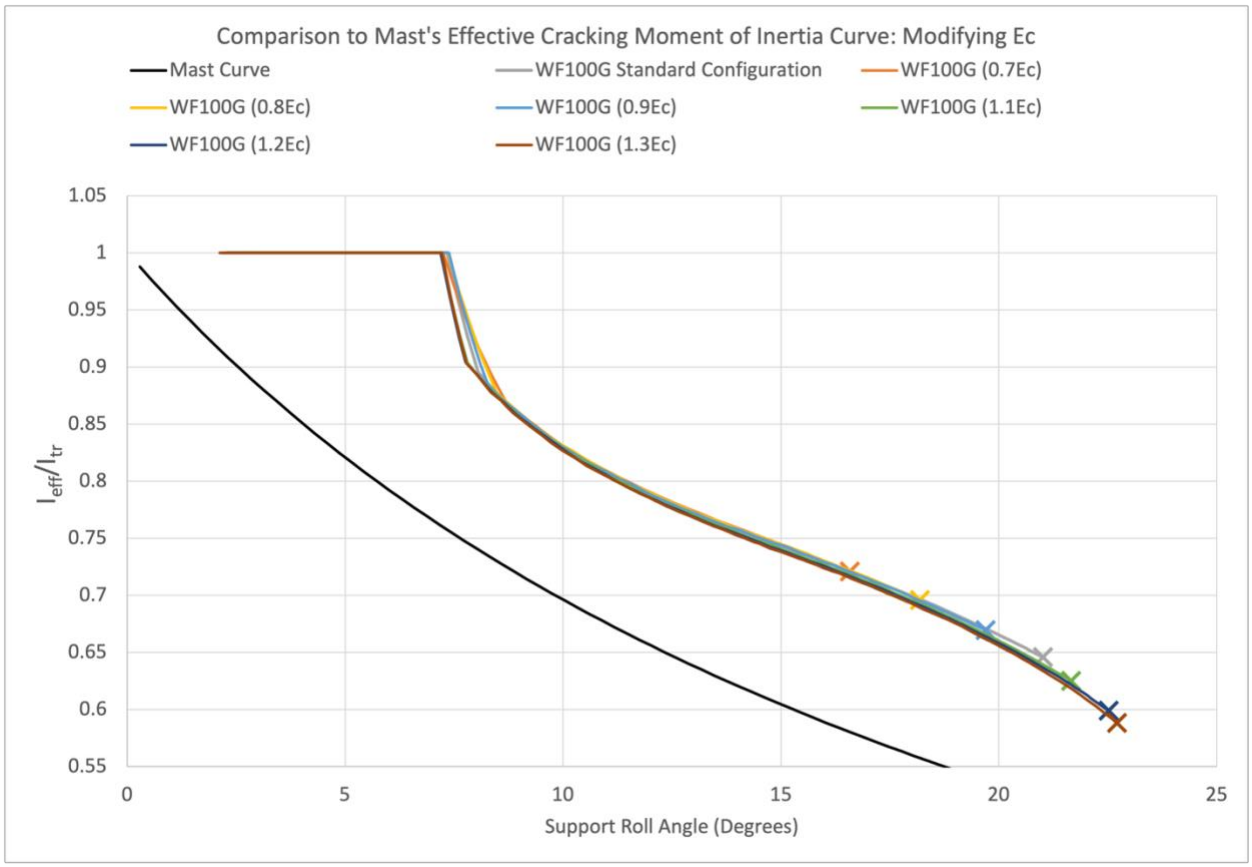

Figure 7.10 Independently Modifying the Concrete Modulus of Elasticity, E_c

Unlike the previous parameters' variation in G, modifying E_c does not change the cracking onset angle or the rate of degradation in lateral stiffness as cracking progresses. Rather, modifications to E_c simply change the location on the curve that the girder finally fails. Girders with the highest E_c failed at the greatest roll angle while the lowest E_c girders failed the soonest, i.e., at the lowest roll angle. Aside from this final failure point, which a girder would not allowed to be designed to achieve in practice, there does not appear to be a significant difference in performance as a result of E_c. This would seem to suggest that any differences in behavior for girders made of LWC is a function not of E_c, but of their varied rupture strength or of their lighter self-weight combined with identical section moduli. Another possible explanation for the behavior seen in Figure 7.10 depends on the steel in the girder cross-sections. After cracking, the effective stiffness of the section depends more on the steel than before. Since the steel

configuration did not change along with the concrete modulus of elasticity, this could go some way towards explaining the similar rate of stiffness degradation.

7.4.3. **Modifying Initial Concrete Strength**

The next parameter was the initial concrete strength, f'_{ci}. The concrete strength was assumed to be 8.0 ksi in the Standard Configuration. This generally corresponds with the upper range of initial strength values in the CTC WSDOT WF Girder Span Capability design chart as well as those designated for the 70th Ave WF100G, which is of similar layout to the Standard Configuration girder (Concrete Technology Corporation, 2009). Modifying f'_{ci} changes the concrete modulus of elasticity which in turn changes the shear modulus. Additionally, any changes to f'_{ci} will also correspondingly increase or decrease the tensile rupture strength of the concrete. Any corresponding changes to the 28-day concrete strength do not enter this parameter modification since the parametric study was conducted for girders in their lifting condition. In terms of design of the girder, changes to the initial concrete strength would also affect the allowable stress limits of the concrete. The results for this parameter modification are shown in Figure 7.11.

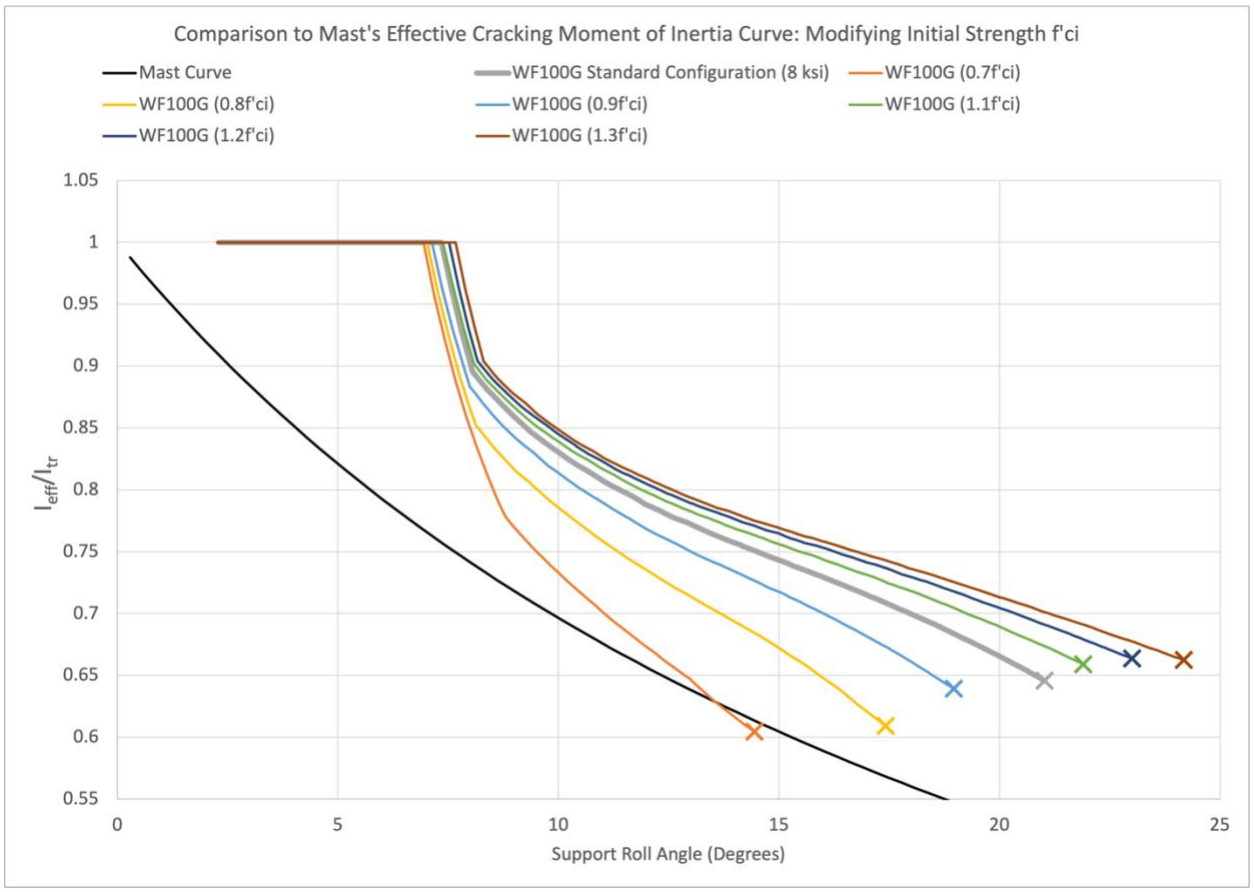

Figure 7.11 Independently Modifying the Initial Concrete Strength, f'_{ci}

There is quite a large variation in performance due to modifications in f'_{ci}. Changing f'_{ci} clearly has a bigger effect on performance than modifications to G or E_c. In practice, the $0.7f'_{ci}$ and $0.8f'_{ci}$ cases would not be allowed—the initial compressive stress limits would be violated (with $0.6f'_{ci}$ used as the limit); however, the purpose of these parametric study plots is not to look at the efficacy or reality of specific designs, but rather it is to understand the trends in the variation in performance that occur due to the manipulation of certain parameters. While it is true that the $0.7f'_{ci}$ and $0.8f'_{ci}$ cases would not pass allowable stress checks—and perhaps that contributes to their poor performance—we can see that, as a trend, lowering the initial concrete strength has quite a detrimental impact on the degradation of stiffness upon cracking and on the final failure angle.

The gains in performance due to further increases in the concrete strength appear to be marginal. The initial cracking angle only slightly increases with f'_{ci}. This makes sense, as the tensile rupture strength is only 24 percent of the square root of the concrete strength. The square root reduces the impact the increases in concrete strength have on tensile rupture strength. Since it takes more stress to crack the higher strength concrete, it makes sense that the degradation of stiffness occurs more gradually for high strength concrete compared to lower strength concrete. LTRB is a self-weight phenomenon. At a given roll angle, the strong and weak axis moments are what they are—there is no live load or superimposed dead load—and thus stronger concretes should not be as cracked as weaker concretes at a given roll angle. They should also be able to roll more before failing, and this trend is reflected in Figure 7.11.

7.4.4. **Modifying Concrete Density**

The final material property parameter examined was the concrete density. Modern long-span girders are often designed with LWC. It is then of interest to see how changing only the concrete density affects the performance of a girder. Changing the concrete density affects the tensile rupture strength (through the λ factor), the modulus of elasticity, and thus the shear modulus. Do these material parameter changes control the behavior of the LWC as it rolls over, or does the lowered self-weight most impact the behavior? The results for the LWC parameter modification are shown in Figure 7.12.

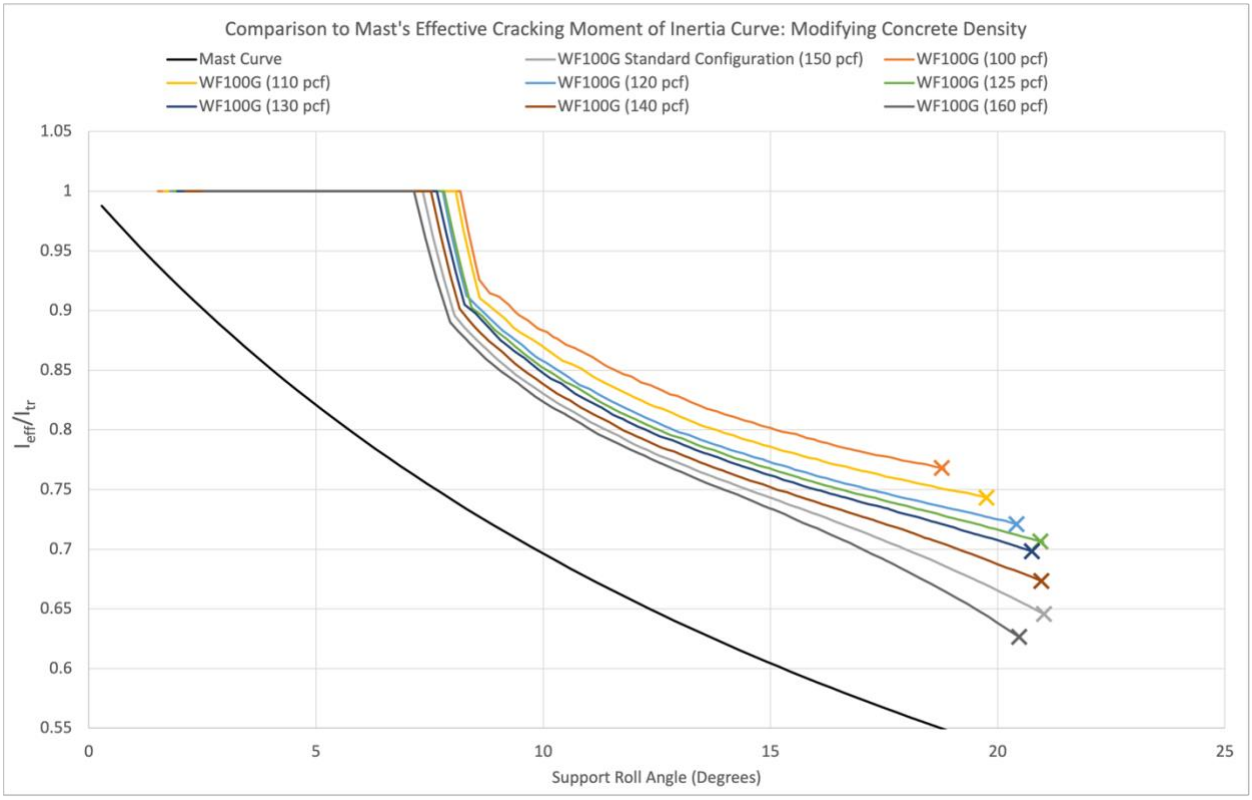

Figure 7.12 Independently Modifying the Concrete Density

From Figure 7.12, the lightest girders perform the best while the densest girders perform the worst in the post-cracking regime. All the concrete densities explored are still conservatively lower bounded by Mast's curve. The final roll angle at failure is approximately constant but begins to decrease for girders lighter than 125 pounds per cubic foot; however, those very same girders crack at the largest roll angle. This also appears to be at odds with the fact that the lightest girders have the least stiffness degradation upon cracking. There is clearly an interaction taking place between the lighter self-weight and the weakened material properties. The large cracking angle of the lightest girders would suggest that their lower self-weight allows the girders to roll farther before there is enough minor axis bending to crack the top flange corner. As the girder rolls farther though, it appears that the denser concrete girders have an advantage due to their higher rupture strengths and moduli of elasticity. The trends are not as drastic as the

modifications in concrete strength, but using LWC appears to be a good practice that could improve lateral stability performance.

Taking the baseline LTRB load, and replacing the following terms: $I_{yy} = Ar_y^2$, $y_r \approx \frac{h}{2}$, and $q_{sw} = -Aw_c$, the ratio of the critical LTRB load to the girder self-weight with equal overhangs can be found to be

$$\frac{q_{LTRB,o}}{q_{sw}} \approx \frac{60}{L}\left(\frac{E_c}{w_c}\right)\left(\frac{h}{L}\right)\left(\frac{r_y}{L}\right)^2 \frac{g(\eta_o)}{f_{LRB}(\alpha)}, \qquad (7-4)$$

where $q_{LTRB,o}$ is the LTRB load for a girder with symmetric overhangs not considering the effects of SAB or prestressing deflections, and $\frac{g(\eta_o)}{f_{LRB}(\alpha)}$ accounts for the effects of torsion and overhangs, as described here in Chapter 2. Changing the concrete density affects only the $\frac{E_c}{w_c}$ ratio. The term $g(\eta_o)$ contains both E_c and *G,* but since the shear modulus is a function of the elastic modulus, the effect of changing concrete density cancels out there, and the ratio $\frac{g(\eta_o)}{f_{LRB}(\alpha)}$ does not change. Per Equation (7 – 1), the Modulus of Elasticity of concrete is related to the square of the concrete density. Thus, the ratio of the LTRB load to the self-weight increases as the concrete density increases, i.e., the self-weight becomes progressively lower than the buckling load, relatively stabilizing the girder, per Equation (7 – 4).

This does not manifest itself in terms of the cracking point in Figure 7.12, nor is it reflected in the degradation of the effective stiffness from the gross properties of heavier girders as they progress through their rollover. Per Equation (7 – 4), it seems like the heavier girders should perform better than the lighter girders. This does not appear to be the case in Figure 7.12; however, the local lateral deflection results used to produce Figure 7.12 show that for a 125 pcf density girder, at a roll of 0.053 Radians (uncracked), the local lateral deflection is approximately 4.75 inches. For a 150 pcf density girder, at a roll of 0.053 Radians (also

uncracked), the local lateral deflection is approximately 4.35 inches. This does reflect the trends that would be predicted by Equation (7 – 4), since the denser girder would in fact have a greater effective local lateral load at the same roll angle as a lighter girder, and yet it still has a lower deflection.

Equation (7 – 4) was derived for uncracked linear elastic girders. The trend predicted by Equation (7 – 4) also holds up when the girder is cracked. For the same two girders at a roll of 0.24 Radians, both are cracked, but the lighter 125 pcf girder has a local lateral deflection of 19.7 inches, while the 150 pcf girder with a local lateral deflection of 17.7 inches. The ratio of $\frac{q_{LTRB,o}}{q_{sw}}$ is higher for the heavier concrete per Equation (7 – 4) and in terms of pure lateral deflections, it performs better than the lighter girder.

In conclusion, for both cracked and uncracked girders, Equation (7 – 4) correctly predicts that heavier girders have lower deflections than lighter girders. However, despite this, lighter density girders crack later (in terms of roll angle) than their heavier counterparts, and they degrade in stiffness less rapidly than the heavier girders. The difference is that the heavier girders have lower "pure" deflections at a given roll angle, while the lighter girders have relatively less degradation from their uncracked transformed properties at that same roll angle. There is clearly an interplay between the negative effects of the greater self-weight and the benefits of stronger material properties that come about from using higher density concretes. In terms of actual deflections and final failure point, the denser concretes generally perform better, but in terms of cracking point and effective lateral stiffness as cracking progresses (degradation from the uncracked transformed properties), the lightest concretes perform best.

7.4.5. **Modifying Number of Temporary Top Strands**

The first non-material parameter analyzed was increasing/decreasing the number of temporary top strands. The cracking mechanism has consistently been through excessive top flange tension up to this point. Increasing the number of temporary top strands—and thus the top flange compression—should at the very least delay the onset of cracking. Reducing the number of temporary top strands should do the opposite. Per the Standard Configuration, the number of temporary top strands depends on the overhang length of the girder, with the WF100G beginning with 9.196 temporary top strands. Recall from Section 7.1 that the Standard Configuration uses non-integer numbers of strands to maintain consistent ratios and relationships between the parameters for all the different cases that were examined. The results for this parameter modification are shown in Figure 7.13.

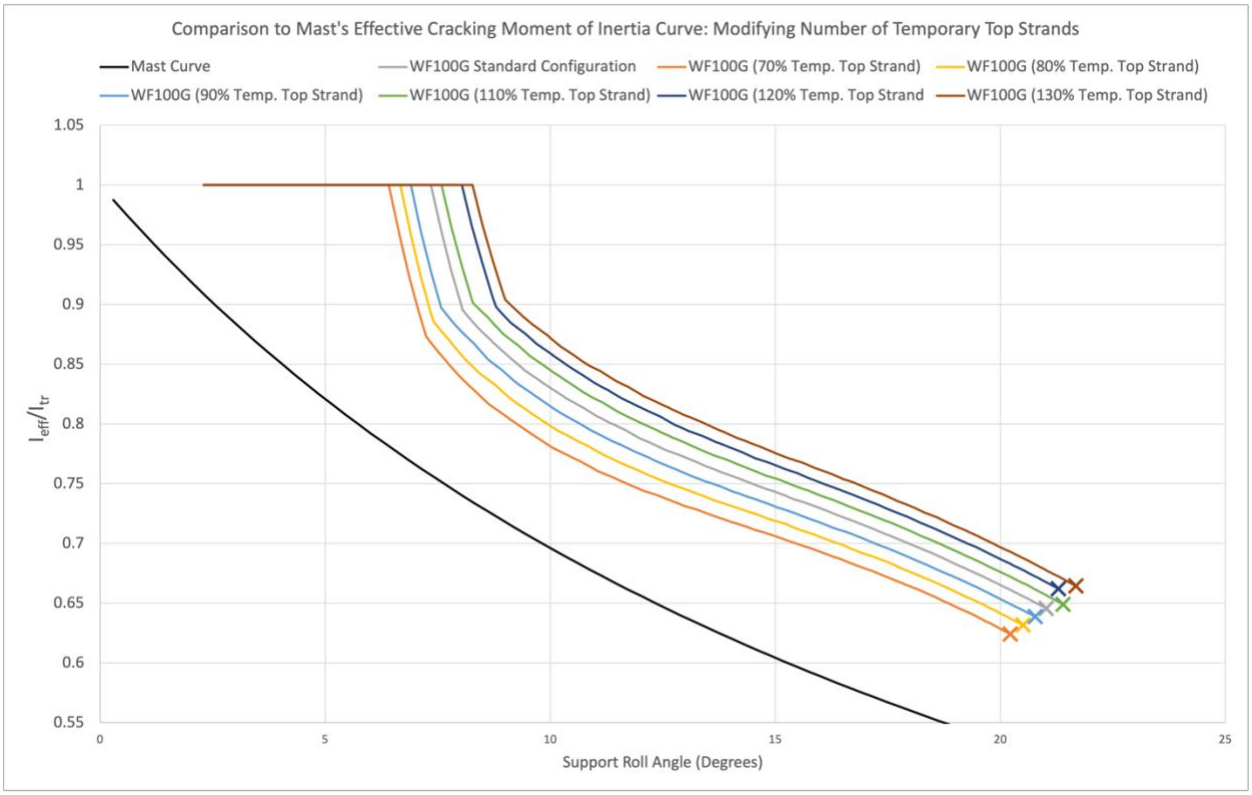

Figure 7.13 Independently Modifying the Number of Temporary Top Strands

There is a very clear trend present in Figure 7.13. Increasing the number of temporary top strands while keeping all other parameters constant increases the cracking roll angle, the final failure angle, and increases the effective moment of inertia at a given roll angle compared to a girder with less top strands. There do not appear to be any negatives associated with increasing the number of temporary top strands. They will reduce bottom compression at midspan which is the most critically stressed area. One potential concern for girders with long overhangs is excessive tension over the supports. While this does not appear to be an issue for the Standard Configuration girders, adding temporary top strands only serves to alleviate any potential issues. Further, these strands will not worsen the girders performance in service as they will be cut before service loads are applied and midspan bottom tension becomes a concern. Temporary top strands appear to be an excellent tool for improving lateral stability and limiting the negative effects of cracking.

While temporary top strands appear to be a “silver bullet” for lateral stability issues, they do present potential practical concerns. For example, if a large number of temporary top strands was selected, the girder manufacturer may have difficulties with applying that much jacking force so high up on the girder cross section, thus causing large overturning moments on the stressing abutments—especially for very deep cross sections like the WF100G. Temporary top strands are a good solution for stability issues, but they should not be blindly adopted without considering potential downstream effects in the girder manufacturing and bridge construction process.

7.4.6. **Modifying Overhang Lengths**

The next parameter explored was modifications to the overhang ratio. The overall length of the girder was maintained while just the overhang length was changed. The Standard Configuration WF100G has 10.25% overhangs. In the Imperfection Study of Chapters 4 and 5, overhangs had a very stabilizing effect on the girder behavior. However, the Imperfection Study was conducted on girders assumed to be linear elastic that did not crack. Here, cracking is allowed to occur. While overhangs do balance the midspan moments with the cantilever moments, that effect also reduces the compression in the top flange at midspan. Like the concrete density parameter, there is an interaction between these effects that impacts the girder's behavior. Further, larger overhangs increase the moment due to the cantilevered overhangs at the supports. This has the potential to lead to top flange cracking over the supports—an undesired behavior. Figure 7.14 presents the results for the overhang parameter modification.

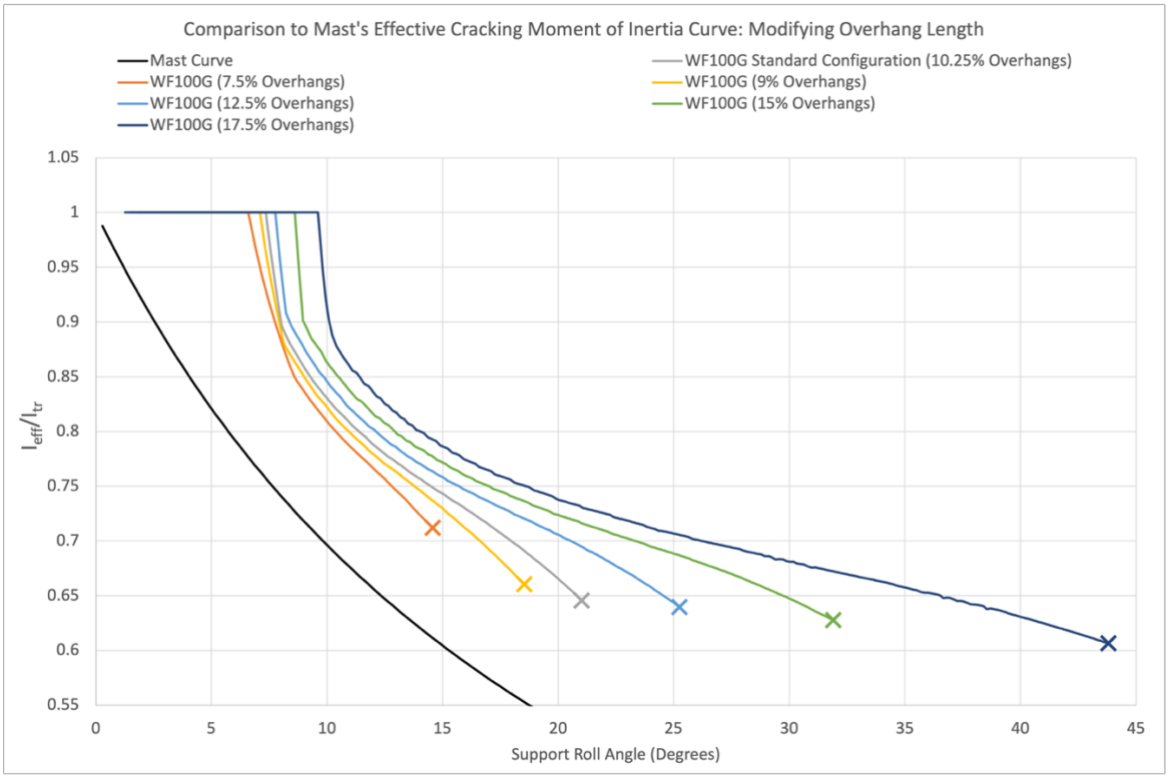

Figure 7.14 Independently Modifying the Overhang Length

Figure 7.14 shows that reducing the overhang length from the Standard Configuration value of 10.25% only serves to worsen the lateral stability performance. The cracking angle, final failure point, and effective stiffness at a given roll angle all drop. The increased external weak axis bending moment (leading to tension in the top flange corner) wins out over the increased top flange compression due to increased strong axis bending in the upright configuration. The opposite is true for girders with larger overhangs. The compression in the top flange due to strong axis bending is lowered because of the overhangs, but the weak axis bending moment is lowered as well, and ultimately the performance is improved due to the lower weak axis bending moment. As the overhangs are increased, the performance improves in all regards through the 17.5% overhangs case. To this point, it would appear as if increasing the overhang ratio, like increasing the temporary top strand is a perfect solution. However, after the 17.5% overhangs case, the cantilever moments at the support become so large that the girder cracks in the top flange over the supports. This behavior is undesirable and would not be allowed to occur in practice. So, while the linear elastic analysis suggests that overhangs up to approximately 25% improve girder stability, at a certain point, depending on the girder design, overhangs can become too large and lead to issues like cracking at the supports (Galik, Stanton, & Wiebe, 2022).

7.4.7. **Modifying the Span-to-Depth Ratio**

The penultimate parameter examined was the span-to-depth ratio. The Standard Configuration consistently uses a span-to-depth ratio of 25. To accurately reflect the effects of changing the span-to-depth ratio, the actual length of the overhangs had to be reduced or increased as the girder was shortened or lengthened. While the overhang length changes, the overhang percentage would then remain constant—thus giving a true representation of how varying the overall length of a girder affects performance without polluting the results from modifications to the overhang ratio. The results for this parameter modification are shown in Figure 7.15.

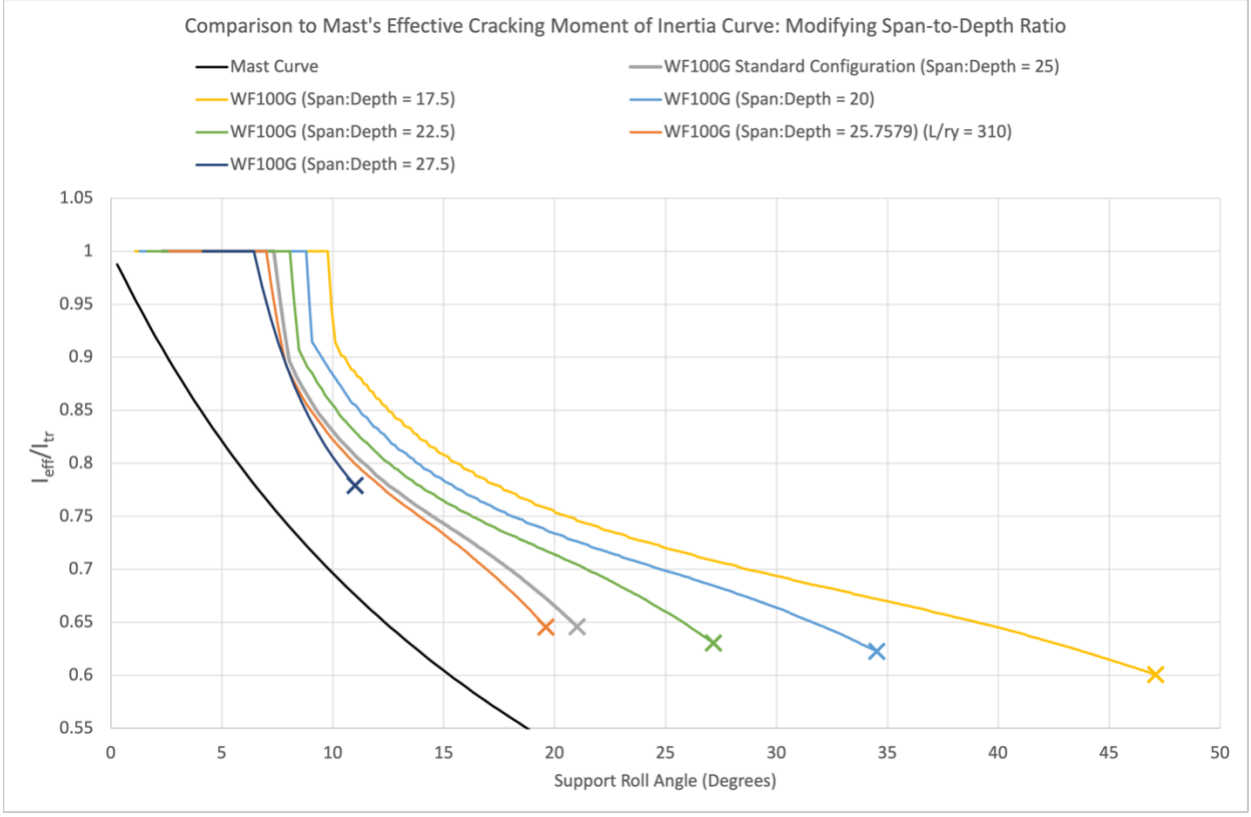

Figure 7.15 Independently Modifying the Span-to-Depth Ratio

Modifying the span-to-depth ratio and keeping all other parameters constant makes a very large difference in girder performance. This makes physical sense; as noted in Chapter 2, the

buckling load is proportional to the fourth power of the length—any modifications to the length will have a large impact on performance. The shortest girders clearly perform the best in terms of cracking angle, stiffness degradation as cracks propagate, and ultimate failure point. The span-to-depth ratio of 17.5 girder fails at a final roll angle more than double the Standard Configuration with its span-to-depth ratio of 25. A span-to-depth ratio of 27.5 is nominally the maximum reasonable case for the Standard Configuration. The girder failed very shortly after cracking for ratios this high.

Note that the orange curve has a span-to-depth ratio of 25.7579. This corresponds with a lateral slenderness ratio of 310, where the lateral slenderness ratio is defined as

$$Lateral\ Slenderness\ Ratio = \frac{L}{r_y}, \qquad (7-5)$$

where r_y is the radius of gyration in the weak-axis direction. This is relevant, as WSDOT girders are limited to a lateral slenderness ratio of 310 in practice (Khaleghi, 2021). Technically, the navy-blue span-to-depth curve of 27.5 is beyond this lateral slenderness ratio limit; however, it shows that there is an upper limit upon the length a certain girder design can be without changing any other design parameters.

Additionally, girder length is unlike the other parameters. Unlike overhang length, for example, which can easily be changed in a design to suit the requirements of a certain scenario, the required span length is likely to be controlled by other, external, considerations. This parameter modification is not so much designed to show how one could vary the length to optimize a design, but rather is designed to show that, all else equal, longer girders perform worse.

7.4.8. **Modifying the Top Flange Width**

The final parameter explored was a modification to the top flange width with no other changes made to the cross section or Standard Configuration. Girders with increased top flange widths have recently been used for long span bridges in Washington State: WSDOT used a modified WF100G with a 61-inch top flange (one-foot wider) (Khaleghi, 2021). It is of interest to see how this modified WF100G performs, as well as girders with incrementally larger top flange widths. These results are shown in Figure 7.16.

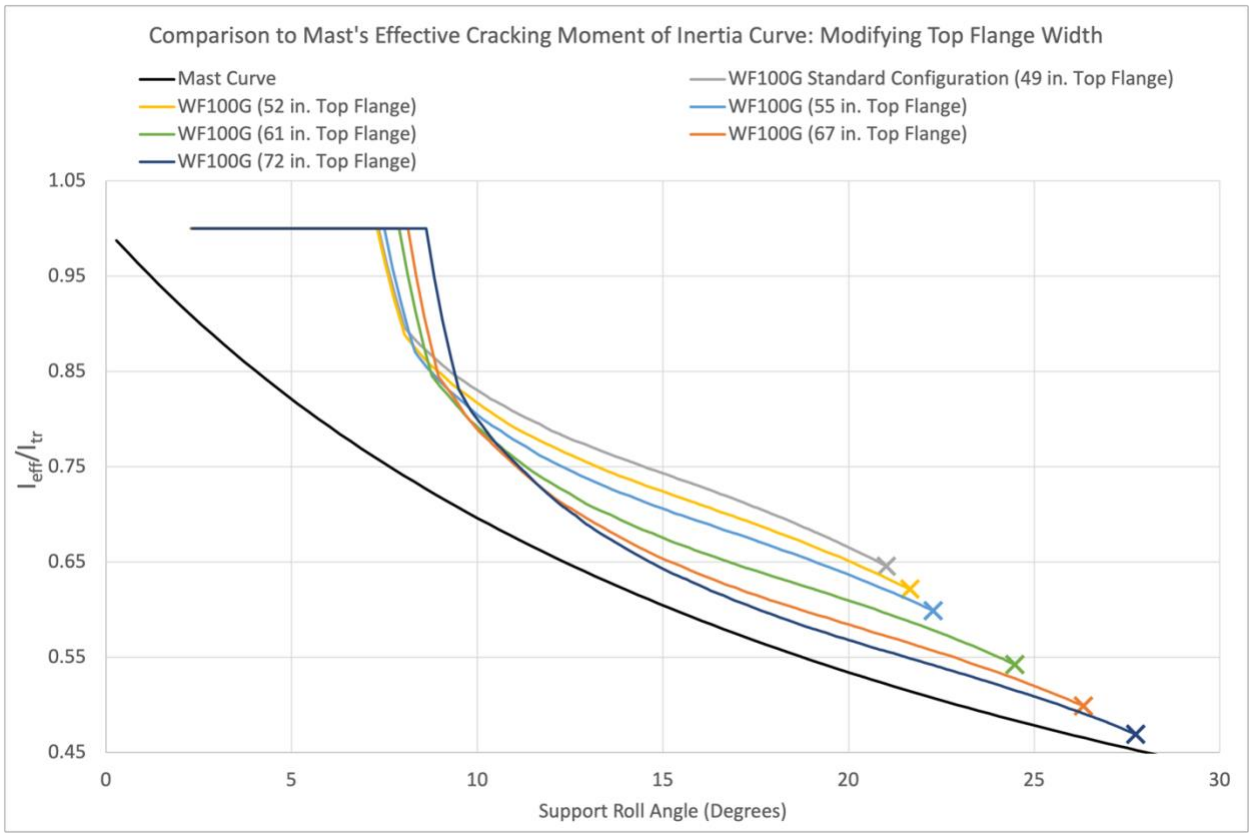

Figure 7.16 Independently Modifying the Top Flange Width

Figure 7.16 depicts some interesting results. Increasing the top flange width increases the initial cracking angle. This makes physical sense, for the center of gravity shifts upwards as the top flange gets wider and the top stresses will then be lower under the same applied moment compared to the original cross section. Girders with the widest top flanges also have the largest

final failure angles; however, along the way there is a cross over point generally in the region immediately after cracking occurs. The girders with the widest top flange have lower effective moments of inertia than girders with a narrower top flange. Although the exact causes of this behavior are unclear, perhaps once cracking occurs, the cracks propagate rapidly down through the wider top flange. Then, the top flange essentially does not contribute any moment resistance and the girder is like an inverted tee. Due to the wider top flange, it is at a more extreme roll angle at cracking, and thus will have greater weak axis bending moments than the girders with less wide top flanges. Much of the weak axis stiffness goes away with the top flange, so then the effective moment of inertia drops rapidly as cracks then propagate quickly from the midspan outwards. Further, this rapidly reduced effective moment of inertia is divided by the large uncracked transformed moment of inertia for the widened top flange girders in Figure 7.16, perhaps contributing to the lower ratio of effective-to-transformed moments of inertia.

The girder does not crack throughout its entire length, however. The uncracked portions near the end, along with the top flange reinforcing steel, keep the girder upright. Girders with wider uncracked top flanges nears the ends of its length will then be able to fail at a larger roll angle than girders with less wide top flanges, as is shown in Figure 7.16.

7.5. **Conclusions from the Parametric Study**

The parametric study showed the following:

- Generally, increasing concrete strength, number of temporary top strands, overhang length, and the top flange width improved performance in terms of initial cracking angle, stiffness degradation upon cracking, and final failure angle.
- Increasing the span-to-depth ratio led to rapid decreases in performance, while decreasing the ratio drastically improved performance.
- If overhangs are made too large without compensatory measures to mitigate additional top tension at the supports, top flange cracking at the supports can occur. If top flange cracking does not occur, overhang ratios up to approximately 25% are a very effective way to increase lateral stability and post-cracking performance.
- Lower density concrete girders may crack later and have relatively less stiffness degradation upon cracking than higher density concrete girders, but their actual deflections are larger. There is not a large difference in final failure angle due to changing concrete density.
- Changing the concrete modulus of elasticity makes very little difference on the rate of post-cracking stiffness degradation, but an increased modulus does correspond with an increase in final failure angle.
- If torsional stiffness were to drop because of flexural or torsional cracking, the girder will lose post-cracking stiffness performance. The rate at which this stiffness drops off, and its corresponding effect on the critical load is not certain. Making the girder torsionally rigid (LRB), improves performance, but not dramatically.

8. Design Examples

Chapter 7 illustrated how different design parameters affect girder lateral stability. Trends in girder behavior could then be seen and the most influential design parameters can be identified. Chapter 8 will explore three lateral stability design examples using a version of the existing WSDOT design procedure, modified to account for torsion, SAB, and prestressing deflections. The design procedure includes simple equations for calculating the cracking onset angle, final equilibrium angle, and the angle at which failure, defined by excessive compressive stress, occurs.

The first example will compare this modified design procedure to the current WSDOT design procedure using a WSDOT WF74G girder configuration from a March 2023 WSDOT lateral stability design webinar. The second example will use the modified design procedure on the Standard Configuration WF100G. The third will explore the lateral stability design of a 250-foot-long LWC modified WF100G girder using the modified design procedure as well.

8.1. **Cracking Angle Equation**

Cracking initiates when the extreme tensile stress in the girder reaches the cracking strength, f_{cr}. The calculations for predicting cracking are rendered much simpler if linear elastic behavior is assumed, and that is done here on the basis that the stresses are low enough to justify it. The lowest cracking onset angle is likely to occur when lifting from the stressing bed because the elastic modulus and tensile strength of the concrete are lowest at that time. The girder is assumed to have undergone roll, twist and lateral bending, as a consequence of some initial imperfection, amplified by the stability effects, so the girder will crack first in top flange tension at midspan. This is also consistent with the results seen in Chapters 6 and 7. If the girder cracks

in top tension with a rupture strength equal to that of Equation (6 – 3), then the sum of stresses in the top corner where cracking occurs is

$$f_{cr} = 0.24\lambda\sqrt{f'_{ci}} = -\frac{F_{pj}}{A_{tr}} + \frac{M_{px}}{S_{x2}} + \frac{M_{gx}}{S_{x2}} + \frac{M_{gy}}{S_{ya}}, \qquad (8-1)$$

where F_{pj} is the jacking force, A_{tr} is the transformed cross-sectional area, S_{x2} is the section modulus of the top of the girder (S_{x2} is negative in sign), S_{ya} is the weak-axis section modulus of the top right of the girder (S_{ya} is positive in sign), M_{px} is the moment due to prestressing (always in the local strong-axis since it is symmetrically placed), and M_{gx} and M_{gy} are the gravity moments due to the self-weight in the local strong and weak axes, respectively. Compressive stresses are assumed to be negative and tensile stresses are assumed to be positive. The sign-convention and coordinate system used are summarized in Section 2.1. The section moduli are for the transformed girder cross section accounting for the concrete, rebar, and prestressing strand. The section moduli and their signs are shown in Figure 8.1.

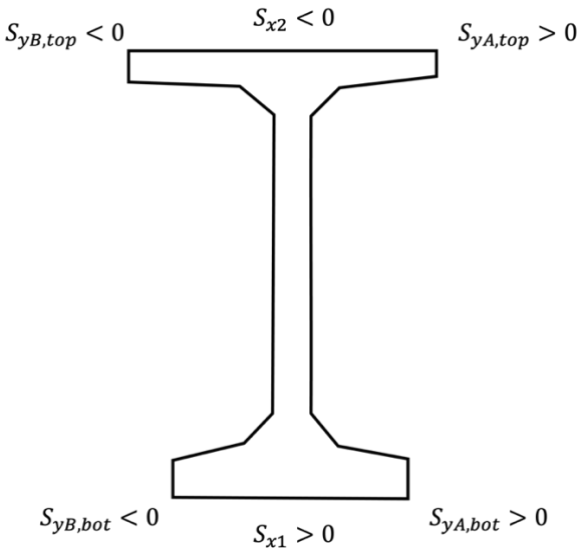

Figure 8.1 Section Moduli and Signs for Stress Analysis

As the girder rolls in the positive roll direction (see Figure 2.1) the gravity moments become

$$M_{gx} = M_g \cos\phi, \tag{8 – 2}$$

and

$$M_{gy} = M_g \sin\phi. \tag{8 – 3}$$

Then, rearranging Equation (8 – 1):

$$f_{cr,net} = \left(f_{cr} + \frac{F_{pj}}{A_{tr}} - \frac{M_{px}}{S_{x2}}\right) = M_g \left(\frac{\cos\phi}{S_{x2}} + \frac{\sin\phi}{S_{yA}}\right) \tag{8 – 4}$$

Where $f_{cr,net}$ is essentially the "reserve" stress capacity available at the top right flange corner prior to cracking, without the gravity moments due to the self-weight applied.

Defining

$$S_o = -\sqrt{S_{x2}^2 + S_{yA}^2}, \tag{8 – 5}$$

then

$$S_{x2} = S_o \cos\psi, \tag{8 – 6}$$

and

$$S_{yA} = S_o \sin\psi, \tag{8 – 7}$$

where

$$\tan\psi = \frac{S_{yA}}{S_{x2}}. \tag{8 – 8}$$

To ensure the correct sign for compression at the top in the strong axis and tension at the right in the weak axis, S_o must be negative, as shown in Eq (8-5).

Substituting Equation (8 – 6) and Equation (8 – 7) into Equation (8 – 4), gives

$$f_{cr,net} = M_g \left(\frac{\cos\phi}{S_o \cos\psi} + \frac{\sin\phi}{S_o \sin\psi}\right). \tag{8 – 9}$$

Using trigonometric identities to simplify, Equation (8 – 9) becomes

$$f_{cr,net} = \frac{M_g \sin(\psi + \phi)}{S_o \sin\psi \cos\psi}, \tag{8 – 10}$$

and then rearranging Equation (8 – 10),

$$\sin(\psi + \phi) = f_{cr,net} \frac{S_o \sin\psi \cos\psi}{M_g}. \tag{8 – 11}$$

The angle at which the girder cracks is then

$$\phi_{crack} = \arcsin\left(f_{cr,net} \frac{S_o \sin\psi \cos\psi}{M_g}\right) - \psi. \tag{8 – 12}$$

Equation (8 – 12) can be further simplified. If we define

$$f_{g2} = \frac{M_g}{S_{x2}}, \tag{8 – 13}$$

where f_{g2} is the compressive stress at the top flange due to gravity loading in the upright configuration, then Equation (8 – 12) becomes

$$\phi_{crack} = \arcsin\left(\frac{f_{cr,net}}{f_{g2}} \sin\psi\right) - \psi. \tag{8 – 14}$$

Equation (8 – 14) can be even further simplified using Taylor Series expansions of *arcsine* and *sine*. If $\frac{f_{cr,net}}{f_{g2}} = c$ is substituted, then by using the Taylor Expansion of *arcsine* first, Equation (8 – 14) becomes

$$\phi_{crack} + \psi \approx c \sin\psi + \frac{(c \sin\psi)^3}{3!} + \frac{9(c \sin\psi)^5}{5!}. \tag{8 – 15}$$

Substituting the Taylor Expansion of *sine* into Equation (8 – 15) one arrives at

$$\phi_{crack} + \psi \approx c\left(\psi - \frac{\psi^3}{3!} + \frac{\psi^5}{5!}\right) + \frac{c^3}{3!}\left(\psi - \frac{\psi^3}{3!} + \frac{\psi^5}{5!}\right)^3 + \frac{9c^5}{5!}\left(\psi - \frac{\psi^3}{3!} + \frac{\psi^5}{5!}\right)^5. \tag{8 – 16}$$

Only keeping terms that are lower than the power of ψ^3 (permissible because Equation (8 – 8) shows that $\psi << 1.0$) gives an even simpler closed-form equation for the cracking angle:

$$\hat{\phi}_{crack} \approx \psi(c-1) = \psi\left(\frac{f_{cr,net}}{f_{g2}} - 1\right). \qquad (8-17)$$

The Standard Configuration for the WF100G was used to check this equation against the results from Rollbuck 2022. The inputs to the calculation are summarized below in Table 8.1.

Table 8.1 Standard Configuration Design Values for WF100G used to Calculate the Cracking Angle

f_{cr}	0.6788 ksi
F_{pj}	3108.6 kips
Net Prestressing Moment, M_{px}	-93177.6 kip-inches
Midspan Gravity Moment, M_g	45801.6 kip-inches
$f_{cr,net}$	0.40566 ksi
S_o	-31946 in^3
$\tan\psi$	-0.10366
ψ	-0.1033
ϕ_{crack} (Equation 8 – 14)	0.1323 Radians (7.58 Degrees)
$\hat{\phi}_{crack}$ (Equation 8 – 17)	0.1323 Radians (7.58 Degrees)
ϕ_{crack} (Rollbuck 2022)	0.1369 Radians (7.843 Degrees)

As can be seen from Table 8.1, both the full result from Equation (8 – 14) and the Taylor Series Expansion give identical results (to the fourth digit) for the WF100G Standard Configuration girder. Further, they differ from those obtained from Rollbuck 2022 by only 3%. Some differences should be expected because this closed-form calculation assumes a linear elastic concrete model and Rollbuck 2022 uses a nonlinear one, but the results are sufficiently close for the purposes at hand. Equation (8 – 17) for the cracking angle of a girder will be used in the following section in a proposed design framework.

8.2. **Proposed Modifications to Current Design Methodology**

WSDOT's existing design methodology for the lateral stability of long-span prestressed concrete bridge girders relies heavily upon Mast's work in his 1989 and 1993 papers (Mast, 1989) (Mast, 1993). As a reminder to the reader, Mast's work assumes that the girder is torsionally rigid and does not have any SAB deflections. To make his results closed-form and easily workable by hand, he used small angle assumptions to eliminate the trigonometric functions present in the equilibrium equations. The Rigid Link Model (RLM) introduced in Chapter 3, and then verified against the imperfection amplification results in Chapters 4 and 5, may be used in place of Mast's calculations to arrive at the final equilibrium tilt angle of an uncracked girder. It represents an improvement because it does not use small angle assumptions, and it accounts for torsion, overhangs, camber, and strong-axis bending while remaining simple to use.

Once a girder design has been established that satisfies service loading, the ***current WSDOT design procedure*** for checking the lateral stability of a girder is generally as follows:

1. Identify lateral sweep and lifting loop eccentricity imperfections, roll-axis height (y_r), and net camber deflections to determine the girder's center of gravity position.
2. Use Mast's equations/procedure from his 1989 and 1993 to determine the equilibrium roll angle (Mast, 1989) (Mast, 1993).
    a. Note that WSDOT accounts for the net camber in initially determining the center of gravity position in Step 1, but the net camber is not included in Mast's equilibrium roll angle calculation.
3. Calculate stresses and Demand-to-Capacity Ratios (DCRs) for the rolled equilibrium configurations.

4. Using Mast's Equations, determine Factors of Safety against cracking and failure (defined by Mast (1993) as a roll of 0.4 radians.)
5. If the girder has cracked, use Mast's $\frac{I_{eff}}{I_{gr}}$ equation, shown here as Equation (6 – 1), to determine the effective cracked moments of inertia.
    a. Iterate on Steps 2 to 5 until converging upon a final answer or modify the design as necessary.

Within step 2, the current WSDOT design procedure checks lateral stability for one case where the girder is lifted and for three cases where the girder is seated on a truck and in the process of being hauled to a job site. Two of the three hauling cases have the girder on a two percent cross slope, with an impact load of 20 percent of the girder weight directed upwards or downwards. The final hauling case simulates the truck parked at job site, without impact loads, but resting on a six percent cross slope. The hauling cases are assumed to occur later in the early life of the girder, with the concrete strength slightly increased and with some prestressing losses having occurred. The procedure for lifted and hauled girders is very similar, except that Mast's equations for a girder supported from below are used for the hauling case (Mast, 1993).

The ***proposed modified design procedure*** maintains the general framework described for the above cases. Instead of using Mast's equations to determine the equilibrium roll angle, the RLM will be used. The RLM incorporates the initial roll angle, which is a function of the imperfections and layout of the girder, the applied load, and the critical load. This formulation inherently accounts for torsion, overhangs, camber, and strong-axis bending. The equation for the RLM is repeated for clarity below:

$$\tan\phi = \frac{\tan\phi_o}{1 - \frac{q}{q_{cr}}\cos\phi}, \qquad \textit{(3 – 32b)}$$

where the tangent of ϕ_o, the initial roll angle, is the inverse of Equation (3 – 20)

$$\tan\phi_o = \left(\frac{-\overline{u}_{sweep,\alpha}}{y_r - \overline{v}_{p,\alpha}}\right) + \left(\frac{e_x}{y_r - \overline{v}_{p,\alpha}}\right) = \left(\frac{-\left(\overline{u}_{sweep,\alpha} - e_x\right)}{y_r - \overline{v}_{p,\alpha}}\right). \qquad (3 - 20)$$

Equation (3 – 32b) is implicit in ϕ, and requires an iterative solution. This iteration is typically not computationally expensive. The form of the critical load which accounts for torsion, overhangs, prestressing deflections, and strong-axis bending is also repeated below

$$q_{LTRB,vp\alpha} = \frac{q_{LRB,o}}{f_{LRB}(\alpha)} \frac{\left(1 + \frac{1}{y_r}\left(\Delta_p(\alpha) - \overline{v}_p\right)\right)}{\left(1 - \frac{I_{yy}}{I_{xx}}\right)} g\left(\eta_{vp\alpha}\right). \qquad (2 - 54)$$

Chapters 4 and 5 showed that the Rigid Link Model accurately predicts the final equilibrium angle, including both roll and twist, SAB, prestressing deflections, overhangs, and imperfections.

Once the equilibrium roll angle has been determined using the RLM, the proposed design procedure is very similar to the existing WSDOT design procedure. The equilibrium roll angle will be compared to the $\hat{\phi}_{crack}$ value from Equation (8 – 17). If the girder has not cracked yet, the equilibrium angle determined by the RLM is the final angle and the stress checks may be performed. If the girder passes the stress checks, it performs satisfactorily considering lateral stability. Chapter 7 showed that there is residual life in the girder even after it cracks. If the girder does not crack, i.e., Factor of Safety against cracking is greater than 1.0, then the Factor of Safety against failure will be even larger—the girder will crack before it fails.

If the girder has cracked, then a knockdown factor for the $\frac{I_{eff}}{I_{gr}}$ ratio is used. For this purpose, Mast proposed Equation (6 – 1), repeated here:

$$\frac{I_{eff}}{I_{gr}} = \frac{1}{1 + 2.5\theta'} \qquad (6 - 1)$$

The knockdown equation will be used to determine the new reduced moments of inertia accounting for cracking. Note that the first design example comparing to WSDOT's lateral stability webinar will use the gross moment of inertia, as that is what WSDOT uses. The second and third design examples use the transformed moment of inertia to account for the steel and to be consistent with Rollbuck 2022 and the use of the jacking forces. The knockdown equation remains unchanged. Equation (6 – 1) appears to provide a safe lower bound to the ratio $\frac{I_{eff}}{I_{gr}}$ for the WSDOT WF girder series, as shown in Chapter 7, so it may be used for them. However, its use is likely not safe with some other girder types, such as the AASHTO, AASHTO-PCI, or DBT girders. For them, a modified version of Equation (6 – 1) would be necessary if cracking were to be allowed in design.

Note that the RLM technically gives the equilibrium roll angle, not the roll plus twist angle. Chapter 5 showed that differences between the RLM, which was derived assuming LRB, and the actual results from Rollbuck 2021 are quite small, only diverging at very large applied loads when torsion becomes more prevalent. Reasonably designed girders will not get out into this range of angles, at least not without cracking and exceeding stress limits, and thus the RLM can be used to accurately predict the final roll plus twist angle of a girder in design checks. However, the effects of torsion are included in the overall formulation through q_{cr}. Thus, this approach essentially assumes (with numerical evidence) that initial imperfections amplify LTRB problems in the same manner that they amplify LRB problems, i.e., that the effects of torsional deformations and imperfections are somewhat de-coupled.

For the hauling case, the RLM can still be used to determine the equilibrium tilt angle, but the modified $y_{r,eq}$ derived in Section 2.5 must be used to account for the truck's rotational stiffness and the fact that the girder is supported from below. Roadway cross-slopes can be

accounted for by adding that angle directly to the initial roll angle, essentially acting as another imperfection. In WSDOT's design methodology, an impact load of plus or minus 20 percent of the girder's weight is also used in the hauling case. This is achieved by performing Mast's equilibrium roll angle calculations but with the weight increased or decreased by 20 percent. This can similarly be achieved using the RLM by increasing or decreasing the self-weight by 20 percent and performing the same calculations.

8.3. **Case Study 1: Comparison of Current and Proposed Methods for WSDOT WF74G Design Example**

8.3.1. **Given Parameters for WF74G Design Example**

At a lateral stability design webinar in March 2023, WSDOT presented a design example for a 163-foot-long WF74G during the lifting and hauling cases using their current design procedure (Brice, 2023). This section will compare the results from the current WSDOT and PCI recommended design procedure to the results from the design procedure proposed here (Precast/Prestressed Concrete Institute, 2016).

Relevant information about the girder section properties and other design parameters are summarized in Table 8.2. Note that the provided properties are for the gross cross-section. This leads to no difference in the cross-sectional properties between the lifting and hauling cases.

Table 8.2: Design Parameters and Cross-Sectional Properties of Example WSDOT WF74G Girder

Girder Design and/or Cross-Sectional Property	**Value**
Length	*163 ft.*
Gross Cross Sectional Area	*923.531 in^2*
Strong-Axis Moment of Inertia, I_{xx}	*734356 in^4*
Weak-Axis Moment of Inertia, I_{yy}	*72018.4 in^4*
Torsional Stiffness, *GJ*	*3.7033E7 kip-in^2*
Distance to Top from Center of Gravity, y_{top}	*-38.343 in.*
Distance to Bot. from Center of Gravity, y_{bot}	*35.657 in.*
Top Strong-Axis Section Modulus, S_{x2}	*-19152.5 in^3*
Bottom Strong-Axis Section Modulus, S_{x1}	*20594.8 in^3*
Top Weak-Axis Section Modulus, S_{yT}	*+/- 2939.5 in^3*
Bottom Weak-Axis Section Modulus, S_{yB}	*+/- 3753.3 in^3*
Concrete and Rebar Allowance Density	*0.165 kip/ft^3*
Initial and Final Concrete Strength	*7.2 ksi ; 8.7 ksi*
Initial and Final Concrete Modulus of Elasticity	*5530.5 ksi ; 5886.9 ksi*
Overhang Length during Lifting and Hauling	*8.25 ft. ; 13.67 ft.*
Net Camber at Lifting and Hauling	*4.025 in. ; 7.338 in.*

The strand amounts and prestressing forces given for the WF74G design example are provided in Table 8.3.

Table 8.3 Numbers of Strands and Prestressing Forces for WF74G Design Example

Strand/Case Description	**Lifting Case**		**Hauling Case**	
Number of Strands	**Force/Strand**	**Total Force**	**Force/Strand**	**Total Force**
44 Straight	39.03 kips	1716.36 kips	37.63 kips	1655.95 kips
17 Harped	39.03 kips	663.53 kips	37.66 kips	640.23 kips
4 Temporary Top	42.03 kips	168.15 kips	40.84 kips	163.38 kips

8.3.2. **WF74G Design Example: Lifting Case**

To begin the proposed design procedure, the initial roll angle needs to be calculated. That equation was repeated above in Section 8.2. The initial lateral imperfection accounts for both lateral sweep and lifting loop eccentricity. The initial vertical imperfection accounts for the deflection due to prestressing, but not the self-weight. The stabilizing effect of the self-weight induced SAB is included in the critical load. As a reminder, the initial roll angle is essentially the angle the girder would adopt to achieve moment equilibrium before deflections due to gravity self-weight loading took place. The initial roll angle calculation is as follows with Table 8.4 summarizing the values used in the calculation:

$$\tan\phi_o = \left(\frac{-\left(\overline{u}_{sweep,\alpha} - e_x\right)}{y_r - \overline{v}_{p,\alpha}}\right). = \frac{-\left((1.304\ in - 0.328\ in) + 0.25\ in\right)}{-38.343\ in + 3.2\ in} = 0.03487$$

$$\phi_o = 0.03485\ Radians = 1.99\ Degrees$$

The numerator in the above calculation determines the initial lateral imperfection. The initial roll angle and the logic behind its concept are described in Chapter 3. For ease of reference, Figure 2.6, showing the various prestressing deflection and sweep measurements necessary for calculating the initial roll angle, is repeated as Figure 8.2.

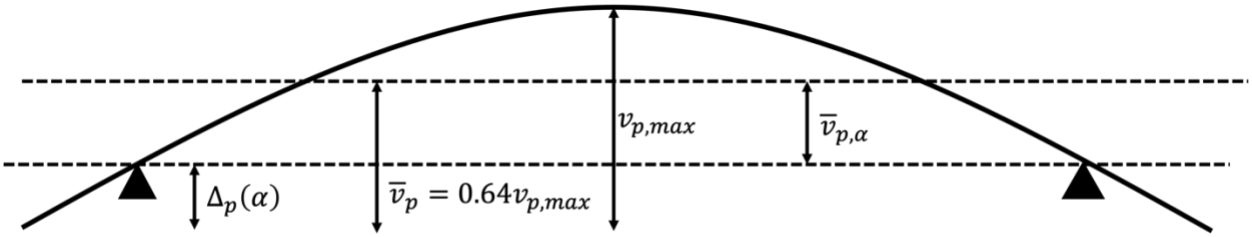

$$\overline{v}_{p,\alpha} = \overline{v}_p - \Delta_p(\alpha)$$

Figure 8.2 Repeat of Figure 2.6: Schematic of Prestressing Deflection Measurements

Recall that the lateral sweep values can be analogously substituted for the prestressing deflection values. All initial roll angle calculations in further examples are performed similarly to the example shown above.

Table 8.4 Parameters for Calculating the Initial Roll Angle for WF74G Example, Lifting Case

Parameters for Calculating Initial Roll Angle	**Results**
Maximum Sweep, u_{sweep}	*2.0375 in.*
Sweep at Support Points, $\Delta_u(\alpha)$	*0.328 in.*
Lifting Loop Eccentricity, e_x	*-0.25 in.*
Lateral Deflection of Center of Gravity, $\overline{u}_{sweep,\alpha} - e_x$	*1.225 in.*
Maximum Prestressing Deflection, $v_{p,max}$	*-6.684 in.*
Camber at Support Points, $\Delta_p(\alpha)$	*-1.077 in.*
Vertical Deflection of Center of Gravity, $\overline{v}_{p,\alpha}$	*-3.2 in.*
Average Prestressing Deflection from Ends of Girder, $\overline{v}_p$	*-4.277 in.*
Tangent of Initial Roll Angle, $\tan \phi_o$	***0.03487***
Initial Roll Angle, ϕ_o	***1.99 Degrees***

Note that this procedure inherently assumes that the sweep and prestressing deflections are of the shape of a simply supported beam subjected to a uniformly distributed load. The WSDOT design procedure reports the net camber which accounts for self-weight deflection. This proposed

design procedure requires the deflection due to prestressing alone. To calculate this value while maintaining consistency with the WSDOT design example, the midspan self-weight deflection for a girder with two uniform overhangs was calculated and then added to the net camber value reported by WSDOT, listed in Table 8.2.

Next, the critical load accounting for torsion, overhangs, prestressing deflections, and SAB needs to be calculated. This critical load equation is repeated above in Section 8.2. The critical load is calculated in an identical way in each following example and is shown once here. As shown in Section 8.2, the critical load consists of the critical LRB load multiplied by modifying factors that account for torsion, overhangs, prestressing deflections, and SAB.

$$q_{LRB,o} = -\frac{120EI_{yy}y_r}{L^4} = -\frac{(120)(3.982E8\ kip\cdot in^2)(-38.343\ in)}{1956^4\ in^4} = 0.125\frac{kip}{in}$$

$$f_{LRB}(\alpha) = 1 - 10\alpha + 30\alpha^2 - 20\alpha^3 - 10\alpha^4$$

$$= 1 - 10(0.0506) + 30(0.0506^2) - 20(0.0506^3) - 10(0.0506^4) = 0.568$$

$$f_{LTB}(\alpha) = (1-2\alpha)^3 = \big(1 - 2(0.0506)\big)^3 = 0.726$$

$$\beta = \sqrt{\left(\frac{y_r}{L}\right)^2 \frac{EI_{yy}}{GJ}} = \sqrt{\left(\frac{-38.343\ in}{1956\ in}\right)^2 \frac{3.982E8\ kip\cdot in^2}{3.703E7\ kip\cdot in^2}} = 0.0642$$

$$\eta_{vp\alpha} = 71.9\beta^2 \left(\frac{f_{LTB}(\alpha)}{f_{LRB}(\alpha)}\right) \frac{\left(1 + \frac{1}{y_r}\left(\Delta_p(\alpha) - \overline{v}_p\right)\right)^2}{1 - \frac{I_{yy}}{I_{xx}}}$$

$$\eta_{vp\alpha} = 71.9(0.0642^2)\left(\frac{0.726}{0.568}\right)^2 \frac{\left(1 + \left(\frac{1}{-38.343\ in}\right)(-1.077\ in + 4.277\ in)\right)^2}{1 - \frac{72018\ in^4}{734356\ in^4}} = 0.452$$

$$g\left(\eta_{vp\alpha}\right) = \frac{2}{\eta_{vp\alpha}}\left(\sqrt{1 + \eta_{vp\alpha}} - 1\right) = \left(\frac{2}{0.452}\right)\left(\sqrt{1 + 0.452} - 1\right) = 0.907$$

$$SAB\ and\ Prestressing\ Factor = \frac{1 + \frac{1}{y_r}\left(\Delta_p(\alpha) - \overline{v}_p\right)}{1 - \frac{I_{yy}}{I_{xx}}} = 1.0161$$

$$q_{cr} = q_{LRB,o} * \frac{Prestressing}{SAB} * \frac{g(\eta_{vp\alpha})}{f_{LRB}(\alpha)} = \left(0.125\frac{kip}{in}\right)(1.0161)\left(\frac{0.907}{0.568}\right) = 0.2031\frac{kip}{in}$$

While calculating the critical load requires plugging into many different equations, each is closed-form and the entire calculation is easily automated. The values for calculating the critical load for the WF74G example are summarized in Table 8.5.

Table 8.5 Values for Calculating the Critical Load for WF74G Example, Lifting Case

Parameters for Calculating Critical Load	**Results**
Critical Baseline LRB Load, $q_{LRB,o}$	*0.125 kip/in*
Factor Accounting for Overhangs, $f_{LRB}(\alpha)$	*0.568*
Overhang Factor Accounting for LTB, $f_{LTB}(\alpha)$	*0.726*
Beta Factor for Calculating Torsional Effect, β	*0.0642*
Eta Factor for Calculating Torsional Effect, $\eta_{vp\alpha}$	*0.452*
Factor Accounting for Torsion, $g(\eta_{vp\alpha})$	*0.907*
Combined Factors due to SAB and Prestressing	*1.0161*
Critical Load, q_{cr}	***0.2031 kip/in***
Ratio of Self-Weight to Critical Load, $\frac{q}{q_{cr}}$	***0.434***

At this point, the initial roll angle and ratio of self-weight to critical load are plugged into the RLM. A simple goal-seek function in a spreadsheet, or similar, can be easily utilized to quickly converge upon an equilibrium angle. Doing so, the final equilibrium angle at midspan (roll plus twist) using this new proposed design procedure is **0.0614 radians, or 3.52 degrees.** Using the simple amplification (RLM with small angle assumption), the result is 0.0616 radians—practically the same. This follows, as the final angle is quite small, and a small angle assumption could reasonably be used.

The WSDOT design procedure arrives at a final equilibrium roll angle for the lifting case of **0.05768 Radians or 3.3 degrees.** The final angle of the proposed design procedure is greater than the result from the WSDOT design example. This makes sense because including torsion is destabilizing while the SAB and prestressing deflection effects largely cancel each other out.

Since the girder has not cracked in this hanging evaluation, the next (and final) step in this check is to check the stresses versus the allowable limits. At the top right corner where cracking would first occur, the stress calculation is as follows:

$$Top\ Right\ Stress = \frac{M_{px}}{S_{x2}} - \frac{F_{pe}}{A_{gr}} + \frac{M_{gx}}{S_{x2}} + \frac{M_{gy}}{S_{yT}}$$

$$Top\ Right\ Stress = \frac{-68831\ kip \cdot in}{-19152\ in^3} - \frac{2549\ kip}{923\ in^2} + \frac{33570\ kip \cdot in}{-19152\ in^3} + \frac{2065\ kip \cdot in}{2939\ in^3}$$

$$= -0.21\ ksi.$$

The top right corner is in compression during the lifting case and as ssuch is not near to its tensile cracking stress. All the other stress calculations for each corner are identical to the one shown above, with the appropriate section moduli substituted as necessary. Equations (8 – 2) and (8 – 3) define the gravity moments in each direction as a function of the final equilibrium angle.

Three possible limiting damage states may be envisaged for evaluating the girder:

1. First cracking in tension (in the top flange “low” corner)
2. First allowable compressive stress limit violation (in the bottom flange “high” corner)
3. Compressive crushing failure

The first two may be reasonably evaluated using linear elastic material models. The compressive stress limit is likely to be reached after cracking, so the equations used to calculate that stress should strictly include the effects of cracking, albeit with a linear constitutive model for the

concrete in compression; however, that greatly increases the complexity, so instead the calculation is done using uncracked assumptions. Computation of the crushing load, using nonlinear models for the steel and concrete, is even more difficult, so the attainment of the (elastic) limiting stress is used as a (safe) proxy for the true roll angle at crushing failure. For the limiting compressive stress, WSDOT uses $0.7f'_{ci}$ (Brice, 2023). The tensile limit against cracking is the rupture stress (assuming that adequate top flange reinforcing steel is provided.) Table 8.6 summarizes the stresses in the four corners of the girder at midspan during the lifting case.

Table 8.6: Stresses and Comparison to Allowable Stress Limits for WF74G, Lifting Case

Compressive Stress Limit, $0.7f'_{ci}$	***-5.04 ksi***	**Tensile Stress Limit, $0.24\lambda\sqrt{f'_{ci}}$**	***0.643 ksi***
Top Left Corner Stress	*-1.621 ksi*	Top Right Corner Stress	*-0.216 ksi*
Top Left Demand-to-Capacity Ratio	*0.321 (OK)*	Top Right Demand-to-Capacity Ratio	*0.042 (OK)*
Bottom Left Corner Stress	*-5.022 ksi*	Bottom Right Corner Stress	*-3.921 ksi*
Bottom Left Demand-to-Capacity Ratio	*0.996 (OK)*	Bottom Right Demand-to-Capacity Ratio	*0.778 (OK)*

The girder does not exceed any of the allowable stress limits, although the bottom left corner is on the verge of exceeding the allowable compressive stress limit. The initial concrete strength could be slightly increased to solve this problem. The stress may not be as close to its limit as it appears since this example with the WF74G used gross, and not transformed, section properties.

WSDOT only reports the equivalent bottom left and top right (they use a different positive rotation direction) stresses at the harping point. Their bottom left stress is -5.04 ksi and their top right stress is -0.207 ksi. These stresses are similar to the values returned from the proposed design procedure. Slight increases in bottom compression and top tension at the harping point relative to midspan would be expected due to the lower gravity moment but equal

prestressing moment; however, due to the incorporation of torsion, at midspan a slight increase in top right tension and bottom left compression would be expected due to the increased equilibrium angle. The separate increases in stresses at these two points likely contributed to the two different locations returning similar total stress values. The stresses at the harping points were not evaluated because cracking initiated at the midspan throughout the parametric study. Further, the contributions of twist and roll to the final equilibrium angle is unknown when using the RLM. To calculate stresses at other locations other than the midspan, perhaps the girder could be conservatively assumed to be rotated as a rigid body equal to the final equilibrium angle, including twist and roll.

In conclusion for the lifting case, the girder does not crack or fail stress checks at any of its four corners at midspan. The midspan equilibrium angle is larger using this proposed design method than the current method used in practice because of the incorporation of torsional deformations.

8.3.3. **WF74G Design Example: Hauling Cases**

The WF74G is then checked in the three hauling condition cases. This includes the truck on a two percent cross slope, with and without a 20 percent impact load (simulated by reducing or increasing the self-weight), and the truck on a six percent cross slope without considering impact.

The relevant design parameters and section properties for the girder during the hauling cases are described above in Table 8.2. As a reminder, the overhang length is increased from 8.25 feet during lifting to 13.67 feet in these hauling cases. The parameters to calculate the initial roll angle are the same for all three hauling cases. The lateral imperfection now includes lateral sweep and an eccentric bunking location of the girder, instead of a lifting loop eccentricity,

which contributes to the imperfection in the same way. The prestressing deflection now accounts for additional long-term deflections due to creep and shrinkage. WSDOT reported the net camber as 7.338 inches. The deflection due to just prestressing (without self-weight deflection) is 9.112 inches upwards. This information is summarized in Table 8.7.

Table 8.7 Parameters for Calculating the Initial Roll Angle of the WF74G Example, Hauling Cases

Parameters for Calculating Initial Roll Angle	**Values**
Maximum Sweep, u_{sweep}	*2.0375 in.*
Sweep at Support Points, $\Delta_u(\alpha)$	*0.539 in.*
Bunking Point Eccentricity	*1.0 in.*
Lateral Deflection of Center of Gravity, $\overline{u}_{sweep,\alpha} - e_x$	*1.764 in.*
Maximum Prestressing Deflection, $v_{p,max}$	*-9.112 in.*
Camber at Support Points, $\Delta_p(\alpha)$	*-2.412 in.*
Vertical Deflection of Center of Gravity, $\overline{v}_{p,\alpha}$	*-3.419 in.*
Average Prestressing Deflection, from Ends of Girder, $\overline{v}_p$	*-5.831 in.*

The initial roll angle is not reported in Table 8.7, nor is the equivalent hanging roll axis height. The equivalent roll axis height depends upon the final equilibrium angle of the girder, and the initial roll angle depends upon the equivalent hanging roll axis height. Due to the roadway cross slope, the equivalent roll axis height equation cannot be linearized by making a small angle assumption, and so hauling cases on cross slopes by nature must be iterative. This adds minimal computational difficulty to the proposed design procedure. If cracking is to be incorporated, iteration is required anyways to use Mast's knock down factor for the effective moment of inertia. To use the full version of the RLM, iteration is required as well. Iteration to solve for the equivalent hanging roll axis height simply requires linking that calculation to the equilibrium angle calculation, an easy task to achieve in a spreadsheet or other computing program.

The initial roll angle is calculated in the same way as shown above in Section 8.3.1, but the equivalent hanging roll axis height is used instead. A sample calculation of the equivalent roll axis height for the six percent cross slope case with relevant values summarized is shown in Table 8.8.The final converged value for the equilibrium angle is used in the calculation.

$$y_{r,eq} = y_{truck} + \frac{K_{\phi,supp}(\phi - \alpha)}{R \sin \phi}$$

$$= (35.657\ in + 48\ in) + \frac{20000 \frac{kip \cdot in}{Rad}(0.134\ Rad - 0.06\ Rad)}{(-86.24\ kip) \sin 0.134\ Rad} = -44.8\ in$$

Note that for the roadway cross slope, a small angle assumption was made in that $\arctan(0.06) = 0.0599\ Radians \approx 0.06\ Radians$. This assumption makes no practical difference on the results for the equivalent hanging roll axis height. Further, the support stiffness and reaction are for only half of the truck stiffness/girder reaction. In full, the truck would have a rotational stiffness of 40000 kip-in/radian, and the girder would weigh approximately 172.5 kips.

The change in girder weight due to impact and the different roll axis heights lead to different critical load parameters for each of the three cases. Those are summarized in Table 8.8, along with the initial roll angles and the final equilibrium angles for all three cases. The critical load is calculated using the same equations and procedures demonstrated in Section 8.3.1.

Table 8.8 Critical Load Parameters and Final Equilibrium Angle, Hauling Cases

Parameter	**2% Cross Slope, -20% Impact**	**2% Cross Slope, +20% Impact**	**6% Cross Slope, No Impact**
R, Reaction	*69 kips*	*103.48 kips*	*86.24 kips*
$K_{\phi,supp}$	*20000 kip-in/Rad (40000 Total)*	*20000 kip-in/Rad (40000 Total)*	*20000 kip-in/Rad (40000 Total)*
$y_{r,eq}$.	*-85.003 in.*	*-55.509 in.*	*-44.828 in.*
$\tan \phi_o$	***0.0416***	***0.0538***	***0.1026***
ϕ_o	*2.385 Degrees*	*3.086 Degrees*	*5.879 Degrees*
$q_{LRB,o}$	*0.295 kip/in*	*0.192 kip/in*	*0.1558 kip/in*
$f_{LRB}(\alpha)$	*0.36*	*0.36*	*0.36*
$g(\eta_{vp\alpha})$	*0.625*	*0.769*	*0.83*
SAB/Prestressing	*1.064*	*1.04*	*1.024*
q_{cr}	***0.546 kip/in***	***0.428 kip/in***	***0.367 kip/in***
$\frac{q}{q_{cr}}$	***0.129***	***0.246***	***0.239***
ϕ_{eq}	***0.0478 Radians***	***0.0717 Radians***	***0.134 Radians***
$\phi_{eq,WSDOT}$	***0.038 Radians***	***0.058 Radians***	***0.114 Radians***

Just as with the lifting case, the results from this proposed design method using the RLM slightly overestimate the results from WSDOT's existing design procedure. This is to be expected due to the incorporation of the destabilizing effects of torsional deformations, and SAB and prestressing deflection's relatively minor effect on the critical load. With a cracking angle of approximately 0.14 radians, the girder remains uncracked in all three cases, although it comes closest to cracking in the six percent cross slope case. The stresses are calculated in the same manner as shown in Section 8.3.1. The allowable stress limits are increased because the concrete has gained strength over time since the initial lifting case. The stresses in the four corners for all three cases are summarized in Table 8.9

Table 8.9 Stresses and Demand-to-Capacity Ratios for WF74G Example Hauling Cases

Compressive Stress Limit $0.7f'_{ci}$	***-6.09 ksi***	**Tensile Stress Limit, $0.24\lambda\sqrt{f'_{ci}}$**	***0.707 ksi***
Location	**2% Cross Slope, -20% Impact**	**2% Cross Slope, +20% Impact**	**6% Cross Slope, No Impact**
Top Left	*-0.733 ksi (DCR 0.12)*	*-1.76 ksi (DCR 0.28)*	*-1.92 ksi (DCR 0.31)*
Top Right	*-0.004 ksi (DCR 0.00)*	*-0.13 ksi (DCR 0.02)*	*0.62 ksi (DCR 0.88)*
Bottom Left	*-5.082 ksi (DCR 0.83)*	*-4.89 ksi (DCR 0.80)*	*-5.53 ksi (DCR 0.9)*
Bottom Right	*-4.511 ksi (DCR 0.74)*	*-3.61 ksi (DCR 0.59)*	*-3.53 ksi (DCR 0.58)*

The girder passes all stress checks for all three hauling cases. In the six percent cross slope case, the top right corner of the girder is in tension, with a demand-to-capacity ratio of 0.88. This reflects the fact that the equilibrium angle in that case is closest to the cracking angle. The six percent cross slope case appears to be the most critical hauling case for at least this girder configuration. It has the most severe equilibrium angle, is the only case with tension, and has the largest compressive demand-to-capacity ratio of the hauling cases as well. The lifting case has the highest compressive demand-to-capacity ratio of 0.99, which would likely control the initial concrete strength. In this sense, the lifting case appears to control the initial stress behavior while the hauling case controls the behavior of the girder for stresses relative to cracking and in terms of final deflections.

From the WSDOT Design Example for the six percent cross slope case, the equivalent top right tensile stress is 0.452 ksi and the equivalent bottom left compressive stress is -5.463 ksi at the harping point (Brice, 2023). These are similar to but slightly lower in magnitude than the same stress results from the proposed designed procedure. This comparison of stresses between the harping point and midspan is discussed in the previous section.

8.4. **Case Study 2: Proposed Design Method for Standard Configuration WF100G**

This section will perform the same lateral stability design checks as done in Section 8.3 using only the new proposed design procedure on the Standard Configuration WF100G. The details of the Standard Configuration are described in Section 7.1. As a reminder, the Standard Configuration and Rollbuck 2022 use the transformed section properties and the jacking stresses for the prestressing forces. Rollbuck 2022 calculates the elastic shortening losses internally. The WF74G design example did not crack in any of the checked cases. The six percent cross slope case almost cracked. Since the Standard Configuration WF100G is approximately 45 feet longer than the WF74G example girder, it is likely to crack, so it provides a platform for evaluating the cracking features of the new proposed design procedure.

8.4.1. **Standard Configuration WF100G Example: Lifting Case**

The relevant section properties and design parameters for the lifting case are summarized in Table 8.10.

Table 8.10 Design Parameters and Section Properties for Lifting Case of Standard Configuration WF100G

Girder Design and/or Cross-Sectional Property	**Value**
Length	*208.33 ft.*
Transformed Cross Sectional Area	*1169 in^2*
Strong-Axis Stiffness, EI_{xx}	*8.2473E9 kip-in^2*
Weak-Axis Stiffness, EI_{yy}	*3.9224E8 kip-in^2*
Torsional Stiffness, *GJ*	*3.6079E7 kip-in^2*
Distance to Top from Center of Gravity, y_{top}	*-53.405 in.*
Distance to Bot. from Center of Gravity, y_{bot}	*46.594 in.*
Top Strong-Axis Section Modulus, S_{x2}	*-31776 in^3*
Bottom Strong-Axis Section Modulus, S_{x1}	*36420 in^3*
Top Weak-Axis Section Modulus, S_{yT}	*3294.2 in^3*
Bottom Weak-Axis Section Modulus, S_{yB}	*4206.2 in^3*
Self-Weight, Accounting for Strand and Rebar	*0.0994 kip/in*
Initial Concrete Strength	*8 ksi*
Initial Concrete Modulus of Elasticity	*4860 ksi*
Overhang Length during Lifting	*21.36 ft.*
Prestressing Deflection (No Self-Weight) at Lifting	*-7.37 in.*

For the WF74G design example, WSDOT reported the net camber at lifting and hauling. That value was replicated (minus the self-weight deflection) to best compare the two design methods. Here, the prestressing deflections were calculated exactly for each strand layer using the equivalent loads imposed upon the girder by the prestressing strands.

The parameters and values necessary to calculate the initial roll angle for the lifting case are summarized in Table 8.11. The initial roll angle was calculated using the same procedure shown in Section 8.3.1.

Table 8.11 Parameters for Calculating the Initial Roll Angle for Standard Configuration WF100G, Lifting Case

Parameters for Calculating Initial Roll Angle	**Results**
Maximum Sweep, u_{sweep}	*2.604 in.*
Sweep at Support Points, $\Delta_u(\alpha)$	*0.837 in.*
Lifting Loop Eccentricity, e_x	*-0.25 in.*
Lateral Deflection of Center of Gravity, $\overline{u}_{sweep,\alpha} - e_x$	*1.079 in.*
Maximum Prestressing Deflection, $v_{p,max}$	*-7.37 in.*
Camber at Support Points, $\Delta_p(\alpha)$	*-2.372 in.*
Vertical Deflection of Center of Gravity, $\overline{v}_{p,\alpha}$	*-2.349 in.*
Average Prestressing Deflection from Ends of Girder, $\overline{v}_p$	*-4.721 in.*
Tangent of Initial Roll Angle, $\tan \boldsymbol{\phi_o}$	***0.0211***
Initial Roll Angle, $\boldsymbol{\phi_o}$	***1.211 Degrees***

Despite the larger prestressing deflections and lateral sweep imperfection, the Standard Configuration WF100G has a smaller initial roll angle than the WF74G example by approximately 0.8 degrees. This is partially due to the larger roll axis height but is primarily a result of the larger overhang ratio in the Standard Configuration WF100G.

The parameters and values used to calculate the critical load for the Standard Configuration WF100G hanging case are reported Table 8.12. The critical load is calculated in the same manner shown in Section 8.3.1.

Table 8.12 Values for Calculating the Critical Load for Standard Configuration WF100G and Final Equilibrium Angle, Lifting Case

Parameters for Calculating Critical Load	**Results**
Critical Lateral-Roll-Buckling Load, $q_{LRB,o}$	*0.064 kip/in*
Factor Accounting for Overhangs, $f_{LRB}(\alpha)$	*0.267*
Overhang Factor Accounting for LTB, $f_{LTB}(\alpha)$	*0.502*
Beta Factor for Calculating Torsional Effect, β	*0.0704*
Eta Factor for Calculating Torsional Effect, $\eta_{vp\alpha}$	*1.2084*
Factor Accounting for Torsion, $g(\eta_{vp\alpha})$	*0.804*
Combined Factors due to SAB and Prestressing	*1.003*
Critical Load, q_{cr}	***0.1943 kip/in***
Ratio of Self-Weight to Critical Load, $\frac{q}{q_{cr}}$	***0.5113***
Final Equilibrium Angle, ϕ_{eq}	***0.04325 Radians***
Cracking Angle, $\widehat{\phi}_{crack}$	***0.1323 Radians***

The critical LRB load for the Standard Configuration WF100G is about one half of the LRB load for the example WF74G; however, despite torsion reducing the critical load approximately 10 percent more here than for the WF74G, the stabilizing effect of the overhang is larger. As a result, the critical load, and ratio of self-weight to critical load, are not that different between the two cases. Since the WF74G example girder has a larger initial roll angle than the WF100G, it ends up having a larger final equilibrium angle than the Standard Configuration WF100G. So, despite its longer length and larger imperfections, the Standard Configuration WF100G has a smaller equilibrium angle than the example WF74G girder in the hanging case.

No further iteration is required since the girder does not crack. The stresses and allowable stresses in the girder are summarized in Table 8.13, with the stresses calculated in the same manner shown in Section 8.3.1.

Table 8.13 Stresses and Comparison to Allowable Stress Limits for Standard Configuration WF100G, Lifting Case

Compressive Stress Limit, $0.7f'_{ci}$	***-5.6 ksi***	**Tensile Stress Limit, $0.24\lambda\sqrt{f'_{ci}}$**	***0.678 ksi***
Top Left Corner Stress	*-1.768 ksi*	Top Right Corner Stress	*-0.565 ksi*
Top Left Demand-to-Capacity Ratio	*0.315 (OK)*	Top Right Demand-to-Capacity Ratio	*0.101 (OK)*
Bottom Left Corner Stress	*-4.431 ksi*	Bottom Right Corner Stress	*-3.49 ksi*
Bottom Left Demand-to-Capacity Ratio	*0.791 (OK)*	Bottom Right Demand-to-Capacity Ratio	*0.623 (OK)*

All corners of the girder comfortably pass the allowable stress checks. The top right corner is still in compression and is not near the cracking stress. The initial concrete strength could likely be reduced from 8 ksi since neither the upright nor tilted configurations are near breaching any stress limits. In conclusion, the lifting case comfortably passes all checks. It does not come near the cracking roll angle of 0.1323 radians and all stresses are comfortably within allowable limits.

8.4.2. **Standard Configuration WF100G Example: Hauling Cases**

The hauling cases occur later in the life of the girder than the initial lifting case. As such, the concrete strength increases from the lifting to the hauling cases, the concrete modulus of elasticity changes per the relevant AASHTO code equation, and the prestressing has some long-term losses occur (AASHTO, 2017). Per the WF74G design example, the concrete strength increased by 1.5 ksi and there were 3.5 percent prestressing losses (Brice, 2023). For the Standard Configuration WF100G, the jacking stresses, accounting for long term losses, would then be 193 ksi and the concrete strength would be 9.5 ksi. The updated section properties and design parameters for the transformed section in the hauling cases are reported in Table 8.14.

Table 8.14 Design Parameters and Section Properties for Hauling Cases of Standard Configuration WF100G

Girder Design and/or Cross-Sectional Property	**Value**
Length	*208.33 ft.*
Transformed Cross Sectional Area	*1163.3 in²*
Strong-Axis Stiffness, EI_{xx}	*8.6759E9 kip-in²*
Weak-Axis Stiffness, EI_{yy}	*4.1266E8 kip-in²*
Torsional Stiffness, *GJ*	*3.8207E7 kip-in²*
Distance to Top from Center of Gravity, y_{top}	*-53.302 in.*
Distance to Bot. from Center of Gravity, y_{bot}	*46.697 in.*
Top Strong-Axis Section Modulus, S_{x2}	*-31627 in³*
Bottom Strong-Axis Section Modulus, S_{x1}	*36100 in³*
Top Weak-Axis Section Modulus, S_{yT}	*3272.8 in³*
Bottom Weak-Axis Section Modulus, S_{yB}	*4178.9 in³*
Self-Weight, Accounting for Strand and Rebar	*0.0994 kip/in*
Concrete Strength	*9.5 ksi*
Concrete Modulus of Elasticity	*5146.5 ksi*
Overhang Length during Hauling	*21.36 ft.*
Prestressing Deflection (No Self-Weight) at Hauling	*-7.171 in.*

The prestressing deflection accounts for additional long term prestressing deflections due to creep and shrinkage. This additional amount was calculated using Naaman's rule of thumb equation

$$\Delta_{add,p} = 1.8\Delta_{ps,i} + 2.2\Delta_{sw,i}, \qquad (8-18)$$

where $\Delta_{ps,i}$ is the initial prestressing deflection (here 7.37 inches upwards) and $\Delta_{sw,i}$ is the initial self-weight deflection (Naaman, 2012). The initial self-weight deflection is the deflection of the girder due to its own self-weight if supported from its ends—in this case 6.13 inches downwards. Per Equation (8 – 18), there are then 0.206 inches of *downwards* long-term deflection due to

creep. The supported-from-ends self-weight deflection case is used here because the girder would likely be stored near its ends and would have long-term creep effects take place in the end-supported configuration during service. The WSDOT design procedure used the 90-day camber value, thus justifying this end-supported self-weight deflection choice.

The parameters for calculating the initial roll angle for the three hauling cases are summarized in Table 8.15.

Table 8.15 Parameters for Calculating the Initial Roll Angle of the Standard Configuration WF100G, Hauling Cases

Parameters for Calculating Initial Roll Angle	**Values**
Maximum Sweep, u_{sweep}	*2.604 in.*
Sweep at Support Points, $\Delta_u(\alpha)$	*0.837 in.*
Bunking Point Eccentricity, e_x	*1.0 in.*
Lateral Deflection of Center of Gravity, $\overline{u}_{sweep,\alpha} - e_x$	*1.829 in.*
Maximum Prestressing Deflection, $v_{p,max}$	*-7.171 in.*
Camber at Support Points, $\Delta_p(\alpha)$	*-2.306 in.*
Vertical Deflection of Center of Gravity, $\overline{v}_{p,\alpha}$	*-2.283 in.*
Average Prestressing Deflection, from Ends of Girder, $\overline{v}_p$	*-4.589 in.*

The initial roll angles and equivalent roll axis height values are not reported in Table 8.15 because they depend on the final equilibrium angle, which will be iteratively solved.

In the plus 20 percent impact case and in the six percent cross slope case, the Standard Configuration WF100G girder cracks. The minimum 40,000 in-kip total truck stiffness used to this point did not work for those two cases. The RLM did not converge upon a solution. The truck stiffnesses were increased until the girder passed all stress checks, aside from the tension stress check, which of course would be violated since the girder cracked.

To calculate an effective cracked moment of inertia, Equation (6 – 1), Mast's knock-down factor is used if the girder cracks. This knock-down factor will be labelled here as κ_{Mast}:

$$\kappa_{Mast} = \frac{1}{1 + 2.5\phi_{eq}} = \frac{I_{eff}}{I_{tr}}. \qquad (8 - 19)$$

The effective cracked moment of inertia knock-down factor κ_{Mast} applies to both the strong- and weak-axis moments of inertia. For the 20 percent impact upwards case, the girder does not crack, and Mast's knock-down factor is unity. In the six percent cross slope case, for example, $\kappa_{Mast} = 0.611$. A sample calculation of κ_{Mast} and how cracking changes $q_{LRB,o}$ is shown below. The final converged values shown in Table 8.16 are used for the sample calculation.

$$\kappa_{Mast} = \frac{1}{1 + 2.5\phi_{eq}} = \frac{1}{1 + 2.5(0.2546)} = 0.611$$

$$EI_{yy,eff} = \kappa_{Mast} EI_{yy} = (0.611)(4.1266E8\ kip \cdot in^2) = 2.5213E8\ kip \cdot in^2$$

$$q_{LRB,cracked} = -\frac{120 EI_{yy,eff} y_{r,eq}}{L^4} = -\frac{(120)(2.5213E8\ kip \cdot in^2)(-60.77\ in)}{(2500^4\ in^4)} = 0.047 \frac{kip}{in}$$

If the girder has not cracked yet, κ_{Mast} will be equal to 1.0. While realistically the $y_{r,eq}$ would be different if the girder were uncracked, a sample calculation using the cracked $y_{r,eq}$ value is shown to demonstrate the effect κ_{Mast} and cracking have on the LRB load, all else remaining equal.

$$q_{LRB,uncracked} = -\frac{120 EI_{yy} y_{r,eq}}{L^4} = -\frac{(120)(4.1266E8\ kip \cdot in^2)(-60.77\ in)}{(2500^4\ in^4)} = 0.077 \frac{kip}{in}$$

These two LRB load values are different by a factor of κ_{Mast}, representing the effect of cracking. Once the effective moments of inertia are calculated for a cracked girder, the calculations are repeated iteratively until the Rigid Link Model converges upon a solution.

The critical loads, parameters for solving them, the initial roll angles, and the final equilibrium angles are reported in Table 8.16. The required truck rotational stiffnesses are also reported in Table 8.16.

Table 8.16 Critical Load Parameters and Final Equilibrium Angle for Standard Configuration WF100G, Hauling Cases

Parameter	**2% Cross Slope, -20% Impact**	**2% Cross Slope, +20% Impact**	**6% Cross Slope, No Impact**
Reaction, R	*-99.4 kips*	*-149.1 kips*	*-124.25 kips*
$K_{\phi,supp}$	*20000 in-kip (40000 Total)*	*25000 in-kip (50000 Total)*	*25000 in-kip (50000 Total)*
$y_{r,eq}$.	*-58.233 in.*	*-58.959 in.*	*-60.77 in.*
κ_{Mast}	*1.0*	*0.645*	*0.611*
$\boldsymbol{\tan \phi_o}$	***0.0526***	***0.0522***	***0.0912***
ϕ_o	*3.019 Degrees*	*2.995 Degrees*	*5.229 Degrees*
$q_{LRB,o}$	*0.0738 kip/in*	*0.0482 kip/in*	*0.047 kip/in*
$f_{LRB}(\alpha)$	*0.267*	*0.267*	*0.267*
$g(\eta_{vp\alpha})$	*0.7804*	*0.834*	*0.8329*
SAB & Prestressing	*1.0087*	*1.009*	*1.0104*
$\boldsymbol{q_{cr}}$	***0.2174 kip/in***	***0.1518 kip/in***	***0.1482 kip/in***
$\frac{\boldsymbol{q}}{\boldsymbol{q_{cr}}}$	***0.3657***	***0.7854***	***0.6705***
$\boldsymbol{\phi_{eq}}$	***0.083 Radians***	***0.2198 Radians***	***0.2546 Radians***
$\widehat{\boldsymbol{\phi}}_{\boldsymbol{crack}}$	***0.1445 Radians***	***0.1307 Radians***	***0.1362 Radians***

The Standard Configuration WF100G cracks in two out of the three hauling cases; however, if the rotational stiffness of the truck is increased sufficiently, the girder can still achieve equilibrium. Cracking can be completely prevented by increasing the truck rotational stiffness. For the two percent cross slope case that cracked, a total truck stiffness of 60000 in-

kip/Radian would need to be used. For the six percent cross slope case, a truck stiffness of 80000 in-kip/Radian would be required to prevent cracking. This is right on the upper limit of stiffnesses available in commercial trucks today. If a greater stiffness were required, alternative solutions to prevent cracking could include increasing overhang length, concrete strength, or the number of temporary top strands.

The parametric study in Chapter 7 showed that there is "life after cracking," especially in the WSDOT WF series girders. Mast's reduction factor for the effective moment of inertia in Equation (6 – 1), represented by κ_{Mast} in Table 8.16, provides a conservative lower bound estimate of stiffness upon cracking. The parametric study showed that even if the girder does crack, it can typically sustain additional deformations before failing. It is difficult, however, to predict with certainty the exact failure point of any girder design; the parametric study showed that the design parameters, and particularly details of the nonlinear concrete model used, greatly affect the exact point of ultimate failure. Additionally, the allowable compressive stress limits, calculated on the basis of uncracked elastic behavior, would be violated before the girder failed. Therefore, the two and six percent cross slope cases that cracked had their truck stiffness increased to the point that they did not fail compressive stress checks at midspan. The angle when this allowable compressive stress failure occurs at the bottom left corner can be derived in the same way as the ϕ_{crack} equation. The expression for the compressive stress failure angle is shown below:

$$\hat{\phi}_{comp} = \psi_{cop}\left(\frac{f_{comp,net}}{f_{g1}} - 1\right), \qquad (8-20)$$

where

$$f_{comp,net} = -0.7f_c' + \frac{F_{pj}}{A_{tr}} - \frac{M_{px}}{S_{x1}}, \qquad (8-21)$$

and

$$f_{g1} = \frac{M_g}{S_{x1}}, \qquad (8-22)$$

and

$$\tan(\psi_{comp}) = \frac{S_{yB}}{S_{x1}}. \qquad (8-23)$$

Note that if the gravity moments are assumed to be positive, then S_{yB} will be negative and S_o (not used in Equation (8 – 20) to (8 – 23) but used in the ϕ_{crack} derivation and this analogous derivation) will be positive.

The stresses for the girders in the three hauling cases for the Standard Configuration WF100G example are shown in Table 8.17, as well as $\hat{\phi}_{comp}$, the angle that the girders would violate the allowable compressive limit.

Table 8.17 Stresses and Demand-to-Capacity Ratios for Standard Configuration WF100G Hauling Cases

Compressive Stress Limit $0.7f'_{ci}$	***-6.65 ksi***	**Tensile Stress Limit, $0.24\lambda\sqrt{f'_{ci}}$**	***0.739 ksi***
Location	**2% Cross Slope, -20% Impact**	**2% Cross Slope, +20% Impact**	**6% Cross Slope, No Impact**
Top Left	*-1.809 ksi (DCR 0.27)*	*-5.084 ksi (DCR 0.764)*	*-4.65 ksi (DCR 0.69)*
Top Right	*0.048 ksi (DCR 0.065)*	***2.241 ksi (DCR 3.029)***	***2.39 ksi (DCR 3.24)***
Bottom Left	*-4.793 ksi (DCR 0.72)*	*-6.46 ksi (DCR 0.97)*	*-6.61 ksi (DCR 0.99)*
Bottom Right	*-3.339 ksi (DCR 0.50)*	*-0.723 ksi (DCR 0.108)*	*-1.08 ksi (DCR 0.16)*
$\hat{\phi}_{comp}$	*0.295 Radians*	*0.2352 Radians*	*0.2591 Radians*
$\hat{\phi}_{comp}/\phi_{eq}$	*3.554*	*1.07*	*1.01*

Except for the two top right corners that cracked (shown in bold font), the Standard Configuration WF100G girder passes all the other stress checks in the hauling cases. In the two cracked cases, the girder is right up against the limiting angle/stress for allowable compressive stress failure. This suggests that a truck with higher stiffness should be used, or perhaps larger overhangs or higher concrete strength should be designed for. The fact that $\hat{\phi}_{comp}$ drops for a girder with effectively more load (+20% impact case) highlights the impact of weak-axis bending on lateral stability performance. The increased weak-axis bending moment and compression on the left side of the girder because of the higher load outweighs the increased tension in the bottom flange because of the strong-axis bending moment. Note that this compressive stress limit angle is still a fair amount below Mast's (1993) maximum allowable roll angle of 0.4 radians. The equilibrium angle for the 6% cross slope case would have a factor of safety against Mast's failure point of 1.55 (his suggested safety factor being 1.5) while the factor of safety against allowable compressive stress failure is only 1.01.

The six percent cross slope case is the most critical of both the hauling cases and the lifting cases. The lifting case may control the minimum required initial strength, but the six percent cross slope hauling case has the largest equilibrium angle, the greatest extent of cracking, and the highest compressive stresses as well.

Following this proposed design procedure, the Standard Configuration WF100G girder could be lifted in its current design, and then successfully hauled to site on a truck with a rotational stiffness of 50000 in-kips/Radian. The girder would crack, but it achieves equilibrium before violating any compressive stress limits and reaching its likely failure point. A truck stiffness of 60000 in-kips/Radian, or larger overhangs, greater concrete strength, and/or more

temporary top strands could perhaps be used instead to keep the factor of safety against compressive failure higher.

8.5. **Case Study 3: Proposed Design Method for 250-foot-span LWC Modified WF100G Girder**

It is of great interest to see what steps are necessary to successfully design very long-span girders while considering lateral stability. To explore this, another design example will be shown here. The girder is made of LWC. It is a WF100G with a modified top flange that is one foot wider than normal (now 61 inches.) The bridge is nominally 250-feet-long, but the girder itself is 248-feet-long, with one foot of abutment at each end of the girder to hit the 250-foot centerline-to-centerline length of the bridge. The equations and ratios within the Standard Configuration become less realistic for very long-span girders. To ensure the most realistic design possible that would satisfy service loading conditions, Richard Brice at WSDOT was kind enough to run the 250-foot modified WF100G through WSDOT's prestressed concrete girder design program, *PGSuper*, to determine a starting design configuration. That design, which would satisfy in place service loading, will then be tested through the proposed design procedure, to see if it passes all lateral stability design checks. The same format and procedure presented in the previous two examples will be used here.

8.5.1. **250-Foot-Long LWC Modified WF100G: Lifting Case**

To satisfy service requirements, the girder has 46 straight strands, 34 harped strands, and 10 temporary top strands. This is the maximum number of strands able to be fit into the WSDOT WF series. Beyond this point, either higher strength strands or larger strands would need to be used to increase the prestressing amount, although fitting the strands into the cross section becomes an issue with larger strands. It is made of LWC, with a density of 125 pcf. The initial concrete strength is 8.4 ksi. The modulus of elasticity was calculated using AASHTO LRFD 2017 Equation 5.4.2.4-1 with K_1 equal to 1.0. The transformed section properties and other relevant design information are shown in Table 8.18.

Table 8.18 Design Parameters and Section Properties for Lifting Case of 250 Foot Modified LWC WF100G

Girder Design and/or Cross-Sectional Property	**Value**
Length	*248 ft.*
Transformed Cross Sectional Area	*1260 in^2*
Strong-Axis Stiffness, EI_{xx}	*7.164E9 kip-in^2*
Weak-Axis Stiffness, EI_{yy}	*4.1946E8 kip-in^2*
Torsional Stiffness, *GJ*	*2.8656E7 kip-in^2*
Distance to Top from Center of Gravity, y_{top}	*-53.1446 in.*
Distance to Bot. from Center of Gravity, y_{bot}	*46.8554 in.*
Top Strong-Axis Section Modulus, S_{x2}	*-35619 in^3*
Bottom Strong-Axis Section Modulus, S_{x1}	*40400 in^3*
Top Weak-Axis Section Modulus, S_{yT}	*3634 in^3*
Bottom Weak-Axis Section Modulus, S_{yB}	*5776.5 in^3*
Self-Weight, Accounting for Strand and Rebar	*0.0876 kip/in*
Initial Concrete Strength	*8.4 ksi*
Initial Concrete Modulus of Elasticity	*3784.5 ksi*
Overhang Length during Lifting	*35 ft.*
Prestressing Deflection (No Self-Weight) at Lifting	*-17.1 in*

The initial roll angle of the girder during the hanging case is calculated in the same way as the previous two examples. The necessary values are reported in Table 8.19.

Table 8.19 Parameters for Calculating the Initial Roll Angle of the 250 Foot Modified LWC WF100G, Lifting Case

Parameters for Calculating Initial Roll Angle	**Results**
Maximum Sweep, u_{sweep}	*3.1 in.*
Sweep at Support Points, $\Delta_u(\alpha)$	*1.348 in.*
Lifting Loop Eccentricity, e_x	*-0.25 in.*
Lateral Deflection of Center of Gravity, $\overline{u}_{sweep,\alpha} - e_x$	*0.885 in.*
Maximum Prestressing Deflection, $v_{p,max}$	*-17.1 in.*
Camber at Support Points, $\Delta_p(\alpha)$	*-7.436 in.*
Vertical Deflection of Center of Gravity, $\overline{v}_{p,\alpha}$	*-3.507 in.*
Average Prestressing Deflection from Ends of Girder, $\overline{v}_p$	*-10.944 in.*
Tangent of Initial Roll Angle, $\tan \phi_o$	***0.0178***
Initial Roll Angle, ϕ_o	***1.0225 Degrees***

Despite its significantly longer length and greater prestressing and sweep imperfections, the 250-foot modified LWC WF100G has a lower initial roll angle than the Standard Configuration WF100G. This is a function of its overhang ratio being roughly four percent higher and highlights the very stabilizing effect of reasonably long overhangs.

The critical load and the final equilibrium angle are calculated in the same way as shown in the first example, and those values are summarized in Table 8.20.

Table 8.20 Values for Calculating the Critical Load and Final Equilibrium Angle for the 250 Foot Modified LWC WF100G, Lifting Case

Parameters for Calculating Critical Load	**Results**
Critical Lateral-Roll-Buckling Load, $q_{LRB,o}$	*0.0341 kip/in*
Factor Accounting for Overhangs, $f_{LRB}(\alpha)$	*0.126*
Factor Accounting for Torsion, $g(\eta_{vp\alpha})$	*0.6855*
Combined Factors due to SAB and Prestressing	*0.992*
Critical Load, q_{cr}	***0.184 kip/in***
Ratio of Self-Weight to Critical Load, $\frac{q}{q_{cr}}$	***0.476***
Final Equilibrium Angle, ϕ_{eq}	***0.0341Radians***
Cracking Angle, $\hat{\phi}_{crack}$	***0.1279 Radians***
Compression Failure Angle, $\hat{\phi}_{comp}$	***0.1078 Radians***

The LRB load is very small in this configuration, despite the wide top flange, because of the long length. The girder does not buckle only because of the stabilizing effect of the overhangs, for the combined SAB and prestressing deflection effects, as well as torsion, are both destabilizing. Because of the overhangs, and partially because of the LWC, the self-weight is less than half of the critical load, and the final equilibrium angle is much smaller than the cracking angle. Interestingly, the compressive failure angle is smaller than the cracking angle. This is a nod towards the large number of prestressing strands in the bottom flange at midspan and the fact that initial compression tends to control the initial required strength.

The stresses in the four corners of the girder in the lifting case are reported in Table 8.21.

Table 8.21 Stresses and Comparison to Allowable Stress Limits for the 250 Foot Modified LWC WF100G, Lifting Case

Compressive Stress Limit, $0.7f'_{ci}$	***-5.88 ksi***	**Tensile Stress Limit, $0.24\lambda\sqrt{f'_{ci}}$**	***0.6521 ksi***
Top Left Corner Stress	*-1.235 ksi*	Top Right Corner Stress	*-0.442 ksi*
Top Left Demand-to-Capacity Ratio	*0.21 (OK)*	Top Right Demand-to-Capacity Ratio	*0.075 (OK)*
Bottom Left Corner Stress	*-5.341 ksi*	Bottom Right Corner Stress	*-4.843 ksi*
Bottom Left Demand-to-Capacity Ratio	*0.908 (OK)*	Bottom Right Demand-to-Capacity Ratio	*0.823 (OK)*

The girder passes all stress checks, with the bottom left corner closest to the compressive limit. For this long of a girder, if the overhang length is increased enough, it does not appear that the lifting case is the most critical scenario for lateral stability. All stress checks are satisfied, and the final equilibrium angle is not that large. The initial strength must be quite high because of the large number of prestressing strands. This appears to be the largest constraint on this design satisfying the lifting checks.

8.5.2. **250-Foot-Long LWC Modified WF100G: Hauling Cases**

The transformed section properties and other relevant design information for the hauling cases are reported in Table 8.22.

Table 8.22 Design Parameters and Section Properties for Hauling Cases for the 250 Foot Modified LWC WF100G

Girder Design and/or Cross-Sectional Property	**Value**
Length	*248 ft.*
Transformed Cross Sectional Area	*1256 in^2*
Strong-Axis Stiffness, EI_{xx}	*7.3245E9 kip-in^2*
Weak-Axis Stiffness, EI_{yy}	*4.2945E8 kip-in^2*
Torsional Stiffness, *GJ*	*2.9423E7 kip-in^2*
Distance to Top from Center of Gravity, y_{top}	*-53.0644 in.*
Distance to Bot. from Center of Gravity, y_{bot}	*46.9356 in.*
Top Strong-Axis Section Modulus, S_{x2}	*-35521 in^3*
Bottom Strong-Axis Section Modulus, S_{x1}	*40160 in^3*
Top Weak-Axis Section Modulus, S_{yT}	*3623.5 in^3*
Bottom Weak-Axis Section Modulus, S_{yB}	*5759.8 in^3*
Self-Weight, Accounting for Strand and Rebar	*0.0876 kip/in*
Concrete Strength	*9.1 ksi*
Concrete Modulus of Elasticity	*3885.8 ksi*
Overhang Length during Hauling	*30'-10"*
Prestressing Deflection (No Self-Weight) at Hauling	*-20.246 in.*

Note that the overhang length was shortened during the Hauling case per the design information from *PGSuper*. The concrete strength and, correspondingly, the modulus of elasticity increased. Prestressing losses of 3.5 percent, which is consistent with the WSDOT WF74G design example, were assumed.

The initial imperfection parameters necessary for calculating the initial roll angle in the three different hauling cases are summarized in Table 8.23.

Table 8.23 Parameters for Calculating the Initial Roll Angle for the 250 Foot Modified LWC WF100G, Hauling Cases

Parameters for Calculating Initial Roll Angle	**Values**
Maximum Sweep, u_{sweep}	*3.1 in.*
Sweep at Support Points, $\Delta_u(\alpha)$	*1.197 in.*
Bunking Point Eccentricity, e_x	*1.0 in.*
Lateral Deflection of Center of Gravity, $\overline{u}_{sweep,\alpha} - e_x$	*1.786 in.*
Maximum Prestressing Deflection, $v_{p,max}$	*-20.246 in.*
Camber at Support Points, $\Delta_p(\alpha)$	*-8.739 in.*
Vertical Deflection of Center of Gravity, $\overline{v}_{p,\alpha}$	*-4.217 in.*
Average Prestressing Deflection, from Ends of Girder, $\overline{v}_p$	*-12.957 in.*

The critical loads, parameters for solving them, the initial roll angles, and the final equilibrium angles are reported in Table 8.24. The required truck rotational stiffnesses are also reported in Table 8.24.

Table 8.24 Critical Load Parameters and Final Equilibrium Angle for the 250 Foot Modified LWC WF100G, Hauling Cases

Parameter	**2% Cross Slope, -20% Impact**	**2% Cross Slope, +20% Impact**	**6% Cross Slope, No Impact**
Reaction, R	*-104.27 kips*	*-156.41 kips*	*-130.34 kips*
$K_{\phi,supp}$	*20000 in-kip/Radian (40000 Total)*	*32500 in-kip/Radian (65000 Total)*	*37500 in-kip/Radian (75000 Total)*
$y_{r,eq}.$	*-58.361 in.*	*-75.762*	*-98.278 in.*
κ_{Mast}	*1.0*	*1.0*	*0.688*
$\boldsymbol{\tan \phi_o}$	***0.0535***	***0.0452***	***0.0791***
ϕ_o	*3.068 Degrees*	*2.595 Degrees*	*4.536 Degrees*
$q_{LRB,o}$	*0.0383 kip/in*	*0.0497 kip/in*	*0.0444 kip/in*
$f_{LRB}(\alpha)$	*0.1796*	*0.1796*	*0.1796*
$g(\eta_{vp\alpha})$	*0.732*	*0.64*	*0.6099*
SAB & Prestressing	*0.9687*	*0.99*	*1.006*
$\boldsymbol{q_{cr}}$	***0.151 kip/in***	***0.1758 kip/in***	***0.152 kip/in***
$\boldsymbol{\frac{q}{q_{cr}}}$	***0.462***	***0.5978***	***0.576***
$\boldsymbol{\phi_{eq}}$	***0.0989 Radians***	***0.111 Radians***	***0.1807 Radians***
$\boldsymbol{\widehat{\phi}_{crack}}$	***0.132 Radians***	***0.1224 Radians***	***0.1266 Radians***
$\boldsymbol{\widehat{\phi}_{comp}}$	***0.2043 Radians***	***0.184 Radians***	***0.1921 Radians***

The two percent cross slope case with impact upwards (less weight effectively) does not crack with the lowest truck stiffness. It is clearly the least critical case. The two percent cross slope case with impact downwards does not crack either, although it is close to its cracking point. With a total truck stiffness of 60000 in-kip/Radian (compared to the current 65000) the girder does crack, and it just barely violates the allowable compressive stress/equilibrium angle. This goes to show the importance of the truck stiffness on lateral stability performance during the

hauling cases. Without changing any other design parameters, a change in truck stiffness can make a girder crack or not and significantly change the final equilibrium angle. The six percent cross slope case is once again the most critical. It requires the largest stiffness to pass the lateral stability design checks and still has the largest equilibrium angle. It has cracked and is approaching the compressive stress limit. A truck stiffness of 110000 in-kip/Radian would be required to completely prevent cracking. This is greater than what is commercially available today. To transport a girder of this length, designers would either need to accept some cracking in the girder or change the design in some way (increase overhangs, temporary top strands, or concrete strength, for example) to prevent cracking.

The stresses in the three different hauling cases are presented in Table 8.25.

Table 8.25 Stresses and Demand-to-Capacity Ratios for the 250 Foot Modified LWC WF100G Hauling Cases

Compressive Stress Limit $0.7f'_{ci}$	***-6.37 ksi***	**Tensile Stress Limit, $0.24\lambda\sqrt{f'_{ci}}$**	***0.678 ksi***
Location	**2% Cross Slope, -20% Impact**	**2% Cross Slope, +20% Impact**	**6% Cross Slope, No Impact**
Top Left	*-1.813 ksi (DCR 0.28)*	*-3.081 ksi (DCR 0.484)*	*-3.42 ksi (DCR 0.53)*
Top Right	*0.311 ksi (DCR 0.43)*	*0.493 ksi (DCR 0.727)*	***1.40 ksi (DCR 2.07)***
Bottom Left	*-5.659 ksi (DCR 0.88)*	*-5.635 ksi (DCR 0.884)*	*-6.28 ksi (DCR 0.98)*
Bottom Right	*-4.322 ksi (DCR 0.67)*	*-3.384 ksi (DCR 0.531)*	*-3.24 ksi (DCR 0.50)*
$\hat{\phi}_{comp}$	*0.2043 Radians*	*0.184 Radians*	*0.1921 Radians*
$\frac{\hat{\phi}_{comp}}{\phi_{eq}}$	*2.065*	*1.657*	*1.063*

All the stress checks are satisfied, except for the one location that cracks in the six percent hauling case. The six percent hauling case is the most critical case both in terms of final equilibrium angle and in terms of stresses; the factor of safety relative to allowable compressive stress failure is 1.063. Compared to Mast's (1993) final failure angle of 0.4 radians (for which he based his factor of safety against failure of 1.5), the six percent cross slope case has a factor of safety of 2.213. This illustrates how the girder is much closer to the allowable compressive stress limit point than it is to Mast's limiting point.

In conclusion, it is possible to satisfy the lateral stability design checks for a girder of this length. The lifting case does not crack or have the largest equilibrium angle, but it is largely constrained by the initial concrete strength. Large required concrete strengths may be necessary to lift such long girders, but manufacturing girders with the required properties may take longer than normal (extended curing periods) and could introduce some delays into the construction process. The girder can be hauled to site successfully, provided high enough truck stiffnesses are used. To completely prevent cracking in the most critical case (six percent cross slope) an unrealistically large truck stiffness would need to be used. Either some cracking would need to be accepted or the design would need to be changed in some way for long-span girders like this to be shipped to site.

Furthermore, this 250-foot length of bridge would likely be the upper bound possible length for the cross-sections currently available. The number of prestressing strands in the cross section is already maximized. Unless larger (difficult to use) or stronger strands were used, or the cross section were changed, the service loading likely constrains the length for girders of this depth. Additionally, as girders get longer, the shipping weight of the girder becomes an increasingly large concern, as does the physical ability to make turns in potentially urban

environments. If this 250-foot length does indeed represent an upper bound, it is then reassuring to know that there are feasible ways for the girder to be shipped to site while still passing lateral stability design checks.

9. Design Trends and Recommendations

This chapter zooms out from the fine details in Chapter 8 to explore trends in some of the relevant lateral stability design parameters for a series of long-span girders. It is focused on a motivating question: what is the longest span girder that can be successfully handled and transported and then perform adequately in service? This chapter will explore what design parameters currently limit span-length, where limits exist that would prohibit increasingly longer girders, and what parameters could be changed to improve lateral stability performance. Ultimately, it will hope to show the maximum span-length that can be reasonably designed/constructed today, and what could be done to optimize that girder.

9.1. **Design Parameter versus Length Plots**

To explore the maximum span-length question, the same design procedure shown in Section 8.5 was repeated for five different girders of lengths of 178, 198, 218, 238, and 248 feet. Note that the bridges of these girders would be the nearest round number long (e.g., 220 ft.), but the abutment design shortens the span of the actual girders by two feet. Their initial designs (number of strands, concrete strengths, prestressing deflections, overhang lengths, truck stiffnesses) were determined by runs of the program *PGSuper*, graciously done by WSDOT. All the girders were LWC with the modified 61-inch-wide top flange used in Section 8.5. The detailed information required for the lifting and hauling designs of these girders, like shown in Chapter 8, is not shown here as that is not the purpose of this section, but the overall layout and design of each girder is summarized in Table 9.1.

Table 9.1 Summary of Girder Designs from *PGSuper* Runs

Length	**180 ft**	**200 ft**	**220 ft**	**240 ft**	**250 ft**
Number of Straight Strands	36	42	46	46	46
Number of Harped Strands	12	15	20	28	34
Number of Temp. Top Strands	4	6	8	8	10
f'_{ci} at Lifting	5.2 ksi	6.2 ksi	7.2 ksi	8.1 ksi	8.4 ksi
f'_c at Hauling	5.8 ksi	6.7 ksi	7.5 ksi	8.5 ksi	9.1 ksi
Lifting Points	12.25 ft	17.75 ft	23.25 ft	35 ft	35 ft
Hauling Bunk Points	8.33 ft	10 ft**	19 ft**	30.833 ft	30.833 ft
$v_{p,max}$ at Lifting	-7.518 in	-9.863 in	-12.436 in	-14.885 in	-17.148 in
Additional Creep Prestressing Deflections at Hauling	-3.807 in	-3.875 in	-3.675 in	-3.348 in	-3.146 in
Total Truck Stiffness $K_{\phi,Supp}$ (inch-kip/Radian)	80,000	80,000	80,000	80,000	80,000
** *PGSuper* Designed 8.33 ft and 15.833 ft for the 200 and 220 ft girders respectively. When ran through Rollbuck 2022, these designs failed immediately upon cracking. The overhang lengths were increased to provide "life after cracking."					

The lifting case and the six percent cross slope case, the most critical of the hauling cases, were analyzed using the proposed lateral design procedure. A series of plots is shown below. The vertical axis on each plot shows a different design parameter or constraint but the horizontal axis is consistently the girder length. The plots will be presented uninterrupted to allow the viewer to compare the different vertical axis parameters against a constant length scale. In order, the plots will show, all versus length:

1. Equilibrium Angle, Cracking Angle, and Compression Angle
2. Number of Bottom Strands
3. Girder Weight

4. Concrete Strength
5. Number of Temporary Top Strands
6. Overhang Ratio
7. Total Truck Stiffness

Where a limit exists, it will be denoted on the plot. For example, a maximum of 80 bottom strands fit into the WSDOT WF series. This will be shown as a horizontal line on plot number two. The consistent horizontal axes allow the viewer to see what the value of an alternative design parameter is when a certain constraint begins limiting the design.

The design values from *PGSuper* will be shown as solid lines. In some instances, dashed lines will be plotted that show the value of a design parameter that would cause a different lateral stability behavior. For example, plot number six will show the overhang ratios that came from *PGSuper*, but it will also show the overhang ratio required to prevent cracking in the hauling case and the minimum overhang ratio required to not have compressive failure in the lifting case, both as dashed lines. In essence, this is like conducting a mini-parametric study. Keeping all other parameters constant, one parameter is modified at a time to determine how it influences the design, and to see whether a design objective, like preventing cracking, is achievable by modifying that parameter. In this way, the reader can see which design modifications could feasibly improve lateral stability performance—making the design of long span girders easier—and which modifications violate current limits or are not realistic. The plots are shown, uninterrupted, in Figure 9.1.

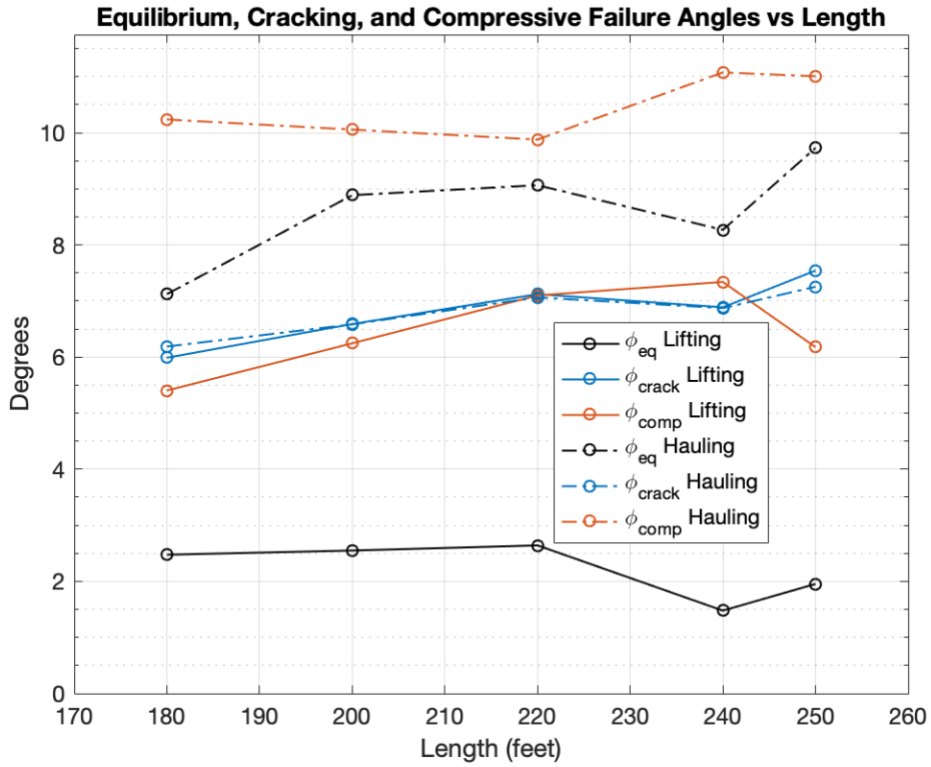
Equilibrium, Cracking, and Compressive Failure Angles vs Length
Degrees
Length (feet)
ϕ_{eq} Lifting
ϕ_{crack} Lifting
ϕ_{comp} Lifting
ϕ_{eq} Hauling
ϕ_{crack} Hauling
ϕ_{comp} Hauling

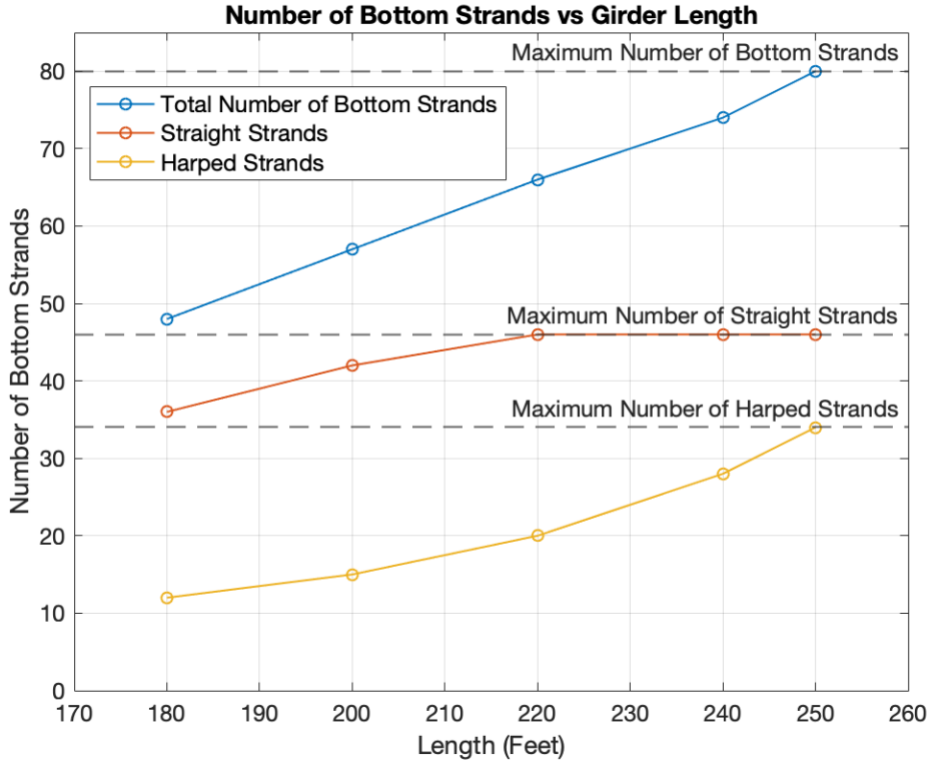
Number of Bottom Strands vs Girder Length
Number of Bottom Strands
Length (Feet)
Total Number of Bottom Strands
Straight Strands
Harped Strands
Maximum Number of Bottom Strands
Maximum Number of Straight Strands
Maximum Number of Harped Strands

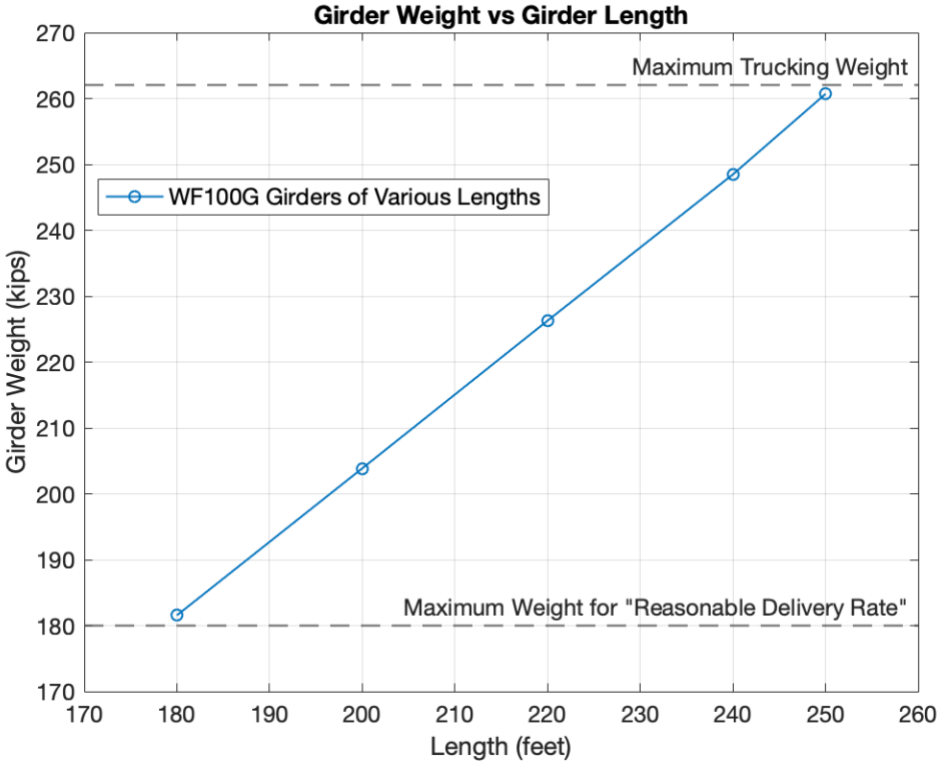
Girder Weight vs Girder Length
Maximum Trucking Weight
WF100G Girders of Various Lengths
Maximum Weight for "Reasonable Delivery Rate"
Girder Weight (kips)
Length (feet)
270
260
250
240
230
220
210
200
190
180
170
170
180
190
200
210
220
230
240
250
260

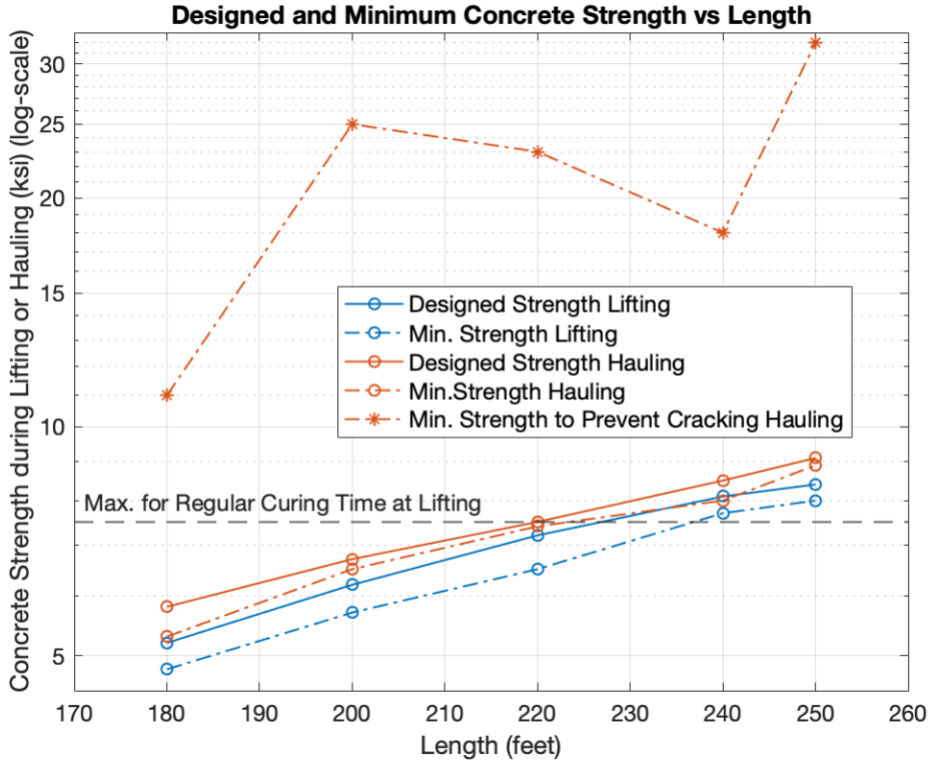
Designed and Minimum Concrete Strength vs Length
Designed Strength Lifting
Min. Strength Lifting
Designed Strength Hauling
Min.Strength Hauling
Min. Strength to Prevent Cracking Hauling
Max. for Regular Curing Time at Lifting
Concrete Strength during Lifting or Hauling (ksi) (log-scale)
Length (feet)
30
25
20
15
10
5
170
180
190
200
210
220
230
240
250
260

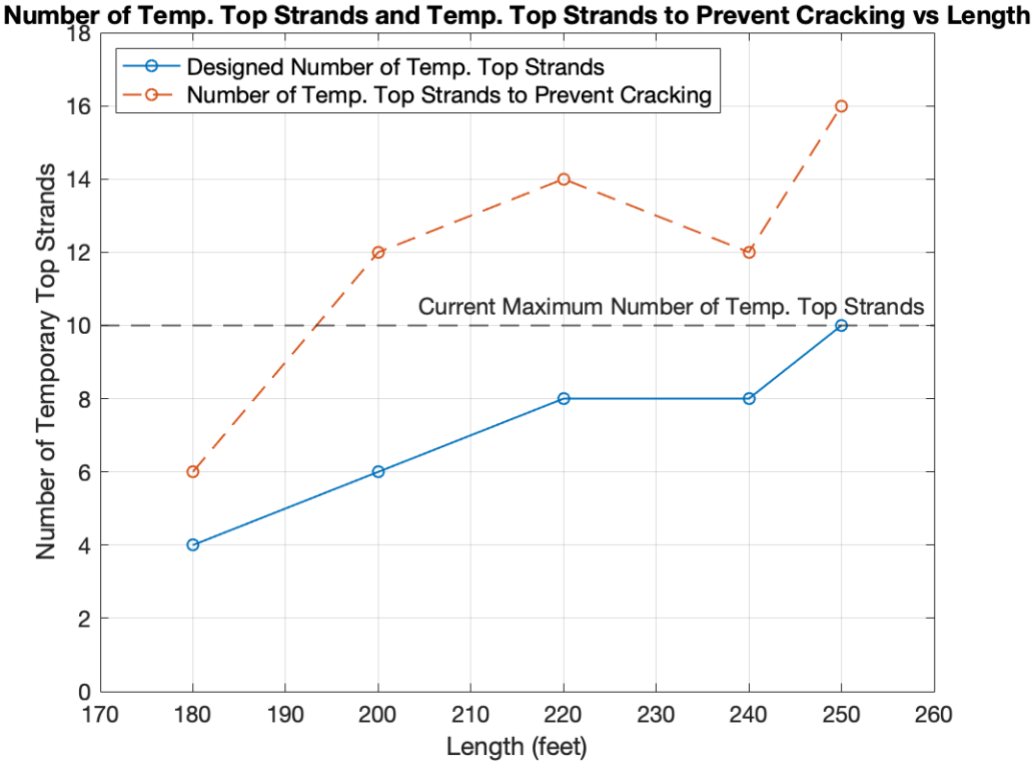
Number of Temp. Top Strands and Temp. Top Strands to Prevent Cracking vs Length
Designed Number of Temp. Top Strands
Number of Temp. Top Strands to Prevent Cracking
Current Maximum Number of Temp. Top Strands
Number of Temporary Top Strands
Length (feet)
0
2
4
6
8
10
12
14
16
18
170
180
190
200
210
220
230
240
250
260

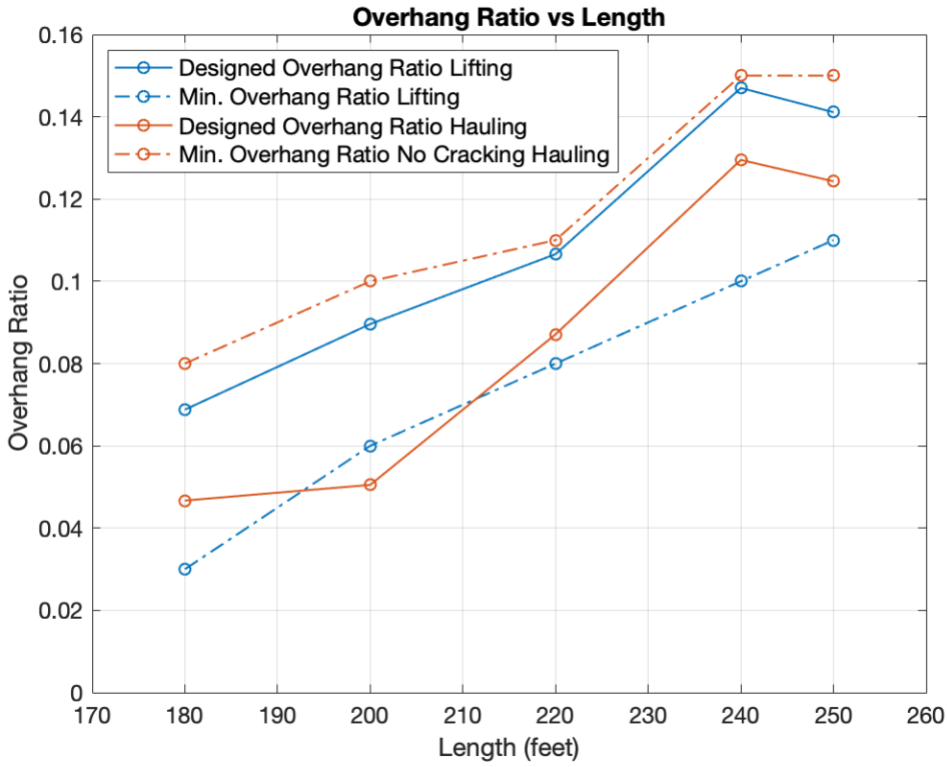
Overhang Ratio vs Length
Designed Overhang Ratio Lifting
Min. Overhang Ratio Lifting
Designed Overhang Ratio Hauling
Min. Overhang Ratio No Cracking Hauling
Overhang Ratio
Length (feet)
0
0.02
0.04
0.06
0.08
0.1
0.12
0.14
0.16
170
180
190
200
210
220
230
240
250
260

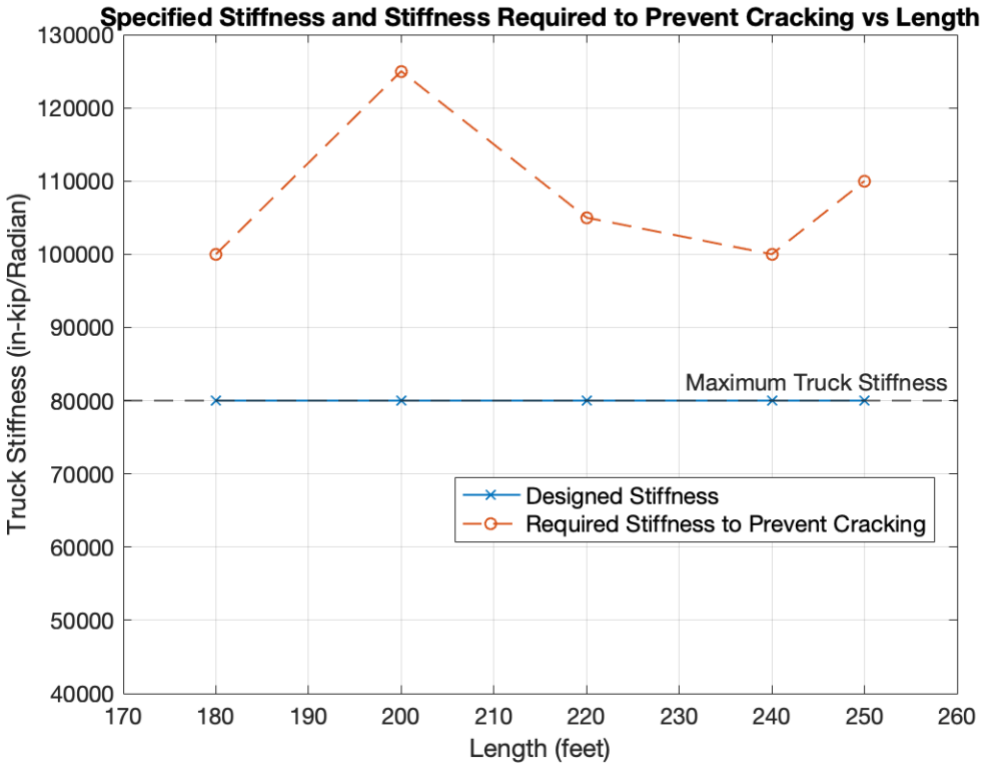

Figure 9.1 Series of Different Design Parameters vs Girder Length. In Order: 1. Equilibrium, Cracking, and Compression Failure Angles; 2. Number of Bottom Strands; 3. Girder Weight; 4. Concrete Strength; 5. Number of Temporary Top Strands; 6. Overhang Ratio; 7. Total Truck Stiffness

The first plot depicts the equilibrium, cracking, and compression failure angles versus the girder length. Throughout, the lifting case performs well. It is well below the compression failure angle and the cracking angle. Except for the 240-foot-long girder, the compression failure angle is lower than the cracking angle in the lifting case—generally the lifting case will violate compression checks before it cracks. This is likely a function of the low strengths at lifting, combined with the highest prestressing levels before most losses have occurred. The cracking angle is very similar between the lifting and hauling cases. The rupture strength is a function of the square root of the concrete strength. Thus, the small increases in concrete strength from the lifting to hauling conditions represent an even smaller increase in rupture strength. Conversely, the compression failure angle goes up quite a bit. The equilibrium angle in the hauling cases is

consistently above the cracking angle, but below the compression angle. Since Chapter 7 showed that the girder has “life after cracking”, i.e., does not need a Factor of Safety of 1.0 against cracking, this suggests that compression failure, rather than cracking, is what should be guarded against in design.

The next plot shows the number of bottom strands versus the girder length. Here, there are limits on the number of strands that can be fit into the WSDOT WF series cross sections: 34 harped strands and 46 straight strands. The shortest girders have less than the maximum 80 total strands, while the longest 250-foot girder utilizes every available strand space. In terms of service load design then, a girder longer than 250 feet could not be used without making some other change in the design. This could include increasing the concrete strength, the strength of the prestressing strands, or the area of the strands to get more prestressing force, but all these modifications add difficulties or cost to the girder design. Most likely, a limit exists on girder length at approximately 250 feet. If enough prestressing could be added to satisfy service loading, a deeper girder could be made to work; however, it would then likely be too heavy and violate the trucking weight limit. To create longer girders, different cross sections would need to be used or significantly different material properties would need to be designed for.

This 250-foot limit also exists in the next plot, which examines girder weight. The 180-foot girder weighs just over 180 kips, while the 250-foot girder weights just under 262 kips. Per a WSDOT bridge design memorandum from April 2021, the maximum weight for a “reasonable delivery rate” is 180 kips, while the maximum weight that can be shipped by road with today’s commercially available equipment, albeit in a limited fashion, is 262 kips (Khaleghi, 2021). From this third plot, the 180-foot girder exceeds the weight limit for “reasonable delivery” rates while the 250-foot girder is just barely within the maximum allowable weight. Beyond this

length, the girder would not be allowed to ship over the road. This would significantly limit the utility of very long span girders, as they could only be used in places that could be accessed by barge. Further, this does not consider potential delays in construction time due to the girders being over 180 kips and there being limited trucking equipment to haul the girders to site.

The next plot shows the concrete strength at lifting and hauling versus the girder length. Note the log-scale of the vertical axis. In solid lines are the designed values. As would be expected, the strength increases as the span (and prestressing force) increases. Below each of the respective lifting and hauling lines is a dashed line. This line indicates the strength the concrete could be lowered to without violating a limit—be it cracking for the hauling girders or compressive failure for the lifting girders. There is some margin in the designs, so these dashed lines are slightly lower than the solid designed-for lines. At much higher strengths is another line indicating the strength that would be required to completely prevent cracking in the hauling case. This strength is unreasonably high for all the girder lengths considered, especially for the LWC that is used. This is likely due to the rupture strength being a function of the square root of the concrete strength. Therefore, increasing the concrete strength by itself to prevent cracking in long-span girders during hauling is not a practical solution.

Another limit is reached in the next plot, depicting the number of temporary top strands versus the girder length. The maximum number of temporary top strands able to be used with a conventional design is currently 10, per section 5.1.3.A of the WSDOT Bridge Design Manual although more force can be generated if larger strands are used (WSDOT Bridge and Structures Office, 2022). This maximum number is hit for the 250-foot girder. Beyond this length, using conventional design standards, relatively less benefit would be gained from the limited number of temporary top strands. The use of temporary top strands is quite beneficial to girder

performance, especially post cracking, as was shown in Chapter 7. Increasing the number of temporary top strands slightly above the current limit of 10 completely prevents cracking in the hauling cases of the 200-foot-long girders, and higher. With these modified-wide-top-flange girders, there is space available for more temporary top strands to be used. One potential limitation of using more temporary top strands would be the increased overturning moments imposed upon the fabricators jacking equipment. If this constraint, or others limiting the number of strands to 10, could be overcome, increasing the number of temporary top strands is a very effective way of quickly improving performance.

The next plot shows the overhang ratio versus the length. The overhang ratio progressively increases with the girder length, until the 240 and 250-foot-long girders, which both have 35-foot overhangs during lifting and 30.83-foot overhangs during hauling per *PGSuper.* The overhang lengths remaining the same but the overhang ratio dropping goes some way towards explaining the jumps in some of the curves for these girder lengths, namely the concrete strength, temporary top strands, and truck stiffness plots. The overhangs play a very large role in the girder's stability. Chapter 8 showed the large increase in critical load that overhangs cause, as did Chapters 4 and 5, while Chapter 7 showed the beneficial post-cracking performance that is gained from large overhangs. There is perhaps a linkage between the designed for overhang length in the hauling case and the concrete strength required to prevent cracking. For example, the 240-foot girder requires a lower concrete strength to prevent cracking than the 250-foot girder, and it simultaneously has a larger overhang ratio (but same overhang length) than the 250-foot girder. This would suggest that the larger overhang ratio leads to a lower concrete strength; however, there are many different parameters affecting the girder's performance, and it is difficult to isolate the effects of any one design decision.

Perhaps the dashed lines are the most telling part of the overhang ratio plot. For the lifting case, the dashed line shows the overhang ratio that could be decreased to without causing cracking or compression failure. Since the lifting case girders don't crack or fail in compression, there is some margin there for lower overhangs to be used, if so desired. The hauling case dashed line shows the minimum overhang ratio that would need be designed for to prevent cracking from occurring at all. It is not significantly larger than the current designs from *PGSuper*. Increasing the overhang length could then be a fairly easy way to improve stability performance and prevent cracking from occurring during transportation, especially if increasing the concrete strength or the truck stiffness is not a realistic option. There are possible restrictions to increasing the overhang length during trucking, such as space limitations between the cab and the front jeep, or top tension over the supports due to the long overhangs. The first issue could be solved by using asymmetric overhangs. The WSDOT lateral stability design webinar revealed that asymmetric overhangs can be reasonably approximated by taking the average of the overhang lengths. Galik, Stanton, and Wiebe (2022) also suggested this workaround. The issue of top tension over the supports could be solved by increasing the number of temporary top strands, space allowing.

The final plot shows the total truck stiffness versus the girder length. *PGSuper* designed each girder considering the maximum available truck stiffness of 80,000 in-kip/Radian. Even with this largest of truck stiffnesses, the girder still cracked in the hauling case. The dashed line in this plot shows the truck stiffness that would need to be provided to completely prevent cracking while hauling. Throughout, it is at least 20,000 in-kip/Radian higher than what is currently available, and thus increasing the truck stiffness is not a reasonable solution for preventing cracking, at least not with these designs. Lower truck stiffnesses could perhaps be

used if cracking was acceptable, or if design parameters like the overhang ratio, concrete strength, or number of temporary top strands were increased. Even if larger truck stiffnesses could be used and cracking could be prevented for very long span girders, the limit of approximately 250 feet described above still exists, regardless of truck stiffness.

9.2. Comparison to Mast's $\frac{I_{eff}}{I_{gr}}$ Equation

The five girders explored above can be compared to Mast's $\frac{I_{eff}}{I_{gr}}$ equation using the same procedure described in Chapter 7 for both the lifting and hauling cases. Note that the transformed section properties are used here rather than the gross ones. Figure 9.2 shows the results for the lifting case compared to Mast's curve.

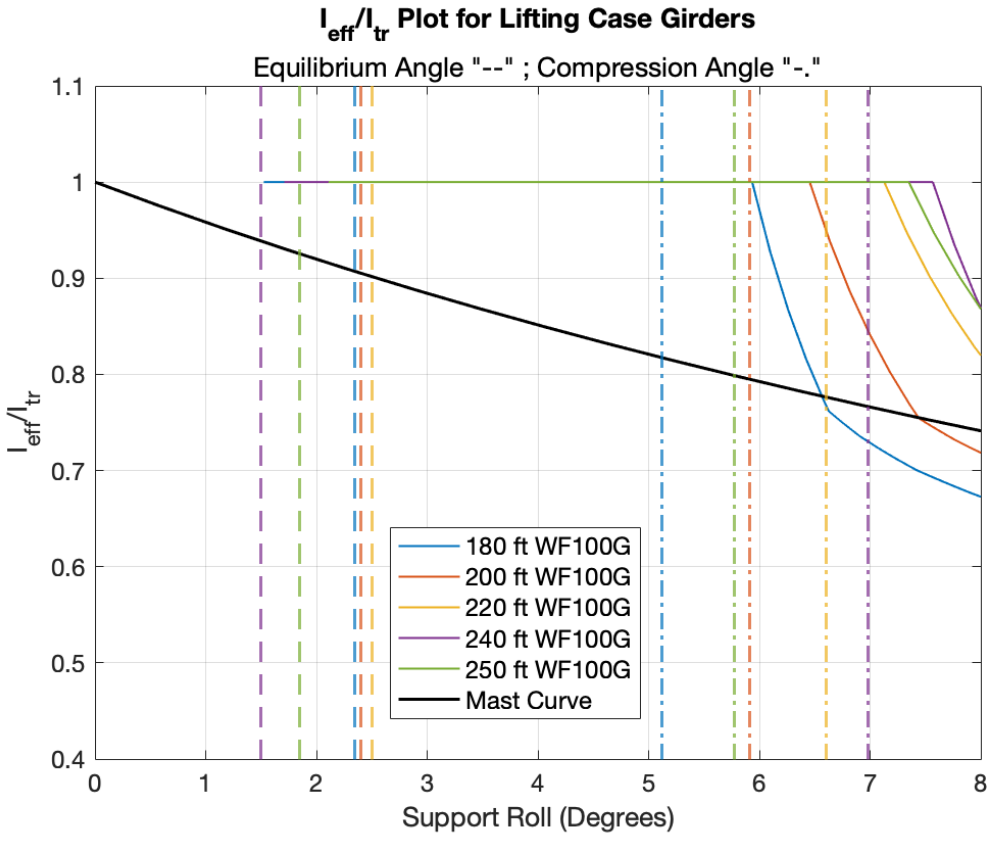

Figure 9.2 Comparison of Lifting Girders to Mast's Equation for the Effective Cracked Moment of Inertia

The results for each girder are grouped by color as indicated in the legend. The first set of vertical lines on the left, represented by dashed lines, indicate the equilibrium angle for each girder. The second set of vertical lines on the right, represented by dashed-dotted lines, indicate the allowable compression stress failure angle for each girder. Figure 9.2 shows that the equilibrium angle is well within the un-cracked range of behavior, which is represented by the plateau at 1.0 for each girder (which would theoretically extend back to the y-axis on the plot for each girder.) The compression failure angle generally being lower than the cracking angle is also shown, in that the second set of vertical lines occurs before the drop off the uncracked plateau. The girders do drop below Mast's curve; however, this occurs at angles much larger than the equilibrium angle, and at angles larger than the compression failure angle. This suggests that a girder in the lifting case would not be allowed to be designed to perform in a region that would be unconservative compared to Mast's curve. This is especially true if the girder fails in compression before Mast's equation even kicks into effect upon cracking. Further, Mast's (1993) factor of safety of 1.5 against failure at 0.4 radians would not be a good limit state for these girders, as they would fail in compression much sooner than Mast's failure point. This suggests that limiting the allowable compressive provides a conservative design compared to designing relative to final failure, approximated as 0.4 by Mast.

Figure 9.3 shows the same type of plot as Figure 9.2, but for the hauling case girders.

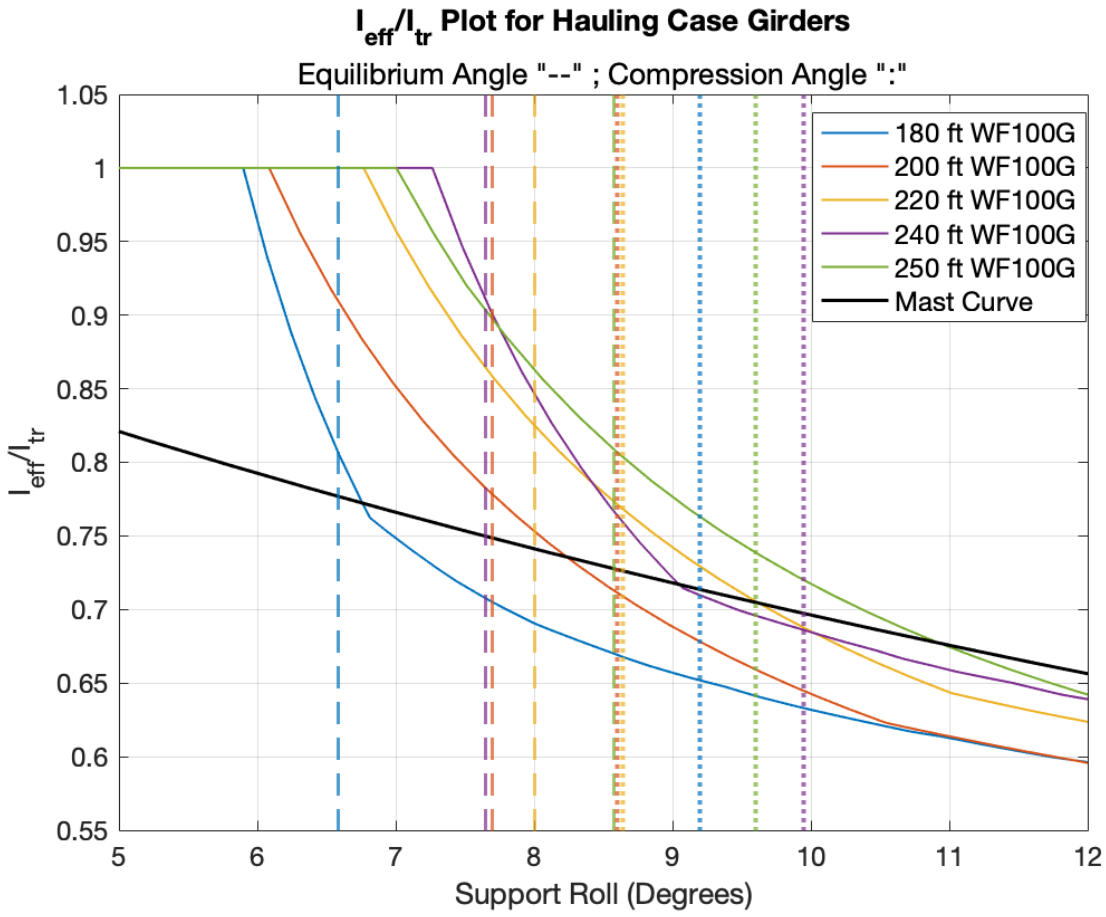

Figure 9.3 Comparison of Hauling Girders to Mast's Equation for the Cracked Moment of Inertia

Here, the dashed lines once again represent the equilibrium angle, while dotted lines represent the compression failure angle now (instead of dash-dot lines, for clarity). As was reflected in the first plot of Figure 9.1, the equilibrium angle in the hauling case occurs after cracking and the drop off the uncracked plateau. Each of the equilibrium angles is lower than their respective compression failure angle. Just as with the lifting girders, the hauling girders also drop beyond Mast's curve into a region where it is unconservative at large angles. However, the equilibrium angles all occur in a region that is conservatively bounded by Mast's curve, and the cracking angles are either likewise in a region conservatively bound by Mast's curve or are just

barely below it. This suggests that for cracking analysis, the girders can still be conservatively analyzed using Mast's equation. Further, Mast's factor of safety of 1.5 against a roll of 0.4 radians represents a maximum roll of 15.27 degrees (Mast, 1993). The allowable compressive stress failure angles are all a fair amount below this allowable angle. This suggests that designing for allowable compressive stress, rather than relative to failure, is conservative.

These plots, and the data in Chapter 7, show that cracking does not lead to immediate failure. Thus, girders could in principle be allowed to crack while being hauled by truck and still be conservatively bound by Mast's equation. The more proper constraint on their behavior is the compression failure angle. This angle occurs after cracking, but well before the ultimate failure point. This suggests that this should be the point that Factors of Safety are based on, not the cracking point. Mast's equation could likely still be used in an unmodified form, at least for the WSDOT WF girders. Even if the girder is slightly below Mast's curve at compression failure, it is not by much, and there is lots of reserve capacity until ultimate failure.

9.3. **Conclusions and Recommendations from Chapter 9**

Based on these results, some conclusions and recommendations from Chapter 9 may be made on optimizing lateral stability performance during lifting and hauling, and on the maximum length of girder that can currently be designed for:

1. In both the lifting and hauling case, girders should be designed so that exceeding allowable compressive stress is the limit state, not cracking. Girders can crack while still being conservatively designed.
2. While the girder does not collapse after exceeding allowable compressive stresses, the angle this occurs at may be unconservative compared to Mast's equation. A factor of safety of 1.5 against a roll of 0.4 radians is even more likely to be unconservative

compared to Mast's equation. A Factor of Safety against the allowable compressive stress limit of at least 1.0 should be used.

3. Per the results of the parametric study in Chapter 7, post-cracking performance relative to Mast's curve can be improved by increasing concrete strength, number of temporary top strands, or the overhang ratio. Low cracking strength in particular leads to a rapid decline in post-cracking stiffness.
4. While avoiding cracking is a design goal, a Factor of Safety against cracking of 1.0 is overly conservative, at least for the WSDOT WF girder series, in terms of stability during shipping and handling.
5. Increasing the Number of Temporary Top Strands or the Overhang Ratio is a quick way to prevent or reduce the likelihood of cracking. This is in contrast to increasing concrete strength or truck stiffness, which are not feasible methods for preventing cracking with currently available materials and trucks.
6. An upper limit on girder length exists at 250 feet for present girder cross-sections. This is not for lateral stability reasons. Overhangs, temporary top strands, and concrete strength all contribute towards making the girder sufficiently stable. Rather, this limit exists because of service design constraints and the maximum allowable shipping weight. New girder cross sections with larger bottom flanges, lighter and stronger concretes, and/or new trucking technology would be required to deliver girders longer than 250 feet to site.
7. If the issues raised in item 6 were resolved, longer girders could theoretically be used. Lateral stability is not necessarily the limiting factor.

10. Summary, Conclusions, and Future Work

10.1. Summary

The work described in this thesis provides advances to the state-of-the-art of lateral-roll buckling in six main areas:

Extensions to the calculated critical load. Previous work by Mast (1989) had provided the critical load for Lateral-Roll Buckling (LRB), and this had been extended by Galik, et al (2022) to include the effects of torsional flexibility. That work was further extended here to include the effects of strong-axis bending (SAB), deflections due to prestressing, overhangs, and the interaction of those factors with torsion included. It was also shown that the critical load for a girder supported from above (e.g., crane cables) or supported from below (e.g. a torsionally flexible truck) could be treated by a single formulation.

Amplification of initial imperfections. As is the case for column behavior, initial imperfections in girders are amplified in a nonlinear manner by the application of vertical load. The primary imperfections considered here are sweep, eccentric placement of lifting loops or truck support, and roadway cross-slope. Three methods were developed for computing that amplification, and they were compared with the predictions of previous researchers. The three methods provide different levels of complication and accuracy throughout the range of applied loads, each with an associated computational cost. In order of decreasing complication, they are referred to as: computer program Rollbuck 2021, the Rigid Link Model (RLM), and the Simple Amplification Model (SAM). The SAM agrees with Southwell's (1932) formulation for imperfection amplification, and the RLM is a large angle version of the SAM.

Imperfection sensitivity study using linear elastic, uncracked response. In this phase of the work, the magnitudes of the imperfections and the assumptions in the governing buckling

load were varied systematically to demonstrate their effects on lateral stability. The study was also used to explore the fidelity of the above three methods for computing the amplification of initial imperfections.

Extension to include cracking. Computer program Rollbuck 2021 was extended (and renamed Rollbuck 2022) to include the effects of flexural cracking. The material nonlinearities required to accurately account for cracking meant the that the calculations had to be numerical, and that exact closed-form amplification factors were no longer possible. The program was validated by comparing its predictions with the responses measured in tests by Mast (1993,1994). No other data, physical or computational, could be found for more extensive validation.

Parametric study of girders including flexural cracking. A parametric study was performed using the WSDOT WF100G girder cross-section. A "Standard Configuration" was established that reflected commonly used design values for the important parameters (e.g. span-to-depth, prestressing stress, overhang length, etc.), and those parameters were then varied systematically from those standard values. The post-cracking behavior was explored, with the results recorded as functions of important quantities like the initial cracking angle, final ultimate failure angle, and post-cracking stiffness degradation as the girder roll angle increased.

New design procedure. A new lateral stability design procedure was developed, based on the imperfection amplification predicted by the Rigid Link Model. It incorporates all the parameters used in the study (twisting deformations, prestressing deflections, cracking, etc.), but is still simpler to execute than the existing procedure. A series of design examples were presented, and some conclusions and recommendations for long-span girder lateral stability design were made.

10.2. Conclusions

- A closed-form equation is presented for the critical load of the girder, accounting for torsional deformations, strong-axis bending, prestressing deflections, and overhangs. It uses the same form as the one presented by Mast (1989) with modification factors accounting for each additional behavior.
- A single equation can be used to determine the critical load, regardless of whether the girder support is tensile (from above) or compressive (and unavoidably torsionally flexible, from below).
- For both Lateral-Roll Buckling (LRB) and Lateral-Torsional-Roll Buckling (LTRB), different imperfections that produce the same initial roll angle will lead to identical amplifications of that initial roll angle as the applied load is increased.
- The amplification of initial imperfections may be determined by any one of three methods developed here: computer program Rollbuck 2021, the Rigid Link Model (RLM), or the Simple Amplification Model (SAM). For typical applied loads and elastic uncracked behavior, they all give results that are essentially identical. In more extreme instances, the listed order reflects decreasing accuracy and computational effort.
- The RLM was originally developed using only lateral bending (i.e. LRB). Nonetheless, it is able to predict with a very high degree of accuracy the response under loads approximately equal to the critical load, indicating that LRB and LTRB amplify imperfections similarly in the pre-buckling range of loads.
- Stability is improved by some characteristics and made worse by others. Overhangs and Strong Axis Bending (SAB) are stabilizing. Upwards deflection due to prestressing and the inclusion of twisting deformations are destabilizing.

- Rollbuck 2022 was developed from Rollbuck 2021 to account for the effects of cracking. It accurately replicates Mast's (1993,1994) results from his physical test.
- Mast's equation for the effective cracked moment of inertia generally provides a (conservative) lower bound for the WSDOT WF girders, and for some, but not all, other girder types.
- After cracking due to lateral bending, the girder loses stiffness. However, in most girders studied, the remaining stiffness was sufficient to allow the girder to carry more vertical load and undergo more rotation.
- While a safety factor of 1.0 against cracking (in present use) is ideal, it is likely unnecessarily conservative for some girder series, but not for others that exhibit rapid drop-offs in post-cracking effective stiffness. Rather, a factor of safety against the allowable compressive stress limit in the post cracking regime should be adopted. Reaching that compressive stress limit would still precede inelastic failure of the girder.
- Increasing overhangs, coupled with corresponding increases in the number of temporary top strands and the concrete strength, is the most effective way to improve performance.
- The design procedure proposed here produced final equilibrium angles slightly larger than predicted by the current WSDOT/PCI lateral stability design procedure. This is attributed to the inclusion of torsional deformations.
- While lateral stability must be considered in the design of long-span girders, it is not necessarily the controlling factor that limits girder length. If a suitable arrangement of overhangs can be used to counteract instability, a combination of practical considerations, such as shipping weight, concrete strength at release, or service loading will likely control the maximum usable girder length for the cross sections presently available.

10.3. **Opportunities for Future Work**

While the degradation in stiffness due to flexural cracking was incorporated in this work, it is relatively unknown how flexural cracking affects torsional stiffness. Work by Lima and El Debs (2005) suggests that there is an approximately 20% decrease in torsional stiffness due to flexural cracking. That conclusion, however, was for reinforced concrete beams with negligible strong-axis bending (and naturally no prestressing), so it is unclear if that principal would apply to a prestressed concrete girder.

Accurately determining the torsional stiffness of the concrete, both pre- and post-cracking, the torque to induce pure torsional cracking, and the complete twist versus torque curve for a prestressed concrete girder would greatly inform lateral stability analysis. Then, the rate in torsional stiffness decline associated with cracking could be factored into the post-cracking analysis of a girder undergoing LTRB, which currently assumes constant linear torsional stiffness. If the girder loses torsional stiffness as a result of cracking, more twist—and thus more torque—could occur, leading to a negative feedback cycle which could exacerbate stability issues for LTRB.

Furthermore, while Rollbuck 2022 was validated against Mast's physical test results, it would be beneficial to compare results from Rollbuck 2022 against physical rollover tests of real girders. This would allow the program to be fine-tuned against experimental data and would allow for measurements of the proportion of twist relative to the total equilibrium angle. Additionally, it would allow the researchers to experimentally validate expected behavior at important points in the rollover behavior, such as the point of initial cracking, point of theoretical torsional cracking, and final failure/collapse point.

This work, and the information potentially gleaned from the tests described above, could be used to explore and optimize girder cross sections for long-span bridges. If designing longer-span bridges is an ultimate goal, the experimentally-fine-tuned Rollbuck 2022 could be used to determine design options that allow for sufficient lateral stability during transportation, handling, and erection while still adhering to other practical limits on girder length, such as maximum shipping weight or service design conditions.

11. References

ACI Committee 318. (2019). *Commentary on Building Code Requirements for Structural Concrete* . American Concrete Institute.

Allen, H. G., & Bulson, P. S. (1980). *Background to Buckling.* Maidenhead, Berkshire, England: McGraw-Hill Book Co. Ltd., England.

American Association of State Highway and Transportation Officials. (2017). *AASHTO LRFD Bridge Design Specifications* (Vol. 8th Edition). Washington, D.C.: American Association of State Highway and Transportation Officials.

Anderson, A. R. (1971). Lateral Stability of Long Prestressed Concrete Beams. *PCI Journal, 16*(3), 7-9.

Bairán, J. M., & Cladera, A. (2014). Collapse of a precast concrete beam for a light roof. Importance of elastomeric bearing pads in the element's stability. *Engineering Failure Analysis, 39*, 188-199.

Bleich, F. (1952). *Buckling Strength of Metal Structures.* New York, New York: McGraw-Hill Book Co., Inc.

Brice, R. (2023, March 22). Lateral Stability of Precast, Prestressed Concrete Bridge Girders. *2.0*, 1-42. Washington: WSDOT Bridge and Structures Office.

Burgoyne, T. J., & Stratford, C. J. (2001). Lateral instability of long-span prestressed concrete beams on flexible bearings. *The Structural Engineer, 79*(6), 23-26.

Chamorro-Varilla, E., & Dario Aristiazabal-Ochoa, J. (2016). Analysis of a Horizontally Curved Long-Span Beam on Two Nonlinear Elastic Supports. *Journal of Bridge Engineering, 21*(5), 040150881-1 - 04015088-14.

Cojocaru, R. (2012). *Lifting Analysis of Precast Prestressed Concrete Beams.* MS Thesis, Virginia Polytechnic Institute and State University.

Concrete Technology Corporation. (2009, August). WSDOT Wide Flange Girder Span Capabilities. 1 - 31. Tacoma, Washington.

Consolazio, G. R., Hamilton, H. R., & Beery, M. S. (2012). *Experimental Validation of Bracing Recommendations For Long-Span Concrete Girders.* University of Florida, Civil and Coastal Engineering. Gainesville, Florida: Florida Department of Transportation.

Costa, L. O., Krahl, P. A., & Lima, M. (2023). Investigation of Lateral Stability of UHPC Beams Supported by Bearing Pads Considering the Nonlinear Liftoff Effect. *Journal of Structural and Engineering, 149*(3), 04022254-1 - 04022254-14.

de la Fuente, A., Aguado, A., Molins, C., & Armengou, J. (2012). Numerical model for the analysis up to failure of precast concrete sections. *Computers and Structures, 106-107*, 105-114.

de la Fuente, A., Bairán, J. M., & Cavalaro, S. (2019). Case study of failure of long prestressed precast concrete girder during lifting. *Engineering Failure Analysis, 100*, 512-519.

Dux, P. F., & Kitpornchai, S. (1990). Buckling of Suspended I-Beams. *Journal of Structural Engineering, 116*(7), 1877-1891.

El Darwish, I. A., & Johnston, B. G. (1964). *Torsion of Structural Shapes.* University of Michigan. Industry Program of the Collete of Engineering.

Galik, W. D., Stanton, J. F., & Wiebe, R. (2022). *Lateral-Torsional-Roll Stability of Long Precast Girders.* University of Washington, Department of Civil Engineering. Seattle: Precast/Prestressed Concrete Institute.

Hansell, W., & Winter, G. (1959). Lateral Stability of Reinforced Concrete Beams. *Journal of the American Concrete Institute, 31*(3), 193-213.

Hurff, J. B. (2010). *Stability of Precast Prestressed Concrete Bridge Girders Considering Imperfections and Thermal Effects.* Doctoral Dissertation, Georgia Institute of Technology, School of Civil and Environmental Engineering.

Hurff, J. B., & Kahn, L. F. (2012). Lateral-Torsional Buckling of Structural Concrete Beams: Experimental and Analytical Study. *Journal of Structural Engineering, 138*(9), 1138-1148.

Hurff, J. B., & Kahn, L. F. (2012). Rollover stability of precast, prestressed concrete bridge girders with flexible bearings. *PCI Journal, 57*(4), 96-107.

Imper, R., & Laszlo, G. (1987). Handling and Shipping of Long Span Bridge Beams. *PCI Journal, 32*(6), 86-101.

Kent, D. C., & Park, R. (1971). Flexural Members with Confined Concrete. *Journal of the Structural Division, 97*(7), 1969-1990.

Khaleghi, B. (2021, April 20). BDM Chapter 5 - Girder Handling Stresses and Stability. 1-5. Washington: Washington State Department of Transportation Bridge and Structures Office.

Krahl, P. A., Carrazedo, R., & El Debs, M. K. (2018). Analytical solutions for rollover instability of concrete beams on elastomeric bearing pads. *Engineering Structures, 174*, 154-164.

Krahl, P. A., Lima, M., & El Debs, M. K. (2015). Recommendations for verifying lateral stability of precast beams in transitory phases. *Ibracon Structures and Materials Journal, 8*(6), 763-774.

Krahl, P. A., Martins, D. O., Carrazedo, R., Silva, I., & El Debs, M. K. (2019). Experimental and analytical studies on the lateral instability of UHPFRC beams lifted by cables. *Composite Structures, 209*, 652-667.

Krahl, P. A., Oliveira, M., Siqueira, G. H., & Lima, M. (2020). Analytical Nonlinear Rollover Behavior of Cambered Precast Concrete Beams on Flexible Supports. *Journal of Structural Engineering, 146*(2), 04019200-1 - 04019200-11.

Lebelle, P. (1959, Setembre). Stabilite elastique des poutres en beton precontraint a l'egard du deversement lateral. *12*(141), 778-831.

Lee, J. H. (2012). Behavior of precast prestressed concrete bridge girders involving thermal effects and initial imperfections during construction. *Engineering Structures, 42*(1-8).

Lee, J. H. (2017). Evaluation of the lateral stability of precast beams on an elastic bearing support with a consideration of the initial sweep. *Engineering Structures, 143*, 101-112.

Lee, J. H., Kalkan, I., Lee, J. J., & Cheung, J. H. (2017). Rollover instability of precast girders subjected to wind load. *Magazine of Concrete Research, 69*(2), 68-83.

Lima, M., & El Debs, M. K. (2005). Numerical and experimental analysis of lateral stability in precast concrete beams. *Magazine of Concrete Researcch, 57*(10), 635-647.

Mandal, P., & Calladine, C. R. (2002). Lateral-torsional buckling of beams and the Southwell Plot. *Internation Journal of Mechanical Sciences, 44*(12), 2557-2571.

Mast, R. F. (1989). Lateral Stability of Long Prestressed Concrete Beams, Part 1. *PCI Journal, 34*(1), 34-54.

Mast, R. F. (1993). Lateral Stability of Long Prestressed Concrete Beams, Part 2. *PCI Journal, 38*(1), 70-88.

Mast, R. F. (1994). Lateral Bending Test to Destruction of a 149 ft Prestressed Concrete I-Beam. *PCI Journal, 39*(4), 54-62.

Meck, H. R. (1977). Experimental Evaluation of Lateral Buckling Loads. *ASCE Journal of Engineering Mechanics, 103*(2), 331-337.

Menegotto, M., & Pinto, P. (1973). Methods of Analysis for Cyclically Loaded Reinforced Concrete Plane Frames Including Changes in Geometry and Non-elastic Behavior of Elements under Combined Normal Force and Bending. *IABSE Symposium on the Resistancce and Ultimate Deformability of Structures Acted on by Well-defined Loads.* Lisbon.

Muller, J. (1962). Lateral Stability of Precast Members During Handling and Placing. *PCI Journal, 7*(1), 20-31.

Naaman, A. E. (2012). *Prestressed Concrete Analysis and Design: Fundamentals* (3rd Edition ed.). Techno Press 3000.

Oesterle, R. G., Sheehan, M. J., Lotfi, H. R., Corley, W. G., & Roller, J. J. (2007). *Investigation of Red Mountain Freeway Bridge Girder Collapse.* CTLGROUP Project No. 262291. Arizona Department of Transportation, Bridge Group.

Oliveira, M., Krahl, P. A., & Lima, M. (2020). Parametric analysis of analytical solutions of the rollover of precast beams on bearing pads. *Ibracon Structures and Materials Journal, 13*(5), 1-20.

Peart, W. L., Rhomberg, E. J., & James, R. W. (1992). Buckling of Suspended Cambered Girders. *Journal of Structural Engineering, 118*(2), 505-528.

Plaut , R. H., Moen, C. D., & Cojocaru, R. (2011). Beam Deflections and Stresses During Lifting. *Proceedings of the Annual Stability Conference: Structural Stability Research Council*, (pp. 1-9).

Plaut, R. H., & Moen, C. D. (2013). Analysis of Elastic, Doubly Symmetric, Horizontally Curved Beams during Lifting. *Journal of Structural Engineering, 139*(1), 39-46.

Plaut, R. H., & Moen, C. D. (2014). Stability of unbraced concrete beams on bearing pads including wind loading. *Engineering Structures, 69*, 246-254.

Popovics, S. (1970). A Review of Stress-Strain Relationships for Concrete. *ACI Journal Proceedings*, *67*, pp. 243-248.

Precast/Prestressed Concrete Institute. (2016). *Recommended Practice for Lateral Stability of Precast Prestressed Concrete Bridge Girders.* Chicago.

Precast/Prestressed Concrete Institute. (2020). *User Manual for Calculating the Lateral Stability of Precast, Prestressed Concrete Bridge Girders.* Precast/Prestressed Concrete Institute.

Precast/Prestressed Concrete Institute. (2023). *Bridge Design*. Retrieved 2022-2023, from Precast/Prestressed Concrete Institute: https://www.pci.org/BridgeDesign

Raynor, D. J., Lehman, D. L., & Stanton, J. F. (2002, September). Bond-Slip Response of Reinforcing Bars Grouted in Ducts. *ACI Structures Journal, 99*(5), 568-576.

Reis, L. C., Krahl, P. A., & Lima, M. (2020). Numerical analysis of the effective stiffness of elastomeric bearing pads under precast beams for the limit load of lateral instability. *Ibracon Structures and Materials Journal, 13*(1), 95-107.

Siev, A. (1960). The Lateral Buckling of Slender Reinforced Concrete Beams. *Magazine of Concrete Research, 12*(36), 155-164.

Southwell, R. V. (1932). On the Analysis of Experimental Observations in Problems of Elastic Stability. *Proceedings of the Royal Society of London, Series A*, *135*, pp. 601-616. London.

Stanton, J. F., Roeder, C. W., Mackenzie-Helnwein, P., White, C., Kuester, C., & Craig, B. (2008). *Rotation limits for elastomeric bearings.* Washington, D.C.: Transportation Research Board.

Stratford, T. J., & Burgoyne, C. J. (1999). Lateral Stability of Long Precast Concrete Beams. *Proceedings of the Institution of Civil Engineers: Structures and Buildings*, *124*, pp. 169-180.

Stratford, T. J., & Burgoyne, C. J. (1999). The toppling of hanging beams. *International Journal of Solids and Structures, 37*, 3569-3589.

Stratford, T. J., Burgoyne , C. J., & Taylor, H. J. (1999). Stability Design of Long Precast Concrete Beams. *Proceedings of the Institution of Civil Engineers: Structures and Buildings*, *134*, pp. 159-168.

Swann, R. A., & Godden, W. G. (1966). The lateral buckling of concrete beams lifted by cables. *The Structural Engineer, 44*, 21-33.

Tarnai, T. (1978). Variational Methods for Analysis of Lateral Buckling of Beams Hung at Both Ends. *International Journal of Mechanical Sciences, 21*, 329-337.

Thorenfeldt, E., Tomaszewicz, A., & Jensen, J. J. (1987). Mechanical Properties of High Strength Concrete and Application to Design. *Proceedings of the Symposium: Utilization of High Strength Concrete*, (pp. 140-159). Stavangar, Norway.

Timoshenko, S. P., & Gere, J. M. (1961). *Theory of Elastic Stability* (2nd Edition ed.). New York: McGraw-Hill Book Co., Inc.

Trahair, N. S. (1993). *Flexural-Torsional Buckling of Structures.* London: E & FN Spon.

Tremblay, R., & Mitchell, D. (2006). Collapse during Construction of a Precast Girder Bridge. *Journal of Performance of Constructed Facilities, 20*(2), 113-125.

Vacharajittiphan, P., Woolcock, S. T., & Trahair, N. S. (1974). Effect of In-Plane Deformation on Lateral Buckling. *Journal of Structural Mechanics, 3*(1), 29 - 60.

West, C. (2019). Prestressed Concrete Girders Achieve Record Lengths. *Aspire, the Concrete Bridge Magazine*, pp. 56-57.

WSDOT Bridge and Structures Office. (2022). *WSDOT Bridge Design Manual (LRFD).* Washington State Department of Transportation.

Yazdani, N., Eddy, S., & Cai, C. S. (2000). Effect of Bearing Pads on Precast Prestressed Concrete Bridges. *Journal of Bridge Engineering, 5*(3), 224-232.

12.Notations and Abbreviations

12.1. List of Notations

- A *Area*
- A_{gr} *Gross Area*
- A_{tr} *Transformed Area*
- E *Modulus of Elasticity*
- E_c *Concrete Modulus of Elasticity*
- F_{pj} *Prestressing Jacking Force*
- G *Shear Modulus*
- I_{eff} *Effective Cracked Moment of Inertia*
- I_{gr} *Gross Moment of Inertia*
- I_{tr} *Transformed Moment of Inertia*
- I_{xx} *Strong-Axis Moment of Inertia*
- I_{yy} *Weak-Axis Moment of Inertia*
- J *Polar Moment of Inertia*
- K_{xx} *Coeff. Relating Moments to Curvatures for Cracking Analysis*
- K_{xy} *Coeff. Relating Moments to Curvatures for Cracking Analysis*
- K_{yx} *Coeff. Relating Moments to Curvatures for Cracking Analysis*
- K_{yy} *Coeff. Relating Moments to Curvatures for Cracking Analysis*
- K_1 *Aggregate Correction Factor (AASHTO, LRFD)*
- K_ϕ *Total Support Stiffness*
- $K_{\phi,supp}$ *Support Rotational Spring Stiffness*
- L *Length*
- M_g *Gravity Moment*
- M_{glo} *Global Moment*
- M_{gx} *x-Axis Gravity Moment*
- M_{gy} *y-Axis Gravity Moment*
- M_{loc} *Local Moment*
- M_{px} *x-x Axis Prestressing Moment*
- M_{ss} *s-s Axis Moment for Cracking Analysis*
- M_{tt} *t-t Axis Moment for Cracking Analysis*
- $M_{xx,loc}$ *Local x-x Axis Moment*
- $M_{yy,loc}$ *Local y-y Axis Moment*
- $M_{z,o}$ *Initial Torsional Moment*
- N *Number of Temp. Top Strands in Standard Configuration*
- N *Ratio of* $-_p/q_{LRB,o}$
- P *Axial Load Applied to Column*
- P_{cr} *Column Buckling Load*
- R *Support Reaction*
- $R_{x,o}$ *Initial Reaction in x-direction*

- $R_{y,o}$ *Initial Reaction in y-direction*
- S_o *Vector Sum of Section Moduli for ϕ_{crack} or ϕ_{comp} Calculation*
- S_{x2} *x-Axis Section Modulus for Top of Cross-Section*
- S_{x1} *x-Axis Section Modulus for Bottom of Cross-Section*
- $S_{yA,bot}$ *y-Axis Section Modulus for Bottom-Right of Cross-Section*
- $S_{yA,top}$ *y-Axis Section Modulus for Top-Right of Cross-Section*
- $S_{yB,bot}$ *y-Axis Section Modulus for Bottom-Left of Cross-Section*
- $S_{yB,top}$ *y-Axis Section Modulus for Top-Left of Cross-Section*
- T *Torque*
- W *Total Weight of Girder*
- c *Algebraic Substitution for $f_{cr,net}/f_{g2}$*
- c_j *Intermediate Factor for Calculating $f_{LRB}(\alpha, t)$*
- e_x *Init. x-Ecc. of Reaction (Lift. Loop or Ecc. Placement on Bearing)*
- e_y *Initial y-Eccentricity of Reaction*
- f_c' *Concrete Strength*
- f_{ci}' *Initial Concrete Strength*
- $f_{comp,net}$ *Reserve Comp. Stress Until Allowable Limit, Pre-Gravity Loading*
- $f_{cr,net}$ *Reserve Tensile Stress Until Cracking, Pre-Gravity Loading*
- f_{cr} *Concrete Cracking Stress*
- f_{g2} *Ratio of M_g/S_{x2}*
- f_{pu} *Prestressing Strand Ultimate Strength*
- f_r *Rupture Modulus*
- f_u *Steel Ultimate Strength*
- f_y *Steel Yield Strength*
- $f_{LRB}(\alpha)$ *Factor Accounting for Symmetric Overhangs' Effect on LRB*
- $f_{LRB}(\alpha, t)$ *Factor Accounting for Asymmetric Overhangs' Effect on LRB*
- $f_{LTB}(\alpha)$ *Factor Accounting for Symmetric Overhangs' Effect on LTB*
- $g(\eta)$ *Factor Accounting for Torsion's Effect on Buckling Load*
- h *Height of Girder*
- k_e *Effective Stiffness in RLM Derivation*
- k_u *Lateral Stiffness in RLM Derivation*
- k_v *Vertical Stiffness in RLM Derivation*
- k_ϕ *Torsional Stiffness in RLM Derivation*
- $m_z(z)$ *Applied Torque Function Along Girder's Length*
- $q_{LRB,o}$ *Baseline LRB Load*
- $q_{LRB,v}$ *LRB Load Accounting for Strong-Axis Bending Deflections*
- $q_{LRB,vp}$ *LRB Load Accounting for Strong-Axis Bending and Prestressing*
- $q_{LRB,vp\alpha}$ *LRB Load Accounting for SAB, Prestressing, and Overhangs*
- $q_{LRB,\alpha}$ *LRB Load Accounting for Overhangs*
- $q_{LTB,o}$ *Baseline LTB Load*
- $q_{LTB,v}$ *LTB Load Accounting for Strong-Axis Bending Deflections*

- $q_{LTB,vp}$ *LTB Load Accounting for Strong-Axis Bending and Prestressing*
- $q_{LTB,vp\alpha}$ *LTB Load Accounting for SAB, Prestressing, and Overhangs*
- $q_{LTB,\alpha}$ *LTB Load Accounting for Overhangs*
- $q_{LTRB,o}$ *Baseline LTRB Load*
- $q_{LTRB,vp}$ *LTRB Load Accounting for Strong-Axis Bending and Prestressing*
- $q_{LTRB,vp\alpha}$ *LTRB Load Accounting for SAB, Prestressing, and Overhangs*
- $q_{LTRB,\alpha}$ *LTRB Load Accounting for Overhangs*
- q *Applied Load per Length (Typically Vertical Load)*
- q_{cr} *Generic Term for Critical Load*
- q_p *Equivalent Uniform Upwards Load Due to Prestressing per Length*
- $q_{p,bal}$ *Equiv. Upwards Prestressing Load that Balances SAB Deflections*
- $q_{p,unstable}$ *Equiv. Upwards Prestr. Load Unconditionally Causing Buckling*
- q_{sw} *Self-Weight Load per Length*
- q_x *Applied Load in x-Direction*
- q_y *Applied Load in y-Direction*
- r_y *y-Axis Radius of Gyration*
- $s_j(t)$ *Intermediate Factor for Calculating* $f_{LRB}(\alpha, t)$
- t *Asymmetric Overhang Factor*
- u *Lateral Deflection, Generic*
- u_{glo} *Global Lateral Deflection*
- u_{loc} *Local Lateral Deflection*
- $u_{loc,i}$ *Initial Local Lateral Imperfection*
- $u_o(z)$ *Lateral Deflected Shape Function Along Girder Length*
- u_{sweep} *Maximum Lateral Sweep Deflection*
- $\overline{u}$ *Average Lateral Deflection Relative to Girder End*
- $\overline{u}_{sweep}$ *Average Lateral Sweep Deflection Relative to Girder End*
- $\overline{u}_{sweep,\alpha}$ *Average Lateral Sweep Deflection Relative to Support*
- v'' *Curvature*
- v_{glo} *Global Vertical Deflection*
- v_{loc} *Local Vertical Deflection*
- $v_{loc,i}$ *Initial Local Vertical Imperfection*
- $v_o(z)$ *Vertical Deflected Shape Function Along Girder Length*
- $v_{p,max}$ *Maximum Prestressing Deflection*
- $\overline{v}$ *Average Vertical Deflection Relative to Girder End*
- $\overline{v}_p$ *Average Prestressing Deflection Relative to Girder End*
- $\overline{v}_{p,\alpha}$ *Average Prestressing Deflection Relative to Support*
- w_c *Concrete Density*
- w_{glo} *Global Longitudinal Deflection*
- w_{loc} *Local Longitudinal Deflection*
- x_{glo} *Global x-coordinate*
- x_{loc} *Local x-coordinate*

- y_{bot} *Distance from Center of Gravity to Bottom of Girder*
- y_{glo} *Global y-coordinate*
- y_{loc} *Local y-coordinate*
- y_r *Roll-Axis Height from Center of Gravity*
- $y_{r,eff}$ *Effective Roll-Axis Height for Asymmetric Overhangs*
- $y_{r,eq}$ *Equivalent Hanging Girder Roll-Axis Height*
- y_{top} *Distance from Center of Gravity to Top of Girder*
- y_{truck} *Distance from Center of Gravity to Rot. Stiff Truck Support*
- z_{glo} *Global z-coordinate*
- z_{loc} *Local z-coordinate*
- $\Delta_{add,p}$ *Additional Long-Term Prestressing Deflections*
- $\Delta_p(\alpha)$ *Prestressing Deflection at Supports Relative to Ends*
- $\Delta_{ps,i}$ *Initial Prestressing Deflection*
- $\Delta_{sw,i}$ *Initial Self-Weight Deflection*
- $\Delta_u(\alpha)$ *Lateral Sweep Deflection at Supports Relative to Ends*
- $\overline{\Delta}_x$ *Flexibility Coefficient for Average x-Deflection*
- Π *Total Potential Energy*
- α *Overhang Ratio*
- α *Roadway Cross Slope Angle*
- α *Angle of s-t Axes Relative to $x_{loc} - y_{loc}$ Axes*
- α_1 , α_2 *Asymmetric Overhang Ratios*
- β *Unitless Parameter for Calc. Torsion's Effect on Buckling Load*
- γ_c *Concrete Density*
- δ *Amplified Imperfection Deflection for Axially Loaded Column*
- δ_o *Initial Imperfection in Axially Loaded Column*
- ζ *Ratio of x/L*
- η_o *Intermediate Parameter for Calc. Torsion's Effect on Buck. Load*
- η_{vp} *η_o Accounting for SAB and Prestressing Deflections*
- $\eta_{vp\alpha}$ *η_o Accounting for SAB and Prestressing Defl. and Overhangs*
- η_α *η_o Accounting for Overhangs*
- θ *Roll Angle in Mast's (1989, 1993) Notation*
- κ *Load Parameter: $q/\sqrt{GJEI_{yy}}$*
- κ_{glo} *Global Curvature*
- κ_{loc} *Local Curvature*
- κ_{Mast} *Mast (1993) Knockdown Factor for Eff. Cracked Mom. of Inertia*
- κ_{ss} *s-s Axis Curvature for Cracking Analysis*
- κ_{tot} *Total Curvature*
- κ_{tt} *t-t Axis Curvature for Cracking Analysis*
- $\kappa_{xx,loc}$ *Local x-Curvature*
- $\kappa_{yy,loc}$ *Local y-Curvature*
- λ *Factor Accounting for LWC Effects*
- ϕ *Tilt Angle; Either Roll Only or Roll and Twist Together*

- ϕ_{crack} *Onset of Cracking Angle*
- ϕ_{eq} *Final Equilibrium Angle of Girder*
- ϕ_i *Initial Roll Imperfection*
- ϕ_o *Initial Roll Angle*
- ϕ_r *Roll Angle*
- ϕ_{roll} *Roll Angle*
- ϕ_{twist} *Twist Angle*
- $\hat{\phi}_{comp}$ *Approximate Allowable Compressive Stress Failure Angle*
- $\hat{\phi}_{crack}$ *Approximate Onset of Cracking Angle*
- ψ *Arctangent of $S_{yA,top}$ to S_{x2}*
- ψ_{comp} *Arctangent of $S_{yB,bot}$ to S_{x1}*

12.2. **List of Abbreviations**

- *AASHTO* *American Association of State and Highway Transportation Officials*
- *ABC* *Accelerated Bridge Construction*
- *BT* *Bulb Tee*
- *CTC* *Concrete Tech Corporation*
- *DBT* *Deck Bulb Tee*
- *DCR* *Demand-to-Capacity Ratio*
- *FEM* *Finite Element Method*
- *LRB* *Lateral-Roll Buckling*
- *LRFD* *Load-Resistance-Factored Design*
- *LTB* *Lateral-Torsional Buckling*
- *LTRB* *Lateral-Torsional-Roll Buckling*
- *LWC* *Lightweight Concrete*
- *NA* *Neutral Axis*
- *NWC* *Normal-weight Concrete*
- *PCI* *Precast/Prestressed Concrete Institute*
- *RB* *Rollbuck*
- *RLM* *Rigid Link Model*
- *SAB* *Strong-Axis Bending*
- *SAM* *Simple Amplification Model*
- *ST* *Sound Transity*
- *UHPC* *Ultra-High-Performance-Concrete*
- *UHPFRC* *Ultra-High-Performance-Fiber-Reinforced-Concrete*
- *UTC* *University Transportation Center*
- *WF* *Wide Flange*
- *WSDOT* *Washington State Department of Transportation*

13. Appendices

13.1. Appendix A: Description of the Rollbuck Program

13.1.1. Program Goals

Rollbuck is a computer program that computes the lateral-torsional response of a girder that is partially restrained against rolling about its longitudinal axis. The intended application is investigations of the behavior of prestressed concrete girders during lifting, handling and transportation. The analysis includes cracking of the girder in its tilted, or rolled, configuration. The girder is prismatic, and symmetric about its vertical axis.

The program was first written to address uncracked girders, but it was later extended to include cracking. Cracking adds considerable complexity, so the uncracked analysis is described first in Appendix A Section 13.1.2. The modifications to incorporate cracking are described in Appendix A Section 13.1.4.

13.1.2. Uncracked Analysis

13.1.2.1. Overall Program Structure

The program computes the response of a girder to loads, when it is supported in such a way that it is partially free to rotate about the "roll axis", defined as the straight line joining the two support points. Equilibrium is established in the deformed configuration. The program computes the nonlinear response but cannot conduct an eigenvalue analysis.

The program uses two separate calculation loops, which are nested inside one main loop.as illustrated in Figure *13.1*

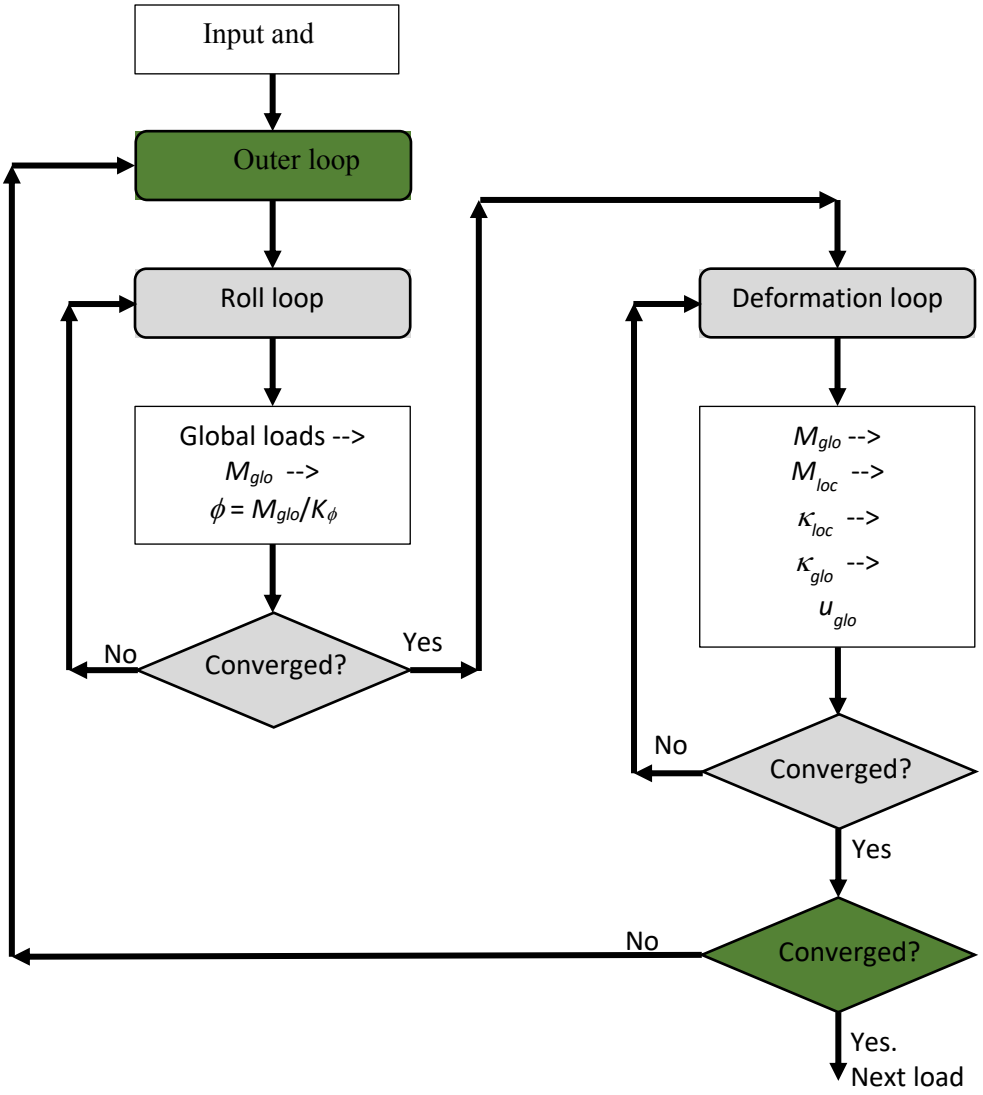

Figure 13.1. Rollbuck Program structure

The main, outer-level, loop iterates to achieve both equilibrium and a converged shape derived from the moments and curvatures. Inside that loop are the "roll" and "deformation" loops. The "roll loop" iterates to achieve rotational equilibrium assuming that the girder rolls as a rigid body about its roll axis but is "frozen" in the deformed shape that is inputted to start the loop. The "deformation loop" iterates to find a deformed shape that is consistent with the applied loads, with no change in the roll. Separate convergence controls exist for the outer loop, and the two inner loops.

The girder is statically determinate, which allows the aforementioned approach to be used. In the roll loop, only the roll angle is calculated, and that calculation has only a single degree of freedom, being based on moment equilibrium about the longitudinal axis. In the deformation loop, the moments are obtained directly by statics, and the deformations can be found directly using the member rigidities. At no point is there a need to formulate or solve a stiffness matrix.

Two sets of axes are used: a fixed, global set, $x_{glo}, y_{glo}, x_{glo}$ and a local set of axes, $x_{loc}, y_{loc}, x_{loc}$, that travels with the girder, including the roll rotation. The origin is the girder center of gravity at one support. For a monosymmetric girder, this allows the local curvatures to be computed as the local moments divided by the bending stiffness, EI_{xx} or EI_{yy}. The sequence used is:

- Global Loads --> (*Global Equilibrium, using Global Displaced Shape*)
- Global Moments --> (*Co-Ordinate Transformation, Global-to-Local*)
- Local Moments --> (*Member Stiffnesses*)
- Local Curvatures --> (*Co-Ordinate Transformation, Local-to-Global*)
- Global Curvatures --> (*Integration*)
- Global Displacements.

13.1.3. **Detailed Program Architecture**

13.1.3.1. Function Map

A general schematic and map of the functions that make up the program, including those needed for cracking, is shown in Figure *13.2*. The details of each sub-routine are not shown, but there are many moving pieces and interacting parts in Rollbuck, especially when cracking is included.

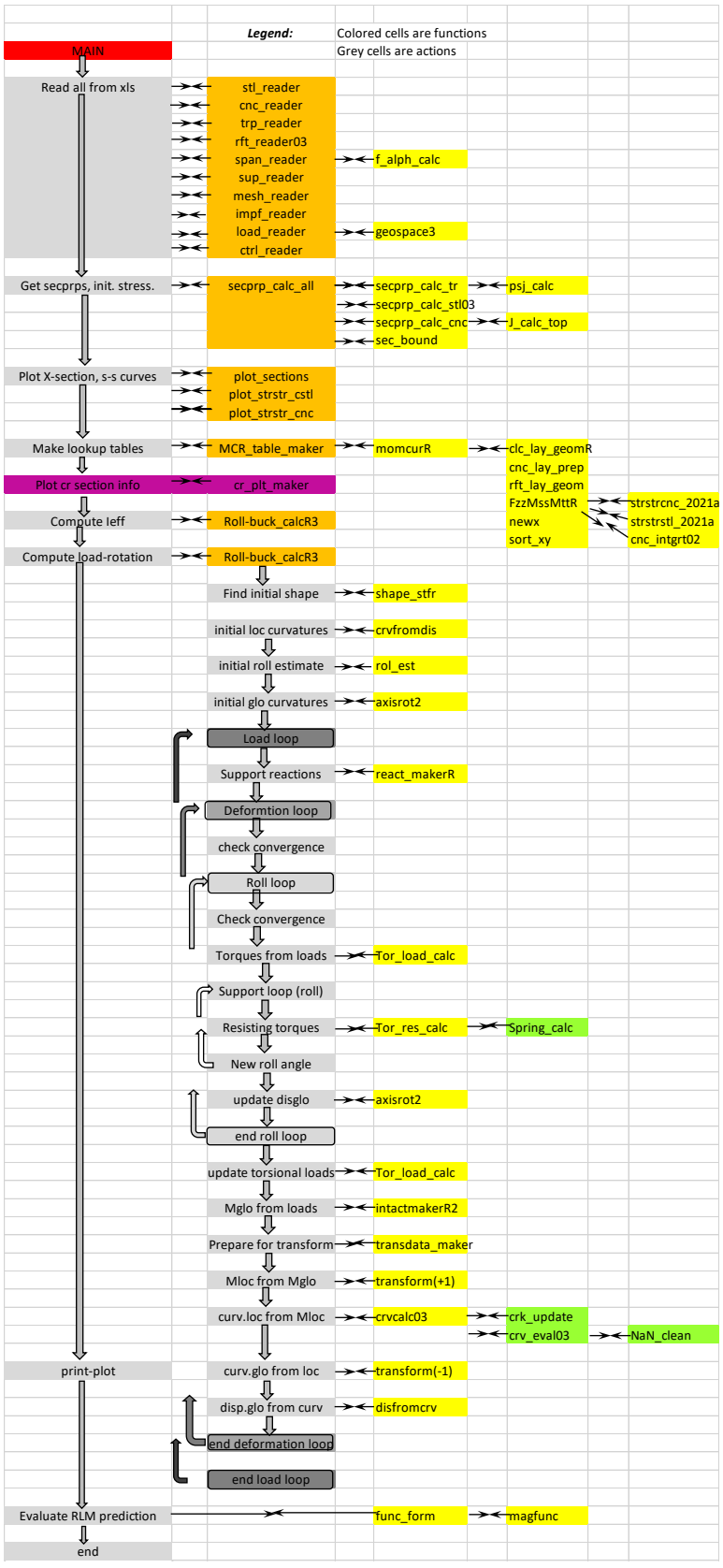

Figure 13.2. Program Function Map

13.1.3.2. Discretization

The girder is modeled by "beam" elements, each of which has properties EI_{xx}, EI_{yy}, GJ. Shear deformations and warping are ignored. The mesh of nodes may be non-uniform, and the element sizes are selected by the user.

13.1.3.3. Member Properties

At present the girder is modeled as prismatic. However, that could be changed (at the expense of more complex input and longer run time), without great difficulty. The coordinates defining the shape of the cross-section are read from an input file, and the program computes the member properties EI_{xx}, EI_{yy}, GJ. For the bending stiffnesses it uses the transformed properties. For GJ, it uses the approximate method developed (for steel I-beams) by Darwish and Johnston (1964), based on the gross concrete geometry. For a typical WSDOT WF series girder, it was found to give results within approximately 5% of those obtained using a fine-mesh Prandtl-FEA calculation.

13.1.3.4. Treatment of Supports

The supports must be able to represent either of two cases: a girder suspended above from cables, or a girder supported from below (e.g. on a truck). In general, the cable-supported case will not have an explicitly rotationally stiff spring, but it will have positive "pendulum stiffness" by virtue of the supports being above the center of gravity. The support is typically at a lifting loop, which is approximately at the top of the girder. The truck-supported case has a negative pendulum stiffness, because the support point is below the girder, but it has a large

rotational spring stiffness (the rotational stiffness of the truck's suspension). The rotational spring stiffness and the vertical location of the support can be explicitly defined in the program.

If the girder is longitudinally symmetric, for example, with equal overhangs beyond each support point, the roll angles at the two supports will be equal. For a non-symmetric configuration, the rigid body roll calculation results in a single roll angle such that the total applied roll moment is equal to the total resisting moment at the two supports, each of which is derived from the relevant support stiffness. The support spring stiffnesses may be nonlinear (to simulate nonlinearity in a bearing or truck suspension's stiffness).

13.1.3.5. Prestressing and Initial Deformed Shape

The prestressing is entered as the jacking stress, and the program computes the deformed shape, and the remaining prestress, after elastic shortening. It does not compute non-elastic losses, such as creep or shrinkage. If they are to be included, they should be represented by use of an artificially low jacking stress. In addition, an initial "stress-free" shape may be defined, to simulate built-in vertical camber (other than the camber due to prestressing) or lateral sweep. Eccentricities of support reactions, to represent either lifting loop eccentricity or eccentric placement on a bearing support, may also be defined.

13.1.3.6. Controlled Roll Option

The program allows the user to conduct a "controlled roll test". This is achieved, at both supports, by supporting the girder at its center of gravity and providing a rotational spring, with a high stiffness, K_z, there. A global moment, M_z is then applied at each support. It causes a roll angle of approximately M_z/K_z, if K_z is much larger than the torsional moment from the self-weight acting at the lateral eccentricity associated with the deformed shape at the time. This

feature was incorporated to permit simulations of physical controlled roll tests, such as was done by Mast (1993, 1994).

13.1.3.7. Running the Program

The program is written in MATLAB, but the input is read from an Excel sheet. This allows the input to be readily organized and changed, without the need to edit the program. This was seen as necessary because, especially with the cracked section analysis described in the following section, the inputs become quite extensive. For example, both the x and y locations of every strand are needed, to allow calculation of the vertical and lateral bending from the prestressing.

13.1.4. **Cracked Analysis**

13.1.4.1. Overview

When the concrete cracks, the moment-curvature relationships about the x and y axes become nonlinear. In the uncracked analysis, those relationships were formulated about the local axes, because that separated the two relationships. That choice was maintained for the cracked analysis. However, the relationships about the x and y axes are now linked. This is illustrated by Equations (A – 1) and (A – 2) in which, for the uncracked case represented by Equation (A – 1) the matrix is diagonal (and the elements are constant) but, for the cracked case of Equation (A – 2) the matrix is full and its elements are all functions of the two moments, $M_{xx,loc}$ and $M_{yy,loc}$.

$$\begin{bmatrix} EI_{xx} & 0 \\ 0 & EI_{yy} \end{bmatrix} \begin{pmatrix} \kappa_{xx,loc} \\ \kappa_{yy,loc} \end{pmatrix} = \begin{pmatrix} M_{xx,loc} \\ M_{yy,loc} \end{pmatrix}. \qquad (A-1)$$

$$\begin{bmatrix} K_{xx} & K_{xy} \\ K_{yx} & K_{yy} \end{bmatrix} \begin{pmatrix} \kappa_{xx,loc} \\ \kappa_{yy,loc} \end{pmatrix} = \begin{pmatrix} M_{xx,loc} \\ M_{yy,loc} \end{pmatrix} \qquad (A-2)$$

For the cracked case, the moment-curvature relationship is highly nonlinear, and can be generated only by choosing curvature and calculating moment. However, here the moment is known, and the curvature is sought, so the problem is reversed. It is further complicated by the fact that the orientation angle of the neutral axis is not directly related to the roll angle of the girder, and thus, implicitly, to the ratio $M_{yy,loc}/M_{xx,loc}$.

13.1.4.2. Use of Lookup Tables

The problem is solved here by creating, at the start of the analysis, "lookup tables" relating moment to curvature; these are subsequently used at each step of the iteration during program execution.

A third set of axes, labeled s and t is defined, with s measured parallel to the neutral axis and t normal to it. The direction s makes an angle α with the local x direction. The axes are illustrated in Figure 13.3. Then, for any chosen angle, α, a moment-curvature analysis is conducted. In that analysis, the curvature κ_{ss} is equal to the total curvature, κ_{tot}, and $\kappa_{tt} = 0$. However, because the neutral axis cuts through the cross-section at an angle α , and the cross-section in the $s - t$ set of axes is consequently asymmetric, $M_{tt} \neq 0$. The procedure is:

- Choose a NA orientation, α.
- Conduct a moment-curvature analysis in the $s - t$ space, recording M_{ss} and M_{tt} for each κ_{tot}.
- At each step, convert the moment pairs (M_{ss},M_{tt}) into pairs ($M_{xx,loc}$, $M_{yy,loc}$) by means of a coordinate transformation.
- For each (α, κ_{tot}) pair, record $(\alpha, \kappa_{tot}, M_{xx,loc})$ and $(\alpha, \kappa_{tot}, M_{yy,loc})$

The result is two tables, one of $M_{xx,loc}(\alpha, \kappa_{tot})$ and the other of $M_{yy,loc}(\alpha, \kappa_{tot})$. These may be plotted as contour plots, if so desired. Figure *13.4* illustrates the outcome.

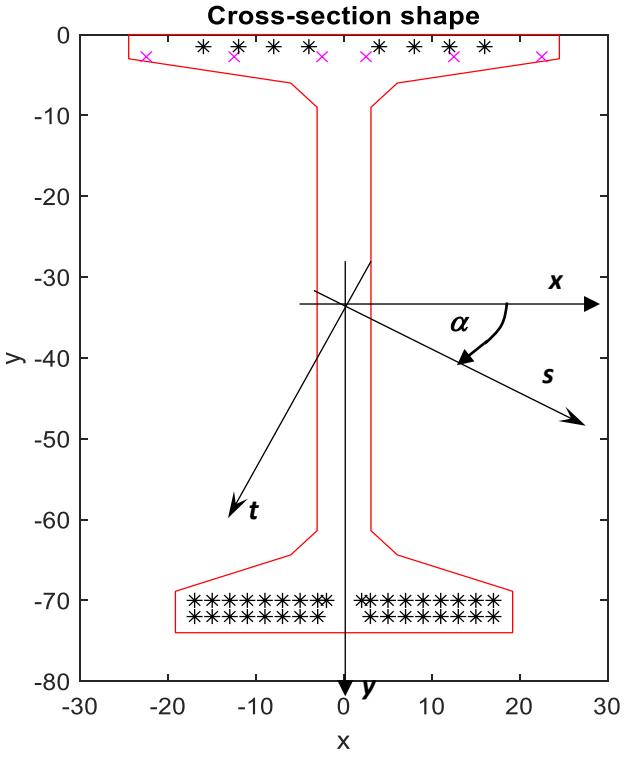

Figure 13.3 s-t Co-Ordinate Axis

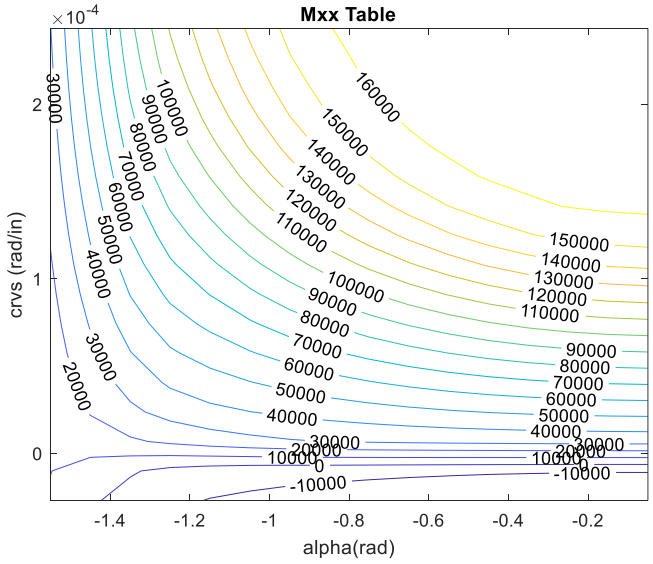

Figure 13.4 Contour plot of $M_{xx,loc}$

13.1.4.3. Details of Moment Curvature Analysis

Within the moment-curvature analysis, moments must be established when the neutral axis is oriented at an angle α with respect to the local axes of the cross-section. The usual approach, with the NA horizontal, is to divide the cross-section into trapezoidal layers, with the top and bottom horizontal, then to conduct a one-dimensional search to find the NA location that results in zero axial force. The internal force and moment are established by computing stress from strain at each trapezoid face, then integrating. That basic approach was adopted here, but it was slightly modified because the layers are no longer parallel to the girder axes. They are also discontinuous in width, as shown in Figure 13.5 which leads to complications in defining the shape of the individual regions of each layer. The solution adopted here was to use the rectangle rule for integration of the concrete layers, with a relatively fine mesh of layers. Then, only the points at which the layer centers intersected the cross-section outline were needed. Trial and error showed that the cracked properties could be established within acceptable tolerances when more than about 100 layers were used to characterize the cross-section.

Note that both M_{ss} and M_{tt} are needed. For M_{ss}, the locations at which the layer intersects the cross-section boundary are needed, because they influence the lever arm for moments in that direction, while for M_{tt} they are not needed.

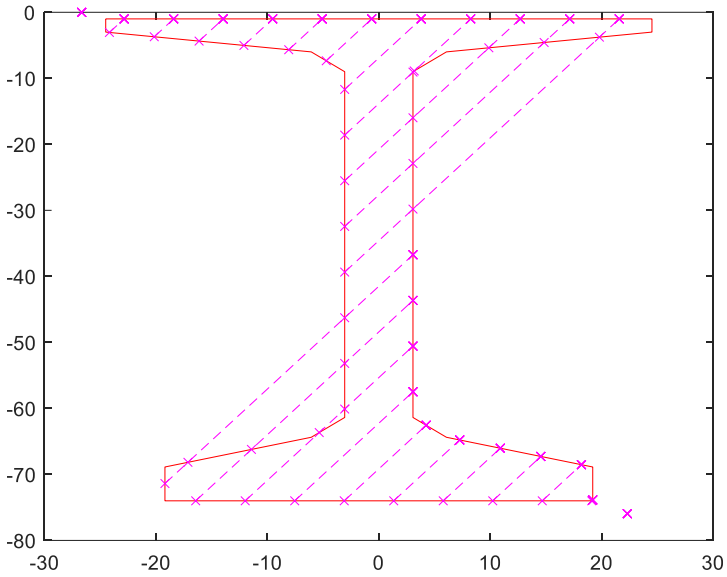

Figure 13.5 Integration layers (shown with 20 layers)

The steel force, for each bar or strand, was found from the strain, constitutive law, and area for each bar. This had to be done for each bar individually, rather than grouping them in layers, to account for the lateral bending when the roll angle was non-zero.

13.1.4.4. Material Constitutive Models

The program contains four constitutive model options for concrete:

- Linear
- Cubic
- Original Popovics (1970) Model
- Popovics Model, as modified by Thorenfeldt, et al (1987)

The linear and cubic models use those polynomials to define the rising part of the curve. Post-peak, the stress drops off linearly until it reaches a constant value, as was done by Kent and

Park (1971). The cubic is the simplest polynomial that allows the user to choose the stress and strain at the peak, and the initial tangent modulus.

Three steel models are available. Each may be used with or without prestress.

- The Raynor (2002) model: Intended for non-prestressed bars, it has parameters that allow the strain hardening of deformed bar steel to be mimicked with reasonable accuracy.
- The Menegotto-Pinto (1973) model: it has been used extensively for strand.
- The PCI model is also intended for use with strand.

The program allows different steel *types* to be defined. Each type may use any of the constitutive models, but still have its own parameters. Thus, for example, two types of steel may be defined, both using the Raynor model, but one has a yield stress of 60 ksi and the other a yield stress of 100 ksi.

13.1.4.5. Finding Curvatures from Moments in Rollbuck

During the execution of the deformation loop in Rollbuck, the local moments $M_{xx,loc}$ and $M_{yy,loc}$ are known and the corresponding local curvatures are needed. The solution procedure is to find (numerically) the contour lines, in terms of (α, κ_{tot}), in the two tables (see, for example, Figure *13.4*) that represent constant values of the relevant $M_{xx,loc}$ and $M_{yy,loc}$, then to find the point (α, κ_{tot}) where those two contour curves intersect. The process involves interpolation between the points in the tables. At that intersection point the (α, κ_{tot}) pair is such that the two local moments have the desired values. The corresponding local curvatures are then

$$\begin{pmatrix} \kappa_{xx,loc} \\ \kappa_{yy,loc} \end{pmatrix} = \begin{bmatrix} \cos\alpha & -\sin\alpha \\ \sin\alpha & \cos\alpha \end{bmatrix} \begin{pmatrix} \kappa_{ss} \\ \kappa_{tt} \end{pmatrix} \qquad (A-3)$$

where $\kappa_{ss} = \kappa_{tot}$ and $\kappa_{tt} = 0$. This process was adopted because it minimizes the iteration that would otherwise be required at each point in the deformation loop, at the expense of creating the look-up tables at the start. The benefits of the choice are greatest when many load points are used, resulting in frequent calls on the relationship between local moments and curvatures. The cracked analysis takes longer to run than the uncracked analysis, but the run time is not unreasonably long. For the rollover analysis mentioned in Appendix A Section 13.1.3.6, the run time was typically less than 10 minutes.

If the curves do not intersect, either the beam has failed or the ranges of κ_{tot} and α chosen to create the lookup tables were too small.